Studies of Baryon Content and Gravitational Lensing Effects in Galaxy Clusters

I-Non Chiu

Munich 2016

Studies of Baryon Content and Gravitational Lensing Effects in Galaxy Clusters

I-Non Chiu

Dissertation
an der Faculty of Physics
der Ludwig–Maximilians–Universität
München

vorgelegt von
I-Non Chiu
aus Taipei, Taiwan

München, den 9th May 2016

Erstgutachter: Prof. Dr. Joseph Mohr
Zweitgutachter: Prof. Dr. Eiichiro Komatsu
Tag der mündlichen Prüfung: 6th June 2016

To Ho.

Acknowledgements

An old Chinese saying goes, “The journey of a thousand miles must begin with a single step”. As many other things worthwhile in life, there are always obstacles arising along the road, and you do not know about it until you begin your first step. So, here I am, the final step toward my doctorate degree. There are many people that I would like to thank for helping me to get over these obstacles and making this thesis possible.

I thank my supervisor Joe Mohr for supporting my doctoral degree and patiently teaching me how to become a good scientist; I couldn’t mentor a student as rebellious as me if I were you. :) I also want to thank Uta Le Guay, Robert Šuhada, Gurvan Bazin, Alex Saro, Jörg Dietrich, Veronica Strazzullo, Matthias Klein, Maurilio Pannella, Kerstin Paech, Shantanu Desai, Mark Olival-Bartley and Tadziu Hoffmann. Huge thanks to Uta for helping me with numerous and “fun” administrative tasks—I could not have survived in Germany without you. Special gratefulness goes to Jörg, and thanks for your weekly Wednesday morning meetings that helped me finish the magnification paper. I specially want to thank Alex for dragging me out for lunch every day, I will miss that (and of course the science discussion we have). I deeply thank Shantanu because of one sweet and “annoying” event: you refused to tell me the path to some stupid catalogs just because you wanted me to take rest instead of overworking on that weekend; for that, you will always be my friend.

I express my deep gratitude to my friends who shared our office (and also tolerate my awkward obsession with Taylor Swift): Alfredo Zenteno, Jiayi Liu, Sebastian Bocquet, Christina Hennig, Corvin Gangkofner, Nikhel Gupta, Raffaella Capasso, Luiz Carneiro, Judith Ngoumou, Sebastian Grandis. Especially Nikhel, thank you for walking me through some downhills and always cheering me up with your (bothersome) optimism. The biggest and deepest gratitude is to my friend, Jiayi. I could never thank you more for teaching me (almost) everything that I need to know here in life or work, helping me to solve various stupid problems, and supporting me to overcome the difficulties even after you left Germany. Meeting you is one of the best things that happened to me here.

I devote my indebted and sincere gratitude to my parents, who have been giving me full freedom to choose anything that I want to do since I was born. Your support is the reason why I can be sitting here in Germany finishing my doctoral degree. Finally, but in no way the least, I would like to thank HoHo. The time I had with you in Taiwan or Europe—either some bad luck ending up eating the dinner in my car under the torrential rain in front of the gas station, or the period of spontaneous wandering among the alleys in Venice after having coffee in the oldest (and most expensive) Cafe—and the dreams I occasionally had in the nights here after a long day work have motivated me to be the best person that I could possibly be.

Zusammenfassung

Der Anfang des 21. Jahrhunderts ist eine boomende Ära für die Cluster-Kosmologie und Astrophysik. In der Vergangenheit wurde Forschungen der Cluster Wissenschaft mangels ausreichender tiefer Beobachtungen in Mehrwellenlängen begrenzt und war Gegenstand heterogenen Proben mit kleinen Größen bei niedrigen Rotverschiebung. Deshalb war es extrem schwierig, Fortschritte zu machen, um die Bevölkerung von Galaxienhaufen in statistisch sinnvolle Weise zu studieren oder die Verwendung von Galaxienhaufen als kosmologisches Werkzeug so wettbewerbsfähig wie andere Sonden zu machen. Diese Situation wurde aufgrund des jüngsten Erfolg der großen mm Wellenlänge Erhebungendie South Pole Telescope (SPT, Carlstrom et al., 2011), Atacama Cosmology Telescope (ACT, Fowler et al., 2007) und the *Planck* mission (The Planck Collaboration, 2006) geändertden Sunyaev-Zel'dovich Effect (SZE, Sunyaev & Zel'dovich, 1970a, 1972) zu identifizieren und Galaxienhaufen mit großer Fülle aus dem frühen und fernen Universum zu forschen. Mit Hilfe von von Proben mit großen Größen, wobei die Galaxie Verwendung zur Forschung von Cluster Kosmologie oder Astrophysik am besten entwickelt wird, ist sie im Zusammenhang mit der Gesamtmasse, Rotverschiebung und Observablen zu klassifizieren. Am wichtigsten ist, wie die Beziehungen zu charakterisieren sinddie Skalierungs Beziehungen genanntdas verbindet Observablen mit den zugrunde liegenden wahren Massen von Galaxienhaufen in verschiedenen Epochen. Aufgrund des kritischen Schritts wird die Art von Galaxienhaufen und das Universum verstanden.

In dieser Arbeit werde ich mit mehreren Wellenlängen Untersuchungen der Beziehungen zwischen verschiedenen Observablen von Galaxienhaufen Skalierung darstellen; Ich will auch ein neues Verfahren zeigen, um direkt die Massen von Galaxienhaufen abzuleiten. Das Verfahren stellt durch den Linseneffekt der Vergrößerung die Kalibrierung von Clustermasse Proxies absolute Masse bereit. In dieser Arbeit werden die von der SPT-SZ-Umfrage und deren Nachfolgebeobachtungen im Fenster mit mehreren Wellenlängen ausgewählten Probe genutzt.

Abstract

The beginning of the 21 Century is a booming era for cluster cosmology and astrophysics. In the past, cluster science was limited by a lack of adequately deep observations in multi-wavelength and was subject to heterogeneous samples with small sizes at low redshift. As a result, it was extremely difficult to make progress in studying the populations of galaxy clusters in a statistically meaningful way or to make use of galaxy clusters as cosmological tools in ways that would be competitive with the other probes. The situation has been changed due to the recent success of the large mm wavelength surveys—such as the South Pole Telescope (SPT, Carlstrom et al., 2011), the Atacama Cosmology Telescope (ACT, Fowler et al., 2007) and the *Planck* mission (The Planck Collaboration, 2006)—that employ the Sunyaev-Zel'dovich Effect (SZE, Sunyaev & Zel'dovich, 1970b, 1972) to identify and study galaxy clusters in their abundance out to the early and distant Universe. With the promise of obtaining samples with large sizes, one of the most important things toward utilizing galaxy clusters to study cosmology or astrophysics is to measure their total mass, redshift and other observables. Most importantly, one must characterize the relations—called the mass-observable scaling relations—that link observables to the underlying true masses of galaxy clusters at different epochs of formation. With this information one can hope to understand the nature of galaxy clusters and the Universe.

In this thesis, I will present multi-wavelength studies of scaling relations among different observables of galaxy clusters. I will also demonstrate a novel method to directly infer the masses of galaxy clusters; this method provides an absolute mass calibration of cluster mass proxies by using the magnification effect due to gravitational lensing. This thesis heavily leverages the sample selected from the SPT-SZ survey and its follow-up observations at many wavelengths.

I will first give a brief introduction to cosmology and galaxy clusters in Chapter 1. Chapter 2 contains results from a pilot study of the baryon content of 14 massive galaxy clusters selected by the SPT collaboration at redshift $0.57 < z < 1.33$, including a comparison of the measurements to the previous results at low redshift. Chapter 3 follows, containing results of a study of the stellar mass—halo mass relation for 46 low mass galaxy groups and clusters selected using their X-ray emission at redshifts $0.1 \lesssim z \lesssim 1$. This study utilizes the uniform and wide *Spitzer*-South-Pole-Telescope-Deep-Field (SSDF) survey dataset in Near-Infrared (NIR). Chapter 4 contains results of an extension of the work in Chapter 2, including the measurements of the baryon content of 91 SPT-selected clusters at redshifts $0.25 < z < 1.25$. In this work, we intensively use the multi-wavelength data sets accumulated by the SPT collaboration. These include the mm-wave maps from the SPT-SZ survey, uniform follow-up observations in X-ray taken by the *Chandra* X-ray telescope, optical imaging from the Dark Energy Survey (DES, DES Collaboration, 2005), and

dedicated NIR photometry obtained with the *Spitzer* telescope.

To summarize the results of Chapter 2, 3 and 4, we confirm the strong mass trends that exist in the context of stellar and Intracluster Medium (ICM) masses with respect to the total masses M_{500} of massive clusters out to redshift $z \approx 1.3$; the mass budgets of stellar and ICM components are increasing, respectively, as $\propto {M_{500}}^{0.7}$ and $\propto {M_{500}}^{1.2}$, with high significances. Conversely, the redshift trends of stellar and ICM components at fixed mass are all statistically consistent with zero, although the uncertainties are large. This suggests that the baryon content has been assembled in galaxy clusters since redshift $z \approx 1.3$ and—perhaps most interestingly—the strong mass trends of baryon content without significant redshift trends imply that a significant amount of infall into galaxy clusters during their formation must come from the under-dense field.

Chapter 5 contains the demonstration of a method to calibrate mass proxies by using the weak lensing effect of magnification. Although the signal-to-noise ratio of measurements of the magnification is typically lower than those of the weak lensing shear, this method can still deliver absolute mass calibration by utilizing a mass proxy with low scatter—such as the SZE-observable ξ measured by the SPT collaboration and used in this Chapter—and a large sample of clusters to suppress the noise. It is worth mentioning that this method does not require ultra-deep imaging and, therefore, is suitable for typical wide field surveys, such as the ongoing DES or Subaru Hyper-Suprime-Cam survey. With the promise of upcoming all-sky surveys, this method provides an alternative and competitive way to measure cluster masses.

Finally, Chapter 6 contains a summary as well as an outlook for future research.

Contents

List of Figures

List of Tables

Chapter 1

Introduction

In this chapter, the standard cosmological framework, greatly supported by observations, is reviewed in Section 1.1, followed by an introduction to galaxy clusters given in Section 1.2. Finally, an organization of this thesis is provided at the end of this chapter.

1.1 Cosmological Framework

The opportunity of unveiling the nature of the Universe was made possible by two astonishing discoveries in the 19th Century—the expanding Universe and the Cosmic Microwave Background (CMB). They are introduced as follows.

The Expanding Universe Modern cosmology started from one of the greatest discoveries in human history—the expanding Universe—discovered by Edwin Hubble in 1929 (Hubble, 1929). By measuring the velocities and distances of extragalactic galaxies, Hubble found them moving away from us. In addition, the farther a galaxy is, the faster it is moving away. This velocity-to-distance relation can be described by a simple linear relation—called the Hubble Law. The idea that the Universe is expanding was immediately recognized as the only explanation for this observation. Furthermore, this expansion has to be uniform in the sense that the Universe expands without any specific location as the center. The expansion of the Universe is conceptually illustrated in Figure 1.1, where each point is moving away from the others without any specific center of the expansion. Moreover, the farther the source is to us (e.g., the blue point in Figure 1.1), the faster it is moving away.

The Cosmic Microwave Background The Cosmic Microwave Background (CMB)—the microwave radiation across the whole sky—is a relic of the light emitted from the early Universe. Discovered in 1965 by Arno Penzias and Robert Woodrow Wilson (Penzias & Wilson, 1965), CMB provides unambiguous evidence for the Hot Big Bang theory—the idea that the Universe originated from an atomic size and then expanded to its current large scale (Figure 1.2). Later in 1990, the observations made by the *Cosmic Background Explorer* (*COBE*, Smoot et al., 1992)

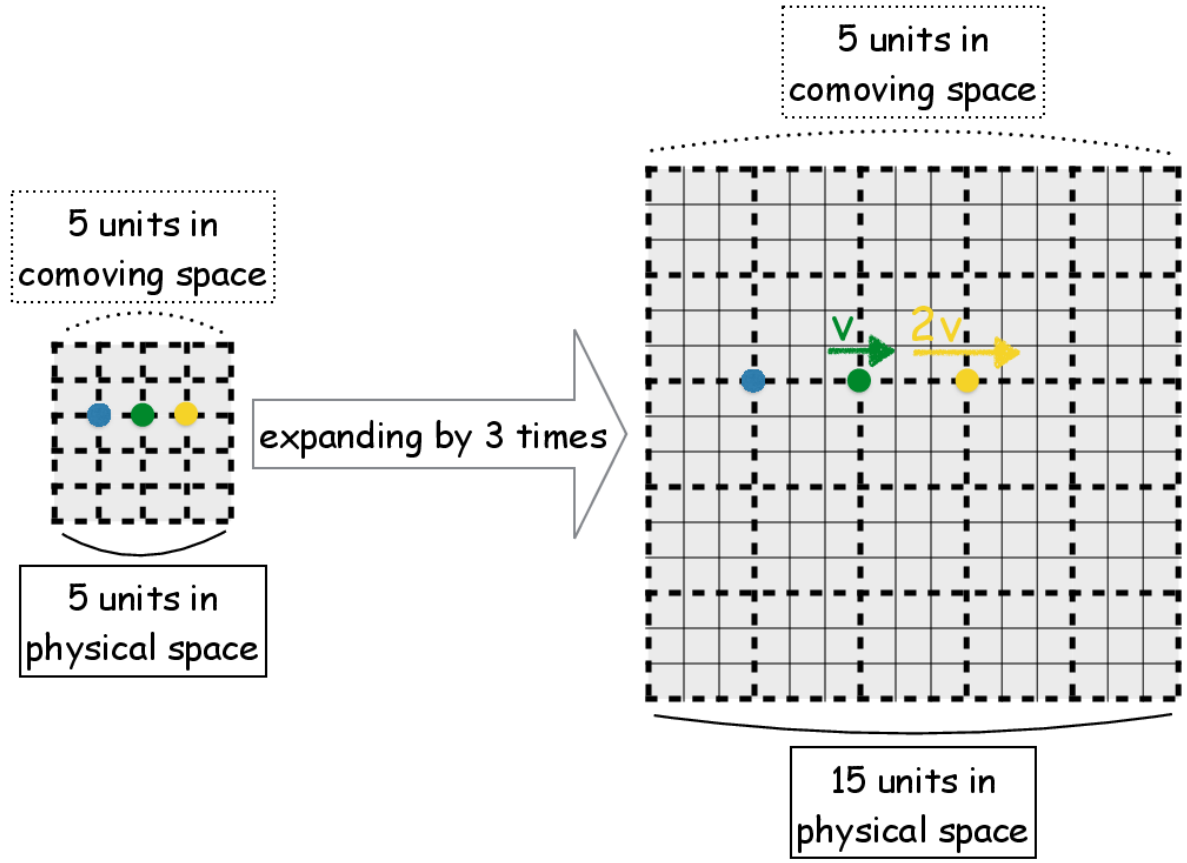

Figure 1.1: A plot to illustrated the Universe as an expanding plane. The plans before and after cosmic expansion are shown at left and right, respectively. The plan at the right is expanded by a factor of three during expansion. The comoving metric is indicated by the dashed lines, while the physical coordinates after expansion are shown by the solid lines at the right. For the reference point (the blue point), the adjacent two points (color coded by green and yellow) are both moving away. Moreover, during expansion the yellow point is moving faster (physical distance from 2 units to 6 units) than the green point (physical distance from 1 unit to 3 units), whose expanding velocity due to cosmic expansion is proportional to the distance to the reference point. Meanwhile, the relative distance between the green (or yellow) and the reference points remain the same in comoving space (the coordinates consisting of the dashed lines).

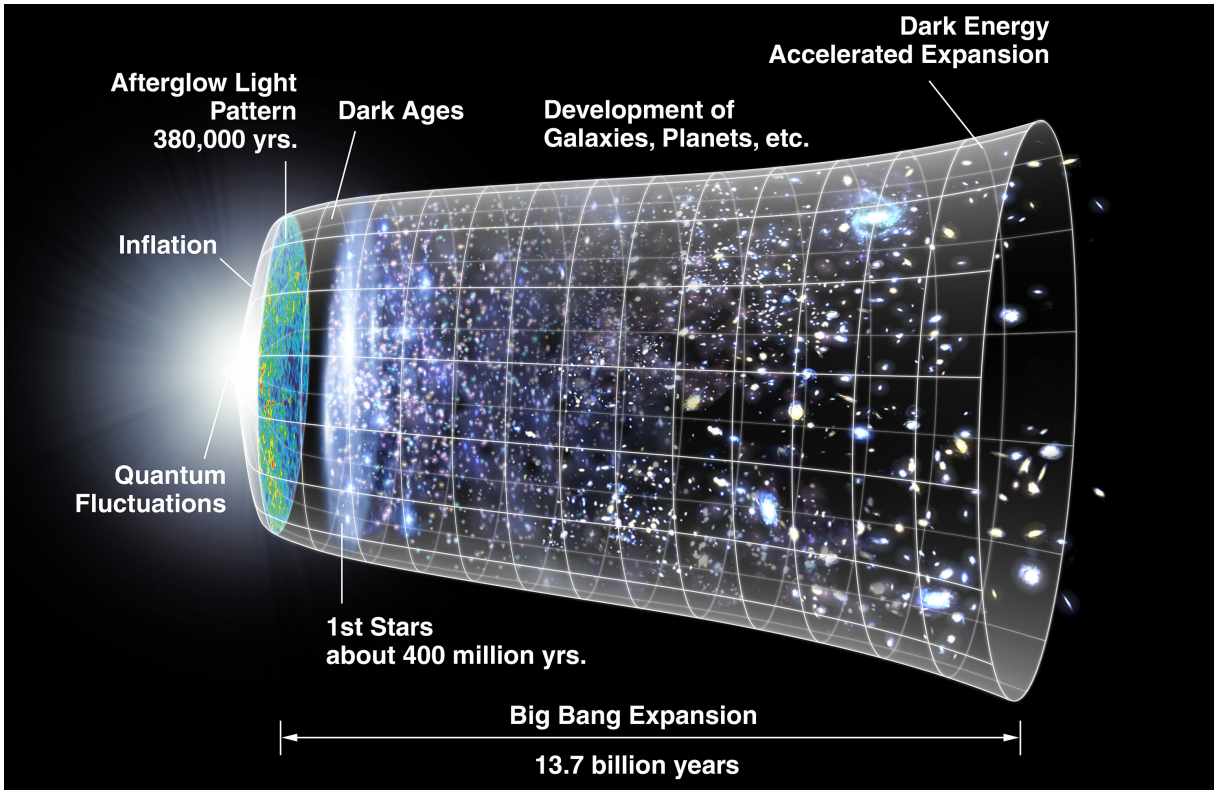

Figure 1.2: The schematic figure of cosmic history. The boundary of the observable Universe is shown by the metric consisting of the white mesh grids. The beginning of the Universe started from the Big Bang $\approx$ 14 Gyr before, which is indicated by the singular point at the leftmost side. The Universe then experienced the Inflation and became transparent after the last scattering (indicated by the CMB map at the cosmic age of 380,000 years), followed by formation of the large-scale structure as illustrated by the stars or galaxies on the figure. Credit: NASA/WMAP Science Team.

satellite directly confirmed that the CMB is made of thermal radiation uniformly across the sky, which is described as a black body at temperature of ≈ 2.73 K. This suggests that the Universe is in a state of thermal equilibrium and was very hot and dense back to its early stages. Conversely, the CMB temperature shows a small amount of anisotropy at the order of 10^{-5}, resulting from the quantum fluctuations in the early Universe, which would eventually grow to the large-scale structure we see today. The discovery of the CMB as well as the confirmation of its blackbody radiation and anisotropy were awarded Nobel Prizes in 1978 and 2006, respectively.

Based on the two fundamental observations above, the basic picture of the Universe is that our Universe started from an extremely dense core on the Planck scale ($\approx 10^{-35}$ m) and expanded to the current size with a lower bound of $\approx 10^{26}$ m over the last 13.8 Gyr. During the expansion of the Universe, the structure and energy content of the Universe evolved. Despite that various cosmological models are developed in order to explain the evolution of the Universe, the picture of the Hot Big Bang Cosmology should be rooted in those models. Nowadays, to confirm or rule out these cosmological models has now become a highly-sought goal of observational cosmology.

I will now briefly introduce the standard cosmological model and the structure formation of the Universe in Section 1.1.1 and Section 1.1.2, respectively.

1.1.1 The Standard Model of Cosmology

The standard model of cosmology is based on two fundamentals. The first is the concept of the Hot Big Bang Cosmology that the Universe has been expanding after the Hot Big Bang, while the second is the Cosmological Principle stating that the Universe is homogeneous and isotropic on the large scale. This picture is framed by General Relativity with the exact metric of space and time—the Friedmann-Robertson-Walker (FRW) metric—as follows.

$$c^2 \mathrm{d}s^2 = c^2 \mathrm{d}t^2 - a(t)^2 \left(\frac{\mathrm{d}r^2}{1 - kr^2} + r^2 \mathrm{d}\Omega^2 \right) , \tag{1.1}$$

where c is the speed of light, t is time, (r, Ω) is the polar coordinate in the comoving space, s is the metric of space and time, k is the spatial curvature of the Universe, in which the flat (closed sphere, open hyperboloid) Universe is characterized by $k = 0$ ($k = 1$, $k = -1$), and the $a(t)$ is the scale factor as a function of cosmic time t only.

The scale factor $a(t)$ characterizes how the coordinate system has changed according to the expansion of the Universe. Specifically, the (r, Ω) describes the comoving space (the dashed lines in Figure 1.1) which is independent of the expansion of the Universe, and the physical distances (the solid lines in Figure 1.1) governed by the expansion are obtained by multiplying the scale factor to the comoving distance. Because the scale factor $a(t)$ is a monotonically increasing function depending only on cosmic time, it is convenient to denote the age of the Universe (or the lookback time) via the ratio of the scale factors now and at the specific time t—called the redshift z as defined in Equation 1.2.

$$1 + z \equiv \frac{1}{a(t)} , \tag{1.2}$$

where the scale factor is unity in the current age of the Universe. In this way, any age of the Universe corresponds to a specific redshift, and vice versa.

With FRW metric, the Einstein equations can then be reduced to the Friedmann equations (Friedmann, 1922):

$$H^2 = \frac{8\pi G}{3}\rho + \frac{\Lambda}{3}c^2 - \frac{kc^2}{a^2} \tag{1.3}$$

$$\dot{H} + H^2 = -\frac{4\pi G}{3}\left(\rho + \frac{3p}{c^2}\right) + \frac{\Lambda}{3}c^2 \tag{1.4}$$

$$H \equiv \frac{\dot{a}}{a} = \frac{\mathrm{d}\ln a}{\mathrm{d}t}, \tag{1.5}$$

where G is the Newtonian constant, Λ is the cosmological constant, $\rho(z)$ and $p(z)$ are respectively the energy density and pressure of the content in the Universe, and $H(z)$ is the Hubble parameter at redshift z. Under this framework, the Hubble Law can be formulated as

$$v_{\mathrm{H}} = H \times R, \tag{1.6}$$

where R is the physical distance of the source to us and v_{H} is the Hubble flow describing the speed of cosmic expansion.

Assuming that the energy content of the Universe consists mainly of radiation and matter ($\rho = \rho_{\mathrm{rad}} + \rho_{\mathrm{M}}$), Equation 1.3 can be rewritten in another conventional form as follows.

$$\begin{aligned}
E(z)^2 &= \Omega_{\mathrm{rad}}|_{z=0}(1+z)^4 + \Omega_{\mathrm{M}}|_{z=0}(1+z)^3 + \Omega_k|_{z=0}(1+z)^2 + \Omega_\Lambda \\
E(z) &\equiv \frac{H(z)}{H_0} \\
\rho_{\mathrm{crit}}(z) &\equiv \frac{3H(z)^2}{8\pi G} \\
\Omega_{\mathrm{rad}}(z) &\equiv \rho_{\mathrm{rad}}(z)\,\rho_{\mathrm{crit}}(z)^{-1} \\
\Omega_{\mathrm{M}}(z) &\equiv \rho_{\mathrm{M}}(z)\,\rho_{\mathrm{crit}}(z)^{-1} \\
\Omega_\Lambda(z) &\equiv \frac{\Lambda c^2}{8\pi G}\,\rho_{\mathrm{crit}}(z)^{-1} \\
\Omega_k(z) &\equiv \frac{-3kc^2}{8\pi G}\,\rho_{\mathrm{crit}}(z)^{-1},
\end{aligned} \tag{1.7}$$

where $\rho_{\mathrm{crit}}(z)$ is the critical density of the Universe at redshift z, H_0 is the current Hubble parameter at $z = 0$, $E(z)$ describes the growth of the Hubble parameter with respect to H_0; $\Omega_k(z)$, $\Omega_\Lambda(z)$, $\Omega_{\mathrm{M}}(z)$ and $\Omega_{\mathrm{rad}}(z)$ are the energy fractions of the curvature, cosmological constant, matter and radiation of the Universe at redshift z, respectively.

For a given set of Ω_k, Ω_Λ, Ω_{M} and Ω_{rad} estimated at $z = 0$, the evolution of the energy content in the Universe can be concisely described by the function of redshift. Specifically, the contribution of Ω_k, Ω_{M} and Ω_{rad} is proportional to $(1+z)^2E(z)^{-2}$, $(1+z)^3E(z)^{-2}$ and $(1+z)^4E(z)^{-2}$, respectively, and $\Omega_\Lambda E(z)^2$ has remained constant since the beginning of the Universe.

Table 1.1: The energy content of the Universe and the velocity of cosmic expansion in the present day. The energy of total matter (DM and baryon), radiation, DE and the curvature are expressed by the fractions of the critical density (see Equation 1.7), while the expanding velocity is indicated by the Hubble parameter H_0 in the unit of km/s/Mpc.

Contents	Contribution to current Universe
$\Omega_{\rm M}$	≈ 0.3
$\Omega_{\rm rad}$	$\approx 8.4 \times 10^{-5}$
Ω_Λ	≈ 0.7
Ω_k	≈ 0
H_0	≈ 70 km/s/Mpc

On the other hand, Equation 1.4 describes how the expansion of the Universe accelerates or decelerates according to the energy content of the Universe. For example, an energy density with a positive $\ddot{a}$ leads to the accelerating expansion of the Universe.

One of the most important tasks in modern cosmology is to precisely and accurately measure these cosmological parameters (e.g., $\Omega_{\rm M}$, Ω_Λ or H_0) and, furthermore, interpret these observational results to constrain or rule out cosmological models. The unambiguous evidence provided by the CMB observations (e.g., Komatsu et al., 2011) suggests that the current energy content of the Universe is made up by $\approx 30\%$ of matter and $\approx 70\%$ of an unknown energy form—called *Dark Energy* (DE). Radiation occupies less than 0.01% of the energy budget of the current Universe. Moreover, $\approx 80\%$ out of matter is in an unknown form—called *Dark Matter* (DM). The ordinary matter that is greatly understood by the human knowledge only contributes less than 5% of the total energy budget. The fiducial values of the cosmological parameters based on the current observational results are summarized in Table 1.1, and the constraints on the cosmological parameters obtained from the different probes are illustrated in Figure 1.3.

The measured cosmological parameters imply that the Universe was dominated by radiation at the early stages before entering into the matter-dominated era and is recently governed by DE. The epoch of the radiation-matter equality $z_{\rm eq}$ such that $\Omega_{\rm rad}(z_{\rm eq}) = \Omega_{\rm M}(z_{\rm eq})$ takes place at

$$z_{\rm eq} \approx 3600. \tag{1.8}$$

To the first order, the history of the Universe can simply be split into the radiation-dominated and matter-dominated eras for $z > z_{\rm eq}$ and $z < z_{\rm eq}$, respectively. Assuming the Universe is flat ($k = 0$) without the cosmological constant ($\Lambda = 0$), two Friedmann equations (Equation 1.3 and Equation 1.4) can be combined as

$$\frac{{\rm d}\rho}{{\rm d}t} + 3H\rho\,(1+w) = 0 \ \text{, where } w \equiv \frac{P}{\rho c^2}\,. \tag{1.9}$$

Combining Equation 1.9 and Equation 1.3, one can derive

$$a \propto t^{\frac{2}{3(1+w)}}\,. \tag{1.10}$$

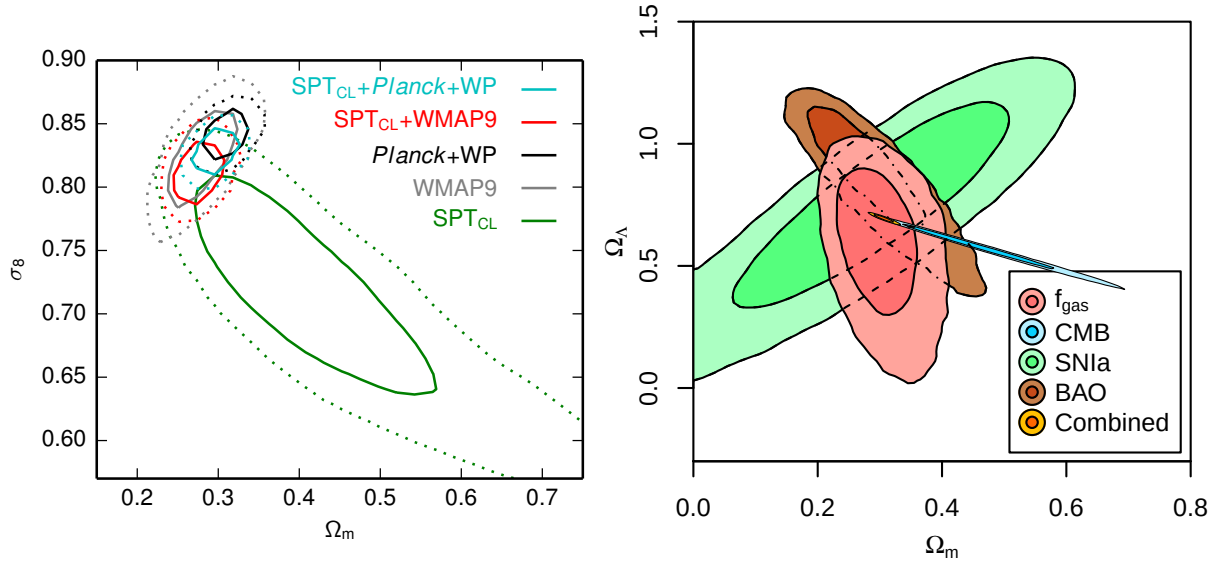

Figure 1.3: The constraints of cosmological parameters based on different probes. The left and right panels show the constraints of σ_8 (the normalization of the matter power spectrum (see Section 1.1.2)) versus $\Omega_{\rm M}$, and the Ω_Λ versus $\Omega_{\rm M}$ using different observational data sets, respectively. Figures taken from Bocquet et al. (2015b) and Mantz et al. (2014).

Given that the equation of state w for radiation and matter are $w = 1/3$ and $w = 0$, respectively, the asymptotic behavior of ρ, a and H can be solved as

$$\begin{aligned} \rho &\propto a^{-4} = (1+z)^4 \\ a &\propto t^{\frac{1}{2}} \\ H &= \frac{1}{2t} \end{aligned} \tag{1.11}$$

in the radiation-dominated era ($z > z_{\rm eq}$) and

$$\begin{aligned} \rho &\propto a^{-3} = (1+z)^3 \\ a &\propto t^{\frac{2}{3}} \\ H &= \frac{2}{3t} \end{aligned} \tag{1.12}$$

in the matter-dominated era ($z < z_{\rm eq}$). That is, the Universe expands as $a \propto t^{\frac{1}{2}}$ ($a \propto t^{\frac{2}{3}}$) in the radiation-dominated (matter-dominated) era, for which the energy density of radiation (matter) decays as $\rho \propto a^{-4}$ ($\rho \propto a^{-3}$).

As illustrated above, the history of the Universe can be obtained by extrapolating the Universe observed today based on cosmological models. However, the actual evolution of the Universe is more complicated and depends upon complex energy content of the Universe as well as the interactions among them. The further we go back in time, the hotter the Universe is and more particles were coupled in the thermal pool—therefore more sophisticated interactions were among

them. Despite the sophisticated evolution of the Universe, a general picture can still be inferred as follows, assuming that the Universe started at the time of the Hot Big Bang ($t = 0$).

The Inflation Epoch (10^{-36} s $\lesssim t \lesssim 10^{-32}$ s) It is believed that the Universe has to experience a very rapid expansion—called *Inflation*—right after the Hot Big Bang at 10^{-36} s $\lesssim t \lesssim 10^{-32}$ s. During the Inflation epoch, the size of the Universe was increased by a factor of 10^{26} (or called 60 e-folds because of $e^{60} \approx 10^{26}$). After the inflation, the Universe was "flattened" and entered into a homogeneous and isotropic phase, where small perturbations originated from the quantum fluctuations were distributed and gradually grew to the large-scale structure we see today.

Early Universe (10^{-6} s $\lesssim t \lesssim 10$ s) In the early Universe, the temperature was high enough that the particles and antiparticles were in thermal equilibrium, therefore no net particles could form. At this stage, the Universe kept expanding and the temperature was cooling down till the time when the equilibrium was broken down and the annihilation took place. This led to the formation of remaining particles after annihilating with antiparticles. During the time period of 10^{-6} s $\lesssim t \lesssim 1$ s, the temperature of the Universe was low enough (at $\approx 10^{10}$ K) such that the quarks were able to be bonded to form hadrons, such as protons or neutrons. This time period was called the hadron epoch, followed by the lepton epoch during 1 s $\lesssim t \lesssim 10$ s that the net leptons (e.g., electrons) after annihilation were created.

Nucleosynthesis (10 s $\lesssim t \lesssim 20$ mins) The temperature of the Universe at this stage was $\lesssim 10^{10}$ K so that nuclear fusion of—for example, protons and neutrons—was actively ongoing. By the end of the Nucleosynthesis epoch, most of hadrons formed into the nuclei of hydrogen and helium with small amounts of other light elements. In the end of this stage, the baryon composition of the Universe was stable with the mass ratio of the helium to hydrogen at about 1 : 3. Note that the temperature of the Universe was still too high to form neutral atoms, therefore the Universe was filled with ionized plasma, where photons and baryonic matter were heavily coupled together. That is, the Universe was still opaque.

Matter-radiation-Equality Era ($t \approx 5 \times 10^4$ yr **or** $z \approx 3600$) This is the landmark in the cosmic history that the Universe starts to be dominated by matter after this era.

Recombination ($t \approx 380000$ yr **or** $z \approx 1100$) The temperature of the Universe became cool enough (≈ 3000 K) so that the electrons and nuclei could form neutral atoms, preventing photons from scattering with ionized plasma. After recombination, the photons could freely propagate in the space and became the CMB we see today, which is essentially the footprint of the "last scattering" that took place between the plasma and photons at $z \approx 1100$. At this point, the Universe became transparent and baryons were decoupled from the thermal pool.

Late Universe ($t > 380000$ yr) From this point on, the structure formation of baryon in the Universe began. The primordial inhomogeneity set by the quantum fluctuations during the inflation started to grow and has evolved into the large-scale structure we see today.

I will now briefly introduce the structure formation in Section 1.1.2.

1.1.2 Structure Formation

The structure of the Universe grew from primordial quantum fluctuations through gravitational instability, for which the gravitational mechanism is mainly governed by *Dark Matter* (DM)—the hypothetical particle or a form of matter that does not interact with ordinary matter and light except through gravity. Several different studies (Zwicky, 1933; Babcock, 1939; Seielstad & Whiteoak, 1965) in the early twentieth century had already indicated the "missing mass problem" that the mass budgets of visible components were not adequate to explain the observational results. However, it was not until the late twentieth century that the name, DM, was first proposed by Vera Rubin to explain the rotation curves of galaxies (Rubin et al., 1978, 1980), which suggested that this invisible matter is dominating the gravitational mechanism. Later, the need for DM was supported by overwhelming observational evidence (e.g., Burstein et al., 1982; Rubin et al., 1982b,a; Dressler & Sandage, 1983; Hunter et al., 1986; Kent, 1986; Kuhn & Kruglyak, 1987; Persic et al., 1996). Since then, numerous hypothetical candidates (e.g., the axion proposed by Peccei & Quinn, 1977), the experiments for direct detections (e.g., Alcock et al., 1997; Udalski et al., 1997; Alcock et al., 2000; Afonso et al., 2003; Tisserand et al., 2007; Garg, 2008) and theoretical explanations (e.g., the warm or quantum wave-like DM particles, Peebles, 2000; Hu et al., 2000; Bode et al., 2001; Böhmer & Harko, 2007; Chavanis, 2011; Schive et al., 2014) have been proposed to support the existence of DM. However, the nature of DM still remains mysterious to date.

Even so, the debates over DM continue, the simplest and most widely accepted model for DM is the Cold Dark Matter (CDM) model. In the CDM model, DM decoupled from the thermal pool of the Universe at very early stages, and has remained cold (non-relativistic) and collisionless since then. Therefore, the distribution of DM in phase space could be described through the collisionless Boltzmann equation as follows.

$$\frac{\mathrm{d}f}{\mathrm{d}t} = \left(\partial_t + \frac{\mathrm{d}\vec{v}}{\mathrm{d}t}\cdot\partial_{\vec{v}} + \frac{\mathrm{d}\vec{R}}{\mathrm{d}t}\cdot\partial_{\vec{R}}\right) f = 0\,, \tag{1.13}$$

where $f(\vec{R},\vec{v},t)$ is the phase distribution of DM as the function of velocity $\vec{v}$ and position $\vec{R}$. Integrating Equation 1.13 to the zero and first moments of velocity $\vec{v}$, one can recover the fluid equations:

$$\partial_t\rho + \nabla_R\cdot\left(\rho\vec{V}\right) = 0 \tag{1.14}$$

$$\partial_t\vec{V} + \vec{V}\cdot\nabla_R\vec{V} = -\frac{\nabla_R P}{\rho} - \nabla_R\Phi\,, \tag{1.15}$$

where $\nabla_R \equiv \partial_{\vec{R}}$ is the gradient operator with respect to position $\vec{R}$, $\rho \equiv \int f(\vec{R},\vec{v},t)\mathrm{d}^3v$ and $\vec{V} \equiv \int f(\vec{R},\vec{v},t)\vec{v}\mathrm{d}^3v / \int f(\vec{R},\vec{v},t)\mathrm{d}^3v$ are the density and velocity fields at position $\vec{R}$ and time t, respectively; Φ is the gravitational potential, and P is the pressure of the fluid assuming isotropic distribution.

The velocity field $\vec{V}(\vec{R})$ at the position $\vec{R}$ is the superposition of the Hubble flow $\vec{v_{\rm H}}$—which is co-moving along with the expansion of the Universe—and the peculiar velocity $\vec{u}$—which is the velocity field of the particle and is independent of cosmic expansion. Similarly, in the linear regime, the density, pressure and gravitational potential fields can be approximated as the background values plus local fluctuations. i.e.,

$$\begin{aligned} \vec{V} &= H\vec{R}+\vec{u}\,, \\ \rho &= \rho_{\rm bkg}\times(1+\delta_\rho)\,, \\ P &= P_{\rm bkg}\times(1+\delta_P)\,, \\ \Phi &= \Phi_{\rm bkg}\times(1+\delta_\Phi)\,, \end{aligned} \tag{1.16}$$

where the subscript "bkg" indicates the global values of the background. Substituting Equation 1.16 into Equation 1.14 and Equation 1.15 in the comoving space ($\vec{r}\equiv\vec{R}/a, t'\equiv t$), one can obtain

$$\ddot{\delta_\rho}+2H\dot{\delta_\rho}-\frac{P_{\rm bkg}}{\rho_{\rm bkg}}\frac{1}{a^2}\nabla_r^2\delta_P-\frac{\Phi_{\rm bkg}}{a^2}\nabla_r^2\delta_\Phi=0\,. \tag{1.17}$$

Inserting the first order of the Poisson equation

$$\frac{1}{a^2}\nabla_r\Phi_{\rm bkg}\delta_\Phi=4\pi G\rho_{\rm bkg}\delta_\rho$$

and the equation of state

$$P_{\rm bkg}=wc^2\rho_{\rm bkg}$$

into Equation 1.17, a more elegant form is derived as Equation 1.18.

$$\ddot{\delta}+2H\dot{\delta}-\frac{c_{\rm s}^2}{a^2}\nabla^2\delta=4\pi G\rho_{\rm bkg}\delta\,, \tag{1.18}$$

where $c_{\rm s}^2\equiv wc^2$ is the sound speed of the fluid. For convenience, we denote $\delta\equiv\delta_\rho$; the dot and ∇ stand for, respectively, the partial derivative with respect to the time and the gradient with respect to the comoving coordinate.

Equation 1.18 is called the density perturbation equation in the limit of linear and classical Newtonian regime. The solution of Equation 1.18 reflects how the structure forms in the linear and non-relativistic regime. Specifically, the solution of δ depends on three terms: the first one is the dragging term $2H\dot{\delta}$ characterizing the Hubble expansion (or the Hubble flow); the second is the last term on the left that describes the pressure of the fluid to prevent δ from growing; the last one is the term $4\pi G\rho_{\rm bkg}\delta$ indicating the gravitational collapse against the pressure suppression. When gravity overcomes pressure suppression, the structure forms. The physical picture is revealed more clearly in the k-space of the density perturbation equation (Equation 1.20):

$$\delta(\vec{r},t)\propto\int\delta(k,t)e^{i\vec{k}\cdot\vec{r}}{\rm d}^3r\,, \tag{1.19}$$

which implies

$$\left(\partial_t^2 + 2H\partial_t + \frac{c_s^2}{a^2}k^2 - 4\pi G\rho_{\rm bkg}\right)\delta(k,t) = 0\,. \tag{1.20}$$

Equation 1.20 defines the characteristic length—called Jeans length $\lambda_{\rm J}$—as

$$\lambda_{\rm J} \equiv \frac{2\pi}{k_{\rm J}} \equiv \frac{2\pi c_s}{a\sqrt{4\pi G\rho_{\rm bkg}}}\,, \tag{1.21}$$

and the growing mode of $\delta(k,t)$ exists if and only if

$$k < k_{\rm J} \text{ or } \lambda > \lambda_{\rm J}\,. \tag{1.22}$$

Equation 1.22 is called the Jeans Instability that the structure grows when the scale λ is larger than the Jeans scale, and vice versa. Moreover, the Jean length $\lambda_{\rm J}$ depends on the energy content $\rho_{\rm bkg}$ of the Universe at the cosmic time t. In the matter-dominated era, the third term on the left of Equation 1.20 can be ignored, and the growing mode of the DM perturbation can be solved as follows:

$$\delta(k,t) = \delta_0(k)D(t) \text{ and } D(t) \propto a \propto t^{\frac{2}{3}}\,, \tag{1.23}$$

where $\delta_0(k)$ is the initial condition of the perturbation at the scale k, and D is the growth factor describing how the overdensity grows. Since the growth of the perturbation δ is linearly proportional to $D(t)$, it is also referred as the linear growth of the structure.

However, the statement above is only valid when the DM perturbation δ at the scale of interest is linear and within the "horizon"—which is the maximum distance that light can travel since the beginning of the Universe. If the scale is larger than the horizon, then the relativistic correction has to be applied. It can be shown in most textbooks of cosmology (e.g., Dodelson, 2003) that the DM perturbation, including the relativistic correction at the scale larger than the horizon, was still growing as $\delta \propto a^2$ and $\delta \propto a$ in the radiation-dominated and matter-dominated eras, respectively. Only the perturbation that entered into the horizon at the radiation-dominated era could not grow and remained constant because the expansion of the Universe was too fast for structure to grow (Meszaros effect Meszaros, 1974). This caused the delay of the structure formation at that scale between the time when the mode was entering the horizon and started to grow in the matter-dominated era later. This picture is conceptually demonstrated in Figure 1.4, where the increasing horizon (red line) and the time of matter-radiation equality at $t = t_{\rm eq}$ (dotted line) divide the Universe into four growing modes in the diagram of scale λ versus time t. Conventionally, we refer to any perturbation at the time $t_{\rm in}$ entering the horizon in the matter-dominated era as the primordial fluctuation $\delta_{\rm primordial}(k,t_{\rm in})$ (e.g., the dashed circle in Figure 1.4). As a result, it is very convenient to define the transfer function $T(k)$ as a function of k to characterize all the deviations from the linear growth of the primordial fluctuation (e.g., the constant $\delta(k)$ in the radiation-dominated era). Schematically, the full expression of the perturbation $\delta(k,t)$ in the linear regime at scale k can be expressed as

$$\delta(k,a) = \delta_{\rm primordial}(k,t_{\rm in})T(k)\frac{D(t)}{D(t_{\rm in})}\,. \tag{1.24}$$

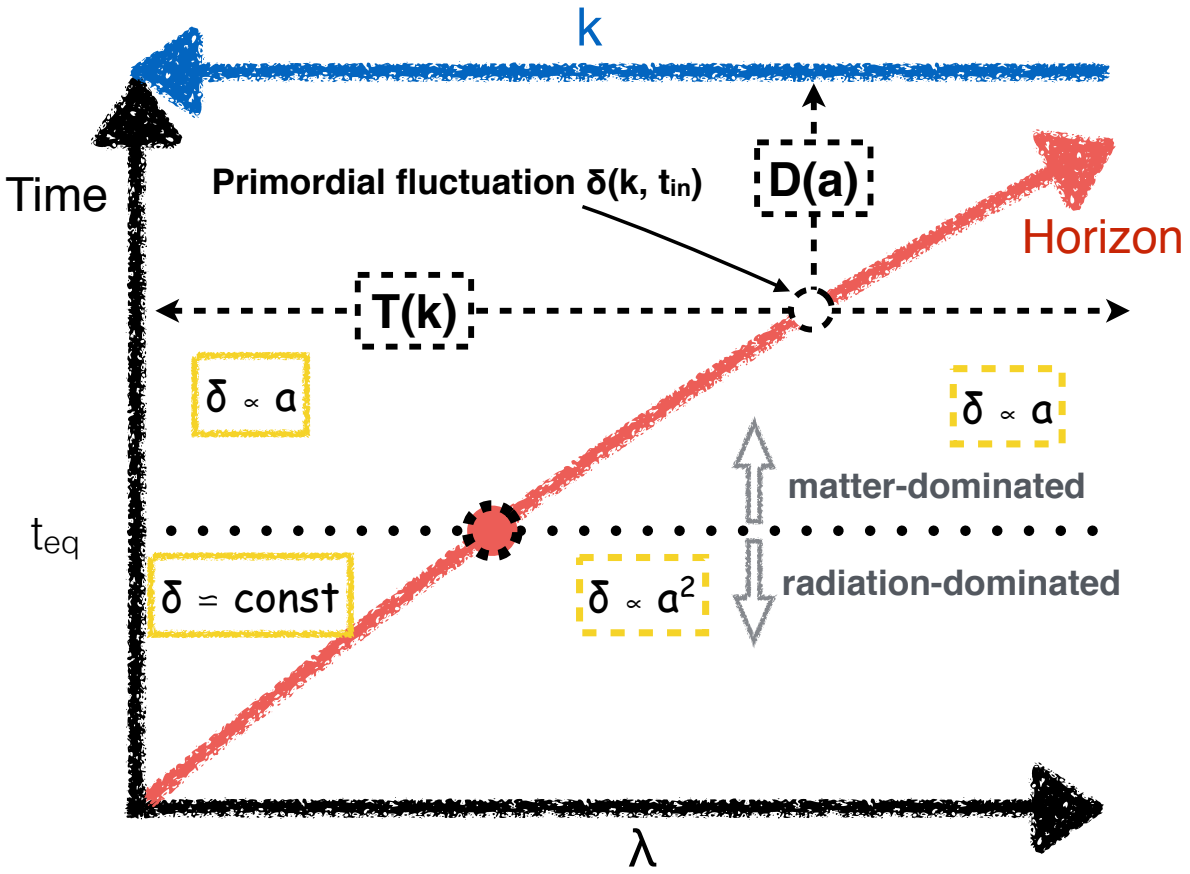

Figure 1.4: A schematic plot demonstrating the growing modes of DM perturbations at scale λ in different cosmic eras. The y- and x-axes show the cosmic time and scale λ where the density perturbation is considered, respectively. The wave number k corresponding to the scale λ is also shown by the blue line on the top. The red line indicates the horizon as a monotonically increasing function of time, for which the red solid point is the scale of horizon at the time $t_{\rm eq}$ of matter-radiation-equality era. The black dotted line splits the cosmic history into two: the Universe is dominated by the matter (radiation) at the time $t > t_{\rm eq}$ ($t < t_{]\rm eq}$) shown above (below) the dotted line. Similarly, the horizon curve (the red line) splits the scales into two at any given time: the perturbations within the horizon (left to the red line) and the perturbations outside the horizon (right to the red line). The DM perturbations have four growing modes by the regimes defined by the horizon curve (the red line) and $t = t_{\rm eq}$ (the dotted line): the structure would grow as $\delta \propto a^2$ ($\delta \propto a$, $\delta \propto a$ and $\delta \approx$constant) when the scale λ outside (outside, inside, inside) the horizon at the time $t < t_{\rm eq}$ ($t > t_{\rm eq}$, $t > t_{\rm eq}$, $t < t_{\rm eq}$), color coded by the yellow box which has the dashed boundary if the relativistic correction is applied. For any scale λ, there is a time $t_{\rm in}$ entering the horizon (indicated by the white point), for which the perturbation is marked as the primordial primordial $\delta_{\rm primordial}(k, t_{\rm in})$. The DM density perturbation experiences the linear growth for $t > t_{\rm in}$ starting from the primordial primordial $\delta_{\rm primordial}(k, t_{\rm in})$ described by $D(a)$ (see the text), and the transfer function $T(k)$ corrects the deviation from the linear growth as the function of scale (along the x-direction).

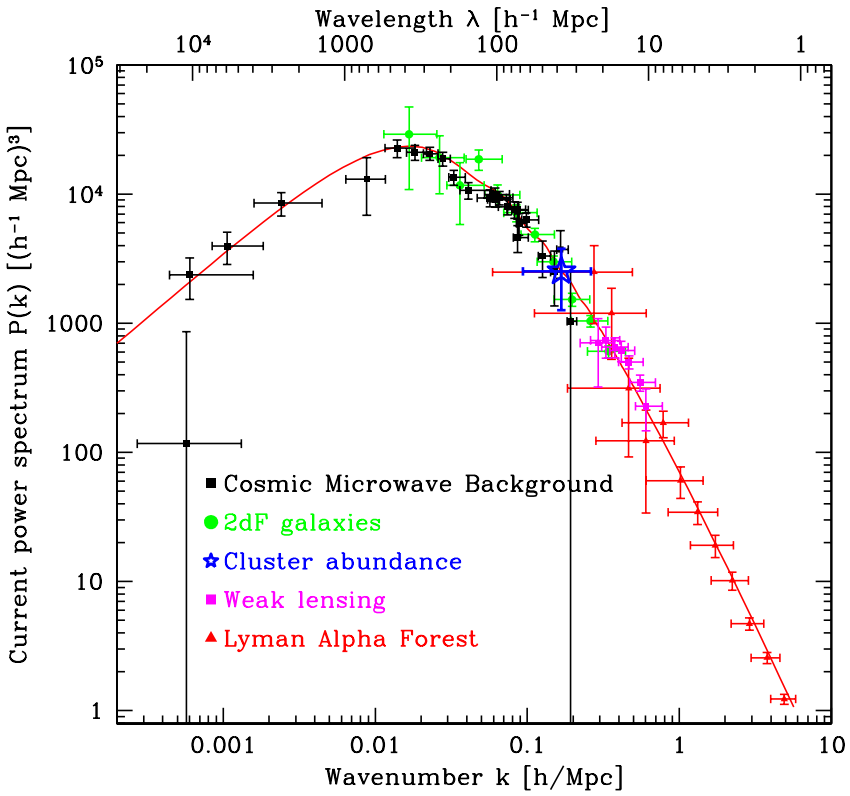

Figure 1.5: The constraints of the power spectrum based on different observational probes. The power spectrum shown by the red solid line is the best-fit to the observed data points, which are indicated by different markers. Figure taken from (Tegmark & Zaldarriaga, 2002).

It is worth mentioning that Equation 1.24 is only valid for the linear regime (i.e., $\delta \ll 1$). The perturbation—especially on a small scale—will eventually enter into the regime of $\delta \lesssim 1$ that the non-linear correction needs to be applied. For the extreme non-linear case $\delta \gg 1$, the gravitationally-collapsed halos or galaxy clusters form, and we describe it in detail in Section 1.2.

The overall picture of structure formation can be summarized as follows. For any random phase of primordial fluctuations—which originated from the quantum fluctuations before the inflation—there is a corresponding density field characterized by δ. Given that the Universe is homogeneous and isotropic, the density field therefore depends only on the scale of interest $k \propto \frac{1}{\lambda}$ and can be described by $\delta(k,t)$, as described above in Equation 1.24. It is then natural to characterize the structure formation of the Universe in a statistical perspective that we describe

the density field by the power spectrum $P(k,t)$—the amplitude of $\delta(k,t)$—which is defined as:

$$P(k,t) = \frac{1}{(2\pi)^3} \langle \delta(k,t) \delta^*(k,t) \rangle \, . \tag{1.25}$$

That is, the statistical properties of structure formation are informed by the power spectrum. It is easy to see in Equation 1.24 and Equation 1.25 that the power spectrum $P(k,t)$ is governed by the growth factor $D(t)$, transfer function $T(k)$ and the primordial power spectrum $P_{\rm primordial}(k)$ as the initial condition. The most straightforward, functional form for the primordial power spectrum is a power law:

$$P_{\rm primordial}(k) = A_0 \, k^{n_{\rm s}} \, , \tag{1.26}$$

where $n_{\rm s}$ is called the spectral index and A_0 is the normalization of the power spectrum. Therefore, the general form of the power spectrum $P(k,t)$ is often expressed as follows:

$$P(k,t) = A_0 \, k^{n_{\rm s}} \, T(k)^2 \, D(t)^2 \, . \tag{1.27}$$

It is convenient to define the effective spectral index $n_{\rm eff}$ such that

$$k^{n_{\rm eff}} \equiv k^{n_{\rm s}} \, T(k)^2 \, , \tag{1.28}$$

and

$$P(k,t) = A_0 \, k^{n_{\rm eff}} \, D(t)^2 \, . \tag{1.29}$$

The shape and amplitude of the power spectrum can be robustly constrained by observational data sets. However, the important concept connecting the theoretical models (e.g., Equation 1.29) and observed Universe is "filtering". Filtering the density field with the specific scale eliminates the contribution from the smaller scale, where the extremely high variance of overdensity—usually in the non-linear regime—is involved. This enables us to study cosmic structures in a statistically meaningful manner. Filtering is typically done by convolving the overdensity field δ with a top-hat window function with the scale of interest $R_{\rm F}$; this is equivalent to performing the multiplication of the overdensity field and window function in Fourier space. Since the density field distributes as a normal distribution, the interesting parameter after the filtering is the variance $\sigma_{R_{\rm F}}$ to the first order, i.e.,

$$\sigma^2_{R_{\rm F}} = \frac{1}{2\pi} \int {\rm d}^3k \, P(k,t) \| W_{R_{\rm F}}(k) \|^2 \, , \tag{1.30}$$

where the $W_{R_{\rm F}}(k)$ is the Fourier transformation of the window function. In this way, the normalization of the power spectrum is mathematically equivalent to the variance $\sigma_{R_{\rm F}}$ of the smoothed density field. Conventionally, this variance is estimated at the scale of $R_{\rm F} = 8 \, h^{-1}{\rm Mpc}$—we denote it by σ_8. The current constraint of the power spectrum normalization is $\sigma_8 \approx 0.8$, and the constraints of the power spectrum based on the different probes are demonstrated in Figure 1.5.

1.2 Galaxy Clusters

In this Section, I will introduce galaxy clusters—gravitationally-collapsed objects—in both theoretical and observational perspectives. The simplest model for gravitationally-collapsed objects—called the spherical collapsed model—is briefly introduced in Section 1.2.1. I then introduce the components of galaxy clusters in Section 1.2.2 and the galaxy cluster surveys in Section 1.2.3, especially the South Pole Telescope Survey. Finally, scaling relations of different observables of galaxy clusters are summarized in Section 1.2.4.

1.2.1 Spherical Collapse Model

As time evolves, the overdensities of density perturbations will eventually grow to extremely non-linear regimes of the large-scale structure—which are identified as gravitationally-collapsed objects (e.g., galaxy clusters). Therefore, galaxy clusters originated from the peaks of perturbations of the primordial density field. There is no general, analytical expression to describe the non-linear evolution of the density field; one has to characterize it by accessing realistic simulations. However, there are some simplified circumstances that we can theoretically address. The simplest case is the Spherical Collapsed Model, which describes gravitational collapses of spherically symmetric systems with curvature $k = 1$ embedded in a flat, matter-dominated, homogeneous and isotropic Universe. Under these assumptions, the Friedmann equations for that system can be written as

$$\left(\frac{\mathrm{d}a}{\mathrm{d}t}\right)^2 = \frac{8\pi G}{3}\rho a^2 - c^2 \,. \tag{1.31}$$

The solution of $a(t)$ therefore describes the expansion and collapse of the system. Moreover, the solution of Equation 1.31 can be solved concisely in the conformal time $\mathrm{d}\eta \equiv c\mathrm{d}t/a$:

$$\begin{aligned} a(\eta) &= A(1-\cos\eta) \\ t(\eta) &= \frac{A}{c}(\eta - \sin\eta) \\ A &= \frac{4\pi G\rho_0 a_0^3}{3c^2}, \end{aligned} \tag{1.32}$$

where ρ_0 and a_0 are the initial conditions of the density and scale factor, respectively.

Equation 1.32 implies that the scale $a(\eta)$ of the system first expands along with the cosmic expansion during the time between $t(\eta) = 0$ and $t(\eta) = \pi$, then reaches the maximum scale (the turnaround point) at $t(\eta) = \pi$, and finally contracts to a single point $a(\eta) = 0$ at $t(\eta) = 2\pi$ (i.e., a collapsed object). To investigate whether a system with mass M would collapse, we can find a corresponding comoving radius r_0 as the initial condition, such that

$$M = \frac{4\pi\rho_0 a_0^3 r_0^3}{3} \text{ and } \rho_{\mathrm{halo}} = \frac{M}{\frac{4\pi}{3}\left(a(\eta)r_0\right)^3}\,.$$

Conversely, the universal background of the matter-dominated Universe is

$$\rho_{\rm bkg} = \frac{3\left(\frac{{\rm d}a}{{\rm d}t}\right)^2}{8\pi G a^2} = \frac{1}{6\pi G t(\eta)^2}\,.$$

One can derive the overdensity δ of the collapsed system as follows.

$$\delta \equiv \frac{\rho_{\rm halo}}{\rho_{\rm bkg}} - 1 = \frac{9}{2}\frac{(\eta - \sin\eta)^2}{(1-\cos\eta)^3} - 1\,. \tag{1.33}$$

Equation 1.33 is the exact solution for the overdensity of a collapsing system as a function of conformal time η with respect to the cosmic background. It is natural to approximate this exact expression in the linear regime ($\eta \to 0$):

$$\begin{aligned} a_{\rm lin}(\eta) = &\quad a(\eta\to 0) \approx &\quad A\frac{\eta^2}{2} \\ t_{\rm lin}(\eta) = &\quad t(\eta\to 0) \approx &\quad \frac{A}{c}\frac{\eta^3}{6} \\ \delta_{\rm lin}(\eta) = &\quad \delta(\eta\to 0) \approx &\quad \frac{3}{20}\eta^2\,. \end{aligned} \tag{1.34}$$

This implies that the overdensity of a collapsed object (when $t_{\rm in} = 2\pi$) predicted by the spherical collapsed model in the linear regime is

$$\delta_{\rm lin}(t_{\rm lin} = 2\pi) \approx 1.69\,. \tag{1.35}$$

Although this model over-simplifies the collapsing process of the real Universe, it still delivers a very clear picture that whether a halo collapses depends only on its density contrast with respect to the universal background—specifically, the overdensity is considered to be a collapsed halo if $\delta_{\rm lin} \geq 1.69$ in the linear regime. Moreover, Equation 1.32 is independent of the halo mass or scale. This property of being scale-independent is called the "self-similarity" of gravitationally-collapsed objects. I will explore this more in Section 1.2.4.

Exploiting that a collapsed halo forms if its linear overdensity $\delta_{\rm lin} \gtrsim 1.69$, the abundance of collapsed halos provides a statistical way to characterize the density field δ assuming that δ is a random Gaussian field. For any halo mass M at redshift z, there is a corresponding enclosed radius such that

$$R_M = \frac{M}{\left(\frac{4\pi}{3}\rho_{\rm bkg}(z)\right)^{1/3}}\,,$$

and therefore the overdensity δ of the random density field smoothed by the filter with the size of R_M can be described by a Gaussian distribution with mean of zero and standard deviation of $\sigma_M \equiv \sigma_M(z)$:

$$P_{M,z}(\delta) = \frac{1}{\sqrt{2\pi}\sigma_M}\exp\left(-\frac{\delta^2}{2\sigma_M^2}\right)\,.$$

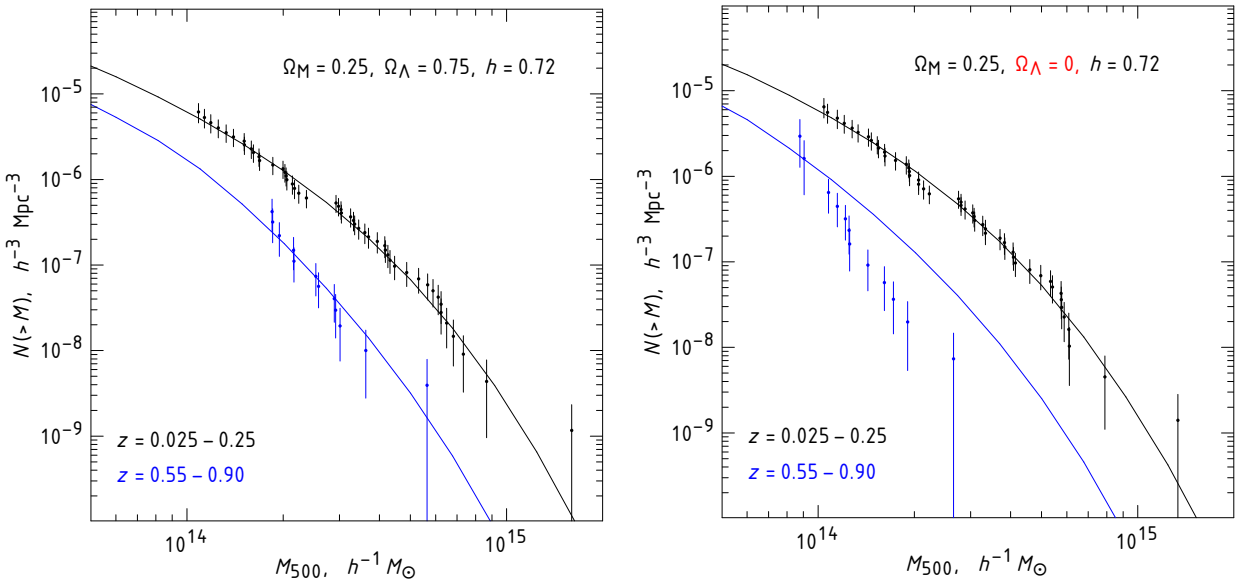

Figure 1.6: The comparison of mass functions and observed halo abundance at different redshift with and without the cosmological constant Λ. The observed halo abundance at low and high redshift is shown by the black and blue, respectively, while the predicted mass functions are plotted as the solid lines with the same color coded. The left panel shows the comparison with cosmological constant $\Lambda = 0.75$, and the right panel is without. A significant offset of halo abundance between the observed and predicted ones is seen for the cosmological framework without the cosmological constant, demonstrating that the cluster abundance is powerful to constrain cosmological parameters. Figures are taken from Vikhlinin et al. (2009b).

As a result, the integrated probability $\wp$ that the halo with mass M can form at redshift z is when the overdensity δ exceeds the threshold value $\delta_{\rm lin} = 1.69$ predicted in the linear regime, i.e.,

$$\wp(M,z) = \int_{\delta_{\rm lin}}^{\infty} P_{M,z}(x)\mathrm{d}x = \frac{1}{\sqrt{2\pi}\sigma_M}\int_{\delta_{\rm lin}}^{\infty}\exp\left(-\frac{x^2}{2\sigma_M^2}\right)\mathrm{d}x\,.$$

Accordingly, the number density of the halos with mass M at redshift z can be derived as

$$\frac{\mathrm{d}n}{\mathrm{d}M}(M,z) \propto -\frac{1}{M/\rho_{\rm bkg}(z)}\frac{\mathrm{d}\wp(M,z)}{\mathrm{d}M} = -\sqrt{\frac{1}{2\pi}}\frac{\rho_{\rm bkg}(z)}{M\sigma_M}\frac{\mathrm{d}\sigma_M}{\mathrm{d}M}\nu\exp\left(-\frac{\nu^2}{2}\right), \qquad (1.36)$$

where $\nu \equiv \delta_{\rm lin}/\sigma_M$ is the "peak height" of the halo with mass M at redshift z. The more massive a halo is, the smaller σ_M and the larger peak height ν are. Equation 1.36 is called the Press-Schechter mass function, which describes the halo abundance as a function of halo mass M and redshift z in a theoretical point of view.

Although Press-Schechter mass function provides a clear picture of the halo abundance in the context of statistical properties, it fails to provide an accurate description for the case in the real Universe due to the over-simplified assumptions made in its derivation. In general, one has

to perform the numerical fitting to the halo abundance derived from large-volume cosmological simulations in order to achieve the accuracy and preciseness required by practical applications. The observed number counts of galaxy clusters and the mass functions derived from the simulations are shown in Figure 1.6. As shown in Figure 1.6, the number density of galaxy clusters at high mass end is exponentially decaying ($\approx \exp\left(-\nu^2/2\right)$ in Equation 1.36) and the abundance of halos is sensitive to cosmological parameters (e.g., $\Omega_{\rm M}$ and Ω_Λ). Therefore, the number counts of galaxy clusters in a given comoving volume can be used to constrain cosmological parameters, providing a complementary and competitive probe in cosmological studies (e.g., see Figure 1.3 and Figure 1.6).

1.2.2 Components of Galaxy Clusters

Galaxy clusters are the largest gravitationally-collapsed systems with masses of $\gtrsim 10^{13}{\rm M}_\odot$ in the Universe. There are three major components of galaxy clusters—DM, Intra-cluster Medium (ICM) and stellar components. Galaxy clusters are dominated by DM, which contributes to $\approx 85\%$ of their total masses, with only $\approx 10-15\%$ and $\approx 1-2\%$ of mass in ICM and stellar components, respectively. These three components can be best visualized by the Bullet Cluster (Markevitch et al., 2002) in Figure 1.7: the blue and red colors indicate the distributions of the DM and ICM, respectively, and the observed cluster galaxies are shown by the pseudo-colors constructed from optical observations.

For the introduction to DM, I defer the readers to Section 1.1.2, and I will describe the ICM and stellar components below.

ICM Since the discovery of diffused X-ray emissions in Coma Cluster in early 20th Century (Limber, 1959; Felten et al., 1966), it has been recognized that galaxy clusters are filled with hot plasma—Intracluster Medium (ICM)—which is trapped inside the gravitational potential and is ionized by the energy released during collapsing. Estimated by the Virial theorem, the temperature $T_{\rm X}$ of ICM is expected to be $\approx 10^7 - 10^8$ K (or $\approx 1-10$ keV). Thus, ICM is emitting X-ray through thermal bremsstrahlung emissions under a such high temperature. The thermal bremsstrahlung emissions give the continuum feature in X-ray spectra, and the emissivity (luminosity per frequency per volume) is proportional to $n_{\rm e}^2\sqrt{T_{\rm X}}$, where $n_{\rm e}$ and $T_{\rm X}$ are the electron density and temperature of ICM, respectively. Apart from the thermal emission of ICM, the line emission is also present due to the metallicities in ICM, which are mainly produced by supernovae explosions of star formation activities in cluster galaxies. The most pronounced feature of the line emission in X-ray spectra is the "Fe line" located at ≈ 7 keV, which is caused by the blended line emissions of Fe^{+24} and Fe^{+25}, respectively, at 6.5 and 7 keV. It is possible to measure redshifts of galaxy clusters from the line emissions in X-ray. However, it is challenging given the difficulty in acquiring high resolution X-ray spectra and that the X-ray emission is dominated mainly by the continuum emission of thermal bremsstrahlung at such high temperatures ($T_{\rm X} \gg 0.1$ keV).

The ICM is cooling down by radiating X-ray. The cooling time of ICM is proportional to $\sqrt{T_{\rm X}}/n_{\rm e}$ at the order of $\approx 10^{10}$ years (comparable to, or larger than, the Hubble time), and

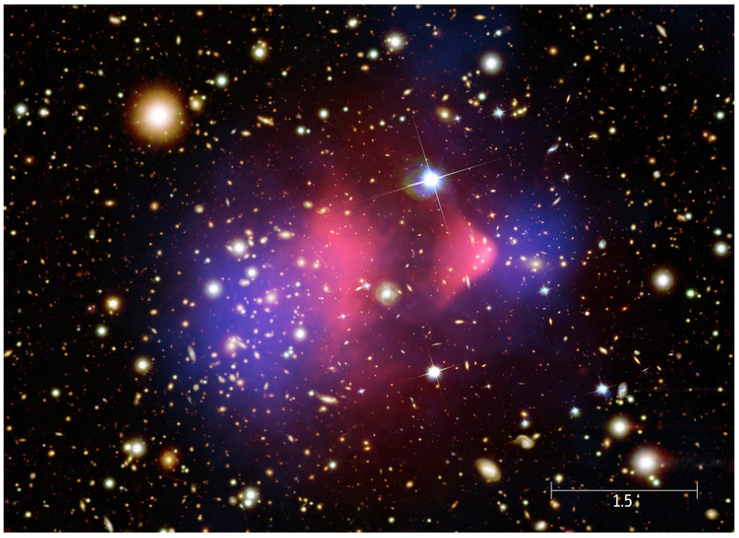

Figure 1.7: The composite image of the Bullet Cluster. The ICM distribution is shown by red, while the cluster mass distribution reconstructed by gravitational lensing is in blue. A clear separation of the ICM and DM is seen. The pseudo color image constructed from optical bands shows the distribution of the cluster galaxies. Image taken from Chandra X-ray Observatory.

this implies that the cooling mechanism is negligible in galaxy clusters. However, the cooling time could be significantly shorter than the Hubble time in the extremely dense cores of galaxy clusters. This suggests that the ICM can be more efficiently cooled down in cluster cores than outskirts, which leads to a "cooling flow" of ICM toward cluster centers. This cooling flow—if it exists—could supply significant amounts of cold gas in central galaxies and further trigger star formation activities. Nevertheless, only very tiny fractions of star formation activities in central cluster galaxies have been observed so far (e.g., the Phoenix cluster, McDonald et al., 2012), suggesting that there could be some heating mechanisms in cluster cores to prevent ICM from efficiently cooling, such as AGN feedbacks (Dunn & Fabian, 2006; Cavagnolo et al., 2008; Hlavacek-Larrondo et al., 2012; Fabian, 2012; Ishibashi et al., 2013; Hlavacek-Larrondo et al., 2013b,a, 2015; McDonald et al., 2015; Ruan et al., 2015; Pike et al., 2014). Significant efforts from both theoretical and observational sides have investigated this "cooling flow problem" (Fabian, 1994), and studying how the heating and cooling mechanisms of ICM regulate star formation activities in cluster galaxies has become one of the most interesting astrophysical questions in galaxy cluster science.

Stellar Components The majorities of stellar components in galaxy clusters are stars bounded in cluster galaxies. Stars are the easiest astronomical objects to observe, and—therefore—naturally galaxy clusters were first identified by overdensities of galaxies (e.g., the Virgo Clusters, Messier, 1781). In the early 20th Century, several pioneering catalogs of galaxy clusters were compiled from optical observations (Abell, 1958; Zwicky & Kowal, 1968), followed by

overwhelming studies of cluster galaxy populations (e.g., Spitzer & Baade, 1951; Rood & Turnrose, 1968; Rood, 1969; Gunn & Gott, 1972a; Rood & Abell, 1973; Oemler, 1974). One of the most influential studies is by Dressler (1980) who established the "Morphology-to-Density Relation", stating that galaxy types and morphologies are strongly correlated with surrounding environments. Specifically, the denser the environment is, the higher the probability that the galaxy is early-type (or elliptical).

Nowadays, strong evidence (e.g., Peng et al., 2010) has shown that galaxy type strongly correlates with not only surrounding environments but also hosting halo mass. In the environment of galaxy clusters, the galaxy populations are dominated by passively evolving galaxies, which are lack of star formations and consist mainly of old and red stars. The most pronounced feature of passively evolving galaxies is the break of their spectra at ≈ 4000 Å, which is caused by the accumulation of the absorption lines of ionized metallicities—especially the Ca II—in interstellar medium. The strength of the 4000 Å indicates the age of the galaxy; the stronger the strength of the 4000 Å break is, the older and more metal-rich stellar populations reside in the galaxy. In the broadband photometry, the spectral feature of the 4000 Å break shows a strong signature in the color between the two bands straddling the break in the observed frame, leading to a clear sequence—often referred to as the "red sequence"—in the "color magnitude diagram" of cluster galaxies. The location of the red sequence in the observed color-magnitude diagram indicates the redshift of the galaxy cluster, while the tilt of the red sequence is informed by the luminosity-to-metallicity relation of the cluster galaxies. Among cluster galaxies, the brightest one is referred to as the "Brightest Cluster Galaxy" (BCG), which is usually the biggest elliptical galaxy of passively evolving populations located at around the potential center.

The other type of stellar components is attributed to Intracluster Light (ICL)—the diffused stars that are not bonded to cluster galaxies. The ICL is believed to be stars stripped from cluster galaxies due to galaxy merging, tidal forces or ram pressure during the period that galaxies fall into potential (Zwicky, 1951). Most ICL resides around the BCG. The detection of ICL is challenging, especially for distant galaxy clusters due to the faintness of individual stars. There have been some attempts to detect and study the ICL of local galaxy clusters (Oemler, 1973; Thuan & Kormendy, 1977; Bernstein et al., 1995; Gregg & West, 1998; Gonzalez et al., 2000), suggesting that the distribution and fractional light of ICL with respect to dominating central galaxies might indicate the dynamical states of galaxy clusters (Feldmeier et al., 2002, 2004).

1.2.3 Galaxy Cluster Surveys and The South Pole Telescope

Galaxy clusters can be detected by overdensities of galaxy populations in optical (Gladders & Yee, 2005; Koester et al., 2007) and Near-Infrared (NIR, Eisenhardt et al., 2008; Muzzin et al., 2009; Papovich et al., 2010), or by the X-ray signatures of ICM (Evrard & Henry, 1991; Truemper, 1993; Ebeling et al., 1996; Rosati et al., 1998; Böhringer et al., 2004; Pierre et al., 2004). However, it is worth mentioning that the cluster surveys in optical or X-ray generally have difficulties in finding galaxy clusters at high redshift: the X-ray surveys suffer from severe cosmological dimming given that the X-ray surface brightness of ICM is proportional to $(1+z)^{-4}$, while the optical detection of galaxy clusters at high redshift becomes challenging due to redshifting of the spectral features of old stellar populations and is sensitive to the projection effect (van

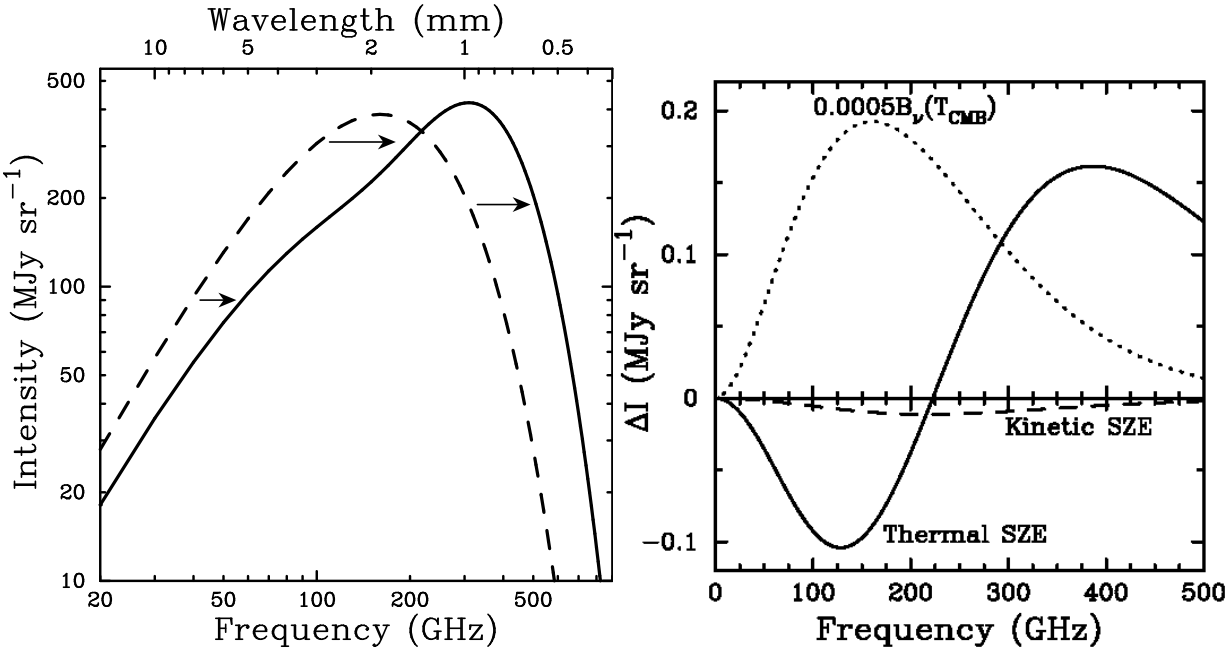

Figure 1.8: The SZE caused by the inverse Compton scattering and the SZ spectra. The "blueshift" of CMB photons after scattering with ICM is shown in the left panel. The thermal SZE and kinetic SZE spectra as well as the CMB spectrum with the amplitude re-normalized by 5×10^{-5} are shown in the right panel. As seen in the right panel, the amplitude of the thermal SZE is at the order of $\approx 10^{-4}$ of the CMB spectrum, while the kinetic SZ spectrum is at the order of only few percent of thermal SZE. This demonstrates the difficulties of detecting the SZE. Figures are taken from Carlstrom et al. (2002).

Haarlem et al., 1997). Therefore, cluster science over the past two decades was subject to small samples or individual systems at low redshift. This situation has changed because of ongoing galaxy cluster surveys at the mm wavelength by employing the Sunyaev-Zel'dovich effect (SZE, Sunyaev & Zel'dovich, 1970a, 1972), as with the South Pole Telescope (SPT, Carlstrom et al., 2002, 2011), Atacama Cosmology Telescope (ACT, Fowler et al., 2007) and the *Planck* mission (The Planck Collaboration, 2006).

The signature of distorted spectra, caused by the inverse Compton scattering between ICM and CMB photons, in the mm wavelength with respect to the primordial CMB spectrum is called the Sunyaev-Zel'dovich effect (SZE). The CMB photons gain energy after scattering with hot ICM, leading to a "blueshift" in the distorted spectrum. This results in a decrement and enhancement to the intensity of the primordial CMB spectrum, respectively, at the frequencies below and above than ≈ 220 GHz (see Figure 1.8). This distortion of CMB spectra caused by ICM can be used to trace galaxy clusters in a redshift-independent way; therefore, the SZE surveys can provide the samples of galaxy clusters that depend only on cluster masses without cosmological dimming. The change in the intensities of CMB spectra due to the "thermal" SZE can be formulated as

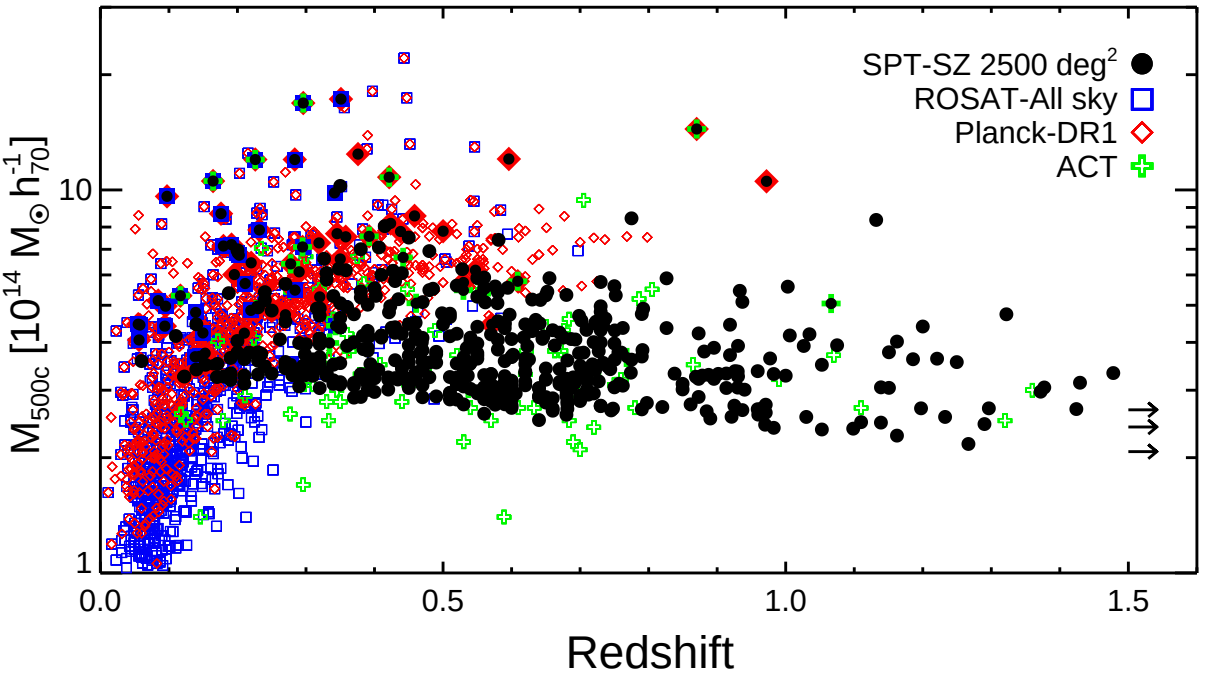

Figure 1.9: The full galaxy cluster catalog detected in the SPT-SZ survey. The black points are the galaxy clusters detected by the SPT-SZ survey, while other clusters detected by other surveys are also plotted for comparison. The SPT-SZ cluster sample shows a selection function that the SPT-SZ survey provides a nearly mass-limited sample out to $\gtrsim 1.5$ and weakly depends on the redshift, and this demonstrates the power of the SZE effect in finding high redshift clusters. Figure is taken from Bleem et al. (2015).

follows:

$$\begin{aligned} \Delta I &= g(x) I_{\rm CMB} y \\ g(x) &= \frac{x^4 e^x}{(e^x-1)^2}\left(x\frac{e^x+1}{e^x-1}-4\right)(1+\delta_{\rm SZE}(x,T_{\rm e})) \\ y &= \int n_{\rm e}\frac{k_{\rm B}T_{\rm e}}{m_{\rm e}c^2}\sigma_{\rm T}{\rm d}l\,, \end{aligned} \tag{1.37}$$

where y is the Compton parameter that is the the fractional energy gained by scattering with ICM along the line of sight l; $\sigma_{\rm T}$ is the Thomas cross-section; $T_{\rm e}$ is the temperature of electrons; $m_{\rm e}$ is the mass of electrons; $n_{\rm e}$ is the density of electrons; $\delta_{\rm SZE}(x,T_{\rm e})$ is the relativistic correction to the distorted spectrum; $I_{\rm CMB}$ is the primordial intensity of the CMB spectrum; and $x \equiv h\nu/k_{\rm B}T_{\rm CMB}$ is the dimensionless frequency normalized by the CMB temperature $T_{\rm CMB}$. Equation 1.37 is called the SZ spectrum, a unique signature in the distorted spectrum caused by the (thermal) SZE.

The another SZE is called the "kinetic" SZE (kSZE), which is caused by the Doppler effect from the relative motion of ICM with respect to the rest frame of the CMB. The change in the

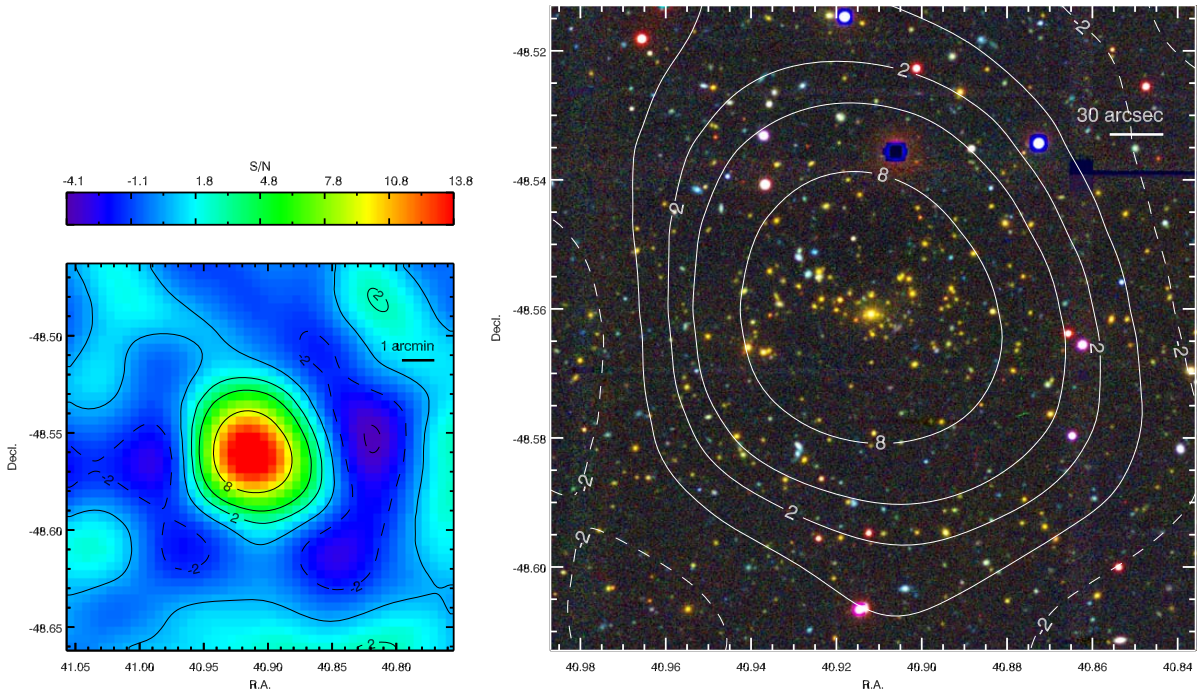

Figure 1.10: The SZE map detected by the SPT-SZ survey and the optical counterpart of the galaxy cluster SPT-CL 0243−4833. The left panel shows the map of the SZE signal-to-noise ratios detected by the SPT, while the right panel is the zoom-in optical image of this cluster center with the SZE signal-to-noise contours over-plotted. Figure is taken from Williamson et al. (2011a).

CMB intensity (in the non-relativistic limit) due to the kSZE is

$$\Delta I \propto \frac{v_{\parallel}}{c},$$

where $v_{\parallel}$ is the peculiar velocity of ICM along the line of sight. The amplitude of the CMB distortion due to the kSZE is typically only a small percent of the thermal SZE, while the thermal SZE is at the order of $\approx 10^{-5} - 10^{-4}$ of the CMB spectrum (the same order of the primordial CMB fluctuations). Seen in Figure 1.8, this subtle distortion of the CMB spectrum makes observations extremely difficult. Hence, the SZE is only possible to detect by the mm-wavelength surveys with very low noise level at few tens of μK. The South Pole Telescope (SPT) is ideal for finding galaxy clusters via the SZE, and the South Pole Telescope SZ survey (SPT-SZ survey) is specifically designed for achieving this goal.

The SPT is a ten meter telescope with a bolometer array of 960 elements and arcminute angular resolution located at Antarctica. Three filters at the frequencies of 95, 150 and 220 GHz are used, for which the filters at 95 and 150 GHz are ideal, by design, for detecting the CMB decrement caused by galaxy clusters via the SZE effect. Therefore, one of the primary science goals of

the SPT experiment is dedicated to the SZE cluster survey (SPT-SZ survey) by mapping an area of 2500 deg^2 in the southern atmosphere. The high angular resolutions of $1'.6$, $1'.1$ and $1'.0$ at 95, 150 and 220 GHz, respectively, are designed to match the expected angular scale of galaxy clusters at high redshift, therefore the SPT-SZ survey can provide a nearly mass-limited sample of galaxy clusters with masses above $\approx 3 \times 10^{14} M_{\odot}$ out to $z \approx 1.5$. The SPT-SZ survey began in 2008 and was completed in 2011. To date, the SPT-SZ survey provides the largest mass-limited sample of SZE-detected galaxy clusters with purity and completeness both higher than 96 % (Song et al., 2012b). The full SPT-SZ catalog, consisting of 409 (677) galaxy clusters with $\xi > 5$ ($\xi > 4.5$), was released in 2015 (Bleem et al., 2015, see Figure 1.9), and several cosmological and astrophysical studies have been done based on the SPT-SZ cluster sample (Vanderlinde et al., 2010; Reichardt et al., 2012, 2013; Benson et al., 2013; Bocquet et al., 2015b). The second generation of the SPT experiment—SPT polarization (SPTpol, Austermann et al., 2012)—is ongoing with higher sensitivity, enabling the detection of "B-mode" polarization caused by the CMB lensing of the large-scale structure. The next generation of the SPT experiment—SPT-3G (Benson et al., 2014)—with a bolometer array of $\gtrsim 15,000$ elements and $\gtrsim 10$ times lower noise levels will find galaxy clusters to a much lower mass threshold with a sample size more than the SPT-SZ survey by an order magnitude.

1.2.4 Scaling Relations

Galaxy clusters originated from the peaks of primordial perturbations of the density field and collapsed via gravitational instability (see Section 1.2.1). If collapsing is purely gravitational, then collapsed systems show self-similar appearances without a preferred scale—this property is called self-similarity (Gunn & Gott, 1972b; Fillmore & Goldreich, 1984; Bertschinger, 1985; Hoffman & Shaham, 1985). Galaxy clusters are the most massive systems in the Universe, and indeed they express a high degree of self-similarity. One of the most famous studies to depict the self-similarity of galaxy clusters is Navarro et al. (1997a), which showed, by employing a purely gravitating simulation, that the density distributions of collapsed dark matter halos can be described by a universal profile—the Navarro-Frenk-White (NFW) model.

Because ICM traces the gravitational potential of galaxy clusters, ICM properties should also behave in a self-similar way. By importing the assumptions of the virial theorem as well as the hydrostatic equilibrium with gravitational potential of ICM—which radiates energy only through thermal bremsstrahlung, contributes a constant fraction of cluster mass, and resides in a spherically symmetric and self-similar DM halo—then, the X-ray properties of ICM can be simply connected to cluster mass by the power law relations—called the X-ray self-similar scaling relations—that were theoretically derived by Kaiser (1986). In the framework of self-similar scaling relations, the X-ray observables can be mutually connected to each other or cluster mass

as follows:

$$\begin{aligned}
\textbf{Temperature to Mass relation} \quad & T_{\rm X} \propto M^{\frac{2}{3}} \\
\textbf{Luminosity to Mass relation} \quad & L_{\rm X} \propto M^{\frac{4}{3}} \\
\textbf{Luminosity to Temperature relation} \quad & L_{\rm X} \propto T_{\rm X}^2 \\
\textbf{ICM mass to Mass relation} \quad & M_{\rm ICM} \propto M \\
Y_{\rm X}\ \textbf{parameter to Mass relation} \quad & Y_{\rm X} \propto M^{\frac{5}{3}} \\
Y_{\rm X}\ \textbf{parameter to Luminosity relation} \quad & Y_{\rm X} \propto L_{\rm X}^{\frac{5}{4}},
\end{aligned}$$

where $T_{\rm X}$, $L_{\rm X}$, $M_{\rm ICM}$ are the temperature, X-ray luminosity and the mass of ICM, respectively; $Y_{\rm X} \equiv M_{\rm ICM} T_{\rm X}$ is the integrated Compton parameter, and M is cluster mass. In practice, the cluster mass is defined by a fixed overdensity with respect to the critical density, which evolves as $E(z)^2$, leading to the following scaling relations:

$$\begin{aligned}
\textbf{Temperature to Mass relation} \quad & T_{\rm X} \propto M^{\frac{2}{3}} E(z)^{\frac{2}{3}} \\
\textbf{Luminosity to Mass relation} \quad & L_{\rm X} \propto M^{\frac{4}{3}} E(z)^{\frac{7}{3}} \\
\textbf{Luminosity to Temperature relation} \quad & L_{\rm X} \propto T_{\rm X}^2 E(z) \\
\textbf{ICM mass to Mass relation} \quad & M_{\rm ICM} \propto M \\
Y_{\rm X}\ \textbf{parameter to Mass relation} \quad & Y_{\rm X} \propto M^{\frac{5}{3}} E(z)^{\frac{2}{3}} \\
Y_{\rm X}\ \textbf{parameter to Luminosity relation} \quad & Y_{\rm X} \propto L_{\rm X}^{\frac{5}{4}} E(z)^{-\frac{9}{5}},
\end{aligned}$$

However, the scaling relations above have been derived under various assumptions of collapsing halos and ICM properties, and any non-gravitational effects (e.g., the energy feedback or substructure merging) would result in a deviation from self-similarity. That is, any effect that violates the assumptions mentioned above perturbs the self-similar scaling relations. Tremendous efforts have been dedicated to studying observed scaling relations of galaxy clusters in the context of X-ray observables (Arnaud & Evrard, 1999; Markevitch, 1998; Mohr et al., 1999; Neumann & Arnaud, 1999, 2001; Stanek et al., 2006; Vikhlinin et al., 2006; Maughan, 2007; Pratt et al., 2009; Vikhlinin et al., 2009a; Andersson et al., 2011; Böhringer et al., 2014; Mantz et al., 2016).

Apart from X-ray observables, self-similar scaling relations also exist in other cluster observables, such as galaxy richness observed in optical (Johnston et al., 2007; Rozo et al., 2009; Saro et al., 2015) or in NIR (Lin et al., 2004), total NIR luminosity embedded in clusters (Lin et al., 2003, 2006; Mulroy et al., 2014; Chiu et al., 2016c), total stellar mass (Lin et al., 2003; Giodini et al., 2009; Gonzalez et al., 2013; van der Burg et al., 2014; Chiu et al., 2016b), BCG stellar mass (Lin & Mohr, 2004; van der Burg et al., 2014; Chiu et al., 2016b), line-of-sight velocity dispersions of cluster galaxies (Saro et al., 2012; Sifón et al., 2013; Ruel et al., 2014), and SZE signal-to-noise measurements (High et al., 2012; Saliwanchik et al., 2013; Bocquet et al., 2015b). This demonstrates that galaxy clusters are highly self-similar systems, and cluster observables

can be connected to each other or cluster mass by simple scaling. One of the most important categorical scaling relations is the "observable-to-mass relation", i.e., the cluster observable—often referred to as the "mass proxy"— is linked to cluster true mass via a power law:

$$\mathscr{O} = A_{\mathscr{O}} \left(\frac{M}{M_{\rm piv}}\right)^{B_{\mathscr{O}}} \left(\frac{f(z)}{f(z_{\rm piv})}\right)^{C_{\mathscr{O}}} , \tag{1.38}$$

where the observable $\mathscr{O}$ is used as a cluster mass proxy, and the normalization of the scaling relation is $A_{\mathscr{O}}$; the power law indices of mass and redshift trends are $B_{\mathscr{O}}$ and $C_{\mathscr{O}}$, respectively. The pivotal mass (redshift) is $M_{\rm piv}$ ($z_{\rm piv}$). The function f describes the functional form of redshift dependence (e.g., $f(z) = E(z)$ in Equation 1.38). However, there exists "intrinsic scatter" of the mass proxies around the mean values predicted by the observable-to-mass relations at fixed cluster mass, which is usually assumed to be a log-normal distribution and denoted by

$$D_{\mathscr{O}} \equiv \ln(\mathscr{O}|M) .$$

Large intrinsic scatter would erase the signature of the trend between the mass proxy $\mathscr{O}$ and cluster mass M if the size of the conducted cluster sample is small.

Scaling relations shed light on cluster cosmology and astrophysics. In the cosmological perspective, observable-to-mass relations promise a way of efficiently estimating cluster masses with large sample sizes and, therefore, the feasibility of using galaxy clusters as a cosmological probe. In order to achieve the precision required by practical cosmological analysis, an observable-to-mass relation with low intrinsic scatter (e.g., the $Y_{\rm X} - M$ relation) has to be utilized; otherwise, the scatter between the derived and underlying true masses would be too large to make galaxy clusters useful in cosmological studies. However, an observable-to-mass relation with low intrinsic scatter usually does not guarantee the bias-free cluster mass estimates. On the other hand, a mass proxy that can provide unbiased mass estimates usually suffers from large intrinsic scatter. Therefore, calibrating the absolute mass scale of a mass proxy with low intrinsic scatter is one of the most critical steps to understand cluster cosmology.

In the astrophysical perspective, the assembly history of galaxy clusters, along with various astrophysical effects (e.g., cool-core of ICM, or star formation of cluster galaxies), imprint features on scaling relations. For example, the mass and redshift trends of stellar-mass-to-halo-mass scaling relations, respectively, reveal assembling properties and evolutionary stages of cluster galaxies. Additionally, intrinsic scatter of scaling relations shows how non-gravitational or astrophysical effects impact the properties of self-similarity during cluster formation. Therefore, studying scaling relations of galaxy clusters unveils how the large-scale structure formed.

Thesis Organization

In the following chapters of this thesis, I will present various observable-to-mass scaling relations of galaxy clusters in the wide range of mass and redshift. Additionally, I will also demonstrate a novel way to estimate cluster masses using the lensing effect, which can be used to perform the absolute mass calibration of mass proxies. The majorities of following chapters are based on the work done within the SPT collaboration.

In Chapter 2, we studied the baryon content—the stellar and ICM masses—of 14 galaxy clusters with masses $M_{500} \approx 6 \times 10^{14} \mathrm{M}_{\odot}$ at high redshift $0.57 < z < 1.33$ selected by their SZE signatures observed by the SPT, and we compare them to the published results from literature at low redshift ($z \lesssim 0.1$). In Chapter 3, we extend the results of Chapter 2 to the galaxy groups or clusters with lower masses ($M_{500} \approx 2 \times 10^{13} \mathrm{M}_{\odot}$) at redshift $0.1 \lesssim z \lesssim 1.0$ by conducting the X-ray data from the XMM-BCS survey, NIR imaging from the *Spitzer*-South-Pole-Telescope Deep Field survey, and the optical data from the Blanco Cosmology Survey. In Chapter 4, we present the complete study of baryon content of massive clusters over cosmic time selected by the SPT; in this chapter, we significantly increase the sample size and use consistent analysis on homogeneous data sets, leading to the state-of-the-art constraints of observable-to-mass scaling relations across redshift $0.25 < z < 1.25$. In Chapter 5, we present a method by exploiting the lensing magnification effect to estimate the masses of SPT-selected galaxy clusters, and we then compare the lensing masses to the masses estimated from the SZE-signatures. We summarize the results and provide an outlook for the future work in Chapter 6.

Chapter 2

Baryon Content of Massive Galaxy Clusters at $0.57 < z < 1.33$

I. Chiu[1,2], J. Mohr[1,2,3], M. McDonald[4], S. Bocquet[1,2], M. L. N. Ashby[5], M. Bayliss[6,5], B. A. Benson[7,8,9], L. E. Bleem[8,10,11], M. Brodwin[12], S. Desai[1,2], J. P. Dietrich[1,2], W. R. Forman[5], C. Gangkofner[1,2], A. H. Gonzalez[13], C. Hennig[1,2], J. Liu[1,2], C. L. Reichardt[14], A. Saro[1,2], B. Stalder[5,15], S. A. Stanford[16,17], J. Song [18], T. Schrabback[19], R. Šuhada[1], V. Strazzullo[1], A. Zenteno[1,20]

[1]Department of Physics, Ludwig-Maximilians-Universität, Scheinerstr. 1, 81679 München, Germany
[2]Excellence Cluster Universe, Boltzmannstr. 2, 85748 Garching, Germany
[3]Max-Planck-Institut für extraterrestrische Physik, Giessenbachstr. 85748 Garching, Germany
[4]Kavli Institute for Astrophysics and Space Research, Massachusetts Institute of Technology, 77 Massachusetts Avenue, Cambridge, MA 02139
[5]Harvard-Smithsonian Center for Astrophysics, 60 Garden Street, Cambridge, MA 02138
[6]Department of Physics, Harvard University, 17 Oxford Street, Cambridge, MA 02138
[7]Fermi National Accelerator Laboratory, Batavia, IL 60510-0500
[8]Kavli Institute for Cosmological Physics, University of Chicago, 5640 South Ellis Avenue, Chicago, IL 60637
[9]Department of Astronomy and Astrophysics, University of Chicago, 5640 South Ellis Avenue, Chicago, IL 60637
[10]Department of Physics, University of Chicago, 5640 South Ellis Avenue, Chicago, IL 60637
[11]Argonne National Laboratory, 9700 S. Cass Avenue, Argonne, IL, USA 60439
[12]Department of Physics and Astronomy, University of Missouri, 5110 Rockhill Road, Kansas City, MO 64110
[13]Department of Astronomy, University of Florida, Gainesville, FL 32611
[14]School of Physics, University of Melbourne, Parkville, VIC 3010, Australia
[15]Institute for Astronomy, University of Hawaii at Manoa, Honolulu, HI 96822, USA
[16]Department of Physics, University of California, One Shields Avenue, Davis, CA 95616
[17]Institute of Geophysics and Planetary Physics, Lawrence Livermore National Laboratory, Liv-

ermore, CA 94550
[18]Korea Astronomy and Space Science Institute 776, Daedeokdae-ro, Yuseong-gu, Daejeon, Republic of Korea 305-348
[19]Argelander-Institut für Astronomie, Auf dem Hügel 71, D-53121 Bonn, Germany
[20]Cerro Tololo Inter-American Observatory, Casilla 603, La Serena, Chile

This chapter is published as Chiu et al. (2016b) in Monthly Notices of the Royal Astronomical Society.

2.1 Abstract

We study the stellar, Brightest Cluster Galaxy (BCG) and intracluster medium (ICM) masses of 14 South Pole Telescope (SPT) selected galaxy clusters with median redshift $z = 0.9$ and mass $M_{500} = 6 \times 10^{14} \mathrm{M}_{\odot}$. We estimate stellar masses for each cluster and BCG using six photometric bands, the ICM mass using X-ray observations, and the virial masses using the SPT Sunyaev-Zel'dovich Effect signature. At $z = 0.9$ the BCG mass $M_{\star}^{\mathrm{BCG}}$ constitutes $0.12 \pm 0.01\%$ of the halo mass for a $6 \times 10^{14} \mathrm{M}_{\odot}$ cluster, and this fraction falls as $M_{500}^{-0.58 \pm 0.07}$. The cluster stellar mass function has a characteristic mass $M_0 = 10^{11.0 \pm 0.1} \mathrm{M}_{\odot}$, and the number of galaxies per unit mass in clusters is larger than in the field by a factor 1.65 ± 0.20. We combine our SPT sample with previously published samples at low redshift and correct to a common initial mass function and for systematic virial mass differences. We then explore mass and redshift trends in the stellar fraction $f_{\star}$, the ICM fraction f_{ICM}, the collapsed baryon fraction f_{c} and the baryon fraction f_{b}. At a pivot mass of $6 \times 10^{14} \mathrm{M}_{\odot}$ and redshift $z = 0.9$, the characteristic values are $f_{\star}$=$1.1 \pm 0.1\%$, f_{ICM}=$9.6 \pm 0.5\%$, f_{c}=$10.7 \pm 1.1\%$ and f_{b}=$10.7 \pm 0.6\%$. These fractions all vary with cluster mass at high significance, with higher mass clusters having lower $f_{\star}$ and f_{c} and higher f_{ICM} and f_{b}. When accounting for a 15% systematic virial mass uncertainty, there is no statistically significant redshift trend at fixed mass. Our results support the scenario where clusters grow through accretion from subclusters (higher $f_{\star}$, lower f_{ICM}) and the field (lower $f_{\star}$, higher f_{ICM}), balancing to keep $f_{\star}$ and f_{ICM} approximately constant since $z \sim 0.9$.

2.2 Introduction

The utility of galaxy clusters for cosmological parameter studies was recognized quite early (Frenk et al., 1990; Henry & Arnaud, 1991; Lilje, 1992; White et al., 1993; White et al., 1993), but the overwhelming evidence of widespread merging in the cluster population (Geller & Beers, 1982; Forman & Jones, 1982; Dressler & Shectman, 1988; Mohr et al., 1995) together with the high scatter in the X-ray luminosity–temperature relation (e.g., Fabian, 1994) left many with the impression that clusters were too complex and varied to ever be useful for cosmological studies. It was some time later that the first evidence that clusters exhibit significant regularity in their intracluster medium (ICM) properties appeared (Mohr & Evrard, 1997; Arnaud & Evrard, 1999; Cavaliere et al., 1999; Mohr et al., 1999); X-ray observations showed that clusters as a population exhibit a size–temperature scaling relation with $\approx 10\%$ scatter, a level of regularity comparable to that known in elliptical galaxies (i.e., Djorgovski & Davis, 1987). This regularity together with the emergence of evidence for cosmic acceleration (Riess et al., 1998; Perlmutter et al., 1999) focused renewed interest in the use of galaxy clusters for precise cosmological studies (e.g., Haiman et al., 2001). Moreover, the existence of low scatter, power law relations among cluster observables provided a useful tool to study the variation in cluster structure with mass and redshift.

Soon thereafter, the regularity seen in the X-ray properties of clusters was shown to exist also in the optical properties of clusters (Lin et al., 2003, hereafter L03). L03 carried out an X-ray and near-infrared (NIR) 2MASS K-band study of an ensemble of 27 nearby clusters, measuring the

mass fraction of the stellar component inside the galaxies ($f_\star$), the ICM mass fraction ($f_{\rm ICM}$), the total baryon fraction ($f_{\rm b}$), the cold baryon fraction ($f_{\rm c}$; hereafter we refer to this as the collapsed baryon fraction) and the metal enrichment of the ICM. This study showed an increasing $f_{\rm b}$ and decreasing $f_\star$ and $f_{\rm c}$ in the more massive halos, suggesting that the star formation efficiency is higher in the low mass halos as well as that feedback associated with this enhanced star formation was having a larger structural impact in low mass than in high mass halos. Over the last decade, additional studies using larger samples and better data have largely confirmed this result (e.g., Gonzalez et al. 2007; Giodini et al. 2009; Andreon 2010; Zhang et al. 2011, hereafter Zha11; Gonzalez et al. 2013, hereafter GZ13).

Understanding how the cluster and group baryon components evolve with redshift is a key question today. While there have been many detailed studies of intermediate and high redshift galaxy clusters, most previous observational studies of large cluster samples have focused on nearby systems due to the difficulty of defining high redshift samples and of following them up in the X-ray and with adequately deep optical or near-infrared (NIR) imaging. That is changing now with the recent analyses of Sunyaev-Zel'dovich effect (Sunyaev & Zel'dovich, 1970b, 1972, hereafter SZE) selected clusters and groups at intermediate and high redshift. The SZE results from inverse Compton interactions of the hot ionized ICM with cosmic microwave background (CMB) photons; because it is a CMB spectral distortion rather than a source of emission, it does not suffer from cosmological dimming. Since the first SZE selected clusters were discovered in the SPT-SZ survey (Staniszewski et al., 2009), this method has been demonstrated to be a useful tool for discovering and studying galaxy cluster populations out to high redshift (Zenteno et al. 2011; Hilton et al. 2013, hereafter H13; Bayliss et al. 2014). In addition, NIR selected clusters and groups at high redshift are now also being used to study the evolution of galaxy populations (e.g. van der Burg et al., 2014, hereafter vdB14). In this work we focus on an SZE selected cluster sample at redshift higher than 0.6 that originates from the first 720 deg^2 of the South Pole Telescope (Carlstrom et al., 2011) SZE (SPT-SZ) survey (Song et al., 2012c; Reichardt et al., 2013).

To study the evolution of $f_\star$ one needs robust stellar and virial mass estimates. Stellar masses are typically estimated by converting the observed galaxy luminosity into the stellar mass using the mean mass-to-light ratio constructed from theoretical models. This approach is sensitive to the galaxy spectral templates and needs to be modelled carefully to reduce possible biases (vdB14). For accurate stellar mass measurements with less model-dependence, one requires deep multi-wavelength observations that allow the spectral energy distribution (SED) to be measured on a galaxy by galaxy basis. For clusters at $z \approx 1$, this typically requires photometry using 8 m telescopes like the VLT together with space-based NIR data from the *Spitzer* Space Telescope.

The cluster virial mass measurements typically have come from X-ray mass proxies such as the emission weighted mean temperature or from galaxy velocity dispersions. The calibration of the X-ray mass proxies has often been based on the assumption of hydrostatic equilibrium, which in some circumstances can underestimate the mass by 20 – 40% due to the non-thermal pressure components in these young structures (see Molnar et al., 2010; Chiu & Molnar, 2012, and references therein). Velocity dispersion mass estimates, although likely less biased than hydrostatic mass estimates, have been shown to have quite high scatter on a single cluster basis (e.g., White et al., 2010; Saro et al., 2013; Ruel et al., 2014). Therefore, a study of the redshift

variation of $f_\star$ would benefit from a low scatter mass proxy from the X-ray or SZE that has been calibrated to mass using low bias measurements such as weak lensing or velocity dispersions together with a method that accounts for selection effects and cosmological sensitivity. The masses we use in this analysis are based on the SZE signal-to-noise for each cluster as observed in the SPT-SZ survey and are calibrated in just such a manner (Bocquet et al., 2015b).

In addition to robust, low scatter mass estimates one should use a uniformly selected cluster sample whose selection is not directly affected by variations in $f_\star$. ICM based observables such as the X-ray luminosity or the SZE signature enable this, although connections between the physics of star formation and the structure of the ICM remain a concern. Also, if one wishes to probe the regime beyond the group scale at high redshift, one must survey enough volume to find significant numbers of the rare, massive clusters. Large solid angle SZE surveys like those from SPT, the Atacama Cosmology Telescope (ACT, Fowler et al., 2007) and *Planck* (Tauber, 2000) provide a clean way to discover clusters. Indeed, because the SZE signature for a cluster of a given mass evolves only weakly with redshift in an arcminute resolution SZE survey, the SPT-SZ survey provides a cluster sample that is well approximated as a mass–limited sample above redshift $z \approx 0.3$ (e.g. Vanderlinde et al., 2010).

In this paper, we seek to study the baryon content, including the ICM and the stellar mass components, of massive high redshift clusters discovered within the SPT-SZ survey. We attempt also to constrain the evolution of the baryon content of these clusters by combining our high redshift, massive clusters with other samples, primarily studied at low redshift. The paper is organized as follows. We describe the cluster sample and the data in Section 2.3. In Section 3.4 we provide detailed descriptions of the ICM, the stellar mass and the total mass measurements for the clusters. We present the stellar mass function (SMF) in Section 2.5 and present results on the mass and redshift trends of the baryon composition in Section 2.6. We discuss these results in Section 2.7 and summarize our conclusions in Section 5.7.

We adopt the concordance ΛCDM cosmological model with the cosmological parameters measured in Bocquet et al. (2015b) throughout this paper: $\Omega_{\rm M} = 0.299$, $\Omega_\Lambda = 0.701$ and $H_0 = 68.3\ {\rm km\,s^{-1}\,Mpc^{-1}}$. These constraints are derived from a combination of the SPT-SZ cluster sample, the *Planck* temperature anisotropy, *WMAP* polarisation anisotropy and Baryon Acoustic Oscillation (BAO) and SN Ia distances. Unless otherwise stated all uncertainties are indicated as 1σ, the quantities are estimated at the overdensity of 500 with respect to the critical density ($\rho_{\rm crit}$) at the cluster's redshift, all celestial coordinates are quoted in the epoch J2000, and all photometry is in the AB magnitude system.

2.3 Cluster Samples and Data

In this section we briefly summarize the SPT cluster sample and the follow-up data acquisition, reduction, calibration as well as the literature cluster sample we compare to. The deep optical observations from the VLT and the *HST*, together with the near-infrared observations from the *Spitzer*, enable us to measure the integrated stellar masses of our clusters accurately. The ICM masses are extracted from *Chandra* and XMM-*Newton* X-ray observations. Cluster total masses are derived from the SPT SZE observable ξ as calibrated using the external data sets (see

Table 2.1: Cluster properties and photometric depths: The columns contain the cluster name, redshift and coordinates of the X-ray center and BCG followed by the 10σ depths in each band.

Cluster	Redshift	α_X [deg]	δ_X [deg]	α_{BCG} [deg]	δ_{BCG} [deg]	$m_{b_H}^{10\sigma}$	$m_{F606W}^{10\sigma}$	$m_{I_B}^{10\sigma}$	$m_{z_G}^{10\sigma}$	$m_{[3.6]}^{10\sigma}$	$m_{[4.5]}^{10\sigma}$
SPT-CL J0000−5748	0.702	0.2500	−57.8093	0.2502	−57.8093	23.61	26.36	24.94	24.19	22.04	20.79
SPT-CL J0102−4915	0.870	15.7340	−49.2656	15.7407	−49.2720	24.34	26.31	24.51	24.14	22.21	21.86
SPT-CL J0205−5829	1.320	31.4437	−58.4856	31.4511	−58.4801	24.51	26.44	24.54	23.74	22.21	20.76
SPT-CL J0533−5005	0.881	83.4060	−50.0965	83.4144	−50.0845	24.64	26.84	24.66	23.99	22.01	20.56
SPT-CL J0546−5345	1.067	86.6548	−53.7590	86.6569	−53.7586	24.64	26.56	24.51	23.71	21.86	20.89
SPT-CL J0559−5249	0.609	89.9329	−52.8266	89.9300	−52.8242	24.49	26.46	24.31	24.06	22.09	20.71
SPT-CL J0615−5746	0.972	93.9570	−57.7780	93.9656	−57.7802	24.49	26.26	24.11	23.86	21.99	20.76
SPT-CL J2040−5726	0.930	310.0631	−57.4287	310.0552	−57.4208	24.51	26.34	24.69	24.21	22.24	20.76
SPT-CL J2106−5844	1.132	316.5179	−58.7426	316.5192	−58.7411	24.84	26.24	24.61	23.71	22.31	20.49
SPT-CL J2331−5051	0.576	352.9634	−50.8649	352.9631	−50.8650	24.04	26.41	24.94	23.51	22.29	20.71
SPT-CL J2337−5942	0.775	354.3523	−59.7056	354.3650	−59.7013	24.66	26.36	24.59	23.86	22.24	20.86
SPT-CL J2341−5119	1.003	355.3000	−51.3287	355.3014	−51.3291	24.59	26.24	24.81	23.89	22.26	20.49
SPT-CL J2342−5411	1.075	355.6916	−54.1849	355.6913	−54.1847	24.46	26.31	24.31	23.91	22.26	20.64
SPT-CL J2359−5009	0.775	359.9327	−50.1697	359.9324	−50.1722	24.84	26.19	24.66	23.91	21.74	20.66

Section 2.4.1). The literature sample we compare with in this study is described in Section 2.3.2.

2.3.1 SPT Cluster Sample

The 14 clusters we analyze are drawn from early SPT-SZ cluster catalogs, which covered the full 2500 deg^2 with shallower data (Williamson et al., 2011b) or included the first 720 deg^2 of the full depth SPT-SZ survey (Reichardt et al., 2013). The full 2500 deg^2 catalog has meanwhile been released (Bleem et al., 2014). These 14 systems have high detection significance ($\xi > 4.8$) and were selected for further study using *HST* and the VLT. All fourteen have measured spectroscopic redshifts (Song et al., 2012c).

We study the virial region defined by R_{500} in each cluster, where R_{500} is extracted from a virial mass estimate (M_{500}) that is derived from the SPT SZE observable (see Section 2.4.1). We adopt the X-ray centroid as the cluster center, because the SZE cluster center measurement uncertainties are larger. A previous analysis of the offset between the SPT measured cluster center and the Brightest Cluster Galaxies (BCG) positions in a large ensemble of the SPT clusters (Song et al., 2012c) indicated that once the SPT positional measurement uncertainties are accounted for, this offset distribution is consistent with that seen in local samples where the X-ray center is used (e.g., Lin & Mohr, 2004). In our sample the BCG positions, X-ray centers and SZE centers are all in reasonably good agreement (see Figure 2.1). Importantly, these offsets have a negligible impact on our analysis, because we are comparing average properties determined within the radius R_{500}.

We present the names, redshifts and the sky positions in J2000 (α, δ) of the X-ray center and BCG of our SPT sample in Table 2.1. The virial mass M_{500} and the virial radius R_{500} for each cluster are listed in Table 2.4.

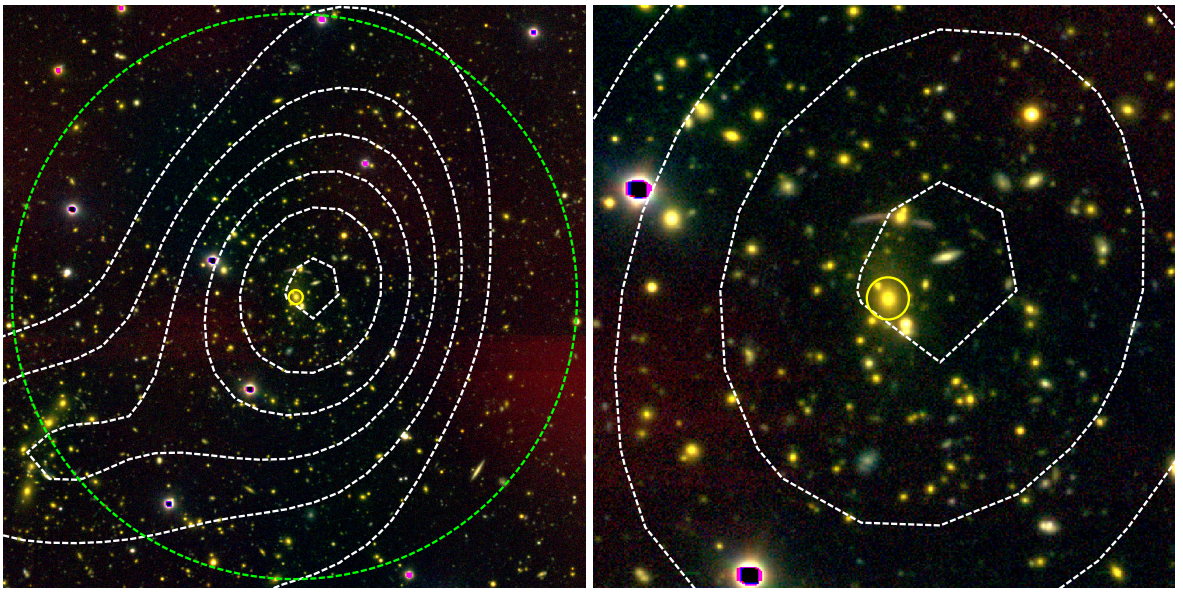

(a) SPT-CL J2331-5051 at z=0.576 (b) SPT-CL J2331-5051 (zoom in)

Figure 2.1: VLT pseudo-color images of SPT-CL J2331−5051 constructed from b_H, I_B and z_G. The left and right panels respectively show cluster R_{500} and $R_{500}/3$ regions centered on the X-ray peak. The SZE signal-to-noise contours from 0 to 10 with steps of 2 are white, the R_{500} region is the green circle and the BCG is marked by the yellow circle. The VLT pseudo-color images for the other thirteen clusters are available online.

Optical and Infrared Photometry

VLT/FORS2 imaging in the bands b_{High} (b_H), I_{Bessel} (I_B), and z_{Gunn} (z_G) was obtained for the fourteen clusters under programs 088.A-0889 and 089.A-0824 (PI Mohr). Observations were carried out in queue mode under clear conditions. The nominal exposure times for the different bands are 480 s (b_H), 2100 s (I_B) and 3600 s (z_G). These exposure times are achieved by coadding dithered exposures with 160 s (b_H), 175 s (I_B), and 120 s (z_G). Deviations from the nominal exposure times are present for some fields due to repeated observations when conditions violated specified constraints or observing sequences that could not be completed during the original planned semester. The pseudo-color images of the 14 SPT clusters constructed from VLT bands b_H, I_B, and z_G are shown in Figure 2.1. Each image shows also SZE contours (white), the R_{500} virial region (green circle) and the BCG (yellow circle).

Data reduction is performed with the THELI pipeline (Erben et al., 2005; Schirmer, 2013). Twilight flats are used for flatfielding. The I_B- and z_G-band data are defringed using fringe maps extracted from night sky flats constructed from the data themselves. To avoid over-subtracting the sky background, the background subtraction is modified from the pipeline standard as described by Applegate et al. (2012).

The FORS2 field-of-view is so small that only a few astrometric standards are found in the common astrometric reference catalogs. Many of them are saturated in our exposures. While we

use the overlapping exposures from all passbands to map them to a common astrometric grid, the absolute astrometric calibration is adopted from mosaics of F606W images centered on our clusters from the complementary ACS/*HST* programs C18-12246 (PI Stubbs) and C19-12447 (PI High). Each cluster is observed in the well-dithered mode through F606W and F814W filters. For F606W imaging, the cluster is imaged by four pointings with minimal overlap to remove the chip gap; these mosaics span a field of view of 6.7×6.7 arcmin^2 centered on the cluster core. For F814W imaging, only one pointing centered on cluster core is acquired. In this work we use only the F606W observations for deriving the stellar masses.

Cataloging of the VLT images is carried out using SExtractor (Bertin & Arnouts, 1996) in dual image mode. The detection image is created through the combination of I_B and z_G. Cataloging of the *HST* images is carried out separately, also using SExtractor. Galaxy photometry is extracted using MAG_AUTO. The VLT and HST photometry is matched at the catalog level with a $1''$ match radius.

Because VLT data are generally not taken in photometric conditions, the photometric calibration is also carried out using data from the *HST* programs. We derive a relation between F814W magnitudes and the FORS2 I_B filter

$$m_{I_B} - m_{F814W} = -0.052 + 0.0095(m_{F606W} - m_{F814W}) \, ,$$

from the Pickles (1998) stellar library, which is valid for stars with $(m_{F606W} - m_{F814W}) < 1.7$ mag. After deriving the absolute photometric calibration of the FORS2 I_B passband from this relation, the relative photometric calibrations of the other bands are fixed using a stellar locus regression (e.g. High et al., 2009; Desai et al., 2012) in the $(m_{b_H}, m_{F606W}, m_{I_B}, m_{z_G})$ color-space. The inclusion of F606W data in this process is necessary because the stellar locus in $(m_{b_H}, m_{I_B}, m_{z_G})$ colors has no features.

All our clusters were observed with the *Spitzer* Infrared Array Camera (IRAC; Fazio et al. 2004) at both 3.6 μm and 4.5 μm under programs PID 60099, 70053 and 80012 (PI Brodwin). The images are acquired in dithered mode with exposure times of 8×100 s and 6×30 s for 3.6 μm and 4.5 μm, respectively. We follow standard data reduction procedures to reduce the IRAC observations (Ashby et al., 2009). For each field we generate a pair of spatially registered infrared mosaics: a relatively deep 3.6 μm image and a shallower 4.5 μm image. These images are cataloged with SExtractor in dual image mode, using the 3.6 μm mosaic as the detection image. We use the SExtractor MAG_AUTO and its associated uncertainty. We verify our detections by visually inspecting the SExtractor object check image. Because the IRAC point spread function is significantly larger than in either the *HST* or VLT imaging, we match our two-band IRAC photometry ([3.6] and [4.5]) to the nearest optical counterpart at the catalog level, using a $1''$ match radius. If an object has multiple matches within the *Spitzer* point spread function, we then deblend the IRAC fluxes into the counterparts as described below.

For the objects in the *Spitzer*/IRAC catalog with multiple optical counterparts, we deblend the [3.6] and [4.5] fluxes using the properties of the optical counterparts in z_G. Specifically, we deblend the *Spitzer*/IRAC fluxes assuming the flux ratios of the neighboring objects in the IRAC

band are the same as in the reddest optical band:

$$R_{(i,j)}^{[3.6],[4.5]} \equiv \left.\frac{f_i}{f_j}\right|_{[3.6],[4.5]} = \left.\frac{f_i}{f_j}\right|_{z_G}, \tag{2.1}$$

where f_i is the flux of object i.

We test the relationship between the flux ratios in z_G and the two IRAC bands by estimating the flux ratios of matched objects without close optical neighbors. We find that the intrinsic scatter of $R_{(i,j)}^{[3.6]}$ and $R_{(i,j)}^{[4.5]}$ are of the order of 0.6 and 0.8 dex, respectively. We add this scatter into the flux uncertainties in $[3.6]$ and $[4.5]$ of deblended objects.

Although the uncertainties in the deblended fluxes are large, we find that adding these two IRAC bands– deblended using our method– reduces the uncertainties of the stellar mass estimates by a mean value of 20% and reduces the lognormal scatter of the reduced χ^2 (Section 2.4.3) by 29%. Moreover, through studying an ensemble of pairs of unblended sources that we first artificially blend and then deblend, we find that our method does not introduce biases in the resulting mass estimates.

The fraction of blended IRAC sources lying projected within R_{500} for the 14 clusters varies from 11 to 20% with a mean of 16% and a standard deviation of 2.3%. From 25 to 55% of the sources are blended within $0.5R_{500}$. Thus, the majority ($> 80\%$) of sources used in our analysis is not affected by flux blending.

We derive 10σ depth $m_{\rm filter}^{10\sigma}$ for 6 passbands (filter $= b_H, F606W, I_B, z_G, [3.6], [4.5]$) of each cluster in the catalog stage by estimating the magnitude where the median of the MAG_AUTO error distribution is equal to 0.11. These values are listed in Table 2.1. The $m_{\rm filter}^{10\sigma}$ depths show good consistency to the 10σ depths estimated by measuring the sky variance in $2''$ apertures within the VLT images. The $m_{[3.6]}^{10\sigma}$ depths are about 2 magnitudes deeper than our estimated m^* for each cluster, and hence the cluster galaxies should be detected without significant incompleteness.

We estimate the m^* of each passband for each cluster using a Composite Stellar Population (CSP) model (Bruzual & Charlot, 2003). This model has a burst at $z = 3$ that decays exponentially with e-folding timescale of $\tau = 0.4$ Gyr. The tilt of the red sequence is modelled by using 6 CSPs with different metallicities and by calibrating those models to reproduce the Coma red sequence (for more details see Song et al., 2012a). This model has been shown to be adequate to derive accurate red sequence redshifts within SPT-selected clusters to $z > 1$ with the root-mean-square of the cluster's photo-z error $\Delta z/(1+z)$, calibrated with spectroscopic clusters, of 0.02 (Song et al., 2012c, Hennig in prep.). This model provides a good representation of the color and tilt of the red sequence and the evolution of m^* in SPT selected galaxy clusters extending to $z \approx 1.2$ (Hennig in prep.).

X-ray Data

Eleven out of the fourteen clusters in our sample have been targeted by the *Chandra* X-ray telescope with program Nos. 12800071, 12800088, and 13800883. The remaining three clusters, SPT-CL J0205−5829 ($z = 1.32$; see Stalder et al., 2013), SPT-CL J0615−5746 ($z = 0.972$) and SPT-CL J2040−5726 ($z = 0.93$) have been observed with XMM-*Newton* with program 067501

(PI Andersson). The X-ray follow up observations are designed to observe the SPT clusters uniformly with the goal of obtaining between 1500 and 2000 source photons within R_{500}. These photons enable us to measure the ICM projected temperature, the density profile and the mass proxy Y_X(the product of the ICM mass and X-ray temperature) with $\sim$15% accuracy.

The *Chandra* data reduction is fully described in previous publications (Andersson et al., 2011; Benson et al., 2013; McDonald et al., 2013). We include an additional cluster with Chandra data (ObsID 12258), the massive merging cluster SPT-CL J0102-4915 (Menanteau et al., 2012; Jee et al., 2014) at $z = 0.87$, which we analyze in an identical way to those previous works (Benson et al., in prep). For the XMM-*Newton* data, we use SAS 12.0.1 to reduce and reprocess the data. All three cameras (MOS1, MOS2 and pn) are used in our analysis. The background flare periods are removed in both hard and soft bands using 3σ clipping after point source removal. We describe the ICM mass measurements in Section 2.4.2.

2.3.2 Comparison Samples For This Study

To place our results in context and to have a more complete view of the possible redshift variation of the baryon content in galaxy clusters, we compare our measurements with the published results from the local universe at $z \leq 0.1$. We include L03, Zha11 and GZ13 because they all provide estimates of $f_\star$, $f_{\rm ICM}$ and $f_{\rm b}$ for large samples over a broader mass range than we are able to sample with the SPT selected clusters. L03 study 27 nearby galaxy clusters selected by optical/X-ray with masses ranging from 10^{14}–10^{15}M$_\odot$; 13 of these have available ICM mass measurements (Mohr et al., 1999). There are 19 clusters in Zha11, in which M_{500} is estimated using velocity dispersions. We discard two clusters, A2029 and A2065, from Zha11 because they argue the virial mass estimates are biased due to the substructures. GZ13 estimate mass fractions for 15 nearby clusters, 12 of those have stellar mass measurements. In addition, we include the clusters and groups from H13 and vdB14 that extend to $z \geq 0.8$, allowing a more complete study at high redshifts. H13 study the stellar composition of 10 SZE selected clusters from ACT, and vdB14 study the Gemini CLuster Astrophysics Spectroscopic Survey (GCLASS) sample, consisting of 10 low mass clusters selected by *Spitzer*/IRAC imaging. We restrict the cluster sample to those with virial masses above 3×10^{14}M$_\odot$, which is the mass regime probed by the SPT-SZ sample. This results in a total of 34 clusters in the comparison sample. We note that the majority of the vdB14 sample is in the low mass regime and therefore falls below our mass threshold; our results should not be extrapolated into this lower mass regime.

There are several important differences between these studies and ours. We note that the groups or the clusters in these samples, with the exception of those in H13, are either selected from X-ray or optical/NIR surveys. Thus, these differences in selection method could potentially lead to observable differences in the samples. In addition to these selection differences, there are differences in the stellar mass and virial mass estimates. We describe below the corrections we apply to the comparison sample to address these differences, thereby enabling a meaningful combination with the SPT sample.

Correcting to a Common IMF

The most important systematic factor for estimating stellar mass is the choice of the Initial Mass Function (IMF) for the stellar population models that are then employed when converting from galaxy light to galaxy stellar mass. Different assumed IMFs introduce systematic shifts in the mass to light ratios of the resulting stellar populations (Cappellari et al., 2006). For instance, the conventional Salpeter (1955) IMF with a power law index of -2.35 would predict a mass to light ratio higher by a factor of 2 than the one using the Kroupa (2001) IMF (Kauffmann et al., 2003; Chabrier, 2003; Cappellari et al., 2006). For this analysis we adopt the Chabrier (2003) IMF (see more detailed discussion in Section 2.4.3) and apply a correction to the literature results so all measured stellar masses are appropriate for this IMF. Specifically, we reduce the stellar mass measurements of L03 and Zha11 by 24% (Lin et al., 2012; Zhang et al., 2012), the measurements of GZ13 by 24% (or 0.12 dex), and the measurements of H13 by 42% (or 0.24 dex). Because vdB14 use the same Chabrier IMF as in this work, no IMF correction is needed.

Correcting for Virial Mass Systematics

To enable a meaningful comparison of the baryon content across samples, it is crucial to use a consistent virial mass estimate for all samples. Zha11, H13 and vdB14 estimate M_{500} using velocity dispersions, while the other analyses all use X-ray mass proxies (ICM temperature) to estimate virial masses. Our SPT masses arise from a recent analysis (Bocquet et al., 2015b) that includes corrections for selection effects, marginalization over cosmological parameters and systematic uncertainties and combination with external cosmological datasets (see discussion in Section 2.4.1).

The Bocquet et al. (2015b) analysis quantifies the systematic mass shifts that result for SPT clusters when using only X-ray data, only velocity dispersion data or the full combined dataset of X-ray, velocity dispersions and external cosmological constraints from CMB, BAO and SNe. Namely, when compared to our cluster mass estimates obtained using the full combined dataset, the SPT cluster masses inferred from the X-ray mass proxy Y_X alone have a systematically lower mass by 44%, and masses inferred from velocity dispersions alone have systematically lower masses by 23%. As explained in more detail in Section 2.4.1, we adopt the full combined dataset masses for the analysis of our SPT cluster sample.

For the comparison here, it is not crucial to know which virial mass estimate is most accurate. What we must do is adopt one mass calibration method for our SPT sample and then correct the virial mass estimates in the other samples to a consistent mass definition before making comparisons of the baryon content. To make these corrections we use the results from the recent SPT mass analysis (Bocquet et al., 2015b) to apply a correction to the virial mass scale in each literature sample to bring it into better consistency with our SPT sample.

Specifically, we estimate the M_{500} of the clusters in L03 by using the same $T_X - M_{500}$ relation (Vikhlinin et al., 2009b) used in GZ13; then we increase the L03 and GZ13 masses by 44%, assuming the systematic offset of Y_X derived SPT virial masses is the same for these clusters whose masses were derived using the $T_X - M_{500}$ relation. Similarly, we increase the masses in Zha11, H13 and vdB14 by 23%, because their masses are derived from velocity dispersion

measurements.

Increasing M_{500} increases the virial radius and therefore also increases the stellar and ICM masses. Specifically, a 44% (23%) increase in virial mass leads to a 13.2% (7.4%) and 12.9%(7.1%) increment in $M_\star$ and $M_{\rm ICM}$, respectively, assuming that the cluster galaxies are distributed as an NFW model with concentration $c_{500} = 1.9$ and the ICM near the virial radius falls off as a β-model (Cavaliere & Fusco-Femiano, 1978) with $\beta = 2/3$. In correcting the literature results for comparison to the SPT sample, we apply a correction that accounts for the shifts in all the different masses.

Correcting previously published masses to account for different data sets and analysis methods allows us to more accurately compare the results, but this correction procedure has inherent uncertainties. It is challenging to quantify these remaining uncertainties, but for this analysis we adopt a systematic virial mass uncertainty of 15% (1σ) when constraining the redshift variation with the combined sample. We return to this discussion in Section 2.6 where we present our fitting procedure in detail. Also, in the conclusions we comment on the impact of adopting other systematic uncertainties.

We note in passing that if we had adopted the SPT masses calibrated only using the X-ray mass proxy $Y_{\rm X}$, the SPT cluster virial masses M_{500} would decrease on average by a factor of $1/1.44$. The new values for the SPT sample quantities $M_\star$, $M_{\rm ICM}$, $f_\star$, $f_{\rm ICM}$, $f_{\rm c}$ and $f_{\rm b}$ can be approximated by applying the scale factors 0.87, 0.88, 1.26, 1.27, 0.99 and 1.27, respectively, to the measurements presented in Table 2.4.

2.4 Mass Measurement Methods

In this section we describe the method for estimating the virial, the ICM and the stellar masses.

2.4.1 SPT Cluster Virial Mass M_{500} Measurements

The virial masses (M_{500}) that we use come from the mass calibration and cosmological analysis of Bocquet et al. (2015b). They are derived using the SPT SZE observable ξ, the cluster redshift, and a combination of internal and external calibration data. These data include direct mass information from 63 measured cluster velocity dispersions (observed using Gemini South, the VLT, and the Magellan Baade and Clay telescopes, see Ruel et al., 2014) and 16 $Y_{\rm X}$ measurements (Andersson et al., 2011; Foley et al., 2011; Benson et al., 2013). In addition, mass information derives from the 100 cluster candidates extracted from the first 720 deg^2 of the SPT-SZ survey. These SPT data are then jointly analyzed in combination with *Planck* temperature anisotropy, *WMAP*9 polarization anisotropy, BAO and SNIa constraints.

As explained in Bocquet et al. (2015b) (see Figure 2), adopting such strong external cosmological constraints has a dramatic impact on the cluster masses, pushing them higher to better match the masses expected within the preferred cosmological model, given the ξ and redshift distribution of the cluster sample. In contrast, the $Y_{\rm X}$ constraints prefer lower masses, and the velocity dispersions prefer masses in the middle. By combining all the constraints one ends with a mass calibration that prefers higher masses than the masses one would obtain when using solely

the Y_X's or velocity dispersions as calibrators (see also further discussion in Section 2.3.2). We adopt these masses that arise from a combination of internal and external calibration data for the analysis below.

Our SPT masses are corrected for Eddington bias that arises from the scatter between the mass and the selection variable ξ and the steep cluster mass distribution. The intrinsic scatter in mass at fixed ξ is approximately 16%, and there is an additional measurement scatter that reaches $\approx 14\%$ at $\xi = 5$. Final mass uncertainties include marginalization over all cosmological and scaling relation parameters. Thus, our masses and mass uncertainties include a combination of the systematic and statistical uncertainties. Typical final mass uncertainties are $\sim 20\%$. The masses are then used to calculate R_{500}, which has a characteristic uncertainty of $\approx 7\%$. We refer the reader to Bocquet et al. (2015b) for additional details. The virial mass systematics correction for the comparison sample is described in Section 2.3.2.

2.4.2 ICM Mass Measurements

In this work we adopt the X-ray ICM mass $M_{\rm ICM}$ measurements extracted within R_{500}. We determine the center of the cluster (α_X,δ_X) iteratively as the centroid of X-ray emission in the 0.7 – 2.0 keV energy band within a 250 – 500 kpc annulus (see Table 2.1). The final centroid is visually verified on the smoothed X-ray emission map and is adjusted to match the center of the most circularly symmetric isophote if it deviates significantly from the peak. The ICM density profile is estimated by fitting the X-ray surface brightness profile extracted in the energy range 0.7 – 2.0 keV assuming spherical symmetry and centered on the derived centroid. For *Chandra* observations, we fit the modified single β-model (Equation 1 and Equation 2 in Vikhlinin et al. (2006)) to the X-ray surface brightness profile. The details of the X-ray analysis are given elsewhere (Andersson et al., 2011; McDonald et al., 2013).

Because we cannot simultaneously constrain all the parameters in the modified single β-model for the XMM-*Newton* observations, we instead fit a single β-model for SPT-CL J0205-5829 ($z = 1.32$), SPT-CL J0615-5746 ($z = 0.972$) and SPT-CL J2040-5726 ($z = 0.93$). For these clusters the single β-model provides a good fit to the XMM-*Newton* X-ray surface brightness profile. The best fit X-ray surface brightness profile then provides the radial distribution of the ICM, and we use the flux of the cluster within the 0.15 – 1.0 R_{500} annulus to determine the central density (e.g., Mohr et al., 1999). We assume the metal abundance of the ICM is 0.3 solar, resulting in $n_e/n_p = 1.199$ and $\mu \equiv \rho_{\rm ICM}/(m_p n_e) = 1.16$, where the subscripts p and e denote proton and electron, respectively.

To estimate $M_{\rm ICM}$, we integrate the measured ICM profile to R_{500} obtained from the SZE derived M_{500}. The uncertainty of $M_{\rm ICM}$ is estimated by propagating the uncertainties of the best-fit parameters. Deriving the X-ray temperature of the ICM free from the instrumental calibration bias can be challenging; however, the ICM mass and density profile is insensitive to the temperature (Mohr et al., 1999) and to instrumental systematics (Schellenberger et al., 2014; Martino et al., 2014; Donahue et al., 2014). Thus, we do not expect significant systematics in the ICM masses.

2.4.3 Stellar Mass Measurements

In the sections below we describe the SED fitting to determine galaxy stellar masses and our method of making a statistical background correction.

SED Fitting

We use the multiband photometry to constrain the spectral energy distribution (SED) of each galaxy and to estimate its stellar mass. The photometry of the six bands ($b_H F606W I_B z_G [3.6] [4.5]$) is used for each galaxy. We use the Le Phare SED fitting routine (Arnouts et al., 1999; Ilbert et al., 2006) together with a template library that consists of stellar templates (Pickles, 1998) and galaxy templates from CSP models (Bruzual & Charlot, 2003) derived using a Chabrier (2003) IMF. The systematics correction for the different IMF used in the comparison sample is described in Section 2.3.2. The stellar templates include all normal stellar spectra together with the spectra of metal-weak F- through K dwarfs and G through K giants. The galaxy library includes templates that cover: (1) a wide range in metallicity $Z = 0.004, 0.008, 0.02$; (2) an e-folding exponentially decaying star formation rate with characteristic timescale $\tau = 0.1, 0.3, 1.0, 2.0, 3.0, 5.0, 10.0, 15.0, 30.0$ Gyr, (3) a broad redshift range between 0.0 and 3.0 with steps of 0.05, and (4) the Calzetti et al. (2000) extinction law evaluated at $E(B-V) = 0.0, 0.2, 0.4, 0.6, 0.8, 1.0$. Our galaxy library contains no templates with emission lines.

We run the Le Phare routine with this template library on every object that lies projected within R_{500} and is brighter than $m^* + 2.0$ within the z_G passband (except that we use [3.6] for the two clusters at $z > 1.1$). This ensures we are selecting the galaxy population in a consistent manner over the full redshift range. For each galaxy, we adopt a uniform prior on the extinction law $E(B-V)$ between 0.0 and 1.0 and a weak, flat prior on the stellar mass between $10^8 M_\odot$ and $10^{13} M_\odot$.

For the SED fit we increase the MAG_AUTO flux uncertainties for all 6 passbands by a factor of 2. We estimate this correction factor by examining the *photometric repeatability* of the galaxies that appear in multiple individual VLT exposures (Desai et al., 2012; Liu et al., 2014). With this correction the resulting magnitude uncertainties correctly describe the scatter in the repeated photometric measurements of the same galaxies. Rescaling the uncertainties has no significant impact on the final result but increases the uncertainty of the stellar mass estimate for each galaxy by 25%.

For each cluster we first estimate the stellar mass of the BCG, $M_\star^{\rm BCG}$, fixing the redshift to the cluster redshift. The BCG is chosen to be the brightest cluster galaxy projected within R_{500}; we select this galaxy visually using the NIR and optical imaging and then confirm in the catalog (z_G and $[3.6]$) that it is the brightest galaxy. We find that the BCGs in our cluster sample all prefer the templates with the characteristic e-folding timescale for the star formation rate to be $\tau \leq 1$ Gyr. This indicates that the rapid star forming activity seen in the SPT selected Phoenix Cluster BCG (McDonald et al., 2014b) is not present in our cluster sample. This result is consistent with the view that the evolution of the typical BCG is well described by a CSP model with $\tau \approx 0.9$ Gyr out to redshift 1.5 (Lidman et al., 2012). For the final $M_\star^{\rm BCG}$ estimates we restrict the template library to $\tau \leq 1$ Gyr, which results in a $\approx 6\%$ reduction in the stellar mass uncertainties as compared

to fitting across the full range of τ. This small change in uncertainty has no impact on our final result. We then estimate the stellar mass for the remaining galaxies using the same configuration except that we allow the redshift to float and fit the templates without restricting τ.

We adjust the Le Phare routine to output the best-fit mass $M_\star^{\rm best}$, the median mass $M_\star^{\rm med}$, the mass at the lower (higher) 68% confidence level $M_\star^{\rm lo}$ ($M_\star^{\rm hi}$) and the best-fit χ^2 extracted over the full template library. We discard the objects from the analysis where the best fit χ^2 arises for a stellar template. This stellar removal works well; testing on the COSMOS field (Capak et al., 2007; Sanders et al., 2007; Ilbert et al., 2009) indicates we have a residual stellar contamination and a false identification rate for galaxies under 1.5% and $\sim$0.15%, respectively. The mass-to-light ratios Υ and their rms variations in the observed frame [3.6] band for all clusters are provided in Table 2.4. These are extracted from the subset of galaxies projected within the virial region that have photo-z's that are within $\Delta z = 0.1$ of the cluster spectroscopic redshift.

We examine those galaxies with $M_\star^{\rm best} > M_\star^{\rm BCG}$ closely, because we expect no galaxy to be more massive than the BCG. We find that most of these galaxies can be excluded because they have redshifts far higher than the cluster. In total, there are 37 out of 2640 galaxies with $M_\star^{\rm best} > M_\star^{\rm BCG}$ within R_{500} of the 14 clusters. That is, about 1.5% of the objects are discarded through this process. However, one must take special care in cases of merging clusters, which could host one or more galaxies with masses similar to the most massive one. In a few cases (3 galaxies to be exact) we find through photo-z and visual inspection that these galaxies likely lie in the cluster and have mass estimates slightly larger than the mass of our selected BCG. In these cases we include those galaxies in the stellar mass estimate. We provide further details of our SED fit performance in Appendix 2.9.1.

The stellar mass estimate for the region within R_{500}, including the foreground and background galaxies, is the sum of $M_\star^{\rm best}$. The uncertainty includes the uncertainties on the single galaxy masses (using $M_\star^{\rm lo}$ and $M_\star^{\rm hi}$ and assuming the probability distribution for the stellar mass is Gaussian).

We also calculate the fraction of objects $f_{\rm cor}$ with unphysical mass outputs (i.e., $\log(M_\star^{\rm med}) = -99.0$), which occur mostly due to data corruption. We correct for these missing galaxies by assuming that they share the same distribution of stellar masses as the uncorrupted galaxies. We note that this fraction varies between 3 and 10%. A correction for the masking of the bright stars is also applied. Thus, for each cluster we estimate the total stellar mass $M_\star^{\rm field}$ projected within R_{500} as

$$M_\star^{\rm field} = \frac{\Sigma_i M_{\star,i}^{\rm best}}{(1-f_{\rm mask})\,(1-f_{\rm cor})}\,, \tag{2.2}$$

where $f_{\rm mask}$ is the fraction of area within R_{500} that is masked and $M_{\star,i}^{\rm best}$ is the best stellar mass estimate for galaxy i in the cluster.

Background Correction

We correct the stellar mass from the cluster field $M_\star^{\rm field}$ for the contribution from the foreground and background galaxies $M_\star^{\rm bkg}$ using a statistical correction. Because the FORS2 field of view is

small, the background regions outside R_{500} are contaminated by cluster galaxies. Thus, we use the COSMOS survey to estimate the background correction.

The COSMOS survey has 30-band photometry with wavelength coverage from UV to mid-infrared. To minimize systematics we take two steps to make the COSMOS dataset as similar as possible to our SPT dataset. First, we choose the passbands which are most similar to ours (from Subaru Suprime-Cam and *Spitzer*) and apply color corrections where needed to convert the COSMOS photometry into our passbands. MAG_AUTO photometry is used in the COSMOS field. Second, we degrade the COSMOS photometry to have the same measurement noise as in our dataset.

We then measure the stellar mass for each galaxy in the COSMOS field using the converted photometry, the same *Spitzer* object detection, the same matching algorithm, and the same fitting strategy as we applied to our own data. We correct this background estimate for the fraction of corrupted galaxies as described for the cluster fields in Equation 2.2.

Then, correcting the COSMOS background estimates to the area of each cluster field, we subtract the background estimate $M_\star^{\rm bkg}$, obtaining our estimate of the cluster stellar mass projected within R_{500}. We then apply a geometric factor $f_{\rm geo}$ to correct this projected quantity to the stellar mass within the virial volume $M_\star$ using a typical radial galaxy profile with concentration $c_{500}^{\rm gal} = 1.9$ (Lin et al., 2004, Hennig in prep), which corresponds to a normalization correction of $f_{\rm geo} = 0.71$.

$$M_* = M_\star^{\rm BCG} + f_{\rm geo}\left(M_*^{\rm field} - M_*^{\rm bkg}\right), \tag{2.3}$$

where we have defined $M_\star$ to include $M_\star^{\rm BCG}$, the BCG stellar mass.

In Appendix 2.9.2, we compare the COSMOS background to the background estimated in the non-cluster portions of the VLT imaging where a correction for cluster contamination has been applied. We find that the two backgrounds agree at the 10% level, leading to background corrected cluster stellar mass estimates $M_\star$ that are consistent at the 4% level. Thus, we adopt this difference as the amplitude of the systematic uncertainty associated with our statistical background correction.

2.5 BCG and Cluster Stellar Mass function

In this section we present the components of the cluster stellar mass function (SMF). These include the BCGs (Section 2.5.1), which we discuss first, followed by the full SMF and the luminosity function (LF) of the satellite galaxies (Section 2.5.2).

2.5.1 BCG Stellar Mass

We present $M_\star^{\rm BCG}$ for the 14 SPT clusters and compare them with the measurements of H13 and vdB14, in which groups and clusters at $z \geq 0.3$ are studied. H13 estimated $M_\star^{\rm BCG}$ based on the mass-to-light technique assuming a passive evolution model with the [3.6] magnitude MAG_AUTO. vdB14 applied the same technique using the K_s luminosity together with the Sersic model fitting to the light profile. As noted in vdB14, the magnitude inferred by the Sersic profile

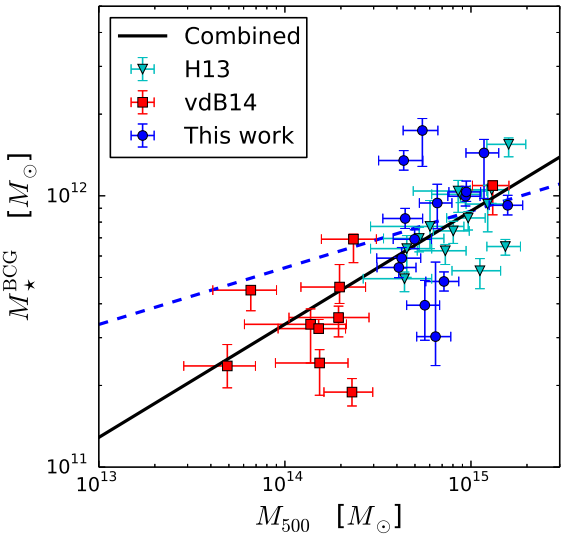

Figure 2.2: The BCG stellar mass ($M_\star^{\rm BCG}$) versus cluster virial mass M_{500} for the SPT sample (blue), H13 (cyan) and vdB14 (red). The H13 sample is corrected to Chabrier IMF. The blue dashed line is the best-fit for the SPT sample alone and the black solid line is the best fit for the combined sample (see Equation 2.4).

could differ from MAG_AUTO by up to 0.2 mag, depending on the shape of the light profile. In this work we estimate $M_\star^{\rm BCG}$ using an SED fit to the six bands available in our survey. No special attempt is made to include or deblend the extended halo or intracluster light (ICL) in any of these studies. We have three clusters in common with H13: SPT-CL J0102−4915, SPT-CL J0546−5345 and SPT-CL J0559−5249. For SPT-CL J0546−5345 our $M_\star^{\rm BCG}$ is about a factor of 2 higher, but in the other two clusters $M_\star^{\rm BCG}$ agrees at better than 10%. We compare the [3.6] photometry of SPT-CL J0546−5345, and find that the magnitude reported by H13 is about 0.5 mag fainter, suggesting that a more sophisticated deblending algorithm is needed for the crowded core of SPT-CL J0546−5345 in this work. We adopt the SED mass estimates for the BCGs in the analyses that follow. The BCGs are marked by yellow circles in the optical images presented in Figure 2.1.

As is clear in Figure 2.2, neither the SPT nor the H13 sample provides strong evidence for a correlation between the BCG mass and the cluster halo mass. However, in combination with the vdB14 sample that extends to much lower mass, we find a best fit $M_\star^{\rm BCG}$–M_{500} relation of

$$M_\star^{\rm BCG} = (5.30 \pm 0.39) \times 10^{11} \left(\frac{M_{500}}{3 \times 10^{14} {\rm M}_\odot} \right)^{0.42 \pm 0.07} , \tag{2.4}$$

for the combined sample, and this relation is plotted in Figure 2.2 (black dashed line). Thus, the BCG stellar mass constitutes about 0.12% of the cluster halo mass at $M_{500} = 6 \times 10^{14} {\rm M}_\odot$. Because $M_\star^{\rm BCG}$ scales with cluster halo mass with a power law index less than one, the fraction of the cluster mass made up by the BCG falls as $M_\star^{\rm BCG}/M_{500} \propto M_{500}^{-0.58 \pm 0.07}$.

The SPT sample scatters significantly about this relation, providing evidence of intrinsic scatter in $M_\star^{\rm BCG}$ at fixed cluster halo mass of $\sigma_{\rm int} = 0.17 \pm 0.034$ dex. The full sample exhibits a

consistent value $\sigma_{\rm int} = 0.15 \pm 0.021$ dex. Thus, the characteristic scatter of the BCG masses at a fixed cluster halo mass is 41%.

2.5.2 Cluster Luminosity and Stellar Mass Functions

We extract the [3.6] LF and the SMF using a statistical background subtraction with the COSMOS field as the source of the background (see Section 2.4.3). We apply a correction from the virial cylinder to the virial volume in the same manner as in Section 2.4.3. The measured LF and SMF are in physical density units of Mpc^{-3}. The uncertainty of each bin is estimated by the Poisson error associated with the galaxy counts in the case of the LF and this error combined with the galaxy stellar mass measurement uncertainties for the SMF.

We stack the LF and SMF from 14 SPT clusters using inverse-variance weighting within each bin. The number densities are corrected to the median redshift of the SPT clusters, $z = 0.9$, by multiplying by the ratio of the critical densities, $\left(\frac{E(0.9)}{E(z)}\right)^2$, where $E(z)^2 \equiv \Omega_\Lambda + \Omega_{\rm M}(1+z)^3$ and z is the redshift of the cluster. We stack the LF within the space of $m - m^*$ with magnitude bins of width 0.5, where m^* comes from the CSP model described in Section 2.3.1. Given that the galaxy population in SPT selected clusters has been shown to be well described by the CSP model (Song et al. (2012c), Hennig et al, in preparation) stacking LFs with respect to the m^* predicted at the redshift of each cluster provides a simple way to extract the information for the normalization and shape of the composite LF. We stack the SMF in the stellar mass range from 10^{10} – $10^{12}\mathrm{M}_\odot$ with bin width of 0.2 dex. Finally, we characterize the stacked LF and SMF with the standard Schechter function (Schechter, 1976). Specifically, we fit the stacked LF directly in log space to:

$$\begin{aligned} \Phi_L(m) &= 0.4\ln(10.0)\phi^* \times 10.0^{-0.4(\alpha_{\rm L}+1)(m-m_0)} \\ &\quad \times \exp(-10.0^{-0.4(m-m_0)}), \end{aligned} \tag{2.5}$$

where m is the magnitude, m_0 is the characteristic magnitude predicted by the passively evolving model (see Section 2.3.1), ϕ^* is the characteristic density and $\alpha_{\rm L}$ is the faint end slope. We fit the stacked SMF directly in log space to:

$$\begin{aligned} \Phi_M(M_\star) &= \ln(10)\phi_M \times 10^{(\alpha_{\rm M}+1)(m_\star - M_0)} \\ &\quad \times \exp(-10^{(m_\star - M_0)}), \end{aligned} \tag{2.6}$$

where $m_\star$ is the stellar mass in units of $\log_{10}(m_\star/\mathrm{M}_\odot)$, M_0 is the characteristic mass, $\phi_{\rm M}$ is the characteristic density, and $\alpha_{\rm M}$ is the faint end slope. We restrict our fit to those galaxies brighter than $m^* + 2$ in the LF analysis. Because the stellar mass is not a linearly-rescaled version of the magnitude, we choose the conservative depth limit used in the SMF analysis, which is based on the mass-to-light-inferred mass at brighter magnitude, $m^* + 1.5$, assuming the passively evolving model for SMF analysis.

The stacked LF and SMF are shown in Figure 2.3 and Figure 2.4, respectively. The best-fit parameters are given in Table 2.2. We convert the SMF and LF from physical number density to the abundance per mass of $10^{15}\mathrm{M}_\odot$ (total baryon and dark matter mass) by using the mean

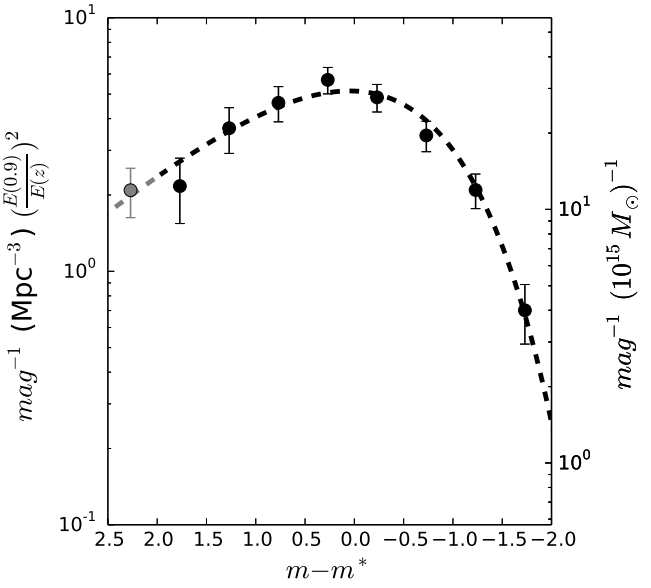

Figure 2.3: The stacked luminosity function of 14 SPT clusters extracted from the [3.6] photometry (black points). The grey point is fainter than $m^* + 2$ and is not included in the fit. The line marks the best fit Schechter function. The LF is plotted versus $m - m^*$, where m^* is obtained from the passive evolution model described in the text (Section 2.3.1). The stacked number densities are corrected for evolution of the critical density ($\rho_{\rm crit} \propto E(z)^2$) and normalized to median redshift $z = 0.9$.

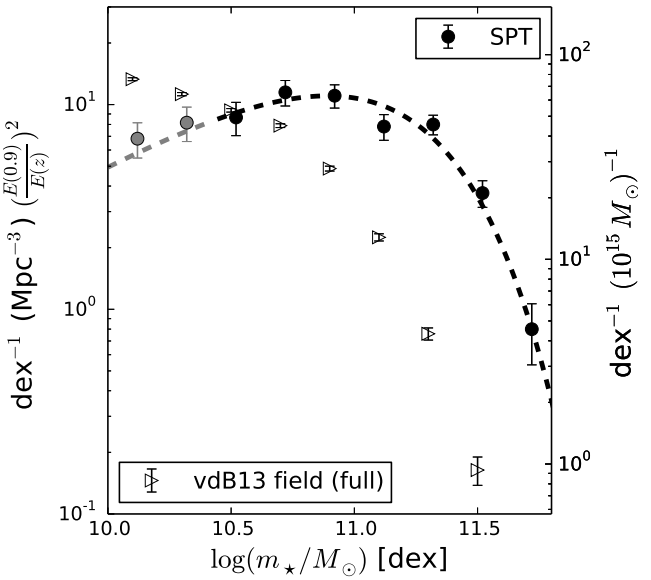

Figure 2.4: The measured stellar mass from (SMF) obtained by stacking 14 SPT clusters. The black line is thebest fit Schechter function (see Table 2.2). The grey points are measurements beyond the depth limit and are not used in the fit. For comparison, we show the field SMF from vdB13.

Table 2.2: Luminosity and Stellar Mass Function Parameters: The luminosity function (top) characteristic density, characteristic magnitude, faint end slope and reduced χ^2 are shown followed (below) by the equivalent stellar mass function parameters.

ϕ^* [$\mathrm{Mpc}^{-3}\mathrm{mag}^{-1}$]	m_0 [mag]	α_L	χ^2_{red}
14.90 ± 1.0	-0.18 ± 0.1	-0.19 ± 0.1	0.6
ϕ_M [$\mathrm{Mpc}^{-3}\mathrm{dex}^{-1}$]	M_0 [dex]	α_M	χ^2_{red}
12.30 ± 1.5	11.06 ± 0.1	-0.32 ± 0.2	1.4

density within the virial region at $z = 0.9$, which is $500\rho_{\mathrm{crit}}(z = 0.9)$. This value is shown on the right y-axis. Similarly, to compare to a field LF or SMF one would convert from Mpc^{-3} to per unit mass by using the mean density of the universe at that redshift $\langle\rho\rangle(z) = \Omega_{\mathrm{M}}(z) \times \rho_{\mathrm{crit}}(z)$.

The best-fit m_0 indicates that the LF deviates from the predicted characteristic $m^*_{[3.6]}$ for the passive evolution model (Section 2.3.1) by -0.18 ± 0.1, suggesting the mild evidence (about 1.8σ) of the blue population at the high redshift clusters. The best-fit SMF and LF are consistent with one another; the characteristic $m^*_{[3.6]}$ at median redshift $z = 0.9$ predicted by the passively evolving model corresponds to the stellar mass of $10^{10.96}\mathrm{M}_\odot$, while the measured characteristic mass is $10^{11.0\pm0.1}\mathrm{M}_\odot$. The faint end slopes and characteristic densities are also in good agreement.

In a recent paper, van der Burg et al. (2013a, hereafter vdB13) compare the SMFs of the GCLASS low mass clusters to the field at redshift $z = 0.85 - 1.2$ and find the number density of galaxies per unit mass (dark matter plus baryons) in the field SMF is lower than that in the groups over the mass range $10^{10}\mathrm{M}_\odot$ to $10^{11.5}\mathrm{M}_\odot$. This suggests that the galaxy formation rate has been lower over time in the field than in the dense group and cluster environments. A similar picture had previously emerged in the local Universe ($z < 0.1$) (Lin et al., 2004, 2006), where the luminosity functions of K-band selected galaxies and of radio sources within clusters are also significantly higher than the field after corrections for the mean matter density differences in the two environments. As seen in Figure 2.4, the normalization of the SMF for the SPT clusters on the massive end ($\log_{10}(m_\star/\mathrm{M}_\odot) \approx 11.2 - 11.5$) is significantly higher than the field (open triangle) measured by vdB13. By integrating the best-fit SMF of SPT above our single galaxy stellar mass threshold of $2.5 \times 10^{10}\mathrm{M}_\odot$, we estimate the number of galaxies per unit total mass for SPT clusters is $\approx 1.65 \pm 0.20$ times higher than the field at $z = 0.85 - 1.2$. Our result reinforces this picture that the cluster environment contains a more biased galaxy population than the field.

2.6 Baryon Composition

In this section we present our measurements for the stellar mass fraction, ICM mass fraction, collapsed baryon fraction and baryon fraction:

$$f_\star \equiv \frac{M_\star}{M_{500}} \tag{2.7}$$

$$f_{\rm ICM} \equiv \frac{M_{\rm ICM}}{M_{500}} \tag{2.8}$$

$$f_{\rm c} \equiv \frac{M_\star}{M_{\rm b}} \tag{2.9}$$

$$f_{\rm b} \equiv \frac{M_{\rm b}}{M_{500}}\,, \tag{2.10}$$

where $M_\star$ is the stellar mass (see Equation 2.3), $M_{\rm ICM}$ is the ICM mass (see Section 2.4.2) and $M_{\rm b} \equiv M_\star + M_{\rm ICM}$ is the total mass in baryons. M_{500} is the halo virial mass, estimated using the SZE observable (see Section 2.4.1).

In addition, we study mass and redshift trends in our SPT clusters and in the combined sample that includes the clusters studied in the literature (discussed in Section 2.3.2). Note that we are not probing the evolution of the baryon content by directly tracing the progenitors, because our SPT sample lacks low mass groups at all redshifts. We instead estimate the baryon content of the massive clusters with respect to the characteristic mass at the different epochs statistically by fitting the scaling relation simultaneously in mass and redshift space (see Section 2.6.1). We also compare our cluster results with more general results coming from external, non-cluster datasets. We use the universal baryon fraction $f_{\rm b}$ estimated using the *Planck* CMB anisotropy observations (Planck Collaboration et al., 2013), and we estimate the universal stellar density parameter $\Omega_\star$, where the mean stellar density at $z = 0$ is extracted from the local K-band galaxy LF (Kochanek et al., 2001) and the mean stellar density at $z = 1$ is extracted from the vdB13 analysis. These values have been corrected to our fiducial cosmology and are appropriate for a Chabrier IMF, enabling comparison to our cluster measurements.

2.6.1 Fitting Procedure

We fit these measurements from our cluster ensemble and also from the combined sample to a power law relation in both mass and redshift:

$$f_{\rm obs}(M_{500}, z) = \alpha_{\rm obs} \left(\frac{M_{500}}{M_{\rm piv}}\right)^{\beta_{\rm obs}} \left(\frac{1+z}{1+z_{\rm piv}}\right)^{\gamma_{\rm obs}} \tag{2.11}$$

where $M_{\rm piv}$ and $z_{\rm piv}$ are the mass and redshift pivot points, obs corresponds to the different observables and $\alpha_{\rm obs}$, $\beta_{\rm obs}$ and $\gamma_{\rm obs}$ correspond to normalization of the best fit relation, the power law index of the mass dependence and the power law index of the redshift dependence, respectively. We perform χ^2 fitting directly in log space using the measurement uncertainties and accounting for intrinsic scatter. For the SPT and combined samples we choose the pivot points

Table 2.3: Mass and Redshift Trends of Baryon Composition with $M_{\rm piv} \equiv 6 \times 10^{14} {\rm M}_{\odot}$: The columns contain the quantity of interested, the normalization at the pivot mass and redshift, mass dependence and redshift dependence (see Equation 2.11) for the SPT sample alone (above) and for the SPT sample together with the literature sample (below).

$f_{\rm obs}$	$\alpha_{\rm obs}$	$\beta_{\rm obs}$	$\gamma_{\rm obs}$ †
SPT Sample Results with $z_{\rm piv} \equiv 0.9$			
$f_\star$	0.011 ± 0.001	-0.09 ± 0.27	1.07 ± 1.08
$f_{\rm ICM}$	0.096 ± 0.005	0.43 ± 0.13	0.20 ± 0.49
$f_{\rm c}$	0.107 ± 0.011	-0.55 ± 0.22	0.81 ± 0.93
$f_{\rm b}$	0.107 ± 0.006	0.39 ± 0.13	0.32 ± 0.50
Combined Sample Results with $z_{\rm piv} \equiv 0$			
$f_\star$	0.0099 ± 0.0005	-0.37 ± 0.09	$0.26 \pm 0.16 \pm 0.08$
$f_{\rm ICM}$	0.1120 ± 0.0032	0.22 ± 0.06	$-0.20 \pm 0.11 \pm 0.22$
$f_{\rm c}$	0.0859 ± 0.0049	-0.65 ± 0.10	$0.39 \pm 0.15 \pm 0.16$
$f_{\rm b}$	0.1227 ± 0.0035	0.22 ± 0.06	$-0.17 \pm 0.11 \pm 0.22$

† The second $\gamma_{\rm obs}$ uncertainty arises from the 15% M_{500} systematic uncertainty.

to be the median mass $M_{500} = 6 \times 10^{14} {\rm M}_{\odot}$. For the SPT sample we adopt the redshift pivot $z_{\rm piv} = 0.9$, consistent with the median redshift of the sample, but for the combined sample we adopt a redshift pivot of $z_{\rm piv} = 0$.

The parameters for the best-fit relations for the SPT sample and for the combined sample are listed in Table 2.3, while the measured cluster virial masses, ICM masses, stellar masses and the derived quantities above are listed in Table 2.4. These results are summarised in Figures 2.5 and 2.6, where the first figure focuses on the mass trends and the second focuses on the redshift trends. In the subsections below we discuss each derived quantity in turn.

Accounting for M_{500} Systematic Uncertainties

We account for systematic differences in M_{500} estimation between the low redshift comparison sample (L03, Zha11 and GZ13) and the high redshift sample (SPT with two additional samples of H13 and vdB14 added when comparing $f_\star$) by adopting a 15% (1σ) systematic virial mass uncertainty (see discussion in Section 2.3.2). These virial mass uncertainties imply corresponding R_{500} uncertainties that lead also to systematic uncertainties in the stellar mass and ICM mass for each cluster. We estimate the systematic uncertainties in the redshift variation parameter $\gamma_{\rm obs}$ (Table 2.3) by perturbing the virial masses of the high redshift sample by $\pm 15\%$ and extracting the best fit parameters in each case. The 1σ systematic uncertainty is estimated as half the difference between the two sets of parameters. This virial mass systematic is only important for the measured redshift trends.

Accounting for Differences in Measurement Uncertainties

We also account for systematic differences in the measurement uncertainties among the different samples by solving for a best fit intrinsic scatter separately for each sample. For the SPT sample, where mass uncertainties include both measurement and systematic uncertainties (Section 2.4.1), we find no need for an additional intrinsic scatter. The best fit estimates of the intrinsic scatter for the other samples are 9% for $f_{\rm ICM}$ and $f_{\rm b}$ in L03, 14% for $f_\star$, $f_{\rm ICM}$ and $f_{\rm b}$ in GZ13, 18% for $f_\star$ in H13 and 20% in vdB14, and 20 to 22% for the fractions in Zha11. Three of the samples with the largest intrinsic scatter (Zha11, H13 and vdB14) employ velocity dispersions for single cluster mass estimation as opposed to X-ray or SZE mass indicators. This is not surprising, because it has been shown that cluster velocity dispersions provide high scatter single cluster mass estimates (see Saro et al., 2013, and references therein). Velocity dispersions can be effectively used in ensemble to calibrate ICM based single cluster mass estimates (Bocquet et al., 2015b).

2.6.2 Stellar Mass Fraction $f_\star$

The stellar mass fraction we estimate here is the mass in stars within cluster galaxies. We make no attempt to account for the ICL component. Figure 2.5 contains a plot of our results (blue). The mean $f_\star$ of our fourteen clusters is 0.011 ± 0.001, and the characteristic value at $z = 0.9$ and $M_{500} = 6 \times 10^{14} {\rm M}_\odot$ is 0.011 ± 0.001. The SPT sample provides no evidence for a mass or redshift trend, but the large mass trend uncertainty ($f_\star \propto M_{500}^{-0.09\pm0.27}$) means the sample is statistically consistent with the trend for more massive clusters to have lower $f_\star$ (L03). In the combined sample, there is 3.7σ evidence for a mass trend $f_\star \propto M_{500}^{-0.37\pm0.09}$, which is also consistent with the L03 result. The combined sample exhibits no significant redshift variation ($f_\star \propto (1+z)^{0.26\pm0.16\pm0.08}$), where the second uncertainty reflects the 15% (1σ) systematic virial mass uncertainty. The characteristic value at $z = 0$ is $f_\star = 0.010 \pm 0.0005$ (statistical), which is in good agreement with the SPT value at $z_{\rm piv} = 0.9$.

Also shown in the shaded region is the $f_\star$ constraint emerging from a combination of the stellar mass density from the K-band local luminosity function (Kochanek et al., 2001), $\Omega_\star h = 3.4 \pm 0.4 \times 10^{-3}$ with $h = 0.683$, with the most recent combined results (*Planck* + *WMAP* polarization+SNe+BAO+SPT clusters) on the cosmological matter density $\Omega_{\rm M} = 0.299 \pm 0.009$ (Bocquet et al., 2015b). The cluster $f_\star$ is in good agreement with this estimate of the universal average field value $f_\star = (0.95 \pm 0.12)\%$ at $z = 0$. However, the average field $f_\star = 0.22 \pm 0.003\%$ (see Figure 2.6) inferred from the SMF measurements at z=0.85–1.2 (vdB13) is significantly lower than the cluster $f_\star$. The cluster or group $f_\star$ may be altered over time through either the accretion of lower mass clusters or groups (higher $f_\star$) or through infall from the field (lower $f_\star$). Presumably, these influences must combine to produce the transformation in $f_\star$ from a lower mass cluster at $z = 1$ to a higher mass clusters at $z = 0$. We return to this discussion in Section 2.7.

We compare the high redshift SPT results to two other samples at high redshift: vdB14 and H13. The virial masses for the majority of the vdB14 systems are below $3 \times 10^{14} {\rm M}_\odot$ and therefore lower mass than our SPT clusters. The one remaining system in this mass range falls near the bottom of our distribution of $f_\star$. The H13 sample shows stellar mass fractions that are in

good agreement with ours. We have three clusters in common; combining these measurements we determine that the differences are 1.11σ, 0.69σ and 0.52σ for $M_\star$, M_{500} and $f_\star$ measurements, respectively. vdB14 express concern that the $M_\star$ estimated by the mass-to-light technique in H13 could possibly be overestimated by as much as a factor of 2. While the largest difference with our sample is indeed with $M_\star$, the level of agreement between the H13 results and our SED fitting results would suggest that the bias is likely smaller (about $10 \pm 23\%$).

2.6.3 ICM Mass Fraction $f_{\rm ICM}$

The majority of the baryonic mass within clusters lies within the hot ICM. The arithmetic mean of $f_{\rm ICM}$ for the 14 SPT clusters is 0.1027 ± 0.0073, and the characteristic value at $z = 0.9$ and $M_{500} = 6 \times 10^{14} {\rm M}_\odot$ is 0.096 ± 0.005. A clear mass trend ($f_{\rm ICM} \propto M_{500}^{0.43\pm0.13}$), significant at the 3.3σ level, is seen for SPT clusters. This trend is steeper than (but statistically consistent with) the trends, $\beta_{\rm ICM} = 0.30 \pm 0.07$ and 0.26 ± 0.03, presented by Zha11 and GZ13, but steeper at 2.1σ than the result $\beta_{\rm ICM} = 0.15 \pm 0.03$ presented by Andreon (2010). The combined sample has a preferred mass trend $\beta_{\rm ICM} = 0.22 \pm 0.06$, which is 1.5σ shallower than the SPT sample.

These results, extending to redshift $z = 1.32$, show the clear tendency for $f_{\rm ICM}$ to be suppressed in lower mass clusters— first shown in studies of individual low redshift clusters (David et al., 1993) and later with a uniform analysis of a large sample of low redshift clusters (Mohr et al., 1999).

The characteristic value of the combined sample at $z_{\rm piv} = 0$ and $M_{\rm piv} = 6 \times 10^{14} {\rm M}_\odot$ is $f_{\rm ICM} = 0.112 \pm 0.0032$ (statistical only), which is higher than the $z = 0.9$ SPT sample $f_{\rm ICM} = 0.096 \pm 0.005$. However, neither the SPT high redshift sample nor the combined sample exhibits evidence for redshift variation in $f_{\rm ICM}$ with $\gamma_{\rm ICM} = -0.20 \pm 0.11 \pm 0.22$. The impact of the halo mass 15% systematic uncertainty on the redshift trend introduces an additional systematic uncertainty of $\sigma_{\gamma_{\rm ICM}} = 0.22$ which is larger than the statistical uncertainty. This underscores the importance of using a homogeneous sample with consistently derived virial mass measurements.

2.6.4 Collapsed Baryon Fraction $f_{\rm c}$

The collapsed baryon fraction $f_{\rm c}$ is the fraction of baryonic mass that has cooled to form stars that lie in galaxies and thereby reflects an integral of the star formation efficiency within the halo averaged over cosmic time (e.g. David & Blumenthal, 1992). As already noted, we make no attempt to include an estimate of the ICL contribution here. The arithmetic mean $f_{\rm c}$ of our fourteen clusters is 0.099 ± 0.007, and the characteristic value at $z = 0.9$ and $M_{500} = 6 \times 10^{14} {\rm M}_\odot$ is 0.107 ± 0.011 (statistical). The SPT sample exhibits no evidence for either a mass or redshift trend. The combined sample exhibits a 6.5σ significant mass trend $f_{\rm c} \propto M^{-0.65\pm0.10}$ with the collapsed baryon fraction falling to lower values in high mass clusters and a characteristic value of 0.0859 ± 0.0049 (statistical) at $z = 0$. The redshift trend from the combined sample $f_{\rm c} \propto (1+z)^{0.39\pm0.15\pm0.16}$ is significant at 1.8σ if we add the statistical and systematic uncertainties in quadrature.

Note that in the case of $f_{\rm c}$ the 15% systematic uncertainty in M_{500} has no impact on the $f_{\rm c}$ measurement, because a shift in R_{500} has approximately the same impact on $M_\star$ and $M_{\rm ICM}$,.

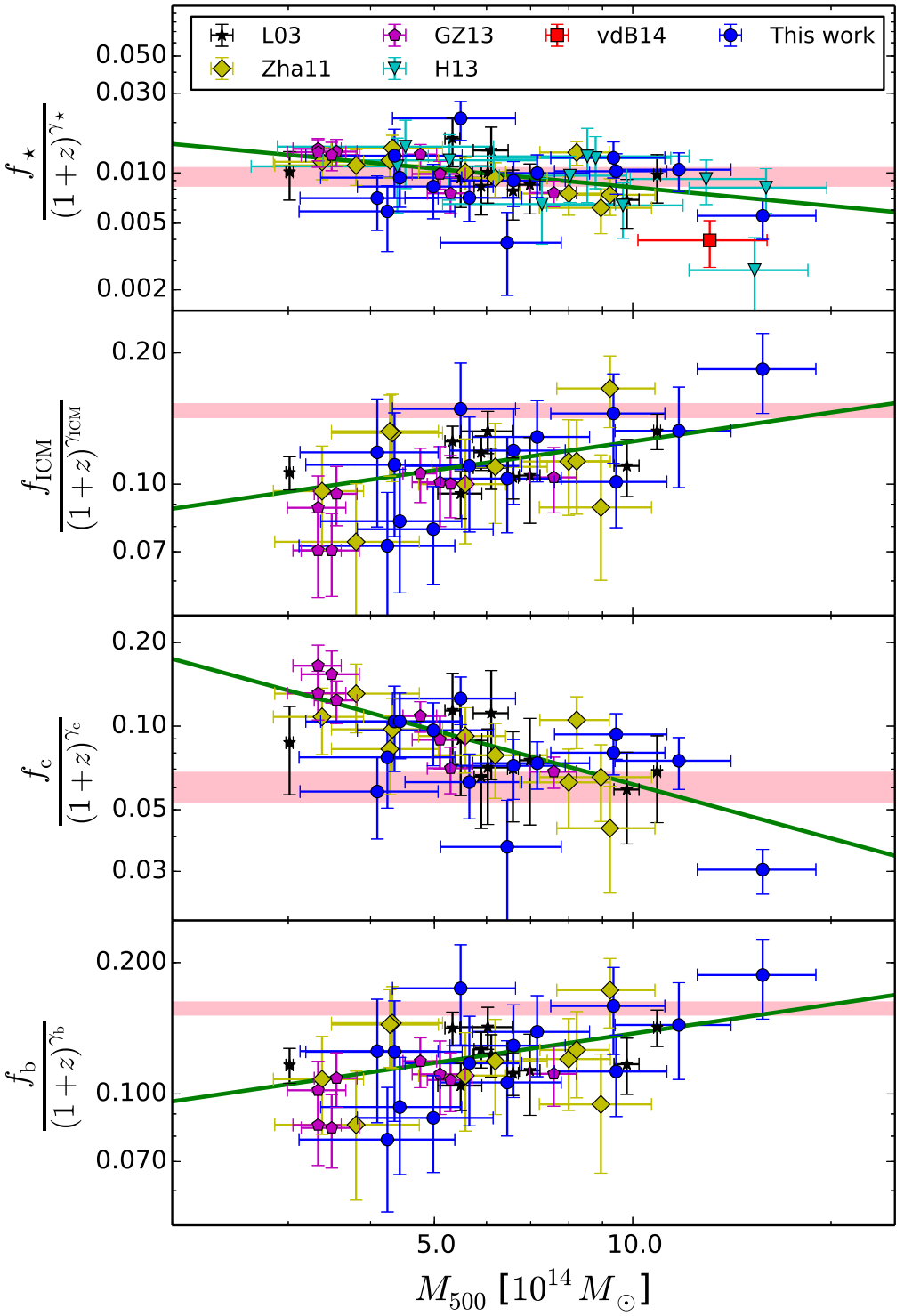

Figure 2.5: The baryonic fractions $f_\star$, $f_{\rm ICM}$, $f_{\rm c}$ and $f_{\rm b}$ are shown as a function of cluster virial mass M_{500} for the combined sample. In all cases the measurements have been corrected to $z = 0$ using the best fit redshift trend. The best fit mass trend is shown in green (Table 2.3). The color coding and point styles are defined in the upper panel and is the same throughout. The red shaded region indicates the universal baryon composition from combining the best-fit cosmological parameters from Bocquet et al. (2015b) together with the local K-band luminosity function (Kochanek et al., 2001).

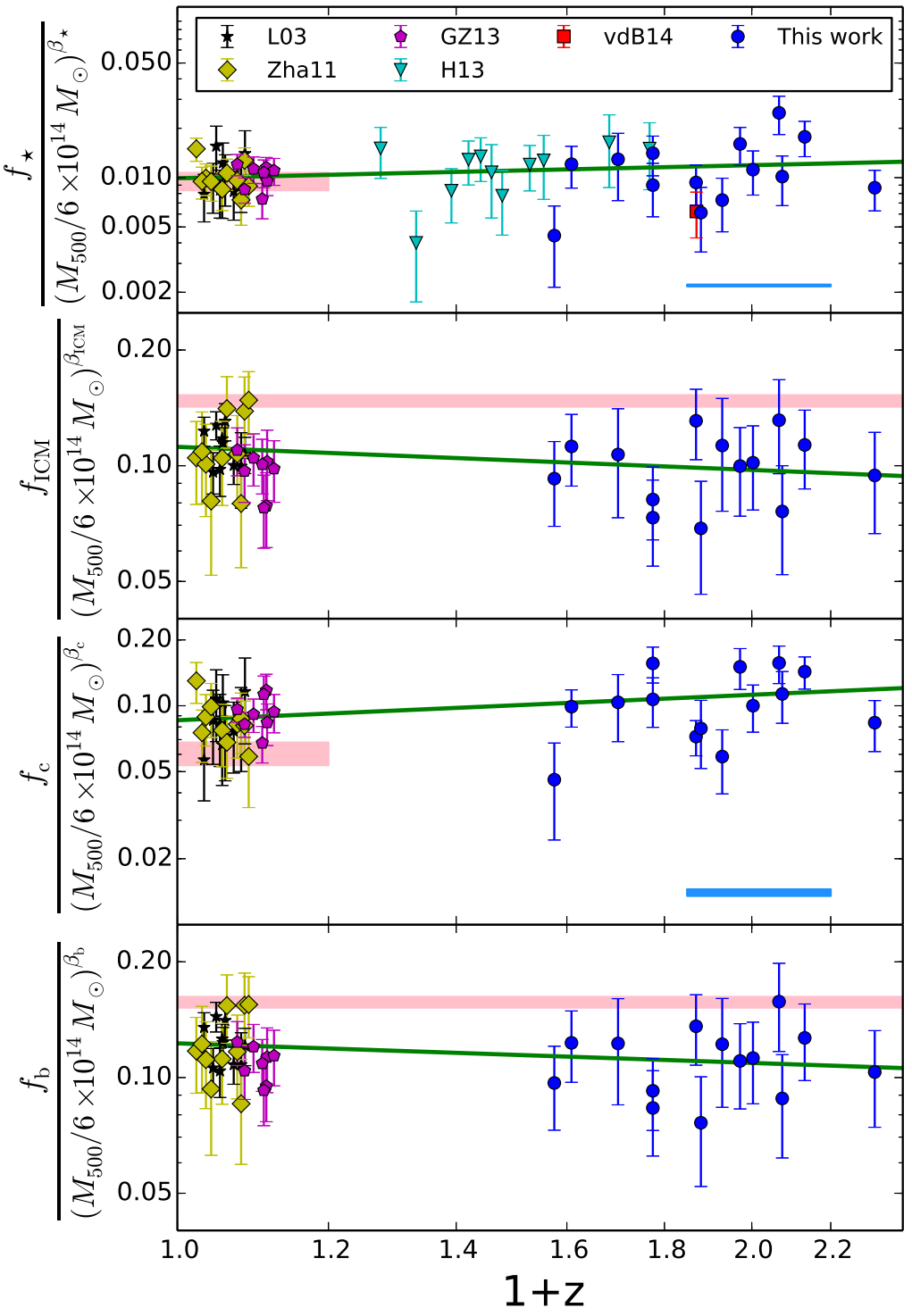

Figure 2.6: The redshift trends of $f_\star$, $f_{\rm ICM}$, $f_{\rm c}$ and $f_{\rm b}$ for the combined cluster sample. The color coding of the points and the red bands are the same as in Figure 2.5. For $f_\star$ and $f_{\rm c}$ we show the universal value at $z = 0$ (red) and at $z = 0.85 - 1.2$ (blue). Measurements have been corrected using the best fit mass trends to the mass $6 \times 10^{14}{\rm M}_\odot$, and the best fit redshift trend is shown in green (Table 2.3).

However, because of the steep mass trend for f_c ($\beta_c \approx -0.6$), a shift in the virial mass of the high redshift sample impacts the best fit redshift trend, because this shift masquerades as a shift in f_c of $\delta f_c \sim -0.6\delta M_{500}/M_{500}$. This impacts the estimate of the systematic uncertainty in γ_c. This process is also at work for the other fractions, but because their mass dependences are weaker, the impact is smaller.

In Figure 2.5 we see that f_c decreases with cluster mass, and the scatter about this trend (especially in the Zha11 sample) is less than in the case of $f_\star$. This measure is interesting because the M_{500} measurements come in only through defining the virial radius, and if the radial variation in $f_{\rm ICM}$ and $f_\star$ are mild, then f_c has only a weak dependence on the virial mass estimates. Thus in cases where the M_{500} estimates exhibit large uncertainties, the f_c can be an effective way of exploring trends in the mix of stars and ICM within clusters.

Our study indicates that over cosmic time the collapsed baryon fraction f_c at fixed cluster halo mass falls. This redshift trend is driven by the slight rise in the ICM mass fraction $f_{\rm ICM}$ and slight fall in stellar mass fraction $f_\star$.

2.6.5 Baryon Fraction f_b

The arithmetic mean of the baryon fraction for our SPT clusters is 0.114 ± 0.008 (statistical only), and the characteristic value at $z = 0.9$ and $M_{500} = 6 \times 10^{14} M_\odot$ is 0.107 ± 0.006 (statistical). This is lower than the characteristic values of the combined sample at $z = 0$ of 0.1227 ± 0.0035 (statistical). However, neither the SPT sample nor the combined sample ($f_b \propto (1+z)^{-0.17\pm0.11\pm0.22}$) provides clear evidence for a redshift trend. The mass systematics between the low and high redshift samples introduce an uncertainty in the redshift trend parameter of $\sigma_{\gamma_b} = 0.22$, which is larger than the statistical uncertainty, implying that controlling mass systematics among the different samples is crucial. The SPT sample exhibits a mass trend $f_b \propto M_{500}^{0.39\pm0.13}$ that has 3σ significance. The combined sample exhibits a mass trend $f_b \propto M_{500}^{0.22\pm0.06}$, which is somewhat shallower and is significant at 3.6σ.

2.7 Discussion

Because our sample includes the highest redshift massive ($M_{500} > 3 \times 10^{14} M_\odot$) clusters studied to date, our analysis is useful for constraining the redshift variation of the ICM and stellar mass components on cluster mass scales. While we do consider intrinsic scatter in fitting the observed properties within our sample, the sample does not provide meaningful constraints on this scatter; thus, our results shed no light on assembly bias, which would link the baryon properties of individual clusters to the properties of the large scale environment within which they formed. A joint analysis of the SPT sample and a comparison sample indicates that the cluster collapsed baryon fraction (accounting only for stars in galaxies) within R_{500} is decreasing from 10.7% to 8.6% on the characteristic mass scale $M_{\rm piv} = 6 \times 10^{14} M_\odot$ since $z \approx 0.9$; the redshift trend is significant at the 1.8σ confidence level when accounting for a 15% virial mass systematic uncertainty between the literature and SPT samples. Moreover our analysis indicates that this change is driven by a weak increase in the ICM fraction ($f_{\rm ICM}$ changes from 9.6% to 11.2%) and

a weak decrease in the stellar fraction from 1.1% to 1.0% over that same redshift range. These same trends in $f_{\rm ICM}$ and $f_\star$ lead to a weak trend in the baryon fraction (from 10.7% to 12.3%) from $z = 0.9$ to the present, a change that is only 0.7σ significant given the systematic mass uncertainties between the high redshift and local comparison samples.

To build a physical picture it is important to take note of the mass trends in the stellar mass fraction $f_\star \propto M^{-0.37\pm0.09}$ that indicate that high mass clusters have $f_\star$ values that lie below those of groups and that are comparable to or even higher than the field $f_\star$ at $z = 0$ (see also L03, vdB13). The ICM mass fractions $f_{\rm ICM}$ behave oppositely $f_{\rm ICM} \propto M^{0.22\pm0.06}$ (see also Mohr et al., 1999), with groups having lower values than massive clusters, whose $f_{\rm ICM}$ values are approaching but still lower than the universal baryon fraction. These mass trends then give rise to the trend of falling collapsed baryon fraction $f_{\rm c}$ with mass $f_{\rm c} \propto M^{-0.65\pm0.10}$.

Because of the clear mass trends and weak redshift trends in $f_\star$ and $f_{\rm ICM}$, a simple merging scenario for halo formation, where the accretion of low mass (group-scale) halos is dominating the mass assembly of massive clusters, does not provide an adequate explanation of the observations. In general, such a scenario would lead to $f_\star$ that is approximately independent of cluster halo mass (Balogh et al., 2008). The massive halos of today form from halos that were lower mass at higher redshift, so if these low mass subclusters had lower $f_\star$ or higher $f_{\rm ICM}$ at higher redshift, then the simple merger scenario could in principle be consistent with the data. However, the weak redshift variation in these fractions at fixed halo mass that we estimate here for massive halos does not help to resolve the situation, because it indicates that $f_\star$ and $f_{\rm ICM}$ at fixed halo mass have changed only weakly over time; if trends on the massive end are coupled with similar trends on the lower mass end, then the simple merging scenario must be flawed. The conclusion that infall from the field and/or the inclusion of stripping processes that modify the apparent stellar fraction during the process of the growth of massive, cluster scale halos is inescapable.

Infall from the field likely plays a critical role in the growth of massive clusters. Studies of the standard hierarchical structure formation scenario on the mass scales of interest here indicate that $\sim$40% of the cluster galaxies have previously been in lower mass group or cluster halos (McGee et al., 2009) and that the rest infall from the field. In the case of $f_\star$, we have shown that the field has lower $f_\star$ in comparison to massive clusters at redshift $z = 0.9$ (Section 2.5.2) and that it has comparable values of $f_\star$ at $z = 0$ (see Figure 2.6). Through an appropriate mix of field and group accretion the $f_\star$ values in massive clusters could in principle either increase or decrease with cosmic time. Our results indicate that this mix of field and group accretion to build up the halos of the most massive clusters must produce halos with $f_\star$ that are similar (at $\sim 10\%$ level) up to (or weakly decreasing since) redshift $z \sim 1$.

Add to this the likely stripping of stellar material from infalling galaxies during the accretion and relaxation process, and one has an additional mechanism to reduce the observed $f_\star$ over cosmic time, because the ICL from these stripped stars is not included in the $f_\star$ measurements here. Lin & Mohr (2004) suggested just such a mechanism to reconcile the falling $f_\star$ with halo mass they observed in the local Universe. They presented a toy model that suggested such a mechanism would have to lead to an ICL mass fraction that increases with halo mass and reaches high values of $\approx$40% of the stars in the central galaxy of the clusters. Neither this trend nor ICL fractions at this high redshift have been observed in recent observational studies (Zibetti et al., 2005; Gonzalez et al., 2013). Presumably, as massive clusters grow, a reduction of $f_\star$ through

both accretion from the field and stripping of stars from cluster galaxies is counterbalancing the increase of $f_\star$ due to accretion of lower mass subclusters. Together these processes must transform high $f_\star$ low mass clusters into lower $f_\star$ high mass clusters. Moreover, these processes must maintain a roughly constant $f_\star$ at fixed halo mass over cosmic time on cluster mass scales.

A similar scenario of infall from the field and accretion of subclusters could explain the trends in $f_{\rm ICM}$ as a function of halo mass and redshift. In the case of $f_{\rm ICM}$, the field value, which is inferred by the *Planck* measurement, is higher than that in the clusters at $z = 0.9$ and remains so to $z = 0$ (see Figure 2.6). Thus, given our observed weakly increasing cluster $f_{\rm ICM}$ at fixed halo mass since $z \sim 1$, the increases in $f_{\rm ICM}$ during cluster growth from infall from the field are compensating for the decreases in $f_{\rm ICM}$ from accretion of subclusters. These constraints, when coupled to a detailed hydrodynamical study, would presumably enable one to constrain processes such as early preheating as well as entropy injection from AGN residing in groups and clusters.

2.8 Conclusions

In this work we study the stellar mass function and baryon composition of 14 high redshift SZE-selected clusters between redshifts 0.572 and 1.32 that have a median mass M_{500} of $6 \times 10^{14}{\rm M}_\odot$. We estimate $f_\star$, $f_{\rm ICM}$, $f_{\rm c}$ and $f_{\rm b}$ within R_{500} (Table 2.4). Our sample provides the highest redshift, uniformly selected sample to date for the study of the baryon content in massive clusters; our measurements together with low redshift measurements in the literature enable us to constrain the redshift variation of these quantities. We summarize our results here.

- We examine the $M_\star^{\rm BCG}$–M_{500} relation by combining our sample with the sample of H13 and vdB14 (Section 2.5.1, Equation 2.4). On the cluster mass scale of $6 \times 10^{14}{\rm M}_\odot$ the BCG stellar mass constitutes $0.12 \pm 0.01\%$ of the halo mass. That fraction falls with cluster mass as $M_{500}^{-0.58\pm0.07}$. BCG stellar masses scatter about the best fit $M_\star^{\rm BCG}$–M_{500} relation with a characteristic value of 41%, a measure of the considerable variation in the BCG population.

- We measure the stacked SMF of these clusters and fit it to a Schechter function (Table 2.2; Section 2.5.2). The characteristic mass is $M_0 = 10^{11.0\pm0.1}{\rm M}_\odot$, consistent with values derived in low mass clusters at high redshift (vdB14) and at low redshift (Vulcani et al., 2013). Moreover, through comparison to constraints on the field SMF in the same redshift range (vdB13), we show that the number of galaxies with stellar mass above our threshold ($2.5 \times 10^{10}{\rm M}_\odot$) per unit total mass is higher in clusters than in the field by a factor of 1.65 ± 0.20.

We take the measurements of the baryon composition in each of our clusters and fit to power law relations in redshift and mass (Equation 2.11). We present best fit trends for the SPT sample and for a combined sample that includes several samples from the literature (Table 2.3). In combining with external samples we homogenise the stellar mass measurements to the Chabrier IMF (Section 2.3.2), we apply corrections for the differences in the virial mass estimates (Section 2.3.2), we adopt a 15% (1σ) systematic virial mass uncertainty (Section 2.6.1), and we

account for differences in the estimates of measurement uncertainties by solving for independent intrinsic scatter estimates for each subsample (Section 2.6.1). The key results are described below.

- The stellar mass fraction has a characteristic value $1.1 \pm 0.1\%$ (statistical) for clusters with mass $M_{500} = 6 \times 10^{14} \mathrm{M}_{\odot}$ at $z = 0.9$ and $1.0 \pm 0.05\%$ (statistical) at $z = 0$. It falls with cluster halo mass $f_{\star} \propto M^{-0.37 \pm 0.09}$ and mildly decreases with cosmic time $f_{\star} \propto (1+z)^{0.26 \pm 0.16 \pm 0.08}$ with 1.45σ significance, where the second component of the uncertainty represents the impact of the 15% systematic mass uncertainty between the low and high redshift samples. A similar result for the mass trend $\beta_{\star} \approx -0.26$ is also seen for low mass clusters and groups at $0.8 \leq z \leq 1.0$ (Balogh et al., 2014). The mass trend and mild redshift trend indicate that the infall from subclusters (which would tend to increase $f_{\star}$) and infall from the field and stripping of stars from cluster galaxies (which would both tend to decrease the observed $f_{\star}$) must combine to enable the transformation of $f_{\star}$ from low mass clusters into that of higher mass clusters having similar $f_{\star}$ over the redshift range $0 < z < 1$. Numerical simulations suggest that approximately 40% of cluster galaxies have been accreted as members of subclusters, and the remainder from the field (McGee et al., 2009), but additional study is warranted to test whether the observed trends in $f_{\star}$ (now constrained both as a function of mass and of redshift) can be reproduced by current structure formation scenarios.

- The ICM mass fraction has a characteristic value in clusters with mass $M_{500} = 6 \times 10^{14} \mathrm{M}_{\odot}$ of $9.6 \pm 0.5\%$ (statistical) at $z = 0.9$ and $11.2 \pm 0.32\%$ (statistical) at $z = 0$. It rises with cluster halo mass $f_{\mathrm{ICM}} \propto M^{0.22 \pm 0.06}$ and evolves weakly with redshift at fixed halo mass as $f_{\mathrm{ICM}} \propto (1+z)^{-0.20 \pm 0.11 \pm 0.22}$, where the 0.22 is due to the 15% systematic mass uncertainty between the low and high redshift samples. The trend of increasing f_{ICM} with mass has been previously observed (Mohr et al., 1999) and can be explained through entropy injection through early preheating or from cluster AGN. A weakly varying f_{ICM} with cosmic time could be explained by infall from the field, where f_{ICM} is larger than that in clusters at $z = 0.9$ and $z = 0$ (see Figure 2.6). Hydrodyamical studies of this scenario are needed.

- The collapsed baryon fraction determines the fraction of the baryonic component that has cooled to form stars. It is the ratio of the stellar mass to the ICM plus stellar mass. The characteristic value at cluster masses $M_{500} = 6 \times 10^{14} \mathrm{M}_{\odot}$ is $10.7 \pm 0.1\%$ (statistical) at $z = 0.9$ and $8.6 \pm 0.5\%$ (statistical) at $z = 0$. It falls with halo mass as $f_{\mathrm{c}} \propto M^{-0.65 \pm 0.10}$, indicating with 6.5σ significance that a smaller fraction of halo baryons is in the form of stars in the most massive halos. The redshift trend is $f_{\mathrm{c}} \propto (1+z)^{0.39 \pm 0.15 \pm 0.16}$, where the second uncertainty is due to the 15% systematic mass uncertainty between the low and high redshift samples. Thus, there is $\approx 1.8\sigma$ evidence that the collapsed baryon fraction is falling with cosmic time, and this is driven by the weak trends of rising f_{ICM} and falling $f_{\star}$ presented above.

- The baryon fraction f_{b} is the fraction of the halo mass that is in ICM and stars. The characteristic value at cluster mass $M_{500} = 6 \times 10^{14} \mathrm{M}_{\odot}$ is $10.7 \pm 0.6\%$ (statistical) at $z = 0.9$ and

$12.3 \pm 0.4\%$ (statistical) at $z = 0$. It rises with halo mass as $f_{\rm b} \propto M^{0.22\pm0.06}$, and this 3.7σ mass trend is affected both by the increase in $f_{\rm ICM}$ and the decrease in $f_\star$ with cluster mass. The evidence for redshift variation at fixed halo mass is weak $f_{\rm b} \propto (1+z)^{-0.17\pm0.11\pm0.22}$, where the second uncertainty is due to the 15% systematic mass uncertainty between the low and high redshift samples. If the two uncertainties are added in quadrature, there is no significant evidence (0.7σ) that the baryon fraction is evolving.

As already discussed in Section 2.7, these mass and redshift trends in baryon quantities are not consistent with a simple hierarchical structure formation merger model where massive clusters form solely through the accretion of lower mass clusters and groups. Significant accretion of galaxies and ICM from the field must also occur, and this accretion together with infall of subclusters can likely explain the weak variation (at fixed cluster halo mass) in $f_\star$ and in $f_{\rm ICM}$ over cosmic time. Additionally, the loss of stellar mass from galaxies through stripping is an additional mechanism that would allow for $f_\star$ to fall as low mass clusters grow to higher mass.

This analysis of the first homogeneously selected high mass cluster sample extending to high redshift allows for interesting initial constraints on the redshift trends in the baryon content; however, these trends are dependent to some extent on the adopted systematic virial mass uncertainty between the low and high redshift samples. If the systematic virial mass uncertainty is 15% there are no statistically significant redshift trends. Higher virial mass systematic uncertainties would further reduce the significance of trends. A reduction of the 15% systematic virial mass uncertainty to 10% or 5% would result in a fractional reduction (to $2/3$ or $1/3$, respectively) for the redshift trend systematic uncertainties $\gamma_{\rm obs}^{\rm sys}$. In the case of a 5% systematic virial mass uncertainty, the significance of the redshift trends for $f_\star$ ($f_{\rm ICM}$, $f_{\rm c}$, $f_{\rm b}$) would increase from 1.12σ (0.81σ, 1.6σ, 0.69σ) to 1.27σ (1.53σ, 2.2σ, 1.28σ). It is clear that what is needed is a systematic study of a large, homogeneously selected cluster sample with high quality mass estimates that spans a broad redshift range.

We acknowledge the support by the DFG Cluster of Excellence "Origin and Structure of the Universe" and the Transregio program TR33 "The Dark Universe". The calculations have been carried out on the computing facilities of the Computational Center for Particle and Astrophysics (C2PAP) and of the Leibniz Supercomputer Center (LRZ). BB is supported by the Fermi Research Alliance, LLC under Contract No. De-AC02-07CH11359 with the United States Department of Energy. BS acknowledges the support of the NSF grants at Harvard and SAO (AST-1009012, AST-1009649 and MRI- 0723073). TS acknowledges the support from the German Federal Ministry of Economics and Technology (BMWi) provided through DLR under project 50 OR 1210. The South Pole Telescope is supported by the National Science Foundation through grant ANT-0638937. Partial support is also provided by the NSF Physics Frontier Center grant PHY-0114422 to the Kavli Institute of Cosmological Physics at the University of Chicago, the Kavli Foundation and the Gordon and Betty Moore Foundation.

Optical imaging data from the VLT programs 088.A-0889 and 089.A-0824, HST imaging data from programs C18-12246 and C19-12447, and Spitzer Space Telescope imaging from programs 60099, 70053 and 80012 enable the SED fitting in this analysis. X-ray data obtained with Chandra X-ray Observatory programs and XMM-*Newton* Observatory program 067501 enable the ICM mass measurements. The SPT survey program SPT-SZ enabled the discovery

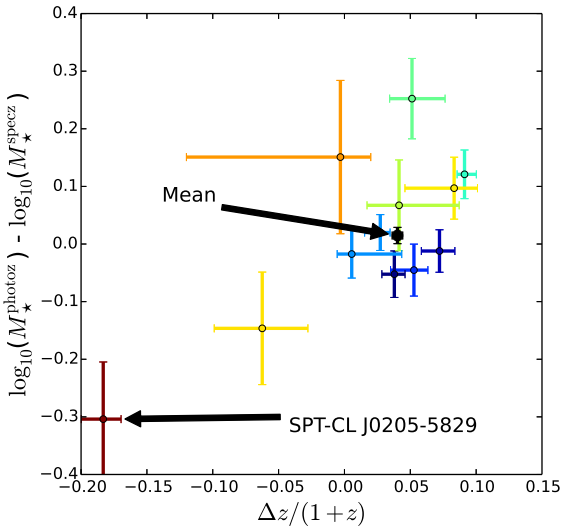

Figure 2.7: A test of SED fitting using galaxies with spectroscopic redshifts. The x-axis is the normalized difference of photo-z and spec-z and the y-axis is the resulting stellar mass difference averaged on a per-cluster basis. The color code from blue to red indicates the clusters from the lowest to the highest redshift. SPT-CL J0205-5829 at $z = 1.32$ is marked as it has the largest mass difference. The black dot indicates the mean of $(\log_{10} M_\star^{\rm photoz} - \log_{10} M_\star^{\rm specz})$ and $\Delta z/(1+z)$ of the ensemble of clusters.

of these high redshift clusters and subsequent analyses have enabled virial mass estimates of these systems. Optical spectroscopic data from VLT programs 086.A-0741 and 286.A-5021 and Gemini program GS-2009B-Q-16, GS-2011A-C-3, and GS-2011B-C-6 were included in this work. Additional spectroscopic data were obtained with the 6.5 m Magellan Telescopes.

Facilities: South Pole Telescope, *Spitzer*/IRAC, VLT: Antu (FORS2), *HST*/ACS, *Chandra*, XMM-*Newton*, Magellan

2.9 Appendix

2.9.1 Performance of SED fitting

With the published spectroscopic sample for SPT clusters (Sifón et al., 2013; Ruel et al., 2014), we are able to quantify how the uncertainty of the photo-z impacts on the stellar mass estimates based on the SED fit using the six band photometry (b_H, F606W, I_B, z_G, [3.6], [4.5]). We cross-match our photometry identified sample with the galaxy sample in Ruel et al. (2014) and repeat the whole SED fit analysis with the redshift fixed to the measured spectroscopic redshift. We show the comparison in Figure 2.7. The photo-z performance is estimated as the mean $\Delta z/(1+z) \equiv (z_{\rm photo} - z_{\rm spec})/(1+z_{\rm spec})$ to be 0.037 ± 0.0083. The difference of the stellar mass estimates $(\log_{10} M_\star^{\rm photoz} - \log_{10} M_\star^{\rm specz})$ when using $z_{\rm photo}$ and $z_{\rm spec}$ is at the level of $\lessapprox 0.2$ with

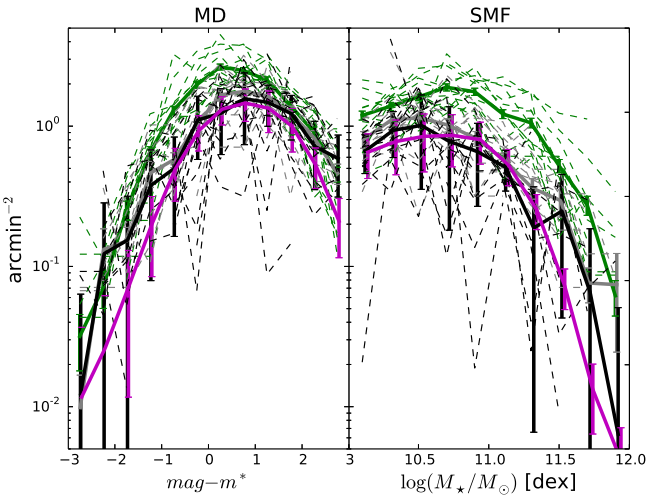

Figure 2.8: The magnitude distribution (MD- left) and stellar mass function (SMF- right) for the full population of galaxies in the SPT clusters. We show the cluster + background estimates from within R_{500} (green), the uncorrected local background (grey), the corrected local background (black), and the background estimated from COSMOS (magenta). The SMFs are derived using SED fitting of six band photometry. The dashed lines indicate the results for individual clusters and the heavy-solid lines are the averages over all clusters. The COSMOS and local, contamination-corrected background estimates are in good agreement. We adopt the COSMOS background correction in this work.

a mean ≈ 0.03. Except for the highest redshift cluster (SPT-CL J0205-5829 at $z = 1.32$), which has only 5 spectroscopic redshifts available for the cluster members, the SED fitting using our six band photometry returns unbiased estimates of the stellar masses.

2.9.2 Tests of Statistical Background Correction

To test the COSMOS background, we extract the local background information from our SPT dataset, applying a correction for the cluster galaxy contamination. We extract the corrected local background between $1.2R_{500}$ and $2.5R_{500}$ for each cluster. We correct for cluster contamination by assuming that the cluster galaxies are distributed as an NFW model with concentration of $c_{500}^{\rm gal} = 1.9$ (Lin et al., 2004, Hennig in prep), and the Stellar Mass Function (SMF) and the Magnitude Distribution (MD) are the same for the region within the cluster R_{500} and for the cluster population that is contaminating the background region. Together with the area extracted for the region within R_{500} and the local background, we solve for the the surface number densities of the SMF and MD using the corrected local background for each cluster. The SMF and MD derived using the corrected local background are noisy for each individual cluster, especially for the lower redshift clusters where the area available for the local background is typically less than 5 arcmin^2. We combine 9 of the 14 independent estimates (those with background area larger than 8 arcmin^2) to create an average local background estimate. In averaging, we use the area

weighted average of the individual background estimates so that clusters with greater area (but not necessarily higher number density) receive higher weight.

Figure 2.8 contains a comparison of the COSMOS and local background estimates for the SMF (right panels) and MD (left panels). The corrected local background estimates (black) for the SMF and MD are in a good agreement with the COSMOS backgrounds (magenta). There is poorer agreement on the bright (massive) end with the tendency that the local background is slightly higher than COSMOS. The cluster plus background SMF and MDs extracted from within R_{500} (green) show significant overdensities with respect to the background estimates. In both the case of the local background estimates (black) and the cluster plus background estimates (green), the individual cluster results are shown with dashed lines and the thick solid lines represent the ensemble average.

On the other hand, the corrected local background for the SMF and MD for the red population is generally lower than the COSMOS estimates. This suggests we are overcorrecting the local backgrounds for cluster contamination in the case of the red population, and this is to be expected given that we do not have the right filter combinations (blue band containing 4000 Å break and one band redward of the break) for the half of our sample that lies at $z > 0.9$. For these reasons we do not present any analyses of the red sequence selected subpopulation in this paper.

We compare the differences between the cumulative stellar mass estimates for the full population when using the two different background corrections. We fit a simple linear relation $M_{\rm local} = 10^x \times M_{\rm COSMOS}$, allowing the normalization 10^x to float, where $M_{\rm local}$ and $M_{\rm COSMOS}$ are the mass estimations for using the local and COSMOS backgrounds, respectively. The resulting best-fit x is -0.018 ± 0.005 (0.045 ± 0.012) for the cluster (background) stellar mass estimation. That is, using the COSMOS background results in $\sim$4% higher stellar mass estimates for the cluster and $\sim$10% lower mass estimates in the background as compared to those using the corrected local background.

Table 2.4: Measured quantities for the SPT cluster sample: Columns contain the cluster name, spectroscopic redshift, M_{500} estimated from the SZE signature, R_{500} inferred from the given M_{500} and redshift, ICM mass $M_{\rm ICM}$, the BCG mass $M_\star^{\rm BCG}$, the total stellar mass $M_\star$, the stellar mass fraction $f_\star$, the collapsed baryon fraction $f_{\rm c}$, the baryon fraction $f_{\rm b}$, the ICM mass fractions $f_{\rm ICM}$ and the stellar-mass-to-light ratios Υ (rms in the parenthesis) in $[3.6]$ band in the observed frame.

Cluster	Redshift	M_{500} $[10^{14}{\rm M}_\odot]$	R_{500} [Mpc]	$M_{\rm ICM}$ $[10^{13}{\rm M}_\odot]$	$M_\star^{\rm BCG}$ $[10^{11}{\rm M}_\odot]$	$M_\star$ $[10^{12}{\rm M}_\odot]$	$f_\star$ [%]	$f_{\rm c}$ [%]	$f_{\rm b}$ [%]	$f_{\rm ICM}$ [%]	Υ $[\frac{{\rm M}_\odot}{L_\odot}]$
SPT-CL J0000-5748	0.702	4.35 ± 1.16	0.90	4.33 ± 0.73	$13.49^{+1.18}_{-1.06}$	6.34 ± 2.22	1.46 ± 0.64	12.76 ± 4.33	11.42 ± 3.51	9.96 ± 3.14	0.37 (0.146)
SPT-CL J0102-4915	0.870	15.75 ± 3.22	1.30	25.51 ± 0.98	$9.23^{+0.82}_{-0.73}$	10.29 ± 1.92	0.65 ± 0.18	3.88 ± 0.71	16.85 ± 3.50	16.19 ± 3.37	0.32 (0.196)
SPT-CL J0205-5829	1.320	5.65 ± 1.14	0.78	5.26 ± 1.13	$3.95^{+0.92}_{-1.02}$	5.01 ± 0.96	0.89 ± 0.25	8.70 ± 2.28	10.20 ± 2.87	9.31 ± 2.74	0.42 (0.158)
SPT-CL J0533-5005	0.881	4.24 ± 1.13	0.83	2.70 ± 0.51	$5.89^{+0.56}_{-0.47}$	2.95 ± 0.98	0.70 ± 0.30	9.85 ± 3.39	7.06 ± 2.24	6.36 ± 2.07	0.33 (0.221)
SPT-CL J0546-5345	1.067	5.48 ± 1.16	0.85	7.05 ± 1.23	$17.41^{+1.86}_{-4.57}$	14.07 ± 2.19	2.57 ± 0.67	16.63 ± 3.24	15.44 ± 3.99	12.87 ± 3.53	0.38 (0.208)
SPT-CL J0559-5249	0.609	7.16 ± 1.44	1.11	8.36 ± 0.55	$4.83^{+0.41}_{-0.38}$	8.10 ± 1.64	1.13 ± 0.32	8.83 ± 1.71	12.80 ± 2.70	11.67 ± 2.47	0.30 (0.171)
SPT-CL J0615-5746	0.972	11.75 ± 2.35	1.13	13.60 ± 2.25	$14.39^{+1.75}_{-4.61}$	14.70 ± 2.45	1.25 ± 0.33	9.75 ± 2.07	12.83 ± 3.21	11.57 ± 3.00	0.36 (0.186)
SPT-CL J2040-5726	0.930	4.10 ± 0.97	0.81	4.25 ± 0.95	$5.44^{+0.49}_{-0.45}$	3.44 ± 0.93	0.84 ± 0.30	7.50 ± 2.43	11.22 ± 3.53	10.38 ± 3.38	0.28 (0.146)
SPT-CL J2106-5844	1.132	9.35 ± 1.84	0.99	11.68 ± 1.43	$9.96^{+0.87}_{-0.79}$	14.06 ± 2.01	1.50 ± 0.37	10.75 ± 1.80	13.99 ± 3.16	12.49 ± 2.89	0.42 (0.171)
SPT-CL J2331-5051	0.576	6.45 ± 1.34	1.08	6.07 ± 0.83	$3.03^{+2.67}_{-0.66}$	2.78 ± 1.31	0.43 ± 0.22	4.38 ± 2.06	9.84 ± 2.42	9.41 ± 2.34	0.37 (0.197)
SPT-CL J2337-5942	0.775	9.44 ± 1.83	1.14	8.52 ± 0.79	$10.33^{+1.00}_{-0.80}$	11.24 ± 2.14	1.19 ± 0.32	11.66 ± 2.18	10.21 ± 2.16	9.02 ± 1.94	0.40 (0.156)
SPT-CL J2341-5119	1.003	6.59 ± 1.31	0.92	6.85 ± 1.00	$9.41^{+1.62}_{-1.84}$	7.12 ± 1.60	1.08 ± 0.32	9.42 ± 2.29	11.47 ± 2.75	10.39 ± 2.57	0.34 (0.183)
SPT-CL J2342-5411	1.075	4.43 ± 1.07	0.79	3.15 ± 0.64	$8.25^{+0.74}_{-0.67}$	5.03 ± 1.17	1.14 ± 0.38	13.77 ± 3.66	8.25 ± 2.47	7.11 ± 2.24	0.39 (0.167)
SPT-CL J2359-5009	0.775	4.98 ± 1.16	0.92	3.50 ± 0.34	$6.92^{+0.58}_{-0.53}$	4.80 ± 1.31	0.96 ± 0.35	12.06 ± 3.07	8.00 ± 2.00	7.03 ± 1.77	0.43 (0.182)

Chapter 3

Stellar Mass to Halo Mass Scaling Relation for X-ray Selected Low Mass Galaxy Clusters and Groups out to Redshift $z \approx 1$

I. Chiu[1,2], A. Saro[1,2], J. Mohr[1,2,3], S. Desai[1,2], S. Bocquet[1,2], R. Capasso[1,2], C. Gangkofner[1,2], N. Gupta[1,2], J. Liu[4]
[1]Faculty of Physics, Ludwig-Maximilians-Universität, Scheinerstr. 1, 81679 Munich, Germany
[2]Excellence Cluster Universe, Boltzmannstr. 2, 85748 Garching, Germany
[3]Max Planck Institute for Extraterrestrial Physics, Giessenbachstr. 85748 Garching, Germany
[4]Bosch Research and Technology Center North America, 4005 Miranda Ave #200, Palo Alto, CA 94304, United States

This chapter is published as Chiu et al. (2016c) in Monthly Notices of the Royal Astronomical Society.

3.1 Abstract

We present the stellar mass-halo mass scaling relation for 46 X-ray selected low-mass clusters or groups detected in the XMM-BCS survey with masses $2 \times 10^{13}\mathrm{M}_{\odot} \lesssim M_{500} \lesssim 2.5 \times 10^{14}\mathrm{M}_{\odot}$ (median mass $8 \times 10^{13}\mathrm{M}_{\odot}$) at redshift $0.1 \leq z \leq 1.02$ (median redshift 0.47). The cluster binding masses M_{500} are inferred from the measured X-ray luminosities L_{X}, while the stellar masses $M_{\star}$ of the galaxy populations are estimated using near-infrared imaging from the SSDF survey and optical imaging from the BCS survey. With the measured L_{X} and stellar mass $M_{\star}$, we determine the best fit stellar mass-halo mass relation, accounting for selection effects, measurement uncertainties and the intrinsic scatter in the scaling relation. The resulting mass trend is $M_{\star} \propto M_{500}^{0.69\pm0.15}$, the intrinsic (log-normal) scatter is $\sigma_{\ln M_{\star}|M_{500}} = 0.36^{+0.07}_{-0.06}$, and there is no significant redshift trend $M_{\star} \propto (1+z)^{-0.04\pm0.47}$, although the uncertainties are still large. We also examine $M_{\star}$ within a fixed projected radius of 0.5 Mpc, showing that it provides a cluster binding mass proxy with intrinsic scatter of $\approx 93\%$ (1σ in M_{500}). We compare our $M_{\star} = M_{\star}(M_{500}, z)$ scaling relation from the XMM-BCS clusters with samples of massive, SZE-selected clusters ($M_{500} \approx 6 \times 10^{14}\mathrm{M}_{\odot}$) and low mass NIR-selected clusters ($M_{500} \approx 10^{14}\mathrm{M}_{\odot}$) at redshift $0.6 \lesssim z \lesssim 1.3$. After correcting for the known mass measurement systematics in the compared samples, we find that the scaling relation is in good agreement with the high redshift samples, suggesting that for both groups and clusters the stellar content of the galaxy populations within R_{500} depends strongly on mass but only weakly on redshift out to $z \approx 1$.

3.2 Introduction

Over the past decade and a half extensive galaxy cluster surveys have been undertaken in the X-ray (e.g. Böhringer et al., 2004; Pierre et al., 2004; Mantz et al., 2008; Vikhlinin et al., 2009b), at mm wavelengths (e.g. Staniszewski et al., 2009; Planck Collaboration et al., 2011; Hasselfield et al., 2013) employing the Sunyaev-Zel'dovich Effect (SZE; Sunyaev & Zel'dovich, 1970a, 1972), and in the optical (e.g. Gladders & Yee, 2005; Koester et al., 2007) and near infrared (NIR; Lacy et al., 2005; Stanford et al., 2014). While the primary goal of many of these surveys has been to use galaxy clusters to study cosmology and, in particular, the dark energy or cosmic acceleration (Haiman et al., 2001; Weller & Battye, 2003), the buildup of large regions of the sky with overlapping, multiwavelength surveys provides not only data for cluster cosmological studies, but also data that enable the study of the clusters themselves.

Of particular importance to cluster studies is the need to account for the impact of the cluster sample selection. A uniform selection can simplify the interpretation of the results. Another element of critical importance is that one needs to have precise mass estimates from low scatter mass proxies where the remaining systematic uncertainties are quantified. Because most properties of the cluster vary with cluster-centric distance, a precise mass is crucial for making it possible to study the same portion of the cluster virial region at all redshifts.

Recently, the stellar and intracluster medium mass trends with cluster binding mass M_{500} and redshift have been studied in a sample of massive ($M_{500} \gtrsim 3 \times 10^{14}\mathrm{M}_{\odot}$), SZE selected clusters at redshfit $z \approx 0.9$ with X-ray, optical and NIR followup data (Chiu et al., 2016b). Cluster binding

masses were determined using the SZE signatures of the clusters, and the X-ray and optical/NIR observations were used to study the intracluster medium and galaxy populations, respectively. This sample exhibits a trend for the stellar mass fraction to fall with cluster binding mass, which has been noted previously (e.g. Lin et al., 2004; Andreon, 2010). In addition, this sample is at relatively high redshift and thus– in combination with results from previous studies of low redshift clusters– these clusters indicate that there is no significant redshift trend in the stellar mass fraction out to redshift $z \approx 1.32$ (Chiu et al., 2016b). Such a result is troubling at first glance, because it suggests that massive halos exhibit different stellar mass fractions than their building blocks, which include the low mass halos.

It must be noted that the current constraints on the trends in stellar mass fraction with redshift suffer from the systematic uncertainties induced from the joint analysis of heterogeneous samples using different mass measurement techniques. Moreover, these constraints are only available for the massive systems, and of course the progenitors of the local high mass clusters are low mass clusters at higher redshift. It is therefore imperative to extend the scaling relation studies to include lower mass halos and to use consistent mass measurement techniques over as wide a range of redshift as possible to improve constraints on the matter assembly history of both groups and galaxy clusters.

In this work, we aim to measure the relationship between stellar and binding mass for the low mass clusters and groups detected in a 6 deg^2 region of the XMM-*Newton*-Blanco Cosmology Survey (XMM-BCS; Šuhada et al., 2012). The XMM-BCS survey employs the XMM-*Newton* telescope (Proposal Id 050538, PI H. Boehringer) to survey a total sky area of 14 deg^2 within a region fully covered by the optical *griz* Blanco Cosmology Survey (BCS; Desai et al., 2012) and the NIR *Spitzer*-South Pole Telescope Deep Field survey (SSDF; Ashby et al., 2013). This sky region has also been imaged in the SZE by the South Pole Telescope (SPT, Carlstrom et al., 2002), and the XMM-BCS cluster sample has already been used to study the SZE signature-halo mass scaling relation (Liu et al., 2015b, L15 hereafter). By combining the SPT-SZ maps and the XMM-*Newton* sample, it was possible to study the relationship between SZE signature and halo binding mass to a mass threshold ≈ 3 times lower than the masses of the SPT-SZ selected clusters (Bleem et al., 2015).

This paper is organized as follows. The cluster sample and data are described in Section 3.3, while the analysis method is given in Section 3.4. We present the results and discussion in Section 3.5. The potential systematics are quantified in Section 3.6, and the conclusions are presented in Section 5.7. Throughout this paper, we adopt the ΛCDM cosmology with the fiducial cosmological parameters $(\Omega_{\rm M}, \Omega_\Lambda, H_0, \sigma_8) = (0.3, 0.7, 70 \text{ km s}^{-1} \text{ Mpc}^{-1}, 0.8)$. Unless otherwise stated, the uncertainties indicate the 1σ confidence level, the halo binding mass M_{500} is estimated at the overdensity of 500 with respect to the critical density at the cluster redshift, and the photometry is in the AB magnitude system.

3.3 Cluster Sample and Observations

In this section we briefly introduce the cluster sample in XMM-BCS catalog in Section 3.3.1 and the SSDF catalog used to derive the stellar masses in Section 3.3.2.

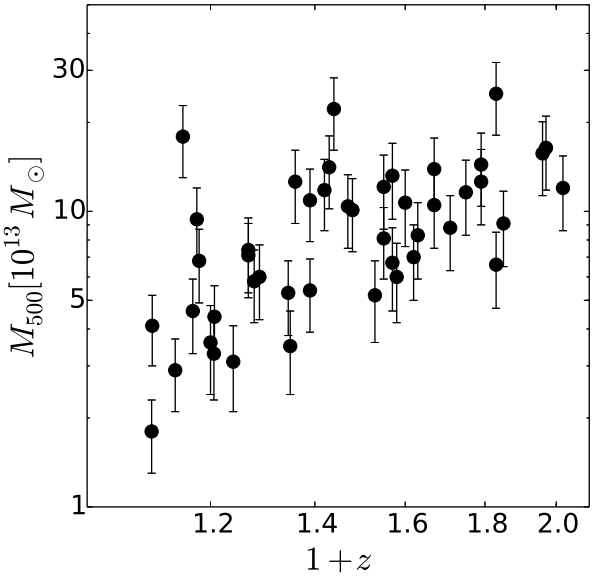

Figure 3.1: The XMM-BCS sample plotted in mass versus redshift (similar to Figure 1 in L15). The cluster masses M_{500} are derived via the X-ray luminosity $L_{\rm X}$ to mass scaling relation, and the redshifts are estimated using the red sequence overdensity technique. The median mass is $M_{500} = 8 \times 10^{13}{\rm M}_\odot$, and the median redshift is $z = 0.47$.

3.3.1 XMM-BCS catalog

We use the galaxy clusters detected in the XMM-BCS survey (S12), which is also the same sample used in L15 to study the SZE signature-halo mass scaling relations. The XMM-BCS sample consists of 46 clusters with the median M_{500} of $8 \times 10^{13}{\rm M}_\odot$ and redshift range from 0.1 to 1.02 with a median of 0.47 (see FIgure 4.1). A full description of the X-ray data reduction, source detection and mass calibration is given in S12, we briefly summarize the XMM-BCS catalog in the following. Each galaxy cluster is detected by their X-ray emission in the energy range $0.5-2$ keV in the central 6 deg^2 footprint of the XMM-BCS survey, this results in a flux-limited sample with the limiting flux $f_{\rm lim} = 10^{-14}{\rm ergs}^{-1}{\rm cm}^{-2}$. After the optical confirmation and redshift estimation (see below), the X-ray luminosity in the energy range $0.5-2$ keV ($L_{\rm X,[0.5-2\ keV]}$) for each cluster is iteratively measured within R_{500}, which is defined as the radius corresponding to the enclosed mass M_{500}, through the X-ray luminosity-halo mass relation (Pratt et al., 2009). The measured X-ray luminosity is then converted into the bolometric luminosity $L_{\rm X,\ bol}$ using the characteristic temperature $T_{\rm X}$ and the redshift for the cluster. The $T_{\rm X}$ is derived from a scaling relation with the observed luminosity. Following L15, we use $L_{\rm X,\ bol}$ (hereafter abbreviated as $L_{\rm X}$) as the mass proxy for XMM-BCS sample through the $L_{\rm X}$-M_{500} relation (Pratt et al., 2009):

$$L_{\rm X} = A_{\rm X}\left(\frac{M_{500}}{2\times 10^{14}{\rm M}_\odot}\right)^{B_{\rm X}} E(z)^{C_{\rm X}}\,, \tag{3.1}$$

with $E(z) \equiv \sqrt{\Omega_{\rm M}(1+z)^3+\Omega_\Lambda}$, $A_{\rm X} = 1.38 \pm 0.12 \times 10^{44}$ erg s^{-1}, $B_{\rm X} = 2.08 \pm 0.13$ and $C_{\rm X} = 7/3$. The intrinsic log-normal scatter of $L_{\rm X}$ for a given mass in equation (3.1) is $D_{\rm X} \equiv \sigma_{\ln L_{\rm X}|M_{500}} = 0.383 \pm 0.061$. Note that the Malmquist and Eddington biases are both taken into account and corrected in fitting equation (3.1).

The redshifts of the majority of the XMM-BCS sample are determined by the BCS photometry except for a few exceptions where the spectroscopic redshifts are available (S12). The photometric redshift for each cluster is estimated by modeling the excess of the red sequence (RS) galaxies within 0.8 Mpc centered on the X-ray center (S12). The RS model is constructed, using the python package `EZGAL` (Mancone & Gonzalez, 2012), by a Composite Stellar Population (CSP) of Bruzual & Charlot (2003, hereafter BC03) model with the formation redshift $z_{\rm f} = 3$ and an exponentially decaying *e*-folding timescale $\tau = 0.4$ Gyr. The Chabrier (2003) initial mass function is used in the model construction. The color-magnitude relation of the RS is determined by using six different metallicities, which are calibrated by the metallicity-luminosity relation of the RS of Coma cluster (for more details see Song et al., 2012a). This model has been used to successfully measure the photometric redshifts of SPT clusters out to redshift $z > 1$ with the root-mean-square of the redshift uncertainties at level of 0.017 (Song et al., 2012c). Calibrating the XMM-BCS clusters with the available spectroscopic redshifts, the photometric redshift estimations for XMM-BCS groups result in the root-mean-square of the redshift uncertainties $\Delta z/(1+z)$ of 0.023 (S12), which is in good agreement with that for SPT clusters.

3.3.2 SSDF catalog

The major goal of the SSDF survey is to enable study the evolution and structure of baryons in the distant Universe by observing the regions overlapping with the multi-wavelength surveys (e.g., SPT, XMM-*Newton* and BCS). The whole survey consists of a sky area of 94 deg^2 and is the largest wide field *Spitzer* extragalactic survey to date. The SSDF survey was completed in 2013 and the data reduction, the photometry calibration and the source extraction is fully described in Ashby et al. (2013). We briefly summarize the survey below.

Two IRAC channels of 3.6 μm and 4.5 μm are imaged in SSDF survey to depths which result in 5σ limiting magnitudes for 4$''$ diameter apertures of 21.79 mag (7.0 μJy) and 21.47 mag (9.4 μJy) for 3.6 μm ([3.6]) and 4.5 μm ([4.5]), respectively. Source detection is performed by running `SExtractor` (Bertin & Arnouts, 1996) in dual-image mode. The 3.6 μm and 4.5 μm mosaic images are used in turn as the detection image, resulting in 3.6 μm-selected or 4.5 μm-selected source catalogs with `MAG_AUTO` mesurements for each object. The completeness of the source catalogs as a function of magnitude $f_{\rm com}(m)$ is derived through simulation. A vast number of simulated objects with a wide range of magnitudes are injected into the mosaics and the same detection pipeline is used to extract those objects and derive the catalog completeness (Ashby et al., 2013). The resulting 90% (50%) completeness of the source detection is at 19.60 mag (21.45 mag) and 19.72 mag (21.47 mag) for 3.6 μm and 4.5 μm, respectively. The completeness function $f_{\rm com}(m)$ in detail is given in Ashby et al. (2013).

We compare the characteristic magnitudes of XMM-BCS clusters and the SSDF limiting magnitudes in [3.6] and [4.5] in Figure 3.2. The characteristic magnitude of each cluster in 3.6 μm and 4.5 μm ($m_{\star,[3.6]}$ and $m_{\star,[4.5]}$) is estimated using the same CSP model used to es-

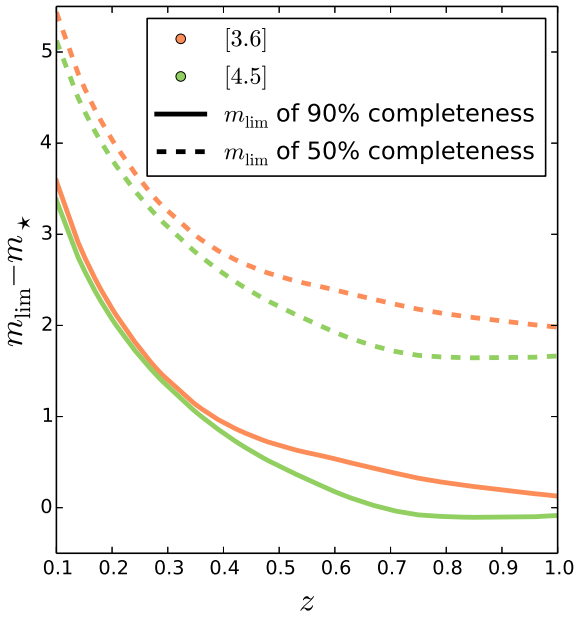

Figure 3.2: The offset of the SSDF survey limiting magnitudes relative to the cluster galaxy population characteristic magnitudes ($m_{\star,[3.6]}$ (red) and $m_{\star,[4.5]}$ (green)) from our CSP model out to redshift $z = 1$. The 90% (50%) completeness magnitudes appear as solid (dashed) lines. The SSDF at 50% completeness has adequate depth to allow us to estimate stellar masses for the XMM-BCS cluster sample.

timate the cluster redshift (see Section 3.3.1). The 50% completeness limit is deeper than the characteristic magnitudes of $m_{\star,[3.6]}$ and $m_{\star,[4.5]}$ by $\gtrsim 1.8$ mag out to redshift $z \approx 1$, thus ensuring that about 70% (80%) of the light emitted from the cluster galaxies out to $z \approx 1$, assuming a Schechter (1976) luminosity function (LF) with a faint end power law index of -1.1 (Lin et al., 2004) (-0.9; see Section 3.4.3), is directly detected after suitable completeness corrections with the SSDF survey. That is, the depth of the SSDF survey is adequate to enable us to measure the stellar masses of the XMM-BCS clusters.

3.4 Methods

For each cluster, we derive the total stellar masses of the galaxies which are photometrically identified in the SSDF 3.6 μm-selected source catalog. The most robust stellar mass estimates would come from spectral energy distribution (SED) template fitting on a single galaxy basis, and that would require photometry in multiple bands (e.g., BCS plus *Spitzer*) with depths that are comparable to the SSDF imaging. However, the BCS optical survey is too shallow to be used for this purpose for all XMM-BCS clusters in a uniform manner out to $z \approx 1$. Therefore, we model the NIR Luminosity Function (LF) for each cluster and then use a derived mass-to-light

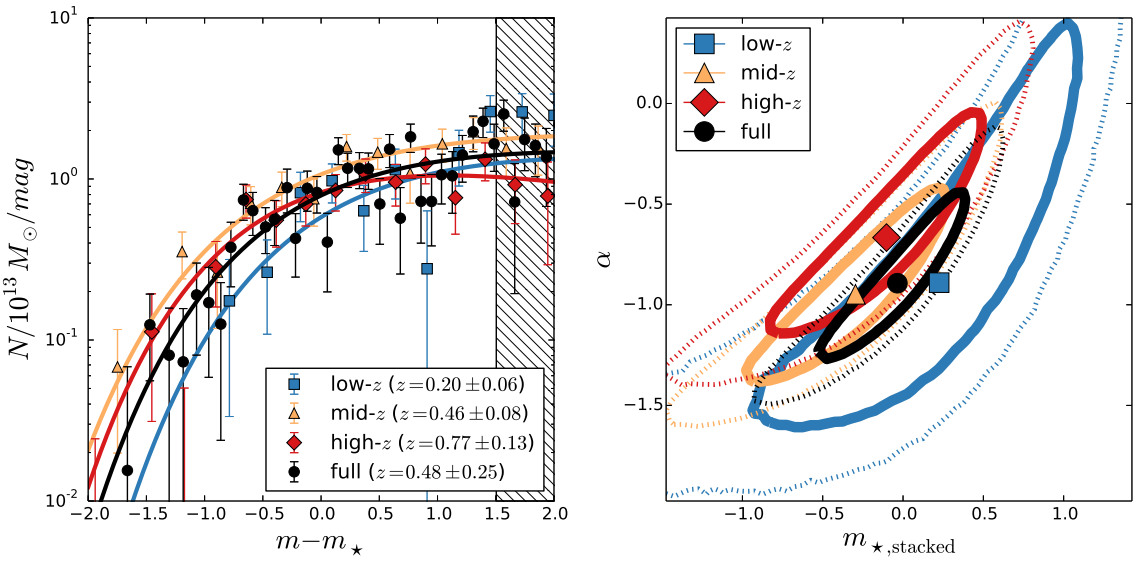

Figure 3.3: The stacked luminosity functions (left) in various redshift ranges together with the best fit LF parameters (right). On the left the x-axis shows the magnitudes with respect to the $m_\star$ predicted by our CSP model, while the y-axis shows the number density of galaxies normalized to per magnitude and per cluster mass of $10^{13}\mathrm{M}_\odot$. The stacked profiles of the full, low-z, mid-z and high-z samples are shown in black circles, blue squares, orange triangles and red diamonds, respectively. The best-fit profiles are in the solid lines with the same color. The shaded region indicates the magnitudes which are fainter than $m_\star + 1.5$, which are not used in the fitting. The mean and the standard deviation of the redshift distribution for the stacked samples are shown in the lower right corner. The joint constraints of $m_{\star,\,\mathrm{stacked}}$ and α appear on the right for the different luminosity functions using the same color coding. The LFs in all redshift ranges are in good agreement with the CSP model, and there is little evidence for a redshift dependence in α.

ratio for a stellar population that includes a group intracluster medium temperature and redshift dependent blue fraction to convert the total stellar luminosity into mass.

We first describe the LF modeling in Section 3.4.1 and then the mass-to-light ratio, which varies depending upon the measured blue fraction, in Section 3.4.2. We describe the measurement of the total stellar mass, which leverages parameters from stacked LFs, in Section 3.4.3. The Bayesian method for fitting the stellar mass-halo mass scaling relation is presented in Section 3.4.4.

3.4.1 Stacked Luminosity Function of XMM-BCS sample

Because the LF parameters are ill-constrained in the case of a single group or low mass cluster, we use information from the stacked profiles to constrain the faint end slope α and to test a model for the characteristic magnitude as a function of redshift $m_\star(z)$ (e.g., Lin et al., 2004). To derive the stacked LF of the XMM-BCS sample, we first construct the observed LF of each individual system.

Using the [3.6] selected catalogs described in Section 3.3.2 above, we first discard the point sources with $[3.6] < 17.75$ mag identified in the stellar branch of the FLUX_RADIUS-[3.6] relation; the FLUX_RADIUS for the stellar branch is between 1.75 and 2.30 pixels (corresponding to $1.05''$ and $1.38''$, respectively). We further discard the non-extended objects which have FLUX_RADIUS smaller than 1.75 pixels. Note that this removal of the non-extended sources will allow some stars to leak into the analysis sample but few if any galaxies will be excluded. The remaining stellar contamination in the extended source list is subtracted during the analysis by statistical foreground and background subtraction (we refer to it as the background subtraction hereafter). The 6 deg^2 XMM-BCS footprint excluding the cluster fields, which are the 3 Mpc diameter apertures centered on each cluster, is defined as the blank sky used to measure the background for our sample.

We then identify the Brightest Cluster Galaxy (BCG) within R_{500} for each cluster in the pseudo-color image reconstructed from the mosaics of 3.6 μm, 4.5 μm and BCS-z filter. For each cluster, we derive the [3.6] magnitude distribution with a bin width of 0.25 mag for the galaxies that lie projected within R_{500} and are fainter than the BCG. The background magnitude distribution is obtained by randomly drawing 25 non-overlapping apertures with the radii of cluster R_{500} from the blank sky. The mean of the 25 background magnitude distributions is used in making a statistical background subtraction. Finally, we apply the completeness correction to the observed overdensity of galaxies within the cluster.

We derive the stacked profiles for the full sample of the XMM-BCS clusters and compare it to the samples which are divided according to the cluster redshifts– namely, the low-z ($0.1 \leq z < 0.33$), mid-z ($0.33 \leq z < 0.58$) and the high-z ($0.58 \leq z \leq 1.02$) subsamples. To construct the stacked LF of the subsample, we first normalize the observed LF of each cluster by dividing by the total mass M_{500} inferred from the X-ray luminosity $L_{\rm X}$. In this way we mostly remove the dependence of the LF's normalization on the cluster mass (Lin et al., 2004). Second, we shift the LF of each individual cluster along the magnitude-axis by subtracting the characteristic magnitude $m_\star$ predicted by our CSP model at the cluster redshift. That is, if one fits the Schechter (1976) LF model to the normalized LFs, then any deviation of the best-fit $m_\star$ from zero implies a deviation of the cluster galaxy population from our CSP model prediction. In the end, we derive the stacked LFs by taking the inverse-variance weighted average of the stacked clusters at each magnitude bin.

After constructing the stacked LF of the samples, we fit the Schechter (1976) LF model– with the normalization ϕ_0, characteristic magnitude $m_{\star,\,\rm stacked}$ and the faint end power law index α varied– to the stacked profiles via χ^2 minimization. We restrict the fitting to magnitudes with $m - m_\star \leq 1.5$ mag, which ensures that all the magnitude bins of the stacked clusters are above 50% completeness (see Section 3.3.2) where the LF modeling is not dominated by the incompleteness. The resulting stacked LF, the best-fit model and the constraints of $m_{\star,\,\rm stacked}$ and α are shown in Figure 3.3.

As shown in the right panel of Figure 3.3, the best fit LF for the full sample stack shows no significant deviation from the CSP model with $m_{\star,\,\rm stacked} = -0.035 \pm 0.31$ mag, and provides a faint end constraint $\alpha = -0.89 \pm 0.29$. This implies that the cluster galaxy population of the XMM-BCS sample can be well described by our CSP model. This value for the faint end slope is consistent with the values $\alpha = -0.84 \pm 0.08$ (Muzzin et al., 2007) and $\alpha = -0.84 \pm 0.02$ (Lin

et al., 2004) published in two previous analyses.

Moreover, the LF parameters derived from the different subsamples exhibit no significant discrepancy among themselves or with the full sample (see Figure 3.3). All four samples are consistent (within $\lesssim 1\sigma$). This implies that the evolution of the characteristic magnitude of the cluster galaxy populations of the XMM-BCS are consistent with the CSP model and that there is no significant redshift trend in α. As a result, for the individual cluster LF fits we use the characteristic magnitude $m_\star$ predicted by the CSP model and the faint end power law index $\alpha = -0.89$ (see Section 3.4.3).

3.4.2 Mass-to-light ratio $\Gamma_\star$ of XMM-BCS sample

The stellar mass of each cluster is estimated by multiplying the total NIR light by the mass-to-light ratio $\Gamma_\star$. In general, $\Gamma_\star$ varies among the types of galaxies. Evidence tends to show that the cluster galaxy population is dominated by early type galaxies (e.g. Dressler, 1980), but with a component of late type galaxies that vary with cluster mass (Desai et al., 2007; Jeltema et al., 2007; Mei et al., 2009). Thus, using a constant $\Gamma_\star$ appropriate for a passively evolving population would unavoidably bias the stellar mass of the cluster galaxies. In this work, we use the synthetic $\Gamma_\star$ in the [3.6] filter for each cluster derived by mixing the mass-to-light ratio of a passive red and a star forming blue galaxy population, using the estimated blue fractions $f_{\rm blue}$ of the XMM-BCS clusters.

We estimate $f_{\rm blue}$ for the 46 XMM-BCS clusters by exploiting the BCS optical catalog (see discussion in Appendix 3.8.1). The estimated $f_{\rm blue}$ for all XMM-BCS clusters is presented in Table 3.1, and $f_{\rm blue}$ is plotted as a function of the XMM-BCS cluster X-ray temperature ($T_{\rm X}$) and redshift z in Figure 3.4. We find no significant redshift trend of $f_{\rm blue}$ for $T_{\rm X} \gtrsim 2$ keV in the XMM-BCS cluster sample, while the mass trend that $f_{\rm blue}$ increases toward low mass (or low $T_{\rm X}$) clusters is apparent. This weak mass trend of $f_{\rm blue}$ is consistent with the recent result based on the sample of clusters at low redshift $z \lesssim 0.05$ (Shan et al., 2015). We extract the $T_{\rm X}$ and redshift trends of $f_{\rm blue}$ from the observed $f_{\rm blue}$ of the XMM-BCS clusters by fitting a model to the estimated $f_{\rm blue}$. Specifically, we fit a function $f_{\rm blue}(T_{\rm X}, z)$, finding

$$f_{\rm blue}(T_{\rm X}, z) = \frac{(0.21 \pm 0.40)z + (0.31 \pm 0.15)}{T_{\rm X}}\,. \tag{3.2}$$

Appendix 3.8.1 contains more details of the fitting of the function $f_{\rm blue}(T_{\rm X}, z)$.

To derive the mass-to-light ratio ($\Gamma_{\star,\rm blue}$) in [3.6] for the blue population, we adopt an extreme star formation history ($\tau = 10$ Gyr) at $z_{\rm f} = 3$ with solar metallicity (see Section 3.3.1 for the model configuration); the resulting $\Gamma_{\star,\rm blue}$ is $\approx (52-59)\%$ of the mass-to-light ratio $\Gamma_{\star,\rm CSP}$ derived from the CSP model for $0.1 \leq z \leq 1.0$.

We derive the synthetic mass-to-light ratio $\Gamma_\star$ for each cluster using the best-fit $f_{\rm blue}$ (equation 3.2), $\Gamma_{\star,\rm blue}$ and the mass-to-light ratio $\Gamma_{\star,\rm CSP}$ estimated from the CSP model, i.e.,

$$\Gamma_\star = (1 - f_{\rm blue}(T_{\rm X}, z))\ \Gamma_{\star,\rm CSP} + f_{\rm blue}(T_{\rm X}, z)\ \Gamma_{\star,\rm blue}\,. \tag{3.3}$$

In this way we use a mass-to-light ratio that accounts for the trends in blue fraction variation with temperature and redshift, allowing us to avoid introducing stellar mass biases over the range

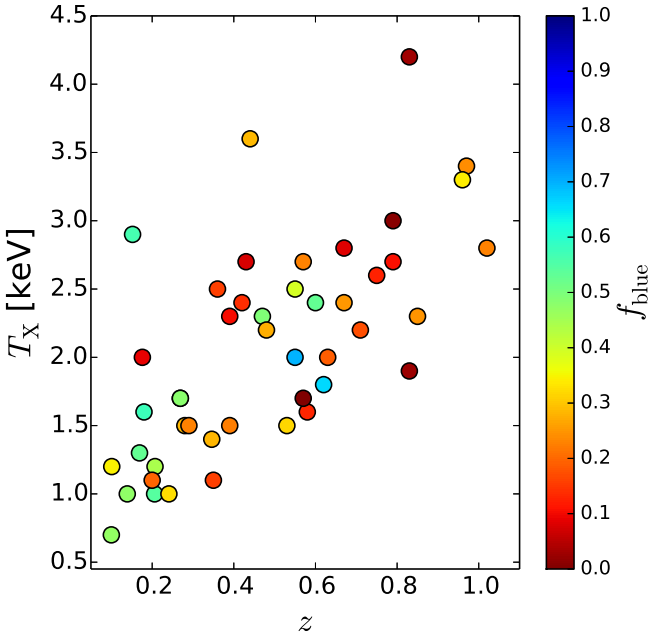

Figure 3.4: A plot of the blue fraction $f_{\rm blue}$ of XMM-BCS clusters as a function of X-ray temperature $T_{\rm X}$ and redshift z. The value $f_{\rm blue}$ for each cluster is color coded according to the scaling given in the colorbar. The uncertainties for $T_{\rm X}$, z and $f_{\rm blue}$ are omitted for clarity (see discussion in Appendix 3.8.1).

of mass and redshift probed by our sample. Using the ensemble fit results provides a way of avoiding the use of the noisy, single cluster blue fraction measurements directly in the mass-to-light ratio calculation.

3.4.3 Stellar Mass Estimations

We derive the total stellar mass of each of the 46 XMM-BCS cluster by multiplying the total luminosity, estimated from the satellite galaxies that lie projected within cluster R_{500} and the BCG, by the derived mass-to-light ratios. To estimate the luminosity of the satellite galaxies (BCG excluded) in 3.6 μm, we fit a model to the observed magnitude distribution of each cluster. Specifically, the magnitude distribution model $M(m)$ is constructed using the observed background magnitude distribution $B(m)$, a Schechter (1976) LF $\phi(m)$ that represents the cluster galaxies and the SSDF completeness function $f_{\rm com}(m)$ as a function of magnitude m:

$$M(m) = \phi(m, \phi_0, m_\star, \alpha) f_{\rm com}(m) + B(m)\,, \tag{3.4}$$

where ϕ_0, $m_\star$ and α are the normalization, characteristic apparent magnitude and the faint end power law index of the LF, respectively. The background $B(m)$ is fixed in the model because the uncertainties of $B(m)$ are small due to its being drawn from an area that is 25 times the area of

the cluster. That is, the uncertainties of the cluster LF are dominated by the cluster field. We use the Cash (1979) statistic with a maximum likelihood estimator $C_{\rm stat}$ to estimate the parameters in the fitting.

$$C_{\rm stat} = 2\sum_j \left(M(m_j) - N(m_j) + N(m_j) \ln\left(\frac{N(m_j)}{M(m_j)}\right)\right), \tag{3.5}$$

where j runs over all the magnitude bins in the fit and N is the observed magnitude distribution for the cluster. Using the estimator $C_{\rm stat}$ allows us to estimate the goodness of fit (GOF) for the data following the Poisson distribution in the same way as a χ^2-distribution. The GOF of the LF fitting is defined by the ratio of the best-fit $C_{\rm stat}$ to the degrees of freedom (d.o.f) (i.e., GOF $= C_{\rm stat}/$d.o.f) and has a corresponding probability to exceed that provides information about tension between the best fit model and the data.

We find that the magnitude distribution is generally too noisy to constrain the three parameters of the LF for the individual clusters. Therefore, we fix $m_\star$ to the $m_{\star,[3.6]}$ predicted by the CSP model and the faint end slope to $\alpha = -0.89$, which is measured in the stacked profile (see discussion in Section 3.4.1). Essentially, we fit for only one parameter ϕ_0 on a single cluster basis. The fit is done using the magnitude range extending from the magnitude of the BCG to the 50% completeness limit.

We convert the BCG magnitude to the rest-frame luminosity ($L_{\star,\rm BCG}$) at the cluster redshift with the k-correction– estimated from our CSP model (Mancone & Gonzalez, 2012). In this work we do not attempt to correct for the contribution from the intracluster light around the BCG. The total luminosity of the cluster galaxies $L_\star$ is the sum of the BCG luminosity $L_{\star,\rm BCG}$ and the luminosity of the satellite galaxies $L_{\star,\rm sat}$ within the R_{500} sphere, where $L_{\star,\rm sat}$ is obtained as follows.

$$L_{\star,\rm sat} = D_{\rm prj} \int_{L_{\rm min}}^{L_{\star,\rm BCG}} \phi(L)\, L\, {\rm d}L, \tag{3.6}$$

where $D_{\rm prj}$ is the deprojection correction from cylinder to sphere, and $L_{\rm min}$ is the lower threshold of the integrated interval. We use $D_{\rm prj} = 0.69$, which is derived by assuming an NFW (Navarro et al., 1996) distribution with concentration $C_{500} = 1.8$ with respect to R_{500} for the distribution of cluster galaxies (Lin et al., 2004). We set $L_{\rm min}$ to be the luminosity corresponding to $m_{\star,[3.6]} + 2$, ensuring that $L_\star$ of each cluster is estimated to a consistent depth. The luminosity is converted from the magnitude at the cluster redshift with the k-correction applied.

The uncertainty of $L_{\star,\rm sat}$ for each cluster is derived by bootstrapping the galaxies in the observed magnitude distribution of the cluster field and repeating the whole process described above. For the photometric uncertainty of the BCG we would like to be able to perform *repeatability tests* (Desai et al., 2012; Liu et al., 2015a) on the multiple single epoch images of a particular BCG. In that process one calculates the scatter of the photometric measurements of the same objects and uses that to characterize the uncertainty. However, we do not have the required data products to carry out this test, and besides this test would likely not include uncertainties due to the extended halo of light surrounding them. So for this analysis we have scaled up the `MAG_AUTO` uncertainties of the BCG using the method in Barmby et al. (2008), which leads to the typical uncertainty of the BCG at the level of $\approx 9\%$. Given that the BCG typically contributes $\approx 10-40\%$ of the total luminosity of the XMM-BCS clusters, this implies that the photometric

uncertainty of the BCG is at the level $\approx 1-4\%$ of the total luminosity and therefore is not the dominant source of uncertainty in our analysis.

In the end, the stellar mass for each cluster is obtained by

$$\begin{aligned} M_{\star,\mathrm{sat}} &= \Gamma_\star \, L_{\star,\mathrm{sat}} \\ M_\star &= \Gamma_{\star,\mathrm{CSP}} \, L_{\star,\mathrm{BCG}} \, + \Gamma_\star \, L_{\star,\mathrm{sat}} \, , \end{aligned} \tag{3.7}$$

where $M_\star$ is the total stellar mass of the cluster, $M_{\star,\mathrm{sat}}$ is the total stellar mass of the satellite galaxies and $\Gamma_\star$ is the synthetic mass-to-light ratio in [3.6] derived in Section 3.4.2. We use the mass-to-light ratio estimated from the CSP model $\Gamma_{\star,\mathrm{CSP}}$ for the BCG, given the evidence that the BCG can typically be well described by a passively evolving model out to redshift ≈ 1.5 (Lidman et al., 2012; Wylezalek et al., 2014).

3.4.4 Stellar Mass to Halo Mass Scaling Relations

The scaling relation of the stellar mass-halo mass is defined as:

$$M_\star = A_\star \left(\frac{M_{500}}{M_{\mathrm{piv}}} \right)^{B_\star} \left(\frac{1+z}{1+z_{\mathrm{piv}}} \right)^{C_\star} , \tag{3.8}$$

with the intrinsic, log-normal scatter $D_\star \equiv \sigma_{\ln M_\star | M_{500}}$ of the observed $M_\star$ for a given cluster mass M_{500}. The normalization, the mass power index and the redshift power law index of the scaling relations are denoted by $A_\star$, $B_\star$ and $C_\star$, respectively. The M_{piv} and z_{piv} are fixed to the median values of the cluster sample: $M_{\mathrm{piv}} \equiv 0.8 \times 10^{14} \mathrm{M}_\odot$ and $z_{\mathrm{piv}} \equiv 0.47$.

We use the same likelihood as in L15 to estimate the best-fit parameters $\mathbf{r}_\star \equiv (A_\star, \, B_\star, \, C_\star, \, D_\star)$ of equation (3.8). Namely, the scaling relation parameters $\mathbf{r}_\star$ are estimated by evaluating the likelihood

$$P(\mathbf{r}_\star) = \sum_i^{N_{\mathrm{cl}}} \frac{\int \mathrm{d}M_{500} \, P(M_{\star i}, L_{\mathrm{X}i} | M_{500}, z_i, \mathbf{r}_\star, \mathbf{r}_{\mathrm{X}}) n(M_{500}, z_i)}{\int \mathrm{d}M_{500} \, P(L_{\mathrm{X}i} | M_{500}, z_i, \mathbf{r}_{\mathrm{X}}) n(M_{500}, z_i)} , \tag{3.9}$$

where N_{cl} is the total number of XMM-BCS clusters, $M_{\star i}$ and $L_{\mathrm{X}i}$ indicate respectively the stellar mass and the X-ray luminosity of the cluster i at redshift z_i, and $\mathbf{r}_{\mathrm{X}}$ denotes the parameters of the L_{X}-M_{500} scaling relation (equation (3.1)) in the same form as for $\mathbf{r}_\star$. The probability of observing the cluster i with $L_{\mathrm{X}i}$, given the mass M_{500}, redshift z and the scaling relation $\mathbf{r}_{\mathrm{X}}$ is $P(L_{\mathrm{X}i} | M_{500}, z_i, \mathbf{r}_{\mathrm{X}})$, and the probability of observing the cluster i with $M_{\star i}$ and $L_{\mathrm{X}i}$ given the mass M_{500} and the scaling relations $\mathbf{r}_\star$ and $\mathbf{r}_{\mathrm{X}}$ is denoted as $P(M_{\star i}, L_{\mathrm{X}i} | M_{500}, z_i, \mathbf{r}_\star, \mathbf{r}_{\mathrm{X}})$. The probabilities in both the numerator and the denominator are weighted by the mass function $n(M_{500}, z_i)$, derived using the Tinker et al. (2008) mass function at cluster redshift z_i within the cosmology framework used in this analysis.

The full derivation of the likelihood is provided in L15, to which we refer the readers. There it is shown that the selection of the sample (in this case the clusters were selected using their X-ray flux) does not impact the derivation of an unbiased scaling relation $\mathbf{r}_\star$.

In L15 it was only possible to constrain the normalization and mass trend of the SZE signal-to-noise mass relation, because of the weak SZE signatures of these low mass systems. In

Table 3.1: The measurements of XMM-BCS clusters. Column 1: the unique ID of the XMM-BCS clusters. Column 2: the cluster redshift. Column 3: the stellar mass estimate of the cluster in units of $10^{12}M_{\odot}$. Column 4: the normalization ϕ_0 of the best-fit LF in units of ${L_{\odot}}^{-1}$. Column 5: the p-value of consistency between the LF model and the data. Column 6: the measured blue fraction $f_{\rm blue}$.

ID	Redshift	$M_{\star}$ $[10^{12}M_{\odot}]$	ϕ_0 $[{L_{\odot}}^{-1}]$	p-value	$f_{\rm blue}$
11	0.970	0.65 ± 0.40	5.83 ± 6.22	0.181	0.241 ± 0.338
18	0.390	2.57 ± 0.50	33.5 ± 8.16	0.368	0.104 ± 0.082
32	0.830	3.48 ± 0.64	40.6 ± 9.83	0.189	0.030 ± 0.077
33	0.790	3.43 ± 0.54	30.5 ± 8.34	0.505	0.009 ± 0.036
34	0.280	2.15 ± 0.41	30.0 ± 6.87	0.805	0.289 ± 0.162
35	0.670	2.33 ± 0.49	29.5 ± 7.90	0.392	0.253 ± 0.199
38	0.390	1.05 ± 0.33	13.4 ± 5.66	0.752	0.223 ± 0.298
39	0.180	0.80 ± 0.24	6.20 ± 3.90	0.983	0.575 ± 0.230
44	0.440	7.81 ± 0.82	$111. \pm 12.8$	0.019	0.287 ± 0.052
69	0.750	2.64 ± 0.48	31.7 ± 7.73	0.057	0.125 ± 0.241
70	0.152	2.67 ± 0.48	37.7 ± 7.69	0.056	0.563 ± 0.233
81	0.850	1.56 ± 0.47	17.1 ± 7.72	0.154	0.248 ± 0.336
82	0.630	2.94 ± 0.54	39.5 ± 8.84	0.336	0.190 ± 0.124
88	0.430	2.44 ± 0.55	32.4 ± 8.82	0.135	0.076 ± 0.097
90	0.580	1.99 ± 0.41	23.5 ± 6.87	0.182	0.131 ± 0.172
94	0.269	0.59 ± 0.28	4.65 ± 4.72	0.451	0.225 ± 0.341
109	1.020	2.98 ± 0.55	36.4 ± 8.73	0.587	0.227 ± 0.231
110	0.470	3.03 ± 0.48	28.3 ± 7.55	0.073	0.496 ± 0.094
126	0.420	1.99 ± 0.46	24.0 ± 7.43	0.568	0.137 ± 0.070
127	0.207	0.81 ± 0.28	7.27 ± 4.86	0.057	0.443 ± 0.201
132	0.960	2.01 ± 0.56	25.1 ± 8.86	0.075	0.340 ± 0.253
136	0.360	3.15 ± 0.54	45.2 ± 8.65	0.469	0.160 ± 0.080
139	0.169	2.01 ± 0.34	29.9 ± 5.76	0.956	0.531 ± 0.123
150	0.176	2.36 ± 0.41	27.1 ± 6.65	0.148	0.090 ± 0.086
152	0.139	0.26 ± 0.14	0.0 ± 2.48	0.273	0.473 ± 0.341
156	0.670	1.30 ± 0.44	9.51 ± 6.96	0.316	0.083 ± 0.221
158	0.550	3.11 ± 0.54	40.7 ± 8.75	0.974	0.391 ± 0.110
210	0.830	1.44 ± 0.41	15.7 ± 6.89	0.137	0.026 ± 0.098
227	0.346	0.98 ± 0.34	6.79 ± 5.78	0.726	0.283 ± 0.311
245	0.620	1.71 ± 0.41	19.8 ± 6.77	0.255	0.663 ± 0.159
275	0.290	0.65 ± 0.30	8.36 ± 5.06	0.852	0.230 ± 0.153
287	0.570	1.65 ± 0.40	21.8 ± 6.73	0.001	0.000 ± 0.000
288	0.600	2.69 ± 0.50	29.1 ± 8.04	0.484	0.529 ± 0.109
357	0.480	3.21 ± 0.53	38.3 ± 8.48	0.463	0.277 ± 0.170
386	0.530	2.83 ± 0.45	39.8 ± 7.71	0.051	0.317 ± 0.136
430	0.206	0.83 ± 0.22	4.24 ± 3.79	0.627	0.543 ± 0.297
444	0.710	2.13 ± 0.45	27.9 ± 7.36	0.556	0.175 ± 0.286
457	0.100	1.05 ± 0.26	16.5 ± 5.04	0.000	0.471 ± 0.321
476	0.101	1.78 ± 0.31	25.2 ± 5.29	0.105	0.347 ± 0.151
502	0.550	1.88 ± 0.46	25.8 ± 7.55	0.035	0.698 ± 0.208
511	0.269	2.91 ± 0.45	42.2 ± 7.48	0.236	0.482 ± 0.115
527	0.790	2.60 ± 0.52	27.1 ± 8.28	0.316	0.107 ± 0.214
528	0.350	0.96 ± 0.28	11.3 ± 5.07	0.382	0.160 ± 0.156
538	0.200	0.91 ± 0.29	13.2 ± 5.13	0.073	0.196 ± 0.230
543	0.570	1.79 ± 0.51	21.3 ± 8.16	0.591	0.228 ± 0.161
547	0.241	0.97 ± 0.28	10.9 ± 5.06	0.198	0.326 ± 0.229

Table 3.2: Stellar mass to halo mass scaling relation parameter constraints and priors. The columns contain the normalization in units of $10^{12}\mathrm{M}_{\odot}$, the mass and redshift power law indices and the intrinsic, log-normal scatter in the observable at fixed mass.

	$A_{\star}[10^{12}\mathrm{M}_{\odot}]$	$B_{\star}$	$C_{\star}$	$D_{\star}$
priors	$[0.1,\ 50]$	$[-3,\ 3]$	$[-6.5,\ 6.5]$	$[0,\ 1.5]$
$M_{\star}$	$1.87^{+0.13}_{-0.12}$	$0.69^{+0.15}_{-0.15}$	$-0.04^{+0.48}_{-0.48}$	$0.36^{+0.07}_{-0.06}$
$M_{\star,\mathrm{sat}}$	$1.37^{+0.11}_{-0.11}$	$0.80^{+0.18}_{-0.18}$	$-0.26^{+0.58}_{-0.58}$	$0.43^{+0.08}_{-0.07}$

the current analysis the relatively higher signal to noise measurements of the stellar mass for XMM-BCS clusters allow us to constrain all four of the parameters of the scaling relation $\mathbf{r}_{\star}$ by maximizing the likelihood of equation (3.9). The parameter space is explored by using `emcee` (Foreman-Mackey et al., 2013), the Python package to search for the maximum likelihood using the Affine Invariant Markov Chain Monte Carlo (MCMC) algorithm. The cosmology parameters and the redshifts of the clusters are fixed in the MCMC likelihood maximization. The measurement uncertainty of L_{X} for each cluster and the intrinsic scatter of the scaling relation $\mathbf{r}_{\mathrm{X}}$ (equation (3.1)), which is assumed to be uncorrelated with the intrinsic scatter of the scaling relation $\mathbf{r}_{\star}$ (equation (3.8)), are taken into account in deriving the stellar mass scaling relation $\mathbf{r}_{\star}$. We study both the total stellar mass to mass scaling relation $M_{\star}(M_{500},z)$ and the equivalent scaling relation when excluding the BCG mass $M_{\star,\mathrm{sat}}(M_{500},z)$. We apply uniform priors as shown in Table 3.2. The widths of these priors are chosen to be larger than the recovered probability distributions.

3.5 Results

We present the estimated stellar masses of 46 XMM-BCS clusters in Table 3.1. In addition to the stellar mass estimates, Table 3.1 contains the cluster ID and redshift, the LF normalization ϕ_0, the p-value that the model LF and observations are drawn from the same parent distribution and the measured blue fraction f_{blue}.

We find that the LF provides a good description for the data for most of the clusters. The observed LFs and the best-fit models of 46 XMM-BCS clusters are shown in Figure 3.7 and Figure 3.8. However, we find two clusters with p-values that indicate inconsistency between model and data at the $\approx 3\sigma$ level. The two outliers are XMM-BCS287 at $z = 0.57 \pm 0.04$ and XMM-BCS457 with a spectroscopic redshift $z = 0.1$. There are five very bright stars in the center of XMM-BCS287 contaminating the photometry of the cluster galaxies and causing the poor fit in the LF. On the other hand, only 7 galaxies brighter than $m_{\star,[3.6]} + 1.5$ are detected within the cluster R_{500} in XMM-BCS457, explaining the high C_{stat} values and low p-values in the fit. We include both of these systems while deriving the scaling relation. In addition, we fail to detect the cluster galaxy population for XMM-BCS152 at $z = 0.139$; there are only two galaxies brighter than $m_{\star,[3.6]} + 1.5$ (before statistical background subtraction) that lie projected within the cluster R_{500} and (corresponding to $[3.6] \approx 18$ mag), this results in $L_{\star,\mathrm{sat}} = 0\ \mathrm{L}_{\odot}$ in the LF

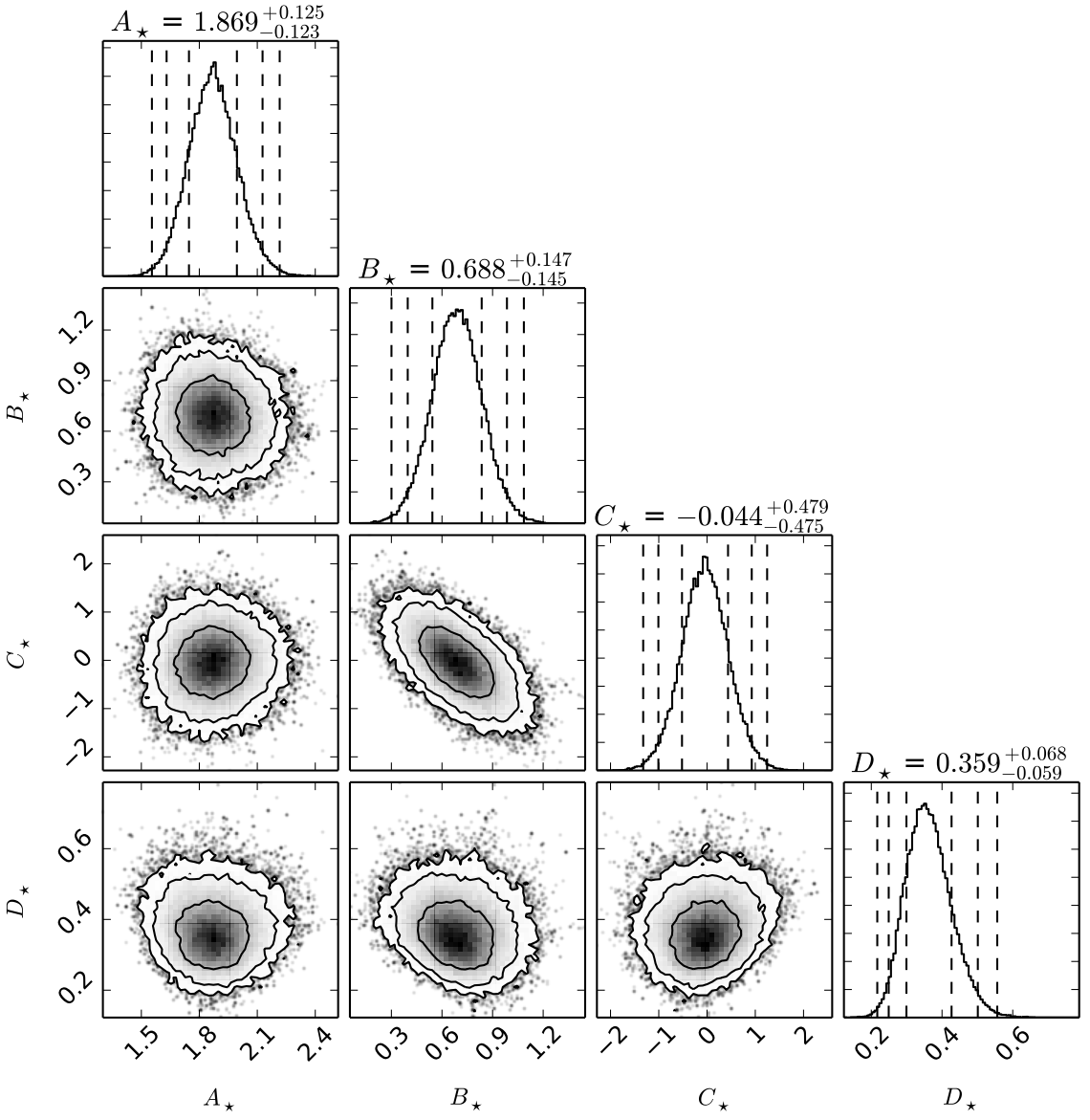

Figure 3.5: Scaling relation parameter $\mathbf{r}_\star$ constraints for $M_\star(M_{500}, z)$. The parameters are the normalization $A_\star$, power law index in mass $B_\star$, power law index in redshift $C_\star$ and the intrinsic log-normal scatter $D_\star$. Both joint and fully marginalized constraints are shown. The numerical values of the best-fit parameters and 1σ uncertainties are quoted at the top of each column, and the off-diagonal plots show joint constraints with 1σ, 2σ and 3σ confidence contours.

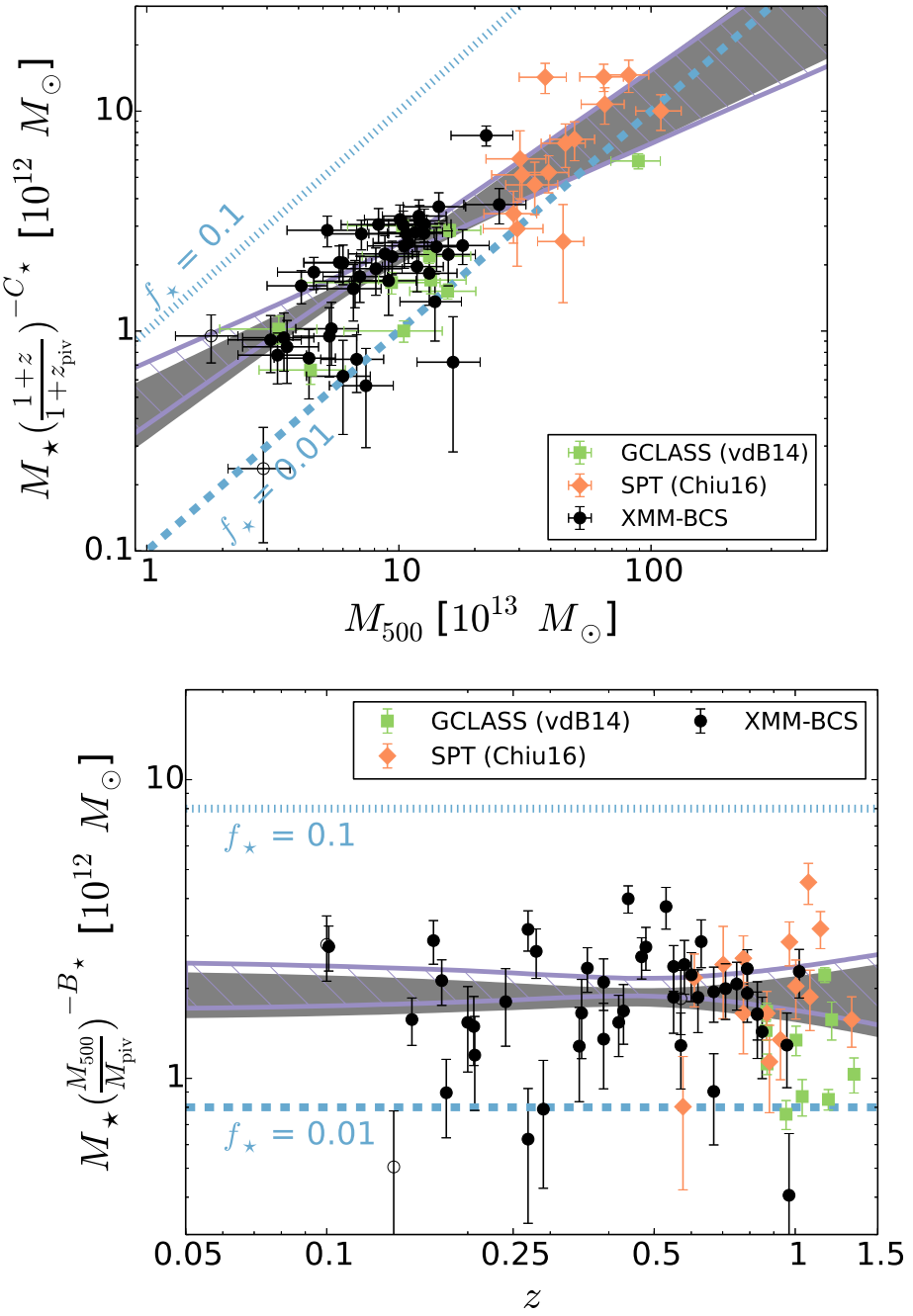

Figure 3.6: The $M_\star$ of XMM-BCS clusters (black) and the comparison samples from SPT (red) and GCLASS (green) along with the best-fit scaling relation obtained in this work. On the left, the total stellar masses corrected to the characteristic redshift $z_{\rm piv} = 0.47$ with the best fit redshift evolution are plotted as a function of cluster mass M_{500}. On the right, the total stellar masses corrected to the pivot mass $M_{\rm piv} = 8 \times 10^{13} M_\odot$ using the best fit mass trend are plotted as a function of cluster redshift. Three problematic clusters (XMM-BCS152, XMM-BCS287 and XMM-BCS457) are shown with open circles. The 1σ confidence region (see Table 3.2) of the best fit scaling relation is shaded. The 1σ confidence region of the best-fit relation assuming $\Gamma_\star = \Gamma_{\star,\rm CSP}$ (see the text in Section 3.6.3) is enclosed by the thick purple lines. For reference, the stellar mass fractions of 0.1 and 0.01 are shown using dotted and dashed lines, respectively. The SPT and GCLASS samples have been corrected for estimated binding mass systematic offsets with respect to the XMM-BCS sample as described in the text.

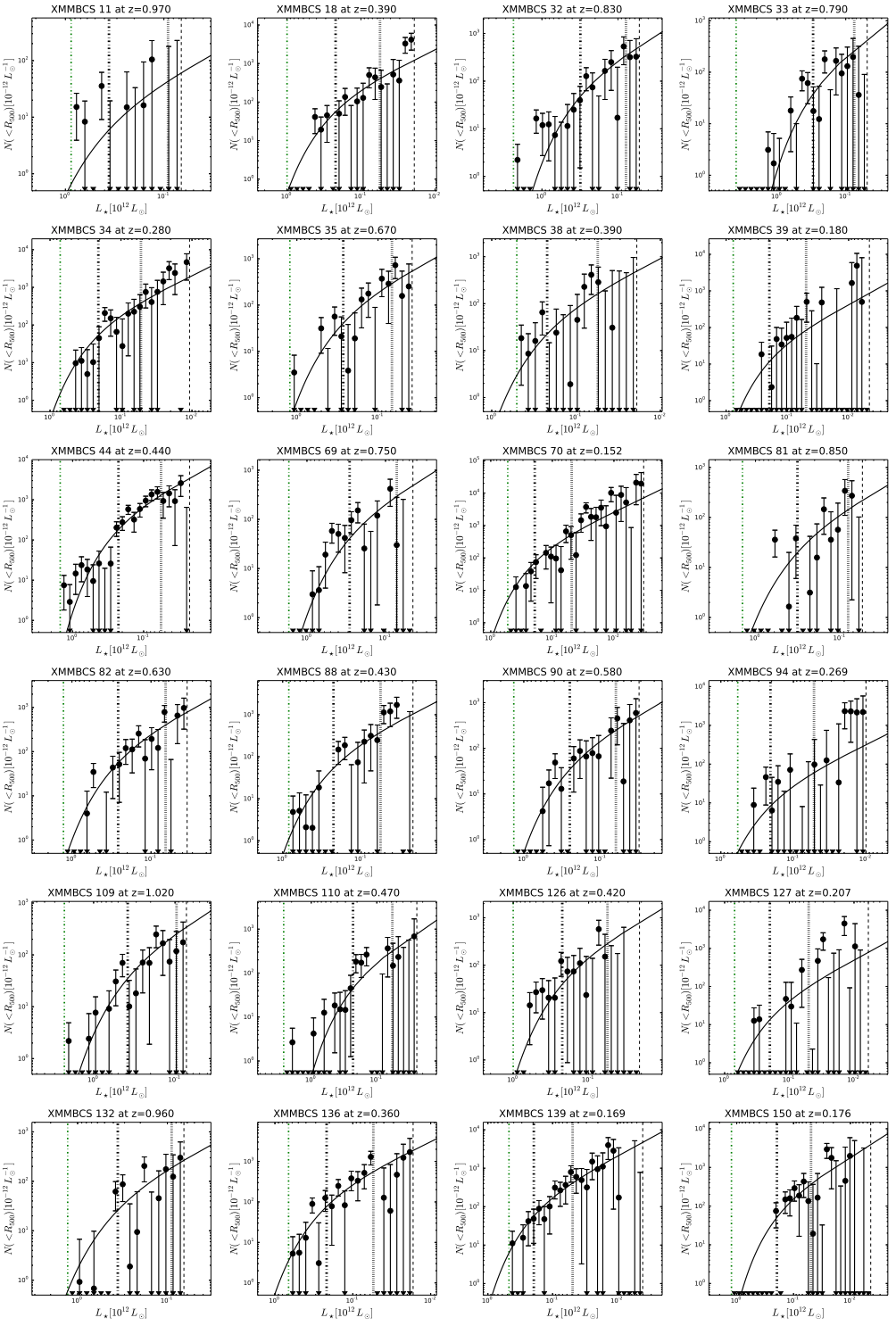

Figure 3.7: The observed LF (points with error bars) and the best-fit model (solid line) for the XMM-BCS clusters. The unique ID and cluster redshift are listed in the title of each plot. The LFs are presented in units of solar luminosity in the rest-frame at the cluster redshift. The green dot-dashed line shows the luminosity of the BCG. The black dot-dashed (dotted) line indicates the luminosity corresponding to the characteristic magnitude $m_\star$ ($m_\star + 1.5$) predicted by our CSP model, while the black dashed line is the luminosity corresponding to the 50% completeness limit in the SSDF survey.

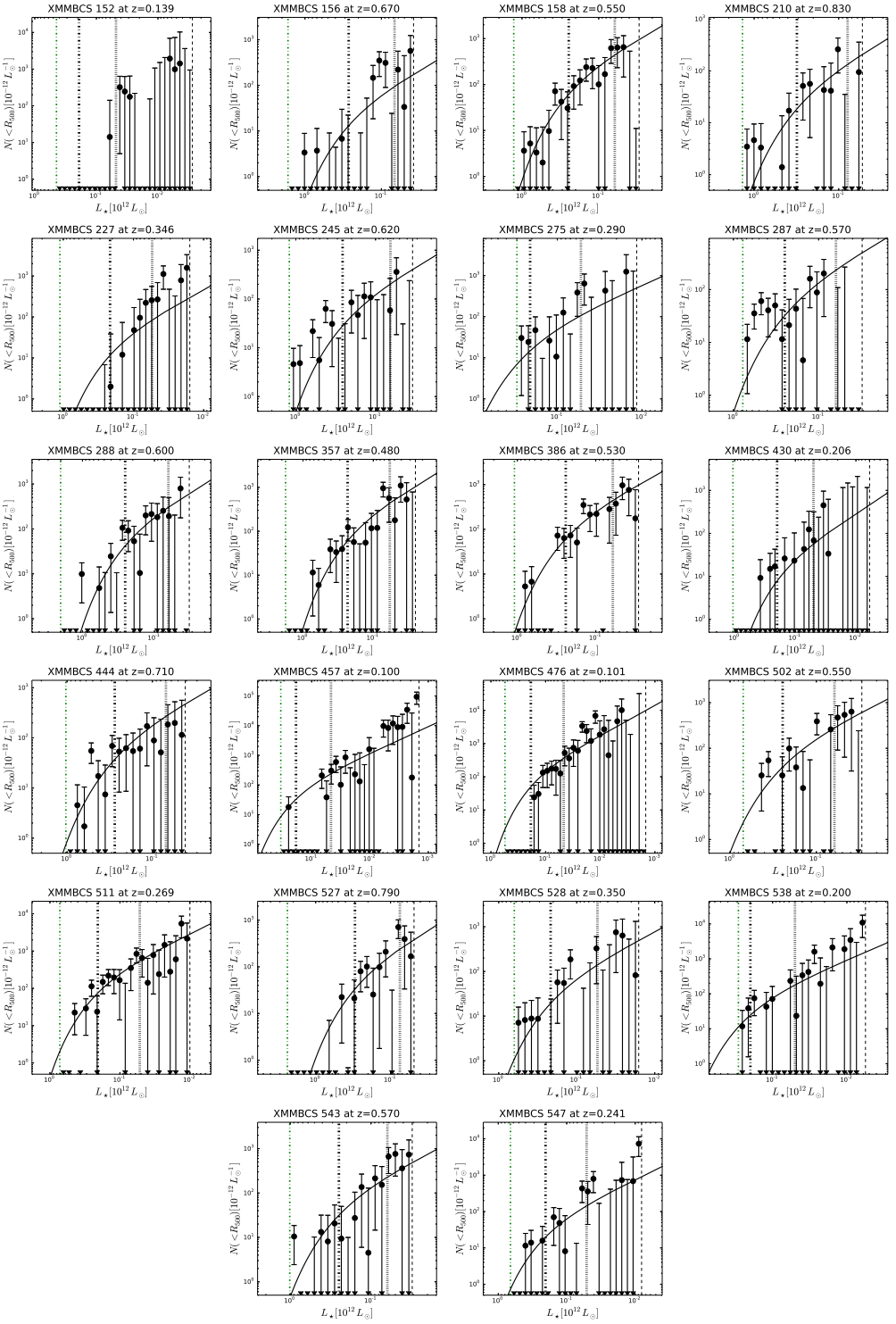

Figure 3.8: See caption in Figure 3.7.

fitting. Nevertheless, we also include XMM-BCS152 in deriving the scaling relation parameters because its BCG is clearly detected although the $L_{\star,\rm sat}$ is statistically consistent with zero. We discuss the systematics caused by these three clusters in Section 3.6.1.

The best-fit parameters of the resulting scaling relations– both total stellar mass $M_\star$ and satellite galaxy stellar mass $M_{\star,\rm sat}$ versus binding mass M_{500}– are presented in Table 3.2. Neither scaling relation shows statistically significant redshift evolution, a point we will discuss more below. The fully marginalized and joint parameter constraints for the total stellar mass $M_\star$–M_{500} relation are shown in Figure 3.5. There is a noticeable covariance between the mass power law index $B_\star$ and the redshift power law index $C_\star$, which is presumably driven by the characteristics of our flux limited sample that leads to the lowest mass systems being found only at low redshift.

We show the observed $M_\star$ and its best-fit scaling relation as a function of cluster mass and redshift in Figure 3.6. The observed $M_\star$ for each cluster is corrected to the pivot redshift ($z_{\rm piv} = 0.47$; left panel) and the pivot mass ($M_{\rm piv} = 8\times10^{13}M\odot$; right panel) using the best-fit scaling relation $M_\star = M_\star(M_{500}, z)$.

The $M_\star$ inside cluster R_{500} increases with cluster masses ($M_\star \propto {M_{500}}^{0.69}$) and no significant redshift trend is observed. The $C_\star$ is statistically consistent with zero, suggesting the stellar contents inside the cluster R_{500} sphere with respect to the halo mass of $M_{\rm piv} = 8\times10^{13}{\rm M}_\odot$ is not evolving out to $z\approx1$. The intrinsic log-normal scatter of $M_\star = M_\star(M_{500}, z)$ is $\sigma_{\ln M_\star|M_{500}} = 0.36$, corresponding to $e^{D_\star} - 1 \approx (43\pm10)\%$ scatter in $M_\star$ at fixed halo mass. Together with the scaling relation power law index in mass, this implies a binding mass scatter for a given $M_\star$ of $\Delta\ln M_{500}|M_\star = D_\star/B_\star \approx (0.52\pm0.09)$, corresponding to $e^{D_\star/B_\star} - 1 \approx (68\pm16)\%$.

The scaling relation where the BCG stellar mass is excluded is similar except with a lower $A_\star$ and a larger $D_\star$ than the values inferred from including the BCG. The amplitude of the total stellar mass scaling relation is $\approx 36\%$ higher than the relation that only includes the light from the satellite galaxies, indicating that the BCG characteristically contains $\approx 27\%$ of the stellar mass in this sample of low mass clusters and groups.

To actually use $M_\star$ as a mass indicator one would typically have only a cluster redshift and no knowledge of the virial radius R_{500}. Thus, we examine also the $M_\star$–M_{500} scaling relation when the $M_\star$ is extracted within a fixed metric radius of 0.5 Mpc. The analysis yields the parameters $(A_\star/10^{12}{\rm M}_\odot, B_\star, C_\star, D_\star)$

$$(1.77^{+0.11}_{-0.11}, 0.50^{+0.13}_{-0.13}, 0.15^{+0.43}_{-0.43}, 0.33^{+0.06}_{-0.05}),$$

which indicates an M_{500} scatter of $e^{D_\star/B_\star} - 1 \approx (93\pm11)$ % at fixed $M_\star$(0.5 Mpc, z).

We compare XMM-BCS results with two other high-z cluster samples from the literature. The first one is the Gemini CLuster Astrophysics Spectroscopic Survey (GCLASS; van der Burg et al., 2014, hereafter vdB14) sample for which they studied the 10 low mass clusters or groups selected from a NIR survey at redshift between 0.86 and 1.34, while the second one is the SPT-selected sample (Chiu et al., 2016b, hereafter Chiu16) consisting of 14 massive clusters with $M_{500} \gtrsim 3\times10^{14}{\rm M}_\odot$ at redshift between 0.56 and 1.32.

As demonstrated in Chiu16, the systematics, such as the different mass calibrators (velocity dispersion σ_V or X-ray luminosity $L_{\rm X}$) or the different initial mass functions, could lead to spurious mass or redshift trends if no homogenization is applied to the different samples. For

example, the M_{500} inferred from the X-ray mass proxies (e.g., L_X) and velocity dispersion σ_v could be underestimated by $\approx 44\%$ and $\approx 23\%$, respectively, as compared to the SZE-inferred masses including the CMB cosmological constraint (Bocquet et al., 2015b).

We therefore homogenize the vdB14 and Chiu16 samples before the comparison by bringing all three mass scales to the mass scale of the XMM-BCS sample, whose masses are determined from the X-ray L_X calibrated using X-ray hydrostatic masses. Specifically, the M_{500} of vdB14 and Chiu16 samples are multiplied by $1.23/1.44$ and $1/1.44$ to reach the mass floor inferred by the X-ray mass proxy (L_X) used in this work. Following the same procedure in Chiu16, we multiply the BCG-excluded stellar masses by the factors 0.95 and 0.88 in the vdB14 and Chiu16 samples, respectively, which corrects for the change in $M_\star$ caused by the reduction in R_{500} that comes from the lower M_{500}. The same initial mass function Chabrier (2003) has been used in all three studies.

The comparison is shown in Figure 3.6. The XMM-BCS clusters are in good agreement with the GCLASS and the SPT samples, with the GCLASS and the SPT clusters serving as extensions of the high redshift and high mass ends of the XMM-BCS sample. The scaling relation $M_\star(M_{500},z)$ of XMM-BCS results in a mass trend $B_\star = 0.69 \pm 0.15$ which is statistically consistent with the GCLASS ($B_\star = 0.62 \pm 0.12$) and SPT ($B_\star = 0.63 \pm 0.09$) clusters. Interestingly, our measured mass trend is also in good agreement with results extracted from cluster and group samples in different redshift ranges and using a variety of techniques (Lin et al., 2003; Giodini et al., 2009; Lin et al., 2012; Ziparo et al., 2015). The consistent values of $B_\star$ affirm that a similar relationship between the stellar and halo masses exists for all systems above the mass scale $M_{500} \approx 2 \times 10^{13} \mathrm{M}_\odot$.

The redshift trends of the SPT ($M_\star \propto (1+z)^{0.26\pm0.18}$) and XMM-BCS ($M_\star \propto (1+z)^{-0.04\pm0.47}$) samples are both statistically consistent with zero, suggesting that the stellar masses of galaxies within R_{500} do not evolve out to redshift $z \approx 1.35$ over the full mass range of groups and clusters. This result is in excellent agreement with that from a sample of 94 massive clusters at $0 \leq z \leq 0.6$ (Lin et al., 2012), and the same picture is also implied by studies of X-ray or optically selected groups, some of which extend to redshifts $z \approx 1.0-1.6$ (Giodini et al., 2009; Connelly et al., 2012; Leauthaud et al., 2012; Ziparo et al., 2013). Combining the GCLASS/SPT sample at $0.6 \lesssim z \lesssim 1.35$ and our XMM-BCS clusters extending to the low mass end between redshift ≈ 0.1 and ≈ 1, we conclude that the stellar masses inside the cluster R_{500} sphere are well established for halo masses $M_{500} \gtrsim 2 \times 10^{13} \mathrm{M}_\odot$ since $z \approx 1.35$.

3.6 Systematics

We discuss the potential systematics due to the problematic clusters, the LF fitting, the mass-to-light ratio $\Gamma_\star$, the blending in the *Spitzer* imaging and the mass estimates below.

3.6.1 The problematic clusters

We find that the LF modeling of two clusters (XMM-BCS287 and XMM-BCS457) shows inconsistency between the model and observed data at the $\approx 3\sigma$ level; in addition, we do not detect

the non-BCG galaxy population for XMM-BCS152. To quantify the systematics caused by these problematic clusters, we repeat the whole likelihood maximization excluding these clusters and compare the scaling relation parameters. The parameters $(A_\star/10^{12}\mathrm{M}_\odot, B_\star, C_\star, D_\star)$ for the scaling relation $M_\star = M_\star(M_{500}, z)$ excluding these clusters are

$$(1.89^{+0.13}_{-0.12}, 0.67^{+0.15}_{-0.15}, -0.12^{+0.46}_{-0.46}, 0.34^{+0.07}_{-0.06}),$$

which are statistically consistent with the values including these clusters (see Table 3.2). Therefore, our result is not biased by these clusters.

3.6.2 The LF fitting

To quantify the systematics raised from the LF fitting, we estimate the stellar masses of all XMM-BCS clusters by fixing $m_{\star,\,\mathrm{stacked}}$ and α to the values, which are shifted by 1σ from the best-fit values determined by fitting to the full stacked sample, and repeat the whole analysis to obtain the resulting scaling relation parameters. Specifically, we use the two extreme cases, the 1σ shift from the best-fit values of $m_{\star,\,\mathrm{stacked}}$ and α (the black circle in the right panel of Figure 3.3) toward the upper right ($1\sigma_{\mathrm{right}}$) and lower left ($1\sigma_{\mathrm{left}}$) along the direction of the parameter degeneracy. Accordingly, the $1\sigma_{\mathrm{left}}$ ($1\sigma_{\mathrm{right}}$) shift implies that the characteristic magnitude $m_\star$ predicted by our CSP model is fainter by ≈ -0.51 mag (brighter by ≈ 0.37 mag) and $\alpha = -1.25$ ($\alpha = -0.43$). The resulting parameters $(A_\star/10^{12}\mathrm{M}_\odot, B_\star, C_\star, D_\star)$ for scaling relation $M_\star = M_\star(M_{500}, z)$ are

$$(1.80^{+0.13}_{-0.12}, 0.72^{+0.15}_{-0.15}, 0.23^{+0.48}_{-0.49}, 0.36^{+0.07}_{-0.06}),$$

and

$$(1.98^{+0.13}_{-0.13}, 0.65^{+0.15}_{-0.15}, -0.16^{+0.47}_{-0.47}, 0.36^{+0.06}_{-0.06})$$

for $1\sigma_{\mathrm{left}}$ and $1\sigma_{\mathrm{right}}$ shift, respectively. The resulting parameters of the scaling relations are all statistically consistent (within 1σ) with the values obtained using $m_{\star,\,\mathrm{stacked}} = 0$ and $\alpha = -0.89$ as in Table 3.2; therefore we conclude that the systematics associated with adopting the best fit LF parameters from the cluster stack when fitting the LF in individual clusters are not dominant.

3.6.3 The mass-to-light ratio $\Gamma_\star$

The mass-to-light ratio $\Gamma_{\star,\mathrm{blue}}$ of the blue population is estimated assuming the synthetic galaxy population with the star formation history ($\tau = 10$ Gyr) and one solar metallicity at formation redshift $z_\mathrm{f} = 3$. Using $\Gamma_{\star,\mathrm{blue}}$ derived from $\tau = 5$ Gyr raises the stellar mass estimates by 1.3%, 2.1% and 2.5% for the cases of $f_{\mathrm{blue}} = 0.2$, $f_{\mathrm{blue}} = 0.3$ and $f_{\mathrm{blue}} = 0.4$, respectively. Using $\Gamma_{\star,\mathrm{blue}}$ derived from $\tau = 15$ Gyr lowers the stellar mass estimations by 0.4%, 0.7% and 1.2% for the cases of $f_{\mathrm{blue}} = 0.2$, $f_{\mathrm{blue}} = 0.3$ and $f_{\mathrm{blue}} = 0.4$, respectively. Changing the metallicity or increasing the formation redshift to $z_\mathrm{f} = 5$ in deriving $\Gamma_{\star,\mathrm{blue}}$ has only negligible impact on the $\Gamma_{\star,\mathrm{blue}}$ derived from $\tau = 10$ Gyr and $z_\mathrm{f} = 3$ model. That is, the systematic uncertainty raised from the blue population is dominated by the large scatter of the estimated f_{blue} rather than the assumed $\Gamma_{\star,\mathrm{blue}}$.

If we re-run the likelihood maximization using $\Gamma_\star = \Gamma_{\star,\mathrm{CSP}}$ for all cluster galaxies, the resulting parameters $(A_\star/10^{12}\mathrm{M}_\odot, B_\star, C_\star, D_\star)$ of the scaling relation $M_\star = M_\star(M_{500}, z)$ are

$$(2.03^{+0.14}_{-0.13}, 0.65^{+0.15}_{-0.15}, -0.04^{+0.48}_{-0.48}, 0.37^{+0.07}_{-0.06}).$$

This result is effectively assuming there is no blue galaxy population in our sample and thus represents an upper limit to the $M_\star$ estimation for each system. We show the best-fit model assuming $\Gamma_\star = \Gamma_{\star,\mathrm{CSP}}$ as the purple region in Figure 3.6. As seen in Figure 3.6, including the f_{blue} correction causes a steeper $B_\star$ at the $\approx 0.2\sigma$ level and has no significant effect on the redshift trends. However, assuming $\Gamma_\star = \Gamma_{\star,\mathrm{CSP}}$ leads to an $M_\star$ estimate, which is biased high by $\approx 8.5\%$, which is equivalent to a $\approx 0.86\sigma$ shift, for a cluster of mass $M_{500} = 0.8 \times 10^{14}\mathrm{M}_\odot$ at $z = 0.47$. Our best-fit f_{blue} model of XMM-BCS clusters suggests that the $f_{\mathrm{blue}} \approx 18 \pm 10\%$ for a cluster with $T_{\mathrm{X}} = 3$ keV at $z = 1$, while the mean of the f_{blue} estimates for the entire XMM-BCS sample is $\approx (31 \pm 4)\%$.

3.6.4 Blending

For the [3.6] band used in this work, the FWHM is $\approx 1.8''$, making it challenging to deblend the fluxes from the multiple neighboring objects without introducing external information on the source distribution. However, the blending among cluster galaxies does not affect the total luminosity estimated in this work, because integrating the best-fit LF is equivalent to estimating the excess light of the cluster galaxy population. Blending of cluster and non-cluster galaxies, on the other hand could bias the cluster light, and this would be most likely in denser cluster core around the BCG.

We quantify the systematic effects of BCG blending with non-cluster galaxies as follows. We first calculate the probability $P_{\mathrm{blend}}(m)$ of BCG blending with the fore/background galaxies with magnitude m. Specifically, the $P_{\mathrm{blend}}(m)$ is derived by re-normalizing the background magnitude distribution of the background aperture (i.e, R_{500}) to the angular area of the BCG. The angular area of the BCG is approximated by the aperture with the radius of $2 \times$ `FLUX_RADIUS`, which is a parameter derived by `SExtractor`. Assuming a Poisson distribution for $P_{\mathrm{blend}}(m)$ for a given magnitude m, we find by sampling 1000 realizations that the probability of BCG blending with the fore- and background galaxies is $\approx 25 \pm 14\%$. Note that the majority of the non-cluster members blending with the BCG takes place in the fainter magnitude range because of the more abundant faint galaxy population.

Second, we estimate the total flux blending with the BCG from 1000 realizations where blending takes place. The resulting mean excess of the flux from the non-cluster members (i.e., the fore- and background) contributes on average an additional $\approx 11 \pm 6\%$ to the BCG flux if blending takes place. In the end, we calculate the expected excess flux due to blending by weighing the extra blended flux by the probability of the BCG being blended. As a result, we find that the expected excess of the blended flux from the fore- and background over the whole XMM-BCS sample results in a bias in the BCG flux at the level of $\approx 2.3 \pm 1.5\%$, which is well below the statistical uncertainties in our analysis. Moreover, the excess flux due to blending estimated from our 1000 realizations shows no trends in mass and redshift over the XMM-BCS

sample. If the flux of the BCG is catastrophically overestimated by a factor of two due to blending with the non-cluster galaxies, then the total stellar mass estimation $M_\star$ would be overestimated by $\approx 10\%$ for XMM-BCS sample. However, a factor of two overestimation of the BCG fluxes is a rare occurrence. Moreover, our calculation shows that this systematic would not introduce biases into the mass or redshift trends of the scaling relation.

3.6.5 Cluster Binding Masses

We further quantify systematics associated with the binding mass M_{500}, which is inferred from the X-ray luminosity. For XMM-BCS clusters, the uncertainty of M_{500} ($\approx 30\%$) results in an uncertainty of R_{500} at the level of $\approx 10\%$, and this radius is used to define the region from which the $M_\star$ is extracted. The resulting uncertainty in $M_\star$ is at the level of $\approx 8\%$ given the NFW distribution of the galaxies. Given that our measurement uncertainties for $M_\star$ are already larger than this, this additional scatter does not impact our analysis.

However, there are also systematic uncertainties in M_{500}. We quantify the systematics between the M_{500} estimates inferred from the mass proxies of the SZE-signatures and X-ray luminosities following the work of Bocquet et al. (2015a), where measurements of SZE-inferred cluster binding masses calibrated using X-ray data, velocity dispersions and a cosmological analysis with information from external probes were compared. In our baseline analysis we adopt the X-ray luminosity-mass relation as calibrated using X-ray hydrostatic masses (Pratt et al., 2009). If we instead adopt the SZE-inferred masses for our analysis, then the resulting M_{500} and $M_\star$ would be higher by 44% and 13.6%, respectively, following the procedure described in Section 3.5. Assuming this systematic offset of the mass proxies has no dependence on the cluster mass and redshift (i.e., it only affects the absolute scale of cluster mass), adopting the SZE-inferred mass would lead to the normalization $A_\star$ of the scaling relation dropping by $1 - 1.136/1.44^{B_\star} \approx 11.5\%$.

We also estimate the impact of adopting the weak lensing based luminosity-mass relation from a recent study of 70 clusters and groups at $0.1 \leq z \leq 0.83$ with masses ranging from $\approx 2 \times 10^{13} \mathrm{M}_\odot$ to $\approx 2 \times 10^{15} \mathrm{M}_\odot$ (Kettula et al., 2015). We first estimate the mass scale offset between the Kettula et al. (2015) and Pratt et al. (2009) luminosity-mass relations. Specifically, we derive the X-ray masses for the 70 cluster sample using the core-extracted L_X–M_{500} relation from Pratt et al. (2009) and then compare those X-ray derived masses to the lensing mass measurements. We find that the mean of the ratio of the lensing masses to the X-ray masses is 1.22 ± 0.10, and there is no significant mass dependence. Thus, the gravitational lensing measurements prefer masses that are $\approx 22\%$ higher than the X-ray masses. If we scale up our X-ray masses by 22%, then the resulting stellar masses would increase by 7.2% due to the increasing radius R_{500}. The 22% increment in M_{500} and 7.2% increment in $M_\star$ would lead to the normalization $A_\star$ of the scaling relation dropping by $1 - 1.072/1.22^{B_\star} \approx 6.5\%$.

3.7 Conclusions

We use IRAC [3.6] band photometry from the wide field SSDF survey (Ashby et al., 2013) together with blue fraction $f_{\rm blue}$ measurements relying on *griz* photometry from the BCS survey (Desai et al., 2012) to estimate the stellar masses of 46 X-ray selected low mass clusters and groups from the XMM-BCS survey (Šuhada et al., 2012). This sample has masses in the range $2\times10^{13}{\rm M}_\odot \lesssim M_{500} \lesssim 2.5\times10^{14}{\rm M}_\odot$ (median mass $8\times10^{13}{\rm M}_\odot$) and redshifts in the range $0.1 \leq z \leq 1.02$ (median redshift 0.47). The stellar masses of the full population and the BCG-excluded population are estimated for each cluster.

We employ a Bayesian likelihood developed in a previous analysis (Liu et al., 2015a) that leverages an existing X-ray luminosity mass relation (Pratt et al., 2009) to constrain the stellar mass-halo mass scaling relations for this sample. The form of the scaling relation is a power law in mass and redshift with log-normal intrinsic scatter. The normalization, the power law indices in mass and redshift, and the intrinsic scatter of the stellar mass at fixed halo mass are fully quantified in this work. The best-fit stellar mass-halo mass scaling relation is

$$\frac{M_\star}{10^{12}{\rm M}_\odot} = 1.87^{+0.13}_{-0.12}\left(\frac{M_{500}}{8\times10^{13}{\rm M}_\odot}\right)^{0.69\pm0.15}\left(\frac{1+z}{1.47}\right)^{-0.04\pm0.47},$$

with log-normal intrinsic scatter $\sigma_{\ln M_\star|M_{500}} = 0.36^{+0.07}_{-0.06}$.

The best-fit scaling relation of XMM-BCS clusters behaves as $M_\star \propto M_{500}^{0.69\pm0.15}$, indicating a strong mass dependence of the stellar mass fraction within R_{500}. The intrinsic log-normal scatter $D_\star = 0.36^{+0.07}_{-0.06}$ of $M_\star$ at a given cluster mass is comparable to the scatter in the X-ray luminosity-halo mass scaling relation ($D_{\rm X} = 0.38\pm0.06$). No significant redshift trend of stellar mass is seen; the best-fit scaling relation that describes the total stellar mass $M_\star$ evolves as $M_\star \propto (1+z)^{-0.04\pm0.47}$. Thus, our analysis provides no evidence for redshift evolution of the stellar mass fraction within R_{500} of low mass clusters and groups out to $z\approx1$.

We compare XMM-BCS clusters with the SPT massive clusters ($M_{500}\approx6\times10^{14}{\rm M}_\odot$; Chiu16) and GCLASS low mass clusters and groups ($M_{500}\approx1\times10^{14}{\rm M}_\odot$; vdB14) at redshift $0.6\lesssim z\lesssim1.3$. After correcting for the systematics of different mass calibrators, we find that there is good agreement among the XMM-BCS, GCLASS and SPT clusters. The mass trend $B_\star$ of XMM-BCS clusters is statistically consistent with the results of the GCLASS and the SPT samples. Together with the results of the GCLASS and the SPT samples extending to the high redshift and the high mass regimes, the XMM-BCS sample provides no evidence for a redshift trend in the stellar mass fraction of the galaxy populations in clusters with masses $M_{500}\gtrsim2\times10^{13}{\rm M}_\odot$ out to redshift $z\approx1.3$. Larger samples with uniform selection and mass estimation would allow for a more precise study of the redshift trend.

We investigate the systematic effects raised from (1) the clusters which have problematic LF fitting, (2) the LF modeling, (3) the blue population in clusters, (4) the blending in the imaging and (5) the cluster mass uncertainty. The systematics raised from the problematic clusters and the LF modeling are smaller than the statistical uncertainties. We find that the blending is more severe in the cluster core, but that the expected bias of the BCG flux due to blending with non-cluster members is at the level of $\lesssim2.5\%$, which is too small to be important in this work. We find

that the most important systematic effect is from the mass-to-light ratio $\Gamma_\star$, making it important to include blue fraction $f_{\rm blue}$ measurements to avoid biasing scaling relation parameters. We estimate the blue fraction $f_{\rm blue}$ using the BCS optical catalog and statistically apply the correction to the $M_\star$ estimations using the measured redshift and X-ray temperature of each system. The mean $f_{\rm blue}$ of the XMM-BCS sample is $31 \pm 4\%$ with a tendency for $f_{\rm blue}$ to be higher in the low mass systems. On the other hand, no significant redshift trend is seen for $f_{\rm blue}$ in the XMM-BCS sample. The absence of a redshift trend is really applicable only to the clusters and higher mass groups in our sample, because due to the X-ray flux limited selection, our sample has low mass groups only at low redshift. Assuming $f_{\rm blue} = 0$ has no statistically significant impact on the mass and redshift trends ($B_\star$ and $C_\star$); however, the normalization $A_\star$ is biased high by $\approx 8.5\%$ (corresponding to a $\approx 0.86\sigma$ shift) at a characteristic mass $M_{500} = 8 \times 10^{13} {\rm M}_\odot$ and redshift $z = 0.47$.

We also examine whether $M_\star$ could be a promising mass proxy. Based on this work we conclude that the stellar mass enclosed by the projected radius $r = 0.5$ Mpc provides a mass proxy with an intrinsic scatter of $\approx 93\%$ (1σ in mass) for the low mass clusters and groups out to redshift $z \approx 1$. This scatter is larger than the mass scatter one sees at fixed K-band luminosity in a group and cluster sample at $z \lesssim 0.05$ (Lin et al., 2004) and larger than the optical richness in a sample of massive, SZE selected clusters extending to $z \approx 0.8$ (Saro et al., 2015). While this scatter is high compared to some other mass proxies such as the X-ray $Y_{\rm X}$ (e.g. Kravtsov et al., 2006; Vikhlinin et al., 2009c; Arnaud et al., 2010), X-ray temperature (e.g. Arnaud et al., 2005), the ICM mass (e.g. Okabe et al., 2010) and the SZE signal to noise (e.g. Benson et al., 2013; Bocquet et al., 2015a), the stellar mass could still be useful as a mass proxy for low mass and high redshift systems where other proxies are typically in short supply.

Our work suggests that the stellar mass enclosed within R_{500} for clusters or groups of a particular binding mass M_{500} exhibits large scatter ($43\% \pm 10\%$, 1σ log-normal) but with a characteristic value that is approximately the same at any point in the last ≈ 9 Gyr of evolution. This is a remarkable result at first glance, given the sharp trend for decreasing stellar mass fraction with halo mass that exists over this same timespan. One is driven to ask how massive halos could exhibit different stellar mass fractions than their building blocks, which include the lower mass halos. However, as has been explored with structure formation simulations (McGee et al., 2009), massive clusters accrete material not only in the form of lower mass clusters and groups but also directly from the surrounding field. As discussed previously in Chiu16, one possible scenario is that as halos accrete and become more massive the material from lower mass halos with higher stellar mass fractions is roughly balanced by accretion of material from the field that tends to have lower stellar mass fraction (for $z \approx 1$ measurement see, e.g., van der Burg et al., 2013b). Within such a scenario, the large scatter in $M_\star$ for systems of similar binding mass M_{500} would reflect differences in assembly histories. Other processes such as the stripping of stellar material from infalling galaxies, which would remove those stars from our galaxy based stellar mass measurements, must also play some role (Lin & Mohr, 2004).

Our current analysis invites a more careful comparison to structure formation simulations that include galaxy formation. In addition, new studies are needed to enable a more precise characterization of the mass and the redshift trends in the cluster galaxy populations; these will require larger samples of clusters and groups that (1) have been uniformly selected over the full

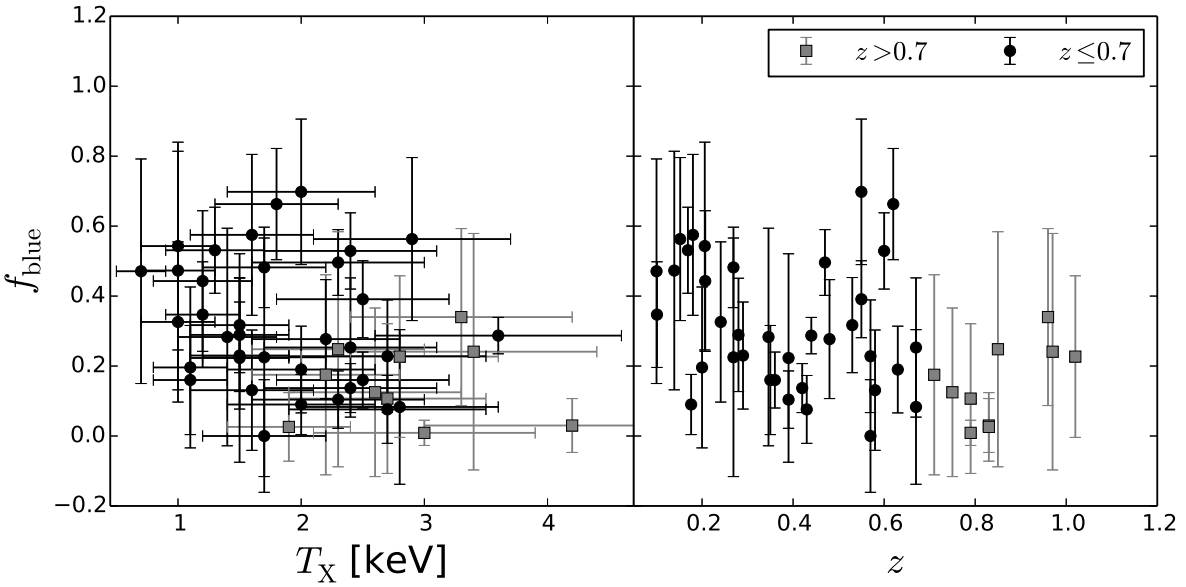

Figure 3.9: The blue fraction $f_{\rm blue}$ of XMM-BCS clusters as a function of cluster X-ray temperature $T_{\rm X}$ (left) and redshift z (right). The XMM-BCS clusters with $z \leq 0.7$ and $z > 0.7$ are shown with black circles and grey squares, respectively.

redshift range in a manner that does not rely on their galaxy population and (2) have low scatter mass proxies where the connection to halo mass is well understood over the full redshift range.

Acknowledgements

We express thanks to Drs. B. Hoyle, J. Song and M. Klein for discussions that led to improvements in this paper. We acknowledge the support by the DFG Cluster of Excellence "Origin and Structure of the Universe", the DLR award 50 OR 1205 that supported I. Chiu during his PhD project, and the Transregio program TR33 "The Dark Universe". This work is based in part on archival data obtained with the *Spitzer* Space Telescope, which is operated by the Jet Propulsion Laboratory, California Institute of Technology under a contract with NASA. This work is based on observations obtained with XMM-*Newton*, an ESA science mission with instruments and contributions directly funded by ESA Member States and the USA (NASA). This paper includes data gathered with the Blanco 4 m telescope, located at the Cerro Tololo Inter-American Observatory in Chile, which is part of the U.S. National Optical Astronomy Observatory, which is operated by the Association of Universities for Research in Astronomy (AURA), under contract with the NSF.

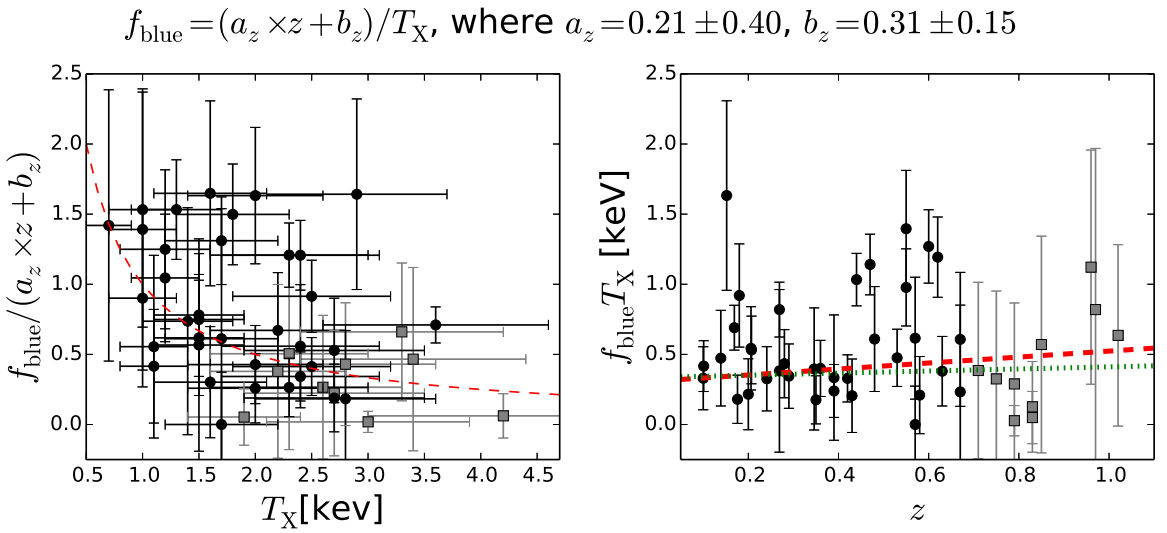

Figure 3.10: The blue fraction $f_{\rm blue}$ of XMM-BCS clusters after correcting for the best-fit mass and redshift trends as a function of X-ray temperature $T_{\rm X}$ after correcting for the best-fit redshift trend $a_z\times z+b_z$ (left) and as a function of redshift after correcting for the mass trend by with $T_{\rm X}$. The XMM-BCS clusters with $z\leq 0.7$ and $z>0.7$ are in the black circles and grey squares, respectively. The red dashed line indicates the best-fit $f_{\rm blue}(T_{\rm X},z)$ relation for the XMM-BCS cluster with $z\leq 0.7$, while the green dotted line is the best-fit model fitting to the full sample.

3.8 Appendix

3.8.1 Blue fractions

To enable a more accurate $\Gamma_\star$ for the galaxy populations we measure the $f_{\rm blue}$ of the XMM-BCS clusters using the BCS optical catalog (Desai et al., 2012). The BCS catalog contains the calibrated photometry of the optical bands *griz* and the derived photometric redshift estimates of the sources identified in the BCS survey. The resulting 10σ depths of the galaxies (point sources) in *griz* are 23.3 (23.9), 23.4 (24.0), 23.0 (23.6) and 21.3 (22.1) mag, respectively. The data reduction, the source extraction, the photometry calibration and the photometric properties are fully described elsewhere (Desai et al., 2012). We describe the estimation of the blue fraction $f_{\rm blue}$ here.

First we perform star/galaxy separation in *i* band by selecting the galaxies with `spread_model_i` $\geq 2\times10^{-3}$ and restrict the catalog to the central $6\,{\rm deg}^2$ region of XMM-BCS survey (see Section 3.4.3). The blank sky used for the statistical background subtraction is defined by the central $6\,{\rm deg}^2$ region of XMM-BCS survey excluding the cluster fields (see Section 3.4.3). Second, we estimate the completeness of the BCS survey by comparing the source count-magnitude relation between the BCS tiles and the COSMOS (Ilbert et al., 2009) survey in the same way conducted in Zenteno et al. (2011). Specifically, we fit a power law, which is assumed to be the complete source count-magnitude relation with the slope fixed to the value derived from COSMOS field, to the observed source count-magnitude in BCS survey in the magnitude range between 18 and 20.

The completeness function $f_{\rm com}(m)$ as a function of magnitude m is then obtained by fitting an error function to the ratio of the observed source counts to the complete source counts predicted by the best-fit power law. The completeness functions are separately derived for four bands *griz* in all BCS tiles overlapping the XMM-BCS survey because the depth variation is large among the tiles and the filters. As a result, we find that the median of the 50% (90%) completeness of the tiles overlapping the XMM-BCS central region is 23.97 (23.18), 23.41 (22.62), 22.76 (21.89) and 21.22 (19.83) mag for *griz*, respectively.

We estimate the blue fractions of the galaxy population projected within the R_{500} of 46 XMM-BCS clusters by separating the galaxies according to their colors. In the similar fashion of estimating the NIR luminosity function (Section 3.4.3), we remove the non-cluster members by statistically subtracting the background galaxy counts from the galaxy counts of the cluster field in the color-magnitude space. For simplicity, we denote the galaxy counts as the position in the color-magnitude space by CMC (color-magnitude-counts) hereafter. The color and the magnitude of the filter used in deriving the CMC are defined (in the rest frame) by the bands straddling the 4000Å and the band redder than 4000Å, respectively. Precisely, the color and the magnitude used in CMC are ($g-r$, r), ($r-i$, i) and ($i-z$, z) for the clusters with redshift $z_{\rm l} \leq 0.33$, $0.33 < z_{\rm l} \leq 0.70$ and $z_{\rm l} > 0.70$, respectively. The steps of 0.05 mag (0.25 mag) are used in binning in color (magnitude) to derive the CMC.

We also construct the completeness map in the observed color-magnitude space by propagating the completeness function of the bands used in the CMC. We discard the galaxies which lie outside the cluster redshift $z_{\rm l}$ at 3σ level if the reliable photometric redshift estimates are available, i.e. we discard the galaxies with $\|\texttt{z\_photo} - z_{\rm l}\| \geq 3 \times \delta_z \times (1+z_{\rm l})$ and $\texttt{z\_photo\_flag} = 1$, where $\delta_z = 0.061$ is the scatter of the photometric redshift performance in BCS survey. To estimate the color distribution of the selected galaxies in the cluster field we project all the galaxies, which lie projected within R_{500} and are brighter (fainter) than $m_\star + 1.5$ (the BCG), to the line perpendicular to the RS tilt predicted by the CSP model at cluster redshift $z_{\rm l}$. The characteristic magnitude $m_\star(z)$ is defined using the CSP model described in Section 3.3.1. Additionally, we take the completeness correction into account by inversely weighting the galaxy counts by the completeness as a function of position in the color-magnitude space.

On the other hand, we construct the mean background CMC (with the same magnitude cut) by extracting the mean value of the CMC of 200 apertures, which are randomly drawn from the blank sky with the same radii of cluster's R_{500}. The completeness correction of each randomly-drawn background aperture is taken into account when we construct the mean background CMC. We then project the resulting mean background CMC to the line perpendicular to the RS tilt of CSP model in the same way of the cluster field.

In the end, the projected color distribution of the cluster galaxy population along the RS tilt predicted by our CSP model is derived by statistically subtracting the projected CMC of the mean background from the cluster field. Similar to Zenteno et al. (2011), we define the blue and the RS populations by the galaxies with $\Delta C < 0.2$ mag and $-0.2 \leq \Delta C \leq 0.2$, respectively, where $\Delta C \equiv C_{\rm gal} - C_{\rm RS}$ is the difference of the projected colors between the galaxy ($C_{\rm gal}$) and the RS ($C_{\rm RS}$) predicted by the CSP model at cluster's redshift. The blue fraction $f_{\rm blue}$ is then calculated as the ratio of the number of the blue galaxies to the sum of the blue and RS galaxies. The uncertainty of the $f_{\rm blue}$ of each cluster is derived as the standard deviation of 10000 realizations,

where each realization is generated from the observed numbers of the blue and RS galaxies assuming Poisson distribution.

The estimated $f_{\rm blue}$ of 46 XMM-BCS clusters are presented in Table 3.1, and we show the estimated $f_{\rm blue}$ of 46 XMM-BCS clusters in Figure 3.9. The scatter of $f_{\rm blue}$ is large and the mean of $f_{\rm blue}$ is $(31 \pm 4)\%$ with the median 25%. Motivated by Urquhart et al. (2010), we extract the mass and redshift trends of the $f_{\rm blue}$ by fitting a parametrized function, which is a function of X-ray temperature $T_{\rm X}$ and cluster redshift, to the estimated $f_{\rm blue}$. We assume that the ensemble of $f_{\rm blue}$ increases linearly as the cluster redshift increases (the BO effect), which is parametrized by two parameters a_z and b_z, while the $f_{\rm blue}$ at given redshift is inversely proportional to the cluster mass, which is linked to the X-ray temperature $T_{\rm X}$. I.e.,

$$f_{\rm blue}(T_{\rm X}, z) = \frac{(a_z \times z + b_z)}{T_{\rm X}}. \tag{3.10}$$

To estimate the best-fit parameters, we fit the model to the synthetic data sets of 10000 realizations, where each realization consists of $\{f_{{\rm blue},i}\}$ (i runs over 46 XMM-BCS clusters) generated from the estimated $f_{\rm blue}$ of each cluster. The best-fit and the 1σ uncertainty of the parameters are estimated as the mean and the standard deviation of the best-fit parameters of these 10000 realizations.

The measurements of $f_{\rm blue}$ of the XMM-BCS cluster sample are in Figure 3.9. We present the best-fit $f_{\rm blue}$ relation of XMM-BCS clusters ($z \leq 0.7$) with the best-fit parameters $(a_z, b_z) = (0.21, 0.31)$ in Figure 3.10. To plot the mass and redshift trends of the estimated $f_{\rm blue}$ of each cluster in Figure 3.10, we correct the redshift and mass trends with respect to the obtained best-fit trends (i.e., eq (3.10) with $(a_z, b_z) = (0.21, 0.31)$). Specifically, the estimated $f_{\rm blue}$ of each cluster is divided by the redshift trend $(a_z \times z + b_z)$ and weighted by the temperature $T_{\rm X}$ in the left and right panels of Figure 3.10, respectively. Although we discard the high redshift clusters ($z > 0.7$) in the fit, their $f_{\rm blue}$ behavior are consistent with the best-fit relation estimated from the low redshift clusters ($z \leq 0.7$) alone.

Chapter 4

Census of Baryon Content in a Complete Sample of Massive Galaxy Clusters Selected by the South Pole Telescope at $0.2 < z < 1.25$

I. Chiu, the SPT and DES collaborations

This chapter is a preliminary result that is currently under the collaboration between the SPT and DES, and we will aim for publication in Monthly Notices of the Royal Astronomical Society.

4.1 Abstract

We present the preliminary results of measurements of stellar and intracluster medium (ICM) masses in 91 Sunyaev-Zel'dovich Effect (SZE) selected galaxy clusters spanning the redshift range $0.25 < z < 1.25$ that have been identified in the 2500 deg^2 SPT-SZ survey. We determine the total mass M_{500} and ICM mass $M_{\rm ICM}$ for the entire sample, while the stellar masses $M_\star$ are currently measured for a subset of 61 clusters. The measurements of M_{500} are estimated from the SPT observable calibrated through external cosmological constraints, while the ICM masses $M_{\rm ICM}$ are obtained by utilizing targeted X-ray follow-up observations with the *Chandra* X-ray Observatory. In 61 clusters we measure the stellar masses $M_\star$ by fitting Spectral Energy Distribution (SED) models to the *griz* band photometry taken by the Dark Energy Survey (DES), supplemented in 36 clusters with dedicated *Spitzer* follow-up near-infrared imaging. By applying a consistent analysis to the homogeneous, multi-wavelength datasets over this large sample of SZE selected clusters that span a broad range of redshift, this study provides constraints on the baryon content of massive clusters as a function of cluster mass and redshift absent many of the systematics that have plagued previous analyses. With measurements of M_{500}, $M_{\rm ICM}$ and $M_\star$, we constrain the $M_{\rm ICM}$–M_{500} and $M_\star$–M_{500} scaling relations, using 91 and 61 clusters, respectively. We find strong mass trends for both scaling relations, while the redshift trends are all statistically consistent with zero, suggesting that the baryon content in massive clusters ($M_{500} \gtrsim 3 \times 10^{14} {\rm M}_\odot$) has changed remarkable little over the past ≈ 10 Gyr of cluster growth through accretion of material from groups and from the field.

4.2 Introduction

Galaxy clusters originate from peaks of primordial fluctuations of the density field in the early Universe and, therefore, the evolution of galaxy clusters carries important information about structure formation. In particular, studying the scaling relations of multi-wavelength observables of galaxy clusters as functions of cluster mass and redshift provides a unique perspective not only on cosmology but also on the astrophysical processes responsible for shaping these systems.

The scaling relations of galaxy clusters are well studied at the local Universe; for example, the scaling relations of Intracluster Medium (ICM) and stellar masses inside galaxy clusters are increasing, respectively, as $\propto {M_{500}}^{1.3}$ and $\propto {M_{500}}^{0.7}$ with increasing cluster total masses M_{500} (Mohr et al., 1999; Lin et al., 2003). However, whether these scaling relations hold at high redshift ($z \gtrsim 0.6$) remains still unclear due to the lack of large, uniformly selected cluster samples and adequately deep datasets. Recent studies of the baryon scaling relations on cluster and group scales at high redshift have shown strong mass trends similar to those observed locally but no significant redshift trend out to $z \approx 1.3$ (Chiu et al., 2016b,c).

The combination of strong mass trends and weak redshift trends within a hierarchical structure formation context suggests that there are significant amounts of material falling into clusters from the field during their formation, enabling the fraction of ICM and stellar components with respect to the total mass to remain approximately constant while clusters grow and become more massive. The picture is broadly consistent with studies of cluster growth in simulations (McGee

et al., 2009), where that material infalling into galaxy clusters consists of $\gtrsim 50$ % from the field with the remainder coming from groups and low mass clusters.

However, it is important to note that current constraints on the redshift trends of scaling relations suffer from significant systematics raised from comparing the heterogeneous cluster samples without a consistent analysis (Chiu et al., 2016b). To overcome these systematics one needs to use a large sample with a well-understood selection function and– most importantly– employ a common unbiased method of mass estimation on homogeneous datasets across the redshift range of interest.

In this study, we aim to study baryon components of massive galaxy clusters selected by the South Pole Telescope (SPT) employing the Sunyaev-Zel'dovich Effect (SZE; Sunyaev & Zel'dovich, 1970a, 1972) using uniform follow-up datasets, which consist of *Chandra* X-ray observations, optical imaging from the Dark Energy Survey (DES) and near-infrared (NIR) data obtained with the *Spitzer* telescope. This study uses a sample of 91 galaxy clusters selected above an SPT detection significance $\xi > 6.8$ over a wide redshift range of $0.2 < z < 1.3$. This sample is the largest complete sample of clusters extending to high redshift ($z \gtrsim 0.6$) with uniform multi-wavelength datasets to date. Moreover, we adopt uniform methodologies to estimate the ICM, stellar and total masses of each galaxy cluster in our sample; this avoids any potential systematics that could bias the derived scaling relations.

This paper is organized as follows. The cluster sample and data are described in Section 4.3, while the analysis method is given in Section 4.4. The results and discussion are presented in Section 5.6, followed by a conclusion made in Section 4.6. Throughout this paper, we adopt the flat ΛCDM cosmology with the fiducial cosmological parameters $(\Omega_{\rm M}, H_0, \sigma_8) = (0.309, 67.74 \text{ km s}^{-1} \text{ Mpc}^{-1}, 0.816)$. Unless otherwise stated, the uncertainties indicate the 1σ confidence regions, the total cluster mass M_{500} is estimated at the overdensity of 500 with respect to the critical density $\rho_{\rm crit}$ at the cluster redshift $z_{\rm l}$, the cluster radius R_{500} is converted from M_{500}[1], and the photometry is in the AB magnitude system.

4.3 Cluster Sample and Data

4.3.1 Cluster Sample

The cluster sample conducted in this work is selected from the SPT-SZ 2500 deg^2 survey (Bleem et al., 2015) based on their SZE signatures. A subset of 80 SPT-selected clusters at $z > 0.4$ with SZE detection significance $\xi > 6.8$ has been followed up by the *Chandra* X-ray Observatory through a X-ray Visionary Project (hereafter XVP, PI Benson). Apart from these 80 clusters, we also extend the cluster sample by including other SPT-selected clusters at redshift $z > 0.2$ also observed by the *Chandra* X-ray Observatory through previous proposals from the SPT, Atacama Cosmology Telescope (ACT; Marriage et al., 2011) or *Planck* (The Planck Collaboration, 2006) consortiums, or from the Data Archive of *Chandra* X-ray Center [2]. As a result, the final sample

[1] $R_{500} = \left(M_{500} / \left(\frac{4\pi}{3} \rho_{\rm crit}(z_{\rm l}) 500\right)\right)^{1/3}$

[2] http://cxc.harvard.edu/

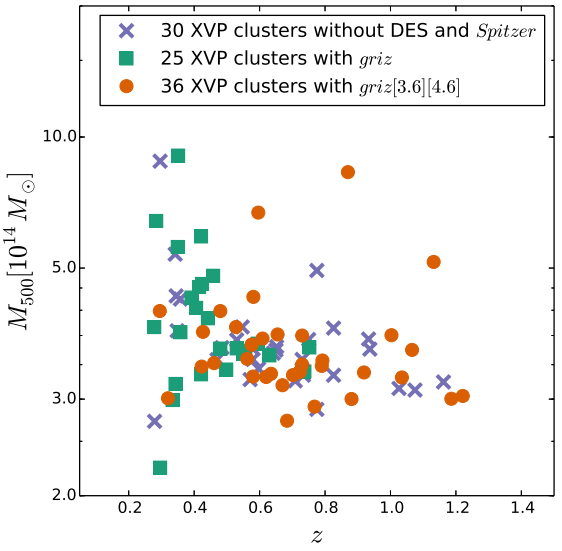

Figure 4.1: The sample of the galaxy clusters selected by the SPT in this work. The total mass M_{500} and redshift z of clusters are plotted, and the uncertainties of the masses and redshifts are omitted for clarity. The subsets of 36 clusters with both optical and NIR datasets, 25 clusters with optical photometry alone and 30 clusters without optical and NIR imaging are marked by the red circles, green squares and the blue crosses, respectively.

consists of 91 galaxy clusters at redshift $0.25 < z < 1.25$, and they are all observed by both SPT-SZ survey and the *Chandra* X-ray observatory. The SZE significance ξ measured by the SPT and the existing X-ray data enable us to determine, respectively, the total and ICM masses of each cluster in the sample.

The redshifts of a subset of 61 clusters in our sample are determined spectroscopically via the spectroscopic follow-up observations (Ruel et al., 2014, Bayliss in prep.). For the rest of the clusters, we use the photometric redshifts that are estimated by using the Composite Stellar Population (hereafter CSP) of the Bruzual and Charlot (BC03; Bruzual & Charlot, 2003) model with formation redshift $z_{\rm f} = 3$ and an exponentially decaying star formation rate with the e-folding timescale $\tau = 0.4$ Gyr. This CSP model is built by running `EzGal` (Mancone & Gonzalez, 2012) and is calibrated by the red sequence (hereafter RS) of Coma Cluster using six different matellicities with the metallicity-to-luminosity relation (see more details in Song et al. (2012a)). The resulting CSP model has been demonstrated to be able to provide photometric redshifts of galaxy clusters with the root-mean-square (rms) of $\Delta z/(1+z) \lesssim 0.025$ by calibrating with available spectroscopic redshifts (Song et al., 2012a,c; Liu et al., 2015a). The full sample of clusters used in this work is shown in Figure 4.1.

4.3.2 X-ray data

All the clusters in our sample are followed up by the *Chandra* X-ray Observatory, and majority of them ($\gtrsim 80$) are observed through the XVP program. The X-ray data are taken in order to determine the X-ray mass proxies for cosmological analysis (Benson et al., 2013; Bocquet et al., 2015a) with the the goal of uniformly obtaining ≈ 2000 photon counts per cluster, by design. With these X-ray data, we are able to estimate the total luminosity $L_{\rm X}$, temperature $T_{\rm X}$ and masses $M_{\rm ICM}$ of ICM and the mass proxy $Y_{\rm X} \equiv T_{\rm X} M_{\rm ICM}$ for each cluster, which have been used in the previous works (Benson et al., 2013; Bocquet et al., 2015a; McDonald et al., 2013, 2014a; Chiu et al., 2016b). In this work, we only use the X-ray data product of $M_{\rm ICM}$, and the cluster total masses are estimated from the SPT observables instead of X-ray mass proxies. The average of ≈ 2000 X-ray photon counts allows us to measure $M_{\rm ICM}$ with an uncertainty $\lesssim 15$ % for each cluster. Similarly to Chiu et al. (2016b), we use the X-ray centers as the centers of clusters in this work. The more details of the X-ray data acquisition, reduction and analysis are fully described elsewhere (Andersson et al., 2011; Benson et al., 2013; McDonald et al., 2013).

4.3.3 Optical and NIR data

To estimate the stellar mass of each cluster in our sample, we employ the optical imaging through the *griz* filters observed by the Dark Energy Survey (DES, DES Collaboration, 2005) and the dedicating Near-Infrared (NIR) follow-up observations taken by the Infrared Array Camera (IRAC, Fazio et al. 2004) of the *Spitzer* telescope.

For the optical data, the Science Verification and Year One of the DES datasets are used to obtain the *griz* photometry. For each cluster, we build Point Spread Function (PSF)-homogenized coadd images of the *griz* bands with the field of view of $\approx 1\,{\rm deg}^2$ centering on the cluster center; this avoids the edge effects that are typical seen in wide field surveys. The optical imaging is processed by the CosmoDM pipeline (Mohr et al., 2012), and the full descriptions of data reductions, source extractions and photometric calibrations are given elsewhere (Desai et al., 2012; Liu et al., 2015a; Hennig et al., 2016). There are 61 out of the 91 clusters covered by the footprints of the Year One and Science Verification DES datasets, and the remaining 30 clusters will be imaged by the continuing DES survey. Therefore, we do not present the stellar mass measurements for the remaining 30 clusters, for which the optical data from DES are not available now.

Following the procedures of the previous works (Zenteno et al., 2011; Chiu et al., 2016a; Hennig et al., 2016), we estimate the completeness of the catalogs by comparing the observed number counts to the ones estimated from the COSMOS field (Capak et al., 2007; Ilbert et al., 2009), which the source detections are complete to $\gtrsim 25.5$ mag for the *griz* bands. Specifically, we first estimate the logarithmic slope of the source count-to-magnitude relation of the COSMOS field assuming that it follows a power law, then compare the histogram of the source counts–which are observed in the cluster field and are away from the cluster center by $> 3R_{500}$–to the derived power law model with the slope fixed to the best-fit value of the COSMOS and the normalization that is fitted to the source counts observed between 19.5 mag and 21 mag in the cluster field, and finally fit an error function to the count ratio in order to obtain the completeness

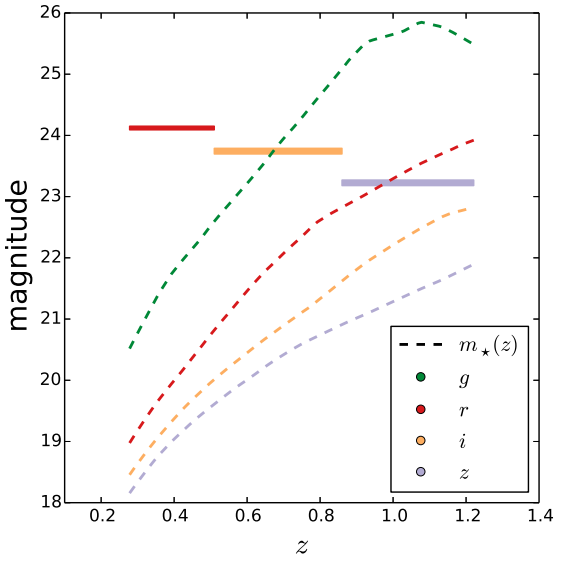

Figure 4.2: The depth and the evolutions of the characteristic magnitude $m_\star$ predicted by the CSP model as the functions of redshift. The median and the uncertainties of the mean of the 50 % completeness of the *riz* bands are shown by the red, orange and the purple bars; the median of the 50 % completeness of the z band is 24.51 ± 0.02 mag, which we do not plot here for clarity. Conversely, the characteristic magnitude $m_\star(z)$ predicted by the CSP model (see Section 4.3.1) at the *griz* bands is plotted as the green, red, orange and the purple lines.

function. The procedure above is done for the *griz* bands for each cluster, and the results are shown in Figure 4.2, where the medians and theirs uncertainties of the 50 % completeness of the 61 observed cluster fields are plotted as the horizontal bars. For clarity, we only show the results of the *riz* bands that we will perform the magnitude cut on our galaxy samples in the following analysis (see Section 4.4.1); the median of 50 % completeness of the g band is 24.51 ± 0.02 mag. On top of the derived completeness in Figure 4.2, we also plot the characteristic magnitude $m_\star(z)$ as the functions of redshift for the *griz* bands predicted by the CSP model (see Section 4.3.1). Overall, the 50 % completeness of the *griz* bands is deeper than $m_\star(z)$ by > 2 mag (≈ 1.5 mag for $z \gtrsim 1.1$), this suggests that the depth of DES optical data is sufficient to detect and estimate the stellar masses of majorities of the cluster galaxies in our sample. The corrections accounting for incompleteness are applied in the following analysis (see Section 4.4.1) based on these derived completeness functions.

On the other hand, the NIR observations are taken through the IRAC channels of 3.6 μm and 4.5 μm with the Program IDs of 60099, 70053 and 80012, resulting in additional photometry of [3.6] and [4.5], respectively. The data acquiring, processing and photometric calibrations of the NIR *Spitzer* observations are fully given in Ashby et al. (2013), for which we defer the readers to for more details. The depths of IRAC observations are deep enough to image the cluster galaxies, which are brighter than $m_\star(z) + 2$ mag in [3.6] and [4.5] predicted by the CSP model (see Section 4.3.1), out to redshift $z \approx 1.5$ with more than 90 % completeness, by design. It is worth

mentioning that the field of view of the *Spitzer* mosaics is $\approx 7' \times 7'$, which is sufficient to cover the R_{500} regions of the clusters in our sample at redshift $z \gtrsim 0.4$. Among the 61 clusters imaged by the DES, there are 36 clusters that are also observed by the *Spitzer* telescope through the follow-up programs. As a result, we have the 25 (36) clusters with the photometry of *griz* (*griz*[3.6][4.5]), and this enables us to estimate the stellar masses of cluster galaxies by conducting the Spectral Energy Distribution (SED) fit technique on the basis of single galaxy. The available datasets for each cluster are color-coded in Figure 4.1.

4.4 Multi-Wavelength Analysis

We estimate the cluster total masses via a cosmological analysis that included external cosmological constraints from the *Planck* CMB temperature anisotropy and the number counts of the SPT galaxy clusters. The full details are given in Bocquet et al. (2015a), to which we defer the readers to for more details. On the other hand, the ICM mass of each cluster is estimated via fitting the X-ray surface brightness profile, and more details can be found in McDonald et al. (2013). In the following subsection, we describe the method of estimating the stellar masses of galaxy clusters.

4.4.1 Stellar Mass Estimates

We start from the optical catalogs of DES *griz* photometry. The `MAG_AUTO` photometry extracted by `SExtractor` (Bertin & Arnouts, 1996) for the *griz* bands is used. For the 36 clusters with available NIR imaging, we construct the joint optical and NIR catalogs by running the `T-PHOT` package (Merlin et al., 2015) to deblend the NIR fluxes. Specifically, we extracted the PSF-matched photometry of [3.6] and [4.5] for each source in the photometric catalogs consisting of *griz* bands, and this enables us to extract the accurate NIR fluxes for blended sources. As a result, we use the catalogs of *griz* and *griz*[3.6][4.5] photometry for the clusters without and with available *Spitzer* follow-up observations, respectively. We stress that all the sources in our photometric catalogs are detected based on the optical detection and are jointly attached with the photometry of [3.6] and [4.5] if available. The same detection algorithm based on the DES images again ensures the uniformity in our analysis.

After constructing the catalogs, we use `Le Phare` (Arnouts et al., 1999; Ilbert et al., 2006) to perform the SED fit on the galaxies that lie in each cluster field. We first compile the library of the SEDs by conducting the templates of the BC03 models with various configurations. The configurations include (1) metallicities $Z = 0.02, 0.008$, (2) star formation rates that are e-folding exponentially decaying with $\tau = 1.0,\ 2.0,\ 3.0,\ 5.0,\ 10.0,\ 15.0,\ 30.0$ Gyr, (3) 40 ages logarithmically increasing from 0.01 Gyr to 13.5 Gyr, (4) redshift range from 0 to 3.0 with steps of 0.02 and (4) the Calzetti extinction law (Calzetti et al., 2000) with reddening $E(B-V) = 0.0,\ 0.1,\ 0.2,\ 0.3$. The Chabrier (2003) Initial Mass Function is used in constructing the library. Then, we run `Le Phare` on each galaxy that lies within the observed footprint to estimate the galaxy stellar mass and photometric redshift (photo-z or $z_{\rm p}$) simultaneously. During the fitting, we interpolate the templates among the redshift steps. The SED fit is performed in flux space, and we increase the

flux uncertainties by a factor of 2 based on the tests of photometric repeatability (Desai et al., 2012; Liu et al., 2015a; Hennig et al., 2016), which accounts for the sky noise that causes the systematic uncertainties of the photometric measurements among the individual exposures.

We show the SED fit performance in the context of comparison between the photo-z and spectroscopic redshift (spec-z or $z_{\rm s}$) in Figure 4.3. The measurements of spec-z are taken from Ruel et al. (2014) and Bayliss in prep. through the previous SPT spectroscopic follow-up programs, where a subset of ≈ 100 SPT-detected clusters is targeted in order to obtain $\approx 25-35$ spectra of galaxies per cluster. In the cluster fields of our sample, there are 1755 galaxies in total with available spec-z measurements for the clusters without the *Spitzer* follow-up observations; for the clusters including photometry of [3.6] and [4.5], it results in a smaller sample with 816 galaxies. With the galaxy sample of available spec-z measurements in the cluster fields, we are able to quantify the performance of the SED fit, which is also served as an end-to-end test for our photometric catalogs. As a result, the mean bias $\Delta z \equiv \left(z_{\rm p}-z_{\rm s}\right)/\left(1+z_{\rm s}\right)$, root-mean-square of Δz and the outlier rate (defined as $\|\Delta z\|>0.2$) are -0.0039, 0.063 and 0.043 (-0.017, 0.066 and 0.053), respectively, for using the photometry of *griz* (*griz*[3.6][4.5]). Overall, the performance of the SED fit is consistent between the cases with and without NIR photometry; however, including the photometry of [3.6] and [4.5] alleviates the photo-z bias seen in some redshift intervals, especially for $z \lesssim 0.4$ and $z \gtrsim 1.0$. Based on the performance of our SED fit, we conclude that we area able to statistically identify the cluster members on the basis of single galaxy in our sample.

After the SED fit, we then select the galaxies that are used in this work by carrying out (1) the star/galaxy separation, (2) the photo-z selection, and (3) the magnitude cut. For the star/galaxy separation, the spread model provides a robust identification of stars down to i-band magnitude of ≈ 22 mag (Desai et al., 2012); therefore we exclude the stars defined by the sources–in i band– with $\|\texttt{spread\_model}\| \leq 2\times10^{-3}$ and magnitude brighter than 22 mag. We also discard any objects with $\texttt{spread\_model} \leq -2\times10^{-3}$, which consists mainly of cosmic rays or non-reliable detections. The remaining faint stars ($i \geq 22$ mag) are excluded by the statistical fore/background subtraction (hereafter background subtraction, see the text below). After discarding the stars, we select the galaxies with the photo-z consistent with the cluster redshift $z_{\rm l}$ by discarding the sources with $\|\left(z_{\rm p}-z_{\rm l}\right)/\left(1+z_{\rm l}\right)\| > 0.2$. Note that we use a photo-z threshold that is $\gtrsim 3$ times of the photo-z rms (i.e., $\gtrsim 3\sigma$) in discarding non-cluster galaxies. In the end, we only select the galaxies brighter than $m_\star$ + 2 mag in the band that is just redder than 4000 Å break in the observed frame. Specifically, we only select galaxies with $\texttt{MAG\_AUTO} \leq m_\star+2$ in the r (i, z) band for clusters at $z \leq 51$ ($0.51 < z \leq 0.86$, $z > 0.86$), where the $m_\star$ is predicted by the CSP model at the cluster redshift $z_{\rm l}$ (see Section 4.3.1). By employing the selections above, this ensures that we study and select the galaxy populations in a consistent manner across the whole redshift range of the cluster sample.

To eliminate the contaminations of (1) faint stats that are not discarded by the spread model cut and (2) non-cluster galaxies raised from the photo-z scatter, we perform the statistical background subtraction. Specifically, we select the footprint with the field of view of $\approx 1\,{\rm deg}^2$ located at the center of the COSMOS field (Capak et al., 2007; Ilbert et al., 2009) as the background field–because this region is also observed by the DES and the *Spitzer* Large Area Survey with Hyper-Suprime-Cam (SPLASH, Capak et al., 2012), covering the same wavelength range used

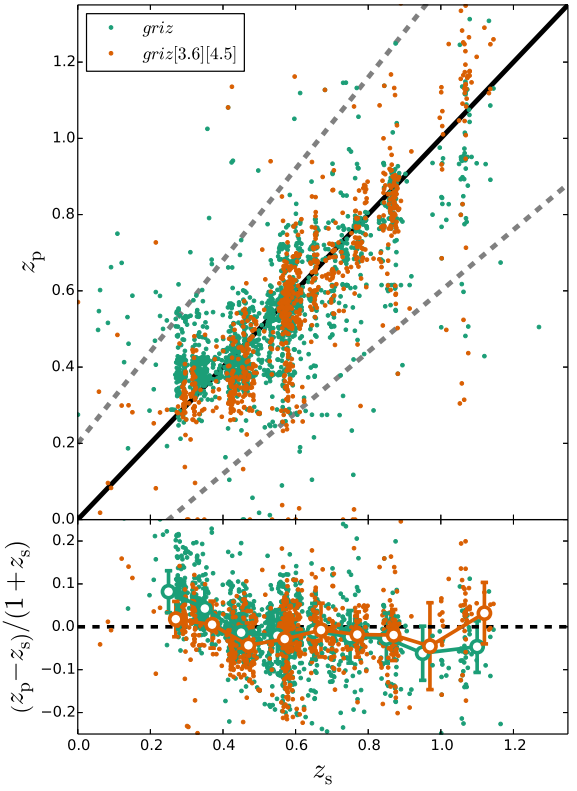

Figure 4.3: The scatter plot of photo-z versus spec-z. The photo-z measured by the SED fit using the photometry of *griz*[3.6][4.5] and *griz* are shown by the red and green points. The upper panel shows the scatter plot, while the lower panel shows the residual $\|\Delta z\|/(1+z)$. The dashed-lines in the upper panel indicate the condition of $\|\Delta z\|/(1+z) > 0.2$.

in the cluster fields. Moreover, we stress that (1) this region is free from any cluster that is as massive as the SPT clusters, (2) we specifically build this background field by coadding the single exposures observed by the DES to reach the comparable depth of the *griz* bands in the cluster fields, and (3) the photometric catalogs of the *griz* bands are also processed and cataloged by the CosmoDM pipeline. For the photometry of [3.6] and [4.5] used in the background field, we match our catalog to the `COSMOS2015` catalog released in Laigle et al. (2016)–using the matching radius of $1''$–to obtain the magnitudes and fluxes observed by the SPLASH survey. That is, the photometric catalog of the background field is also constructed based on the source detection in optical as the same as the cluster fields. Note that the SPLASH survey is much deeper (by $\gtrsim 2$ mag) than the dedicating *Spitzer* follow-up observations of the SPT clusters and–therefore–suit the need of this work. The multi-wavelength datasets, which are taken by the same facilities and are processed by the same pipeline, with the wide field of view assure that this field can provide the estimates of background properties with no systematics existed among the cluster fields; furthermore, this also assures that faint stars and interlopers caused by photo-z scatter can be removed by the statistical background subtraction after applying the identical selections of galaxies.

After constructing the photometric catalog of the background field, we perform the same pipeline of the SED fit (with and without the photometry of [3.6] and [4.5]) and select galaxies based on the identical criteria (e.g., the spread model, photo-z and magnitude cuts) to obtain the background properties for each cluster. In other words, we have the stellar mass estimates–using the photometry of *griz* and/or *griz*[3.6][4.5]–of the galaxy populations selected and analyzed in the same way for each cluster field and its corresponding background field. In the end, we randomly draw the apertures[3] with the same size of cluster R_{500}, then estimate the mean of the sum the stellar mass estimates of these apertures, and finally subtract it from the cluster field. The uncertainties of the mean of these apertures are served as the uncertainties of the background stellar mass estimates. The incompleteness at the faint end (see Section 4.3) is accounted for by bootstrapping the sources–for both cluster and background fields–based on the completeness functions derived at the same band used for the magnitude cut. Due to the insufficient field of view of the *Spitzer* follow-up observations for the 36 clusters with NIR photometry, we also apply the corrections to the stellar mass estimates by calculating the ratios of geometric areas of the IRAC coverages to the apertures with radii of the cluster R_{500}.

4.5 Results and Discussions

In this Section, we present the results of the ICM mass-to-halo mass and stellar mass-to-halo mass relations.

[3]It is generally about $\gtrsim 20$ apertures depending on the cluster size.

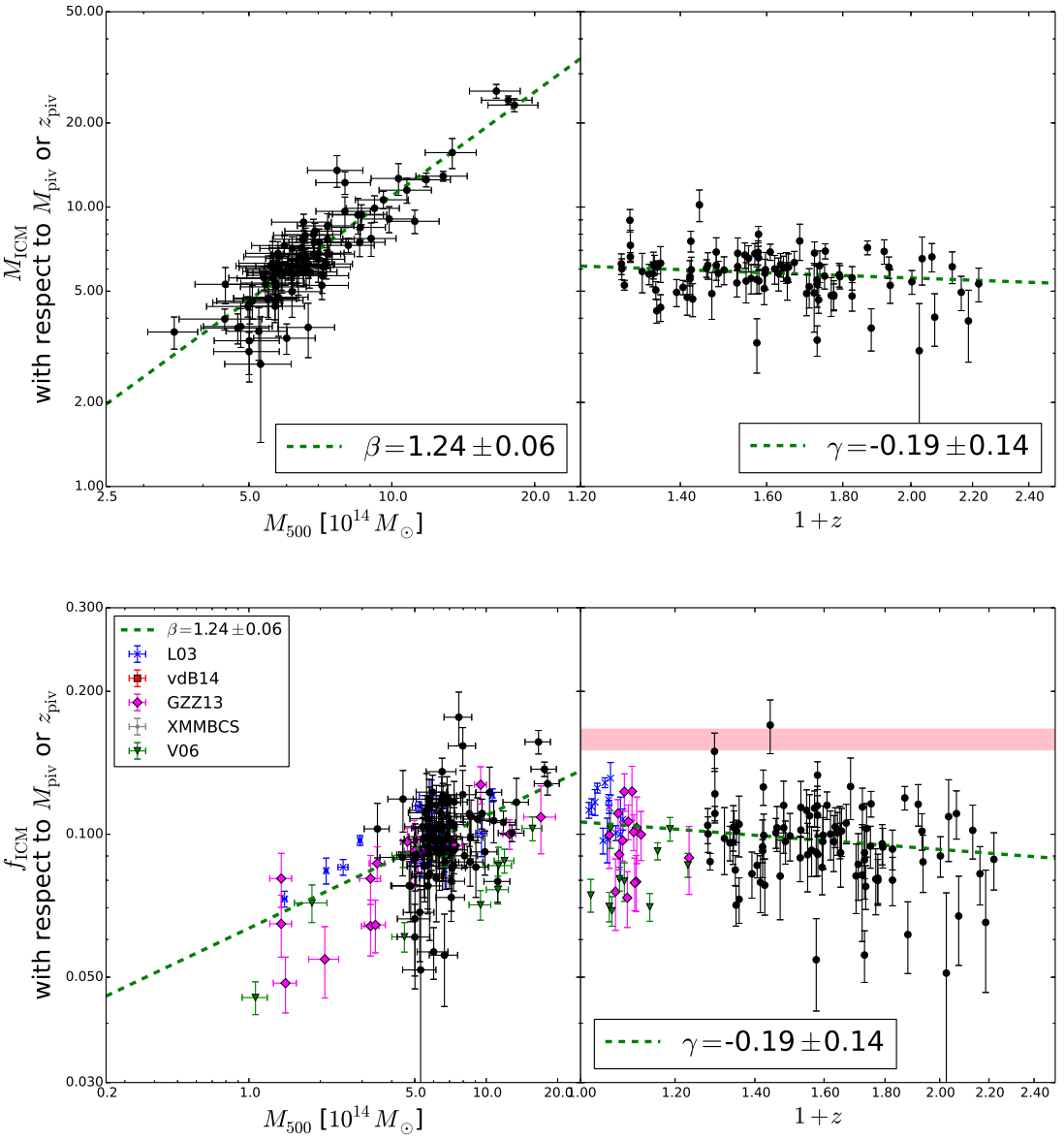

Figure 4.4: The scaling relation of $f_{\rm ICM}$–M_{500} based on the 91 SPT-detected clusters in this work. The left and right panels show the mass and redshift trends with respect to the pivotal mass $M_{\rm piv} = 6 \times 10^{14} {\rm M}_\odot$ and the pivotal redshift $z_{\rm piv} = 0.6$, respectively. The black points are the measurements of $f_{\rm ICM}$ normalized by dividing by $\left(\frac{M_{500}}{M_{\rm piv}}\right)^{B_{\rm ICM}-1}$ ($\left(\frac{1+z}{1+z_{\rm piv}}\right)^{C_{\rm ICM}}$) in the left (right) panel. The comparison samples from the literatures are plotted in the colors that are shown in the legend of the left panel, while the cosmic value of the baryon fraction derived from the the CMB cosmological constraints from *Planck* is indicated by the pink bar.

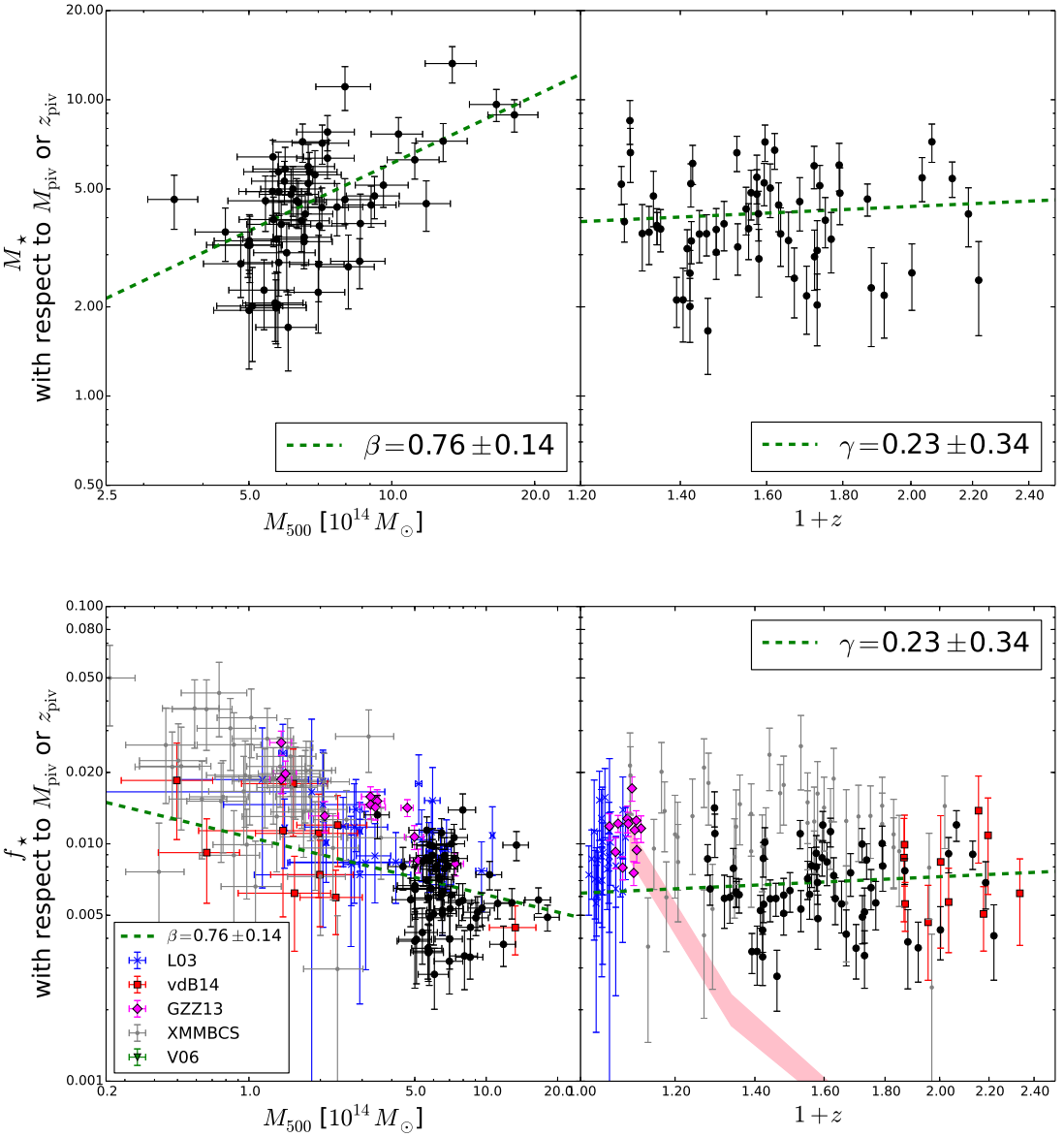

Figure 4.5: The scaling relation of $f_\star$–M_{500} based on the 61 SPT-detected clusters with available optical and/or NIR datasets. The left and right panels show the mass and redshift trends with respect to the pivotal mass $M_{\rm piv} = 6 \times 10^{14} {\rm M}_\odot$ and the pivotal redshift $z_{\rm piv} = 0.6$, respectively. The black points are the measurements of $M_\star$ normalized by dividing by $\left(\frac{M_{500}}{M_{\rm piv}}\right)^{B_\star - 1}$ ($\left(\frac{1+z}{1+z_{\rm piv}}\right)^{C_\star}$) in the left (right) panel. The comparison samples from the literatures are plotted in the colors that are shown in the legend of the left panel, while the cosmic value of the stellar mass fraction derived from the combination of Muzzin et al. (2013) and the CMB cosmological constraints from *Planck* is indicated by the pink bar.

4.5.1 ICM Mass-to-Halo Mass relations

We fit a scaling relation

$$M_{\rm ICM} = A_{\rm ICM}\left(\frac{M_{500}}{M_{\rm piv}}\right)^{B_{\rm ICM}}\left(\frac{1+z}{1+z_{\rm piv}}\right)^{C_{\rm ICM}}, \tag{4.1}$$

where $M_{\rm piv} \equiv 6\times10^{14}{\rm M}_{\odot}$ and $z_{\rm piv} \equiv 0.6$, to the estimated $M_{\rm ICM}$ and M_{500}. We take the uncertainties of $M_{\rm ICM}$ and M_{500} into account by conducting the orthogonal distance regression. The full sample of the 91 clusters is used in deriving the ICM mass-to-halo mass relations. The resulting slopes of the mass and redshift trends are $B_{\rm ICM} = 1.24\pm0.06$ and $C_{\rm ICM} = -0.19\pm0.14$, respectively; this suggests a highly significant mass trend but a redshift trend that is statistically consistent with zero out to redshift $z\approx1.2$. The best-fit normalization $A_{\rm ICM}$ is $(5.82\pm0.13)\times10^{13}{\rm M}_{\odot}$, suggesting that the characteristic ICM mass fraction is about 9.7 ± 0.2 % with respect to the pivotal mass $M_{\rm piv} \equiv 6\times10^{14}{\rm M}_{\odot}$ at redshift $z_{\rm piv} \equiv 0.6$. The result is shown in the upper panel of Figure 4.4, where we normalize the observed ICM mass by dividing the $M_{\rm ICM}$ by the best-fit redshift trend ($\left(\frac{1+z}{1+z_{\rm piv}}\right)^{C_{\rm ICM}}$) and mass trend ($\left(\frac{M_{500}}{M_{\rm piv}}\right)^{B_{\rm ICM}}$) in the left and right panels, respectively. In other words, the mass trend of $M_{\rm ICM}$ at the characteristic redshift $z = z_{\rm piv}$ is shown in the left panel, while the redshift trend of $M_{\rm ICM}$ with respect to $M_{500} = M_{\rm piv}$ is plotted in the right panel. Similarly, we also show the ICM mass fraction $f_{\rm ICM} \equiv M_{\rm ICM}/M_{500}$ normalized to $M_{500} = M_{\rm piv}$ and $z = z_{\rm piv}$ in the lower panel of Figure 4.4. We also plot the comparison samples from Lin et al. (2003, L03), Vikhlinin et al. (2006, V06) and Gonzalez et al. (2013, GZZ13) in Figure 4.4.

4.5.2 Stellar Mass-to-Halo Mass relations

Because we measure the stellar masses $M_{\star}$ based on the SED fit using the photometry of *griz* and *griz*[3.6][4.5] for a subset of 25 and 36 clusters, respectively, we want to examine whether any systematics of the stellar masses raises from including the NIR photometry ([3.6] and [4.5]). This systematics–if it exists without being accounted for–could bias the derived stellar mass-to-halo mass relation, especially the redshift trend due to the fact that majorities of clusters with the available *Spitzer* follow-up observations are at redshift $z \gtrsim 0.6$, and vice versa. To verify this, we exclude the NIR photometry for the 36 clusters with the *Spitzer* follow-up observations (i.e., only using the *griz* photometry), then repeat the end-to-end analysis that is as the same as the other 25 clusters without the available NIR photometry, and finally compare their stellar mass estimates using *griz* alone to the ones using *griz*[3.6][4.5]. As a result, we find that there is a systematic difference of the stellar mass estimates between including and excluding the NIR photometry of [3.6][4.5]–in the sense that the optical-derived masses $M_{\star,\ griz}$ are systematically higher than the optical+NIR-derived mass $M_{\star,\ griz[3.6][4.5]}$. To quantify this, we fit a linear relation with the relative factor η between these two masses,

$$M_{\star,\ griz[3.6][4.5]} = \eta M_{\star,\ griz},$$

to the derived stellar mass estimates of the background fields and the cluster fields before/after the background subtraction. Based on these 36 clusters, the resulting η are 0.75 ± 0.01, 0.82 ± 0.03

and 0.85 ± 0.04 for the stellar mass estimates of the derived background fields and the cluster fields before/after the background subtraction, respectively. The estimated η is consistent with the results of previous works (e.g., Pozzetti et al., 2007; Swindle et al., 2011; Taylor et al., 2011; Banerji et al., 2013, 2015), where they found that the stellar masses estimated from the SED fit using the optical bands along are biased high with respect to the ones including the NIR photometry by $\approx 0.06 - 0.25$ dex (or $\approx 15 - 78$ %), depending on the conducted templates, different bands that are fitted, galaxy samples, different SED fitting codes, or the combinations of them. It has been suggested that the optical-derived masses are biased due to the fact that the *r* band in the rest frame is already shifted to the *z* band in the observed frame since redshift $z \approx 0.35$ (Taylor et al., 2011), causing the observed fluxes are dominated mainly by the population of young stars. Moreover, the optical light is more sensitive to dust attenuation/extinction, which could bias the estimated stellar masses (Banerji et al., 2013). Conversely, the NIR is nearly insensitive to young stars in galaxies and is also less affected by dust. As a result, the NIR light provides a cleaner and more direct tracer of the underlying stellar masses out to redshift $z \gtrsim 1$ (Eisenhardt et al., 2008; Wylezalek et al., 2014; Lin et al., 2003; Lin & Mohr, 2004; Hilton et al., 2013; Patel et al., 2015; Chiu et al., 2016c). Based on the quantification and arguments above, we apply the correction $\eta = 0.85$ to the stellar mass estimates of the 25 clusters with *griz* photometry alone to remove this systematics.

Similarly to Section 4.5.1, we fit the stellar mass-to-halo mass relation to the derived estimates of $M_\star$ and M_{500}. A total of 61 clusters with available measurements of $M_\star$ are used in deriving the best-fit values of equation (4.2). The best-fit stellar mass-to-halo mass scaling relation is

$$M_\star = (4.14 \pm 0.22) \times 10^{12} \mathrm{M}_\odot \left(\frac{M_{500}}{M_{\rm piv}} \right)^{0.76 \pm 0.14} \left(\frac{1+z}{1+z_{\rm piv}} \right)^{0.23 \pm 0.33} . \quad (4.2)$$

The derived scaling relation suggests a strong mass trend $B_\star = 0.76 \pm 0.14$ at $\gtrsim 5\sigma$ significance, while the redshift trend is statistically consistent with zero ($C_\star = 0.23 \pm 0.33$) with a large uncertainty. The normalization $A_\star = (4.14 \pm 0.22) \times 10^{12} \mathrm{M}_\odot$ implies a stellar mass fraction $f_\star$ of 0.69 ± 0.04 % with respect to the pivotal mass $M_{\rm piv} = 6 \times 10^{14} \mathrm{M}_\odot$ at $z_{\rm piv} = 0.6$.

In Figure 4.5, we show the stellar mass $M_\star$ and stellar mass fractions $f_\star$–which are normalized to $M_{500} = M_{\rm piv}$ and $z = z_{\rm piv}$based on the best-fit $B_\star$ and $C_\star$ in the same way of $M_{\rm ICM}$ and $f_{\rm ICM}$ (see Section 4.5.1)–of the SPT clusters in this work and the conducted comparison samples. The comparison samples are Lin et al. (2003, L03), Vikhlinin et al. (2006, V06), Gonzalez et al. (2013, GZZ13), van der Burg et al. (2014, vdB14) and the XMM-BCS samples from Chiu et al. (2016c). For the cosmic value of the stellar mass fraction shown in the pink bar, we combined the measured stellar mass densities from COSMOS/UltraVISTA survey (Muzzin et al., 2013) and the cosmological parameter $\Omega_{\rm M}$ determined by the *Planck*. As seen in the lower right panel, the stellar mass per unit hosting mass in cluster environment is significantly higher than the cosmic value, which represents the environments of under-dense fields. Conversely, the strong mass trend, which extends from the SPT clusters at high mass end to the comparison samples at low mass end, is seen. This clearly suggests that–based on the decreasing mass trend of $f_\star$ without a significant redshift trend–massive clusters can not form by simply merging clusters with lower masses, otherwise the stellar mass fraction $f_\star$ of high mass clusters should be indistinguishable

from low mass clusters. Instead, a significant amount of infall from under-dense fields, which have significantly lower stellar mass fractions, must contribute to matter assembly of clusters such that the stellar mass fraction $f_\star$ remains roughly constant at high mass end over cosmic time.

4.6 Conclusions

We study the scaling relations $M_{\rm ICM}$–M_{500} and $M_\star$–M_{500} based on the sample of 91 galaxy clusters are selected by their SZE signatures in the SPT-SZ survey. This sample spans a mass range from $\approx 3.5\times10^{14}{\rm M}_\odot$ to $1.8\times10^{15}{\rm M}_\odot$ (with median of $6.48\times10^{14}{\rm M}_\odot$) at redshift from $z=0.278$ to $z=1.22$ (median $z=0.58$). The cluster total mass M_{500} of each cluster is determined by the SZE observable via a calibration analysis including external cosmological constraints. The existing X-ray data taken by the *Chandra* telescope enables us to measure the ICM mass $M_{\rm ICM}$ with an uncertainty $\lesssim 15$ % for each cluster. For a subset of 61 clusters, we also measure their stellar masses by utilizing the SED fit technique on the photometry of *griz* taken by the DES and additionally [3.6][4.5] from dedicated *Spitzer* NIR follow-up observations. It is worth stressing that these mass budgets are estimated by applying consistent methods to homogeneous datasets among the clusters with a well-understood selection function; this significantly reduces the systematic effects relative to previous analyses and also leads to the largest and most uniform sample of measurements to date.

With these measurements of total, ICM and stellar masses, we are able to constrain the scaling relations $M_{\rm ICM}$–M_{500} and $M_\star$–M_{500}. We measure mass trends in ICM mass $B_{\rm ICM}=1.24\pm0.06$ and stellar mass $B_\star=0.76\pm0.14$, which confirms the strong mass trends in the ICM and stellar mass fractions reported in previous work. Conversely, we fine no statistically significant redshift trends ($C_{\rm ICM}=-0.19\pm0.14$ and $C_\star=0.23\pm0.34$), although given the scale of the uncertainties it is still possible for small redshift trends in the baryon content of massive galaxy clusters out to $z\approx1.2$. The resulting normalizations of the scaling relations suggest that the ICM (stellar) mass fraction is $\approx 9.7\pm0.2$ % (0.69 ± 0.04 %) with respect to $M_{500}=6\times10^{14}{\rm M}_\odot$ at $z=0.6$.

Acknowledgements

We acknowledge the support by the DFG Cluster of Excellence “Origin and Structure of the Universe”, the DLR award 50 OR 1205 that supported I. Chiu during his PhD project, and the Transregio program TR33 “The Dark Universe”. The data processing has been carried out on the computing facilities of the Computational Center for Particle and Astrophysics (C2PAP), located at the Leibniz Supercomputer Center (LRZ). This work is based in part on archival data obtained with the *Spitzer* Space Telescope, which is operated by the Jet Propulsion Laboratory, California Institute of Technology under a contract with NASA. This work is based on observations obtained with XMM-*Newton*, an ESA science mission with instruments and contributions directly funded by ESA Member States and the USA (NASA). This paper includes data gathered with the Blanco 4 m telescope, located at the Cerro Tololo Inter-American Observatory in Chile, which

is part of the U.S. National Optical Astronomy Observatory, which is operated by the Association of Universities for Research in Astronomy (AURA), under contract with the NSF. Based on data products from observations made with ESO Telescopes at the La Silla Paranal Observatory under ESO programme ID 179.A-2005 and on data products produced by TERAPIX and the Cambridge Astronomy Survey Unit on behalf of the UltraVISTA consortium.

Chapter 5

Detection of Enhancement in Number Densities of Background Galaxies due to Magnification by Massive Galaxy Clusters

I. Chiu[1,2], J. P. Dietrich[1,2], J. Mohr[1,2,3], D. E. Applegate[4], B. A. Benson[5,6,7], L. E. Bleem[6,8,9], M. B. Bayliss[10,11], S. Bocquet[1,2], J. E. Carlstrom[6,7], R. Capasso[1,2], S. Desai[1,2], C. Gangkofner[1,2], A. H. Gonzalez[13], N. Gupta[1,2], C. Hennig[1,2], H. Hoekstra[14], A. von der Linden[15,16,17], J. Liu[1,2], M. McDonald[12], C. L. Reichardt[18], A. Saro[1,2], T. Schrabback[4], V. Strazzullo[1], C. W. Stubbs[10,11], A. Zenteno[19]

[1]Faculty of Physics, Ludwig-Maximilians University, Scheinerstr. 1, 81679 Munich, Germany
[2]Excellence Cluster Universe, Boltzmannstr. 2, 85748 Garching, Germany
[3]Max Planck Institute for Extraterrestrial Physics, Giessenbachstr. 85748 Garching, Germany
[4]Argelander-Institut für Astronomie, Auf dem Hügel 71, D-53121 Bonn, Germany
[5]Fermi National Accelerator Laboratory, Batavia, IL 60510-0500
[6]Kavli Institute for Cosmological Physics, University of Chicago, 5640 South Ellis Avenue, Chicago, IL 60637
[7]Department of Astronomy and Astrophysics, University of Chicago, 5640 South Ellis Avenue, Chicago, IL 60637
[8]Department of Physics, University of Chicago, 5640 South Ellis Avenue, Chicago, IL 60637
[9]Argonne National Laboratory, 9700 S. Cass Avenue, Argonne, IL, USA 60439
[10]Harvard-Smithsonian Center for Astrophysics, 60 Garden Street, Cambridge, MA 02138
[11]Department of Physics, Harvard University, 17 Oxford Street, Cambridge, MA 02138
[13]Department of Astronomy, University of Florida, Gainesville, FL 32611
[14]Leiden Observatory, Leiden University, PO Box 9513, 2300 RA, Leiden, the Netherlands
[15]Kavli Institute for Particle Astrophysics and Cosmology (KIPAC), Stanford University, 452 Lomita Mall, Stanford, CA 94305-4085, USA
[16]Department of Physics, Stanford University, 452 Lomita Mall, Stanford, CA 94305-4085, USA
[17]Dark Cosmology Centre, Niels Bohr Institute, University of Copenhagen Juliane Maries Vej 30, 2100 Copenhagen, Denmark

[12]Kavli Institute for Astrophysics and Space Research, Massachusetts Institute of Technology, 77 Massachusetts Avenue, Cambridge, MA 02139
[18]School of Physics, University of Melbourne, Parkville, VIC 3010, Australia
[19]Cerro Tololo Inter-American Observatory, Casilla 603, La Serena, Chile

This chapter is published as Chiu et al. (2016a) in Monthly Notices of the Royal Astronomical Society.

5.1 Abstract

We present a detection of the enhancement in the number densities of background galaxies induced from lensing magnification and use it to test the Sunyaev-Zel'dovich effect (SZE) inferred masses in a sample of 19 galaxy clusters with median redshift $z \simeq 0.42$ selected from the South Pole Telescope SPT-SZ survey. These clusters are observed by the Megacam on the Magellan Clay Telescope though *gri* filters. Two background galaxy populations are selected for this study through their photometric colours; they have median redshifts $z_{\rm median} \simeq 0.9$ (low-z background) and $z_{\rm median} \simeq 1.8$ (high-z background). Stacking these populations, we detect the magnification bias effect at 3.3σ and 1.3σ for the low- and high-z backgrounds, respectively. We fit NFW models simultaneously to all observed magnification bias profiles to estimate the multiplicative factor η that describes the ratio of the weak lensing mass to the mass inferred from the SZE observable-mass relation. We further quantify systematic uncertainties in η resulting from the photometric noise and bias, the cluster galaxy contamination and the estimations of the background properties. The resulting η for the combined background populations with 1σ uncertainties is $0.83 \pm 0.24({\rm stat}) \pm 0.074({\rm sys})$, indicating good consistency between the lensing and the SZE-inferred masses. We use our best-fit η to predict the weak lensing shear profiles and compare these predictions with observations, showing agreement between the magnification and shear mass constraints. This work demonstrates the promise of using the magnification as a complementary method to estimate cluster masses in large surveys.

5.2 Introduction

Gravitational lensing is one of the most direct methods for measuring the masses of galaxy clusters, because it does not require assumptions about the dynamical or hydrostatic state of the clusters and it probes the total underlying mass distribution. In practice, there are challenging observational systematics that must be overcome (Erben et al., 2001; Leauthaud et al., 2007; Corless & King, 2009; Viola et al., 2011; Hoekstra et al., 2013), and over the past two decades significant progress has been made by calibrating with simulations (e.g., Heymans et al., 2006; Massey et al., 2007; Bridle et al., 2010; Kitching et al., 2012; Mandelbaum et al., 2014; Hoekstra et al., 2015). As a result, modelling the shear distortion of background galaxies that are lensed has been developed into a reliable method to measure cluster masses (Gruen et al., 2014; Umetsu et al., 2014; Applegate et al., 2014; von der Linden et al., 2014a,b; Hoekstra et al., 2015). In comparison, there has until recently been less observational progress using the complementary gravitational lensing magnification effect (Broadhurst et al., 1995; Dye et al., 2002; Joachimi & Bridle, 2010; Van Waerbeke et al., 2010; Heavens & Joachimi, 2011; Hildebrandt et al., 2011; Schmidt et al., 2012; Umetsu, 2013; Coupon et al., 2013; Ford et al., 2014; Duncan et al., 2014).

The changes in the sizes of the background galaxy population due to gravitational lensing magnification results in changes to the fluxes because the surface brightness is conserved. This leads to increases in the number density of flux-selected samples of background galaxies in the neighborhood of mass concentrations. However, the magnification effect also distorts the sky area, leading to a decrease in the number density. Whether the combined effects lead to an overall

increase or decrease of the number density depends on the slope of the source count-magnitude relation at the flux limit. An advantage to measuring the magnification is that it only requires accurate photometry and therefore does not require unbiased estimates of galaxy ellipticity, which are needed for shear studies. Thus, even unresolved galaxy populations can be used in a lensing magnification study. However, the signal-to-noise ratio (SNR) for mass measurements obtained using magnification effects tends to be lower by a factor of 3–5 as compared to those that one obtains using the shear signature imprinted on the same galaxies (Schneider et al., 2000). Due to the lower SNR, a significant detection of the magnification effect is more realistically expected around massive collapsed structures such as galaxy clusters.

There are several ways to detect the magnification around galaxy clusters. The magnification information can be extracted from the angular cross-correlation of high redshift sources, e.g., Lyman break galaxies (Hildebrandt et al., 2009; Van Waerbeke et al., 2010; Hildebrandt et al., 2011; Ford et al., 2012, 2014), measuring the change in the background galaxy sizes or fluxes (Schmidt et al., 2012), simultaneously estimating the increase in the observed number counts and fluxes of the background luminous red galaxies (Bauer et al., 2014), or observing the skewness in the redshift distribution of the background galaxies (Coupon et al., 2013; Jimeno et al., 2015). Another approach, called the *magnification bias*, is to measure the change or bias in the number density of a flux-limited background galaxy sample towards the cluster centre (Broadhurst et al., 1995; Taylor et al., 1998). First proposed by Broadhurst et al. (1995), who measured the mass of an individual cluster with this technique, the magnification bias method has now been applied to a dozen galaxy clusters (Umetsu, 2013). In that analysis, the magnification bias signature is combined not only with shear but also with strong lensing constraints.

The conventional analysis of magnification bias is based on a flux-limited background galaxy population with a nearly flat slope of the source count-magnitude relation, which leads to a depletion of the number density in the mass-concentrated region of clusters (Umetsu, 2013). Detecting this magnification bias requires ultra-deep and uniform observations to achieve adequate statistics in the galaxy counts to suppress the Poisson noise. Therefore, this approach for measuring the cluster masses can be very costly in terms of observing time. On the other hand, the lensing magnification also acts on brighter galaxies where the intrinsic slope is steep. In this case, the increase of the number of galaxies magnified to be above the flux limit overcomes the dilution of the geometric expansion and, therefore, results in an enhancement of number density. However, this density enhancement of the magnification bias has a lower SNR on a per cluster basis due to the lower number density of bright background galaxies. Consequently, one needs to combine the signal from a large sample of massive clusters.

In this work, we aim to detect the density enhancement from the magnification bias effect by combining information from 19 massive clusters. Our study leverages background populations of normal galaxies selected in colour-colour space. The clusters were selected through their Sunyaev-Zel'dovich effect (SZE; Sunyaev & Zel'dovich, 1970b, 1972) in the 2500 deg^2 SPT-SZ survey carried out using the South Pole Telescope (SPT, Carlstrom et al., 2011). These clusters have been subsequently imaged with the Magellan telescope for the purpose of weak lensing studies. It is worth mentioning that our approach is similar to the number count method conducted in Bauer et al. (2014) with the difference that they only used the background populations of the luminous red galaxies with i-band magnitude brighter than ≈ 20 mag, while in this work

we extend the background samples to the normal galaxies at much fainter limiting magnitudes.

This paper is organized as follows: A brief review of the relevant lensing theory is given in Section 5.3. In Section 5.4 we introduce the data used for this analysis. The analysis method is described in detail in Section 5.5. We present and discuss our results in Section 5.6 and provide our conclusions in Section 5.7. Throughout this paper, we assume the concordance ΛCDM cosmological model with the cosmological parameter values recently determined by Bocquet et al. (2015b): $\Omega_{\rm M}$= 0.292, Ω_Λ= 0.708 and H_0 = 68.2 km s^{-1} Mpc^{-1}. Unless otherwise stated, all uncertainties are 68% (1σ) confidence intervals and cluster masses and radii are estimated within a region that has an overdensity of 500 with respect to the critical density of the Universe at the cluster redshift. The magnitudes in this work are all in the AB magnitude system. The distances quoted in this work are all in physical units.

5.3 Theory

In this section we provide a summary of gravitational lensing induced by galaxy clusters. We refer the reader to Umetsu (2011) and Hoekstra et al. (2013) for more complete discussions.

Light traveling from a distant source to the observer is deflected in the presence of a gravitational potential, resulting in the distortion of the observed image. This gravitational lensing effect depends only on the underlying mass distribution along the line of sight and can be formulated with the following lens equation:

$$\alpha = \theta - \nabla_\theta \psi \ , \tag{5.1}$$

where ψ is the effective deflection potential, α and θ are the angular positions on the sky of the source (before lensing) and the observed image (after lensing), respectively. The Jacobian of equation (5.1) therefore reflects how the observed background image is distorted, linking the positions of the source and the gravitational potential of the lens. i.e.,

$$\begin{aligned} \mathbf{J}(\theta) &= \nabla_\theta \alpha \\ &= \begin{pmatrix} 1-\kappa-\gamma_1 & -\gamma_2 \\ -\gamma_2 & 1-\kappa+\gamma_1 \end{pmatrix} \end{aligned} \tag{5.2}$$

and

$$\mathrm{d}\Omega_\theta = \mathbf{J}^{-1}\mathrm{d}\Omega_\alpha \ , \tag{5.3}$$

where κ and $\gamma = \gamma_1 + i\gamma_2$ are, respectively, the convergence and the shear at the sky position of the image; $\mathrm{d}\Omega_\alpha$ and $\mathrm{d}\Omega_\theta$ denote the solid angle on the sky before and after lensing, respectively. The convergence κ is the integrated density contrast against the background along the line of sight. For the case of cluster lensing, κ can be written as

$$\kappa(\theta,\psi) = \frac{\Sigma_{\rm lens}(\theta,\psi)}{\Sigma_{\rm crit}}, \tag{5.4}$$

$$\Sigma_{\rm crit} = \frac{c^2}{4\pi G}\frac{1}{\beta D_{\rm l}}, \text{ and} \tag{5.5}$$

$$\beta = \begin{cases} 0 & \text{for } D_{\rm s} \le D_{\rm l} \\ \frac{D_{\rm ls}}{D_{\rm s}} & \text{for } D_{\rm s} > D_{\rm l} \end{cases} \tag{5.6}$$

assuming that the cluster acts as a single thin lens ignoring the uncorrelated large-scale structure, i.e., an instantaneous deflection of the light ray. Here $\Sigma_{\rm lens}$ is the projected mass density of the cluster, $\Sigma_{\rm crit}$ is the critical surface mass density, β is the lensing efficiency that depends on the ratio of the lens-source distance to the source distance averaged over the population of background galaxies, c is the speed of light, and $D_{\rm l}$, $D_{\rm s}$ and $D_{\rm ls}$ denote the angular diameter distances of the cluster, the source, and between the cluster and the source, respectively. These distances depend on the observed redshifts and the adopted cosmological parameters. In practice, the lensing efficiency averaged over a population $\langle\beta\rangle$ is used for estimating cluster masses.

As seen from equation (5.2), gravitational lensing induces two kinds of changes to the observed image. The first one, characterized by γ, distorts the observed image anisotropically, while the other described by the convergence κ results in an isotropic magnification. Analyzing the information from shear alone can only recover the gradient of the cluster potential, and therefore the inferred mass is subject to an arbitrary mass constant. This so-called mass-sheet degeneracy can be broken by combining shear and magnification (e.g. Seitz & Schneider, 1997).

As seen in equation (5.3), gravitational lensing changes the projected area of the observed image, and because the surface brightness is conserved this results in a magnification μ of the source, which is given by

$$\begin{aligned} \mu &= \det(\mathbf{J})^{-1} \\ &= \frac{1}{(1-\kappa)^2 - \|\gamma\|^2}\,. \end{aligned} \tag{5.7}$$

In the weak lensing limit ($\|\gamma\| \ll 1$ and $\kappa \ll 1$), the magnification can be approximated as $\mu \simeq 1+2\kappa$, i.e. it is linearly related to the dimensionless surface mass density κ.

For $\mu > 1$ the flux of each source is increased, leading to an increase in the observed number density of a flux-limited population of background sources. On the other hand, the lensing magnification introduces an angular expansion on the plane of the sky, which decreases the observed number of background sources per unit area. As a result, the observed number density of a flux-limited background population changes (is either depleted or enhanced) towards the centre of the cluster depending on the two competing effects. The mass of a cluster can hence be estimated by measuring this change given knowledge of the properties of the observed background population prior to lensing.

One important property of the background population is its number count-magnitude relation $n(<m)$, which is the cumulative number of galaxies per unit sky area brighter than a particular magnitude m. This number count-flux relation is typically characterized as a power law $n(<f) = f_0 \times f^{-2.5s}$ where f is flux, f_0 is a normalization and s is the power law index. This can be written in terms of magnitude m as

$$\log n(<m) = \log f_0 + s \times (m - {\rm ZP})\,, \tag{5.8}$$

where ZP is the zeropoint used to convert the flux to magnitude. In the presence of lensing the observed cumulative number density $n(<m_{\rm cut})$ of a given background population can be shown

to be (Broadhurst et al., 1995; Umetsu et al., 2011)

$$n(<m_{\rm cut}) = n_0(<m_{\rm cut})\,\mu^{2.5s-1} \tag{5.9}$$

$$s(m_{\rm cut}) = \left.\frac{{\rm d}\log n(<m)}{{\rm d}m}\right|_{m_{\rm cut}}, \tag{5.10}$$

where $n_0(<m_{\rm cut})$ is the projected number density of galaxies at the threshold magnitude $m_{\rm cut}$ in the absence of lensing and $s(m_{\rm cut})$ is the power law index of the galaxy count-magnitude distribution before lensing (equation (5.8)) evaluated at the limiting magnitude $m_{\rm cut}$. Equation (5.9) can be further reduced to

$$n(<m_{\rm cut}) \simeq n_0(<m_{\rm cut})(1+(5s-2)\kappa) \tag{5.11}$$

in the weak lensing regime.

In the case of $s = 0.4$, one expects no magnification signal while a background population with s greater (less) than 0.4 results in enhancement (depletion) of background objects. To sum up, the cluster mass can be determined by using the magnification bias information alone if the power law slope s, the average lensing efficiency $\langle\beta\rangle$ of the background population, and the local background number counts *before* lensing $n_0(<m_{\rm cut})$ are known.

5.4 Sample and Data

5.4.1 Sample

We study the lensing magnification with 19 galaxy clusters selected by SPT through their SZE signatures. The first weak lensing shear based masses for five out of these 19 clusters have been presented in High et al. (2012), and the full sample is being examined in a subsequent weak lensing shear analysis (Dietrich et al, in preparation). These 19 clusters all have measured spectroscopic redshifts (Song et al., 2012c; Bleem et al., 2015) and span the redshift range $0.28 \leq z \leq 0.60$ with a median redshift of 0.42. The virial masses M_{500} have been estimated using their SZE signature and the SZE mass-observable relation that has been calibrated using velocity dispersions, X-ray mass proxies and through self-calibration in combination with external cosmological datasets that include Planck CMB anisotropy, WMAP CMB polarization anisotropy and SNe and BAO distances (Bocquet et al., 2015b).

Song et al. (2012) show that the Brightest Cluster Galaxy (BCG) position provides a good proxy for the cluster centre, which, for relaxed clusters, is statistically consistent with the centre inferred from the SZE map. Moreover, the offset distribution between the BCG and SZE centres is consistent with the one between the BCG and X-ray centres that is seen in the local Universe (Lin & Mohr, 2004). Therefore, the cluster centre is taken to be the position of the BCG, which is visually identified on pseudo-colour images, in this work. R_{500} is derived from the cluster SZE-inferred mass, its redshift and the critical density at that redshift, given the cosmological parameters. Properties of the 19 clusters are listed in Table 5.1.

Table 5.1: Properties of the cluster sample. Column 1: name. Column 2: spectroscopic redshift. Column 3–4: right ascension α_{2000} and declination δ_{2000} of the BCG. Column 5: the SZE-inferred M_{500} (see Section 5.4.1). Column 6–7: R_{500} corresponding to the SZE-inferred M_{500}. Column 8–10: 90% completeness limit (m_{90}) for g, r and i filters, respectively.

Cluster	Redshift	α_{2000}	δ_{2000}	M_{500}	R_{500}		m^g_{90}	m^r_{90}	m^i_{90}
		[deg]	[deg]	[$10^{14}\mathrm{M}_\odot$]	[Mpc]	[arcmin]	[mag]	[mag]	[mag]
SPT-CL J0234−5831	0.415	38.676189	−58.523644	9.03 ± 1.76	1.30	3.82	23.91	24.54	23.07
SPT-CL J0240−5946	0.400	40.159710	−59.763600	6.38 ± 1.31	1.16	3.50	24.05	24.63	23.21
SPT-CL J0254−5857	0.438	43.564592	−58.952993	8.77 ± 1.70	1.27	3.63	23.83	24.21	22.63
SPT-CL J0307−6225	0.579	46.819712	−62.446544	5.89 ± 1.21	1.05	2.60	24.24	24.83	23.58
SPT-CL J0317−5935	0.469	49.315539	−59.591594	4.71 ± 1.11	1.02	2.81	23.94	24.54	23.07
SPT-CL J0346−5439	0.530	56.730934	−54.648699	6.32 ± 1.28	1.10	2.83	24.26	24.69	23.47
SPT-CL J0348−4515	0.358	57.071292	−45.250059	7.04 ± 1.41	1.22	3.94	24.46	25.13	23.85
SPT-CL J0426−5455	0.630	66.517205	−54.925319	6.01 ± 1.23	1.04	2.46	24.13	24.65	23.21
SPT-CL J0509−5342	0.461	77.339141	−53.703632	5.87 ± 1.21	1.10	3.06	24.21	24.59	23.29
SPT-CL J0516−5430	0.295	79.155613	−54.500493	8.00 ± 1.58	1.30	4.79	23.41	23.98	22.64
SPT-CL J0551−5709	0.423	87.898265	−57.141236	5.77 ± 1.20	1.11	3.24	23.50	24.06	22.61
SPT-CL J2022−6323	0.383	305.541020	−63.397044	4.88 ± 1.13	1.07	3.31	23.68	24.20	22.56
SPT-CL J2030−5638	0.394	307.688610	−56.632185	4.12 ± 1.10	1.01	3.06	23.56	24.09	22.53
SPT-CL J2032−5627	0.284	308.058670	−56.436827	6.29 ± 1.29	1.21	4.56	23.26	24.04	22.22
SPT-CL J2135−5726	0.427	323.914680	−57.437519	7.02 ± 1.39	1.19	3.44	23.45	23.96	22.50
SPT-CL J2138−6008	0.319	324.500020	−60.131848	8.19 ± 1.61	1.30	4.54	22.92	23.46	21.71
SPT-CL J2145−5644	0.480	326.466340	−56.748231	7.85 ± 1.53	1.21	3.27	23.94	24.37	22.98
SPT-CL J2332−5358	0.402	353.114480	−53.974436	6.10 ± 1.23	1.14	3.43	24.26	24.78	23.66
SPT-CL J2355−5056	0.320	358.947150	−50.927604	4.80 ± 1.10	1.09	3.79	24.04	24.78	23.37

5.4.2 Data

The data acquisition, image reduction, source extraction, and the photometric calibration are described in High et al. (2012), to which we refer the reader for more details. In summary, the 19 galaxy clusters studied in this work were all observed using Megacam on the Magellan Clay 6.5-m telescope through g', r' and i' filters. The Megacam field of view is $25' \times 25'$, which at the redshifts of our clusters covers a region around the cluster that extends to over $2.5R_{500}$ and allows us to extract the background number density n_0 at large radii where the magnification effect is negligible. Except for SPT-CL J0516−5430, each cluster was observed through g' and r' filters in a three-point diagonal linear dither pattern with total exposure times of 1200 s and 1800 s, respectively, while a five-point diagonal linear dither pattern was used for i' band imaging with a total exposure time of 2400 s. SPT-CL J0516−5430 was observed with a 2×2 square dither mode and a total of eight pointings through the g', r' and i' filters with total exposure times of 1200 s, 1760 s, and 3600 s, respectively.

Catalogs were created using `SExtractor` (Bertin & Arnouts, 1996) in dual image mode. Given that the r' images have the best seeing with the smallest variation, we use these as detection images. We adopt `MAG_AUTO` for photometry. The stellar locus together with 2MASS photometry is used both to determine zeropoint differences between bands (High et al., 2009) and the absolute zeropoint calibration (Song et al., 2012c; Desai et al., 2012). This results in the systematic uncertainties of colours $g' - r'$ and $r' - i'$ smaller than 0.03 mag. The absolute photometric calibration has uncertainties of $\lesssim 0.05$ mag. Similarly to High et al. (2012), we convert

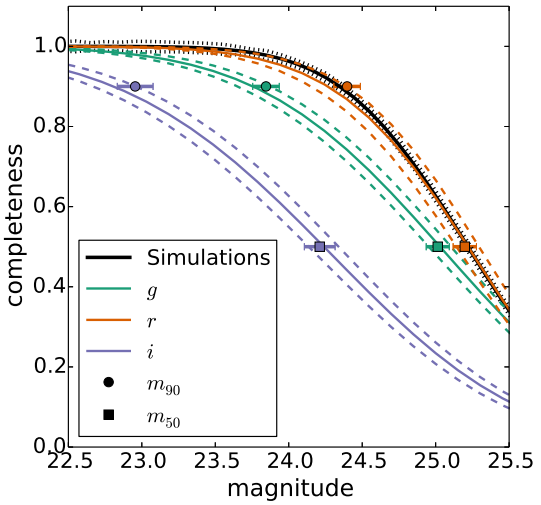

Figure 5.1: The completeness of the source detection as a function of magnitude. The completeness derived from g, r and i source catalogs is plotted in the solid lines while the uncertainty of the mean is represented by the dashed lines. The solid circles and squares are the means of m_{90} and m_{50} measured from the 19 cluster fields, respectively. Completeness functions for g, r and i are colour coded in green, orange and blue, respectively. The completeness function and its uncertainties measured on the mean of our image simulations are the black lines. Note that the derived completeness is based on our catalogs obtained by running `SExtractor` in dual image mode with the r-band imaging as the detection band.

our photometry from the SDSS system to the Canada-France-Hawaii Telescope Legacy Survey (CFHTLS) system (Regnault et al., 2009)[1]. For convenience, we write g instead of $g_{\rm CFHT}$, and equivalently in other bands.

5.5 Analysis

We stack the galaxy count profiles of 19 clusters to enhance the SNR of the magnification bias and then fit a composite model that includes the individual cluster masking corrections, source count-magnitude distribution slope s and the lensing efficiency. This stacked analysis ends in a consistency test of the SZE inferred masses for the cluster ensemble. Details are provided in the subsections below.

5.5.1 Source Catalog Completeness Limits

We estimate the completeness of the source catalog by comparing our number counts to that of a deep reference field where the source detection is complete in the magnitude range of interest in this work. In particular we extract the limiting magnitude where the completeness is 90% (m_{90})

[1] http://terapix.iap.fr/rubrique.php?id_rubrique=241

and 50% (m_{50}) for our source detection. Here we use the CFHTLS-DEEP survey (Ilbert et al., 2006; Coupon et al., 2009), in which the 80% completeness limits lie at magnitudes of $u = 26.3$, $g = 26.0$, $r = 25.6$, $i = 25.4$ and $z = 23.9$. Assuming that the complete source count-magnitude distribution can be described by a power law (i.e., $\log n(m) \propto a \times m + b$, where a is the slope and b is the normalization), we first derive its slope from the reference field using the magnitude range 20 to 24 in each band. Using this slope, we then fit the normalization of the source counts for galaxies brighter than 22 mag observed in the outskirts of our clusters ($r > 2R_{500}$). We use the ratio of the source counts in the cluster field to the derived best-fit power law to model the completeness function for each cluster as an error function. Specifically, the completeness function $F_{\rm c}$ is defined by

$$F_{\rm c}(m) = \frac{1}{2} - \frac{1}{2}\,{\rm erf}\left(\frac{m - m_{50}}{\sigma_{\rm m}}\right), \tag{5.12}$$

where erf is the error function, m_{50} is the magnitude at which 50% completeness is reached, and $\sigma_{\rm m}$ is the characteristic width of the magnitude range over which the completeness decreases.

We use the best-fit parameters of the completeness model for each cluster to derive the 90% completeness limit m_{90}. We show the mean of the completeness functions as well as the measured m_{90} and m_{50} of the 19 clusters for the three filters in Figure 5.1.

The mean m_{90} of the 19 observed clusters is 23.84, 24.39 and 22.95 for the filters g, r and i, respectively. The m_{90}'s for the g, r and i passbands in each cluster are listed in Table 5.1. Note that the depths in the i imaging limit our analysis at magnitudes fainter than 24 mag.

After accounting for differences in primary mirror area, exposure time and quantum efficiency, we compare our completeness limits to those of SDSS Stripe 82 (Annis et al., 2014). We estimate that in the background limited regime our Magellan imaging should be deeper by 1.1 mag, 1.2 mag and 1.3 mag in *gri*, respectively, in comparison to SDSS Stripe 82. Because the seeing is better in our Magellan imaging than in Stripe 82 we would expect these estimates to somewhat underestimate the true differences in the completeness limits. A comparison of our 50% completeness limits m_{50} with theirs (see Figure 7 in Annis et al. (2014)) indicates that our catalogs are deeper by 1.3 ± 0.3, 1.8 ± 0.3, 1.2 ± 0.5 mag, for *gri*, respectively, indicating good consistency with expectation. The comparison of m_{90} in our two datasets leads to the same conclusion.

The source detection is also unavoidably affected by blending, especially in the crowded environment of clusters. We address how the blending affects the completeness of background galaxies with image simulations. With realistic image simulations we can quantify the incompleteness as a function of magnitude and distance from the cluster centre and, therefore, apply a completeness correction to the analysis.

Specifically, we simulate images using GALSIM (Rowe et al., 2015) and derive the completeness of the sources detected by running `SExtractor` with the same configuration we use in the observed images. We simulate 40 images with a set of galaxy populations and stars. Each image contains a spatially uniform distribution of background galaxies and foreground stars.

We simulate background galaxies with a power law index $s = 0.4$ of the source count-magnitude relation between the apparent magnitudes of 20 and 25.5 at $z = 0.9$, which is the median redshift of the low-z background population studied here (see Section 5.5.2). The result-

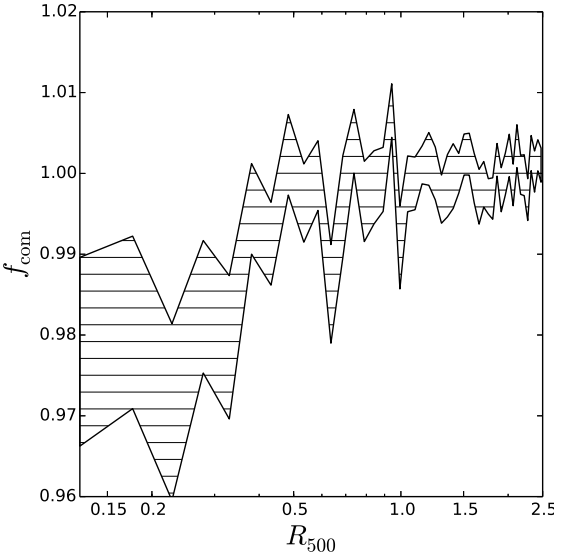

Figure 5.2: The radial completeness $f_{\rm com}$(x) at $m_{\rm cut} = 23.5$ as a function of distance from the cluster centre derived from the simulations. The 1σ confidence region is filled with horizontal lines.

ing average projected number density is ≈ 56 arcmin^{-2}, which matches the projected number densities of our source catalogs. Fifty bright stars with apparent magnitude between 18 mag and 20 mag are simulated. In addition to fore- and backgrounds, we simulate a cluster of $M_{500} = 6 \times 10^{14} \mathrm{M}_{\odot}$ at $z = 0.42$ with the BCG in the centre and a population of early type galaxies spatially distributed following a projected NFW (Navarro et al., 1997b) profile (e.g., Lin et al., 2004). We populate the cluster with galaxies between the apparent magnitudes of 18 and 25.5 according to a Schechter (1976) luminosity function with characteristic magnitude, power law index of the faint end, and normalization measured from Zenteno et al. (2011), which leads to 515 cluster galaxies within the R_{200} sphere. The half-light radius of each galaxy is randomly sampled according to the distribution of `FLUX_RADIUS` from the source catalog extracted from the Megacam images, which is between $0''.15$ and $1''$. The half-light radius for the BCG is randomly sampled from the range $0''.84$–$2''.5$, and to include the effects of saturated stars, the stellar half-light radii are randomly sampled from the range $0''.5$–$3''$. Each object is convolved with a point spread function to reproduce the average seeing of our images. Poisson noise with the mean derived from the *r* data of the Megacam images is added to the images. In the end, we derive the mean of the completeness function for the source detection from these simulated images.

Figure 5.1 shows the comparison between the completeness functions of the real and the simulated data. We find that there is a good agreement for the completeness of the source detections between the simulations and the *r* filter, which is our detection band for cataloging. The completeness is $> 94\%$ for the background galaxies brighter than 24.0 mag. We further derive the completeness correction as the function of the distance from the cluster centre at magnitude cut $m_{\rm cut}$. Specifically, the completeness correction $f_{\rm com}$ at $m_{\rm cut}$ is derived by taking the ratio of

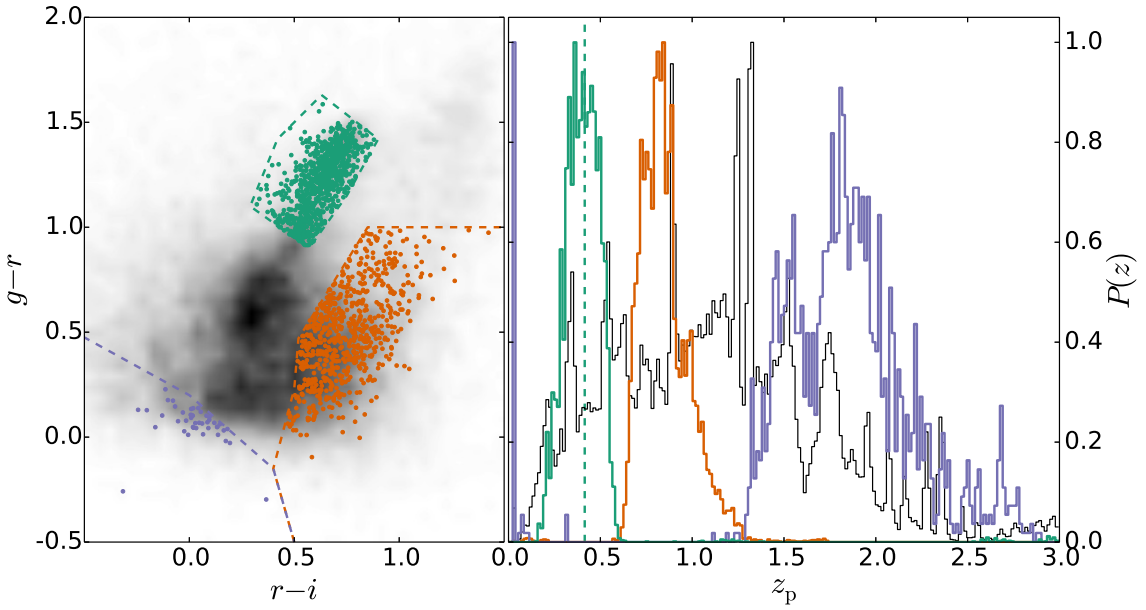

Figure 5.3: Illustration of the colour-colour background selection in the case of SPT-CL J0234−5831 ($z = 0.42$) with magnitude cuts $20.0 \leq g \leq 23.5$. On the left is the $g-r$ versus $r-i$ colour-colour diagram showing the observed galaxy density distribution (gray scale), the passively evolving cluster galaxy population (green), the $z \approx 0.9$ background (orange) and the $z \approx 1.8$ background (blue). The corresponding normalized redshift probability distribution $P(z)$ estimated from CFHTLS-DEEP for each population is shown on the right. The green dashed line marks the cluster redshift.

projected number density of detected galaxies between each radial bin and the radial range of $1.5 \leq x \leq 2.5$., i.e.,

$$f_{\rm com}(x) = \frac{n_{\rm sim}(x)}{n_{\rm sim}(1.5 \leq x \leq 2.5)}\,, \tag{5.13}$$

where $x = r/R_{500}$ and $n_{\rm sim}$ denotes the mean of the projected number density of the galaxies detected in the simulation (i.e., $f_{\rm com} = 1$ stands for no spurious magnification bias signal created by source blending). The derived $f_{\rm com}$ at $m_{\rm cut} = 23.5$ mag, which is the $m_{\rm cut}$ we use in this work (see Section 5.5.5), is shown in Figure 5.2. We find that the incompleteness due to blending is at level of $\approx 2.5\%$ in the inner region of clusters ($0.1 \leq x \leq 0.2$) and we apply this completeness correction as a function of cluster centric radius in our analysis (see Section 5.5.8).

5.5.2 Background Selection

Careful selection of the background galaxies is crucial for any lensing study. It has been demonstrated that the colour selection can effectively separate galaxies at different redshifts (e.g., Adelberger et al., 2004). In our case, the background galaxy population is selected by applying colour

cuts in a $g-r$ versus $r-i$ colour-colour space as well as a magnitude cut in the band of interest. We first split our cluster sample into four redshift bins from 0.25 to 0.65 in steps of 0.1 and define colour cuts corresponding to the different redshift bins.

The colour cut in each redshift bin is defined by three regions: a low redshift background population, a high redshift background population, and the passively evolving cluster galaxies at the redshift of the bin. We define colour-colour cuts for the low- and high-z backgrounds by tracking the colour evolution of early and late types galaxies using the Galaxy Evolutionary Synthesis Models (GALEV, Kotulla et al., 2009). It has previously been shown that the low- and high-z backgrounds can be successfully separated from the cluster galaxies (Medezinski et al., 2010). We conservatively exclude regions where GALEV predicts galaxy colours at the cluster redshift for all types of galaxies.

The low-z background is bluer (redder) than the cluster galaxies by ≈ 0.8 mag (≈ 0.1 mag) in $g-r$ ($r-i$), while the high-z background is bluer than the cluster galaxies by ≈ 1.2 mag and ≈ 0.6 mag in $g-r$ and $r-i$, respectively. By estimating the redshift distribution of the background (see Section 5.5.3), the colour selection leads to the redshift distribution of the low- and high-z background populations with $\langle z\rangle \simeq 0.9$ and $\langle z\rangle \simeq 1.8$, respectively. An example of the background selection for the redshift bin $0.35 \leq z < 0.45$ is given in Figure 5.3.

In this work we study the magnification bias in the g band for galaxies brighter than the limiting magnitude of 23.5, given that the strongest signal for positive magnification bias is expected here (discussed further in Section 5.5.5). We apply a magnitude cut imposing $20 \leq g \leq 23.5$ for the low and high redshift background populations selected by our colour cuts. There are no cuts applied in the other bands. Our final background samples provide pure background galaxy populations at low- and high-z consistent with no cluster member contamination, as we will show in Section 5.5.3.

5.5.3 Background Lensing Efficiency

A reliable estimate of the lensing efficiency of the background galaxies requires their redshift distribution and thus is not possible from our three band data alone. Thus, we estimate the lensing efficiency within the CFHTLS-DEEP reference field where photometric redshifts are known with a precision $\sigma_{\Delta z/(1+z)} = 0.037$ at $i \leq 24.0$ (Ilbert et al., 2006).

To estimate the redshift distribution from the reference field we first select galaxies with reliable photo-z estimates $z_{\rm p}$ by requiring `flag_terapix` $= 0$ and `zp_reliable` $= 0$ in the CFHTLS-DEEP catalog. The cut of `zp_reliable` $= 0$ removes the galaxies due to inadequate filter coverages or problematic template fitting in the spectra energy distributions. This cut removes less than 0.25% of the galaxies in the magnitude range of interest ($g \leq 23.5$ mag, see Section 5.5.5); therefore, we ignore this effect. We then estimate the average lensing efficiency $\langle\beta\rangle$ using the redshift distribution $P(z)$ for each selected background population. Specifically, the $P(z)$ for each background population is derived from the reference field with the measured photo-z after applying the same colour and magnitude selection as in the cluster fields. Results for an example cluster are shown in the right panel of Figure 5.3, where two different background populations are identified and the passively evolving cluster population is shown for comparison. The average lensing efficiency parameter $\langle\beta\rangle$ of the selected background population is estimated

by averaging over the $P(z)$ derived from the CFHTLS-DEEP field as

$$\langle\beta\rangle_{\rm t} = \int P_{\rm t}(z)\beta(z,z_{\rm l})dz\,, \tag{5.14}$$

where t = {low-z, high-z} denotes the background types and $z_{\rm l}$ is the cluster redshift.

We further test the impact of distorted redshift distributions on the estimates of $\langle\beta\rangle$ for the two background populations. The redshift distribution of the background is distorted due to the fact that background galaxies at different redshifts experience different magnifications. For example, a background population with the power law index $s > 0.4$ leads to the redshift enhancement effect (Coupon et al., 2013) and, therefore, the average lensing efficiency deviates from the $\langle\beta\rangle$ estimated from the reference field. We estimate the redshift distortion effect on our $\langle\beta\rangle$ estimations as follows. We assume a background population with a power law index $s = 0.8$ and estimate the fractional change $\langle\beta\rangle_{\rm l}/\langle\beta\rangle$ in the presence of magnification caused by a cluster with $M_{500} = 6\times10^{14}{\rm M}_{\odot}$ at $z_{\rm l} = 0.42$, where

$$\langle\beta\rangle_{\rm l} = \int P_{\rm ref}(z)\mu(M_{500},z_{\rm l},z)^{2.5s-1}\beta(z){\rm d}z \tag{5.15}$$

and $P_{\rm ref}(z)$ is the redshift distribution of the reference field where no lensing effect due to clusters is present.

We parametrize the cluster mass profile by the NFW model assuming the mass-concentration relation of Duffy et al. (2008). This model predicts a fractional change of $\langle\beta\rangle$ of at most $\approx$ 1.6% and $\approx 0.8\%$ in the cluster inner region $0.1 \leq x \leq 0.2$ for the low- and high-z backgrounds, respectively. We note that the redshift distortion is more prominent for the low-z background at $\langle z\rangle \approx 0.9$ because it is closer to the median redshift of our cluster sample ($\langle z_{\rm l}\rangle = 0.42$). Moreover, the power law index s of the low-z background population is much lower than the assumed $s = 0.8$ (see Section 5.5.5). This leads us to the conclusion that the impact of redshift distortion on estimating $\langle\beta\rangle$ is $< 1.6\%$. At this level, corrections for distortions of the redshift distribution to the $\langle\beta\rangle$ estimations are not needed for this analysis.

5.5.4 Cluster Member Contamination

The presence of cluster members in the selected background samples mimics the magnification signal, therefore it is crucial to quantify the cluster member contamination. It is common in lensing studies that the reliable redshift information to separate the cluster members and background samples is not available for the observed cluster fields. Hence, analyses often depend on information from a reference field. By leveraging a reference field, we estimate the cluster member contamination of the selected background populations by statistically connecting the observed magnitudes of the selected galaxies to the redshift information taken from the reference field. Specifically, we use the method developed by Gruen et al. (2014), in which they estimated the fraction of the cluster galaxies contaminating the background population by decomposing the observed distribution of the lensing efficiency, $P(\beta)$, into the known distributions of cluster members and background galaxies. Specifically, we estimate $P(\beta)$ of the cluster members and

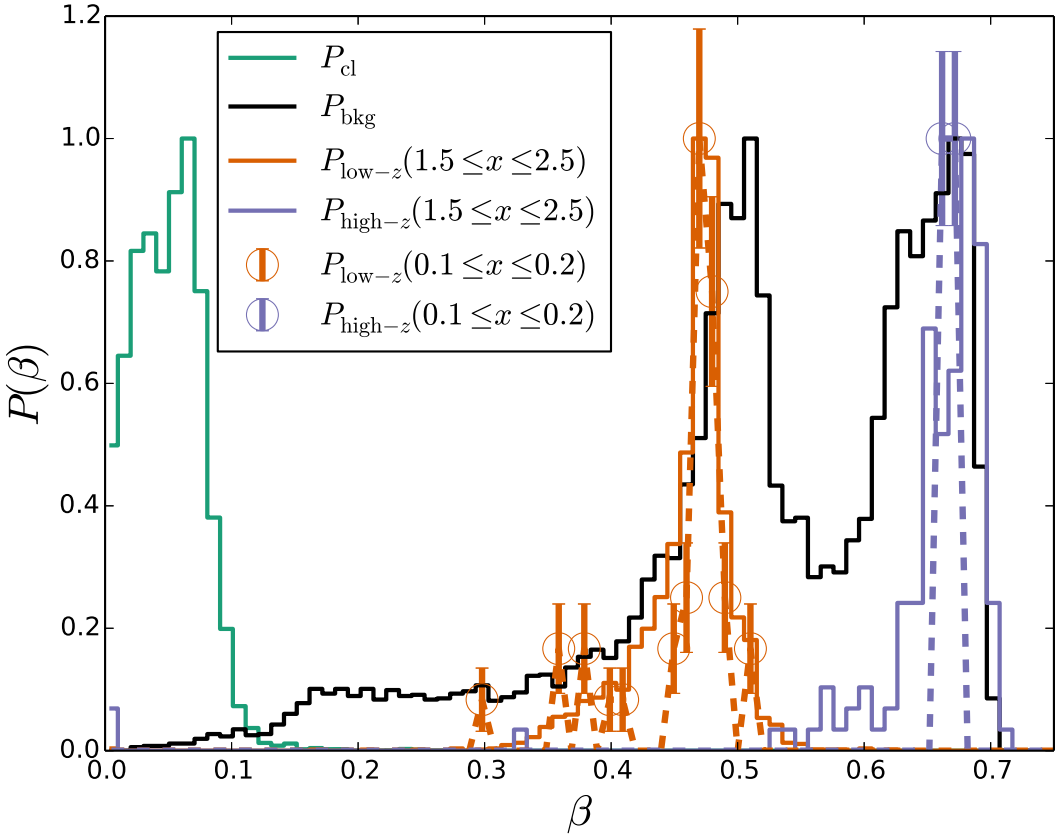

Figure 5.4: Comparison of the distributions of lensing efficiency $P(\beta)$ for clusters at $0.35 \leq z_{\rm l} < 0.45$. The $P(\beta)$ for cluster galaxies (identified by $|z - z_{\rm l}| \leq \Delta z$) and the background (identified $z > z_{\rm l} + \Delta z$) estimated from the reference field are shown in green and black solid lines, espectively. The $P(\beta)$ estimated from the stacked low- and high-z backgrounds are shown in orange and blue, respectively. The estimates from the outskirts ($1.5 \leq x \leq 2.5$) and the inner core ($0.1 \leq x \leq 0.2$) of our cluster fields are shown in solid lines and open circles, respectively, and they are in good agreement with each other and with the $P(\beta)$ for the background determined in the reference field. The large degree of separation between the low- and high-z backgrounds and the cluster galaxies illustrates the effectiveness of colour cuts at removing cluster galaxies from the lensing source galaxy populations. Note that the tiny fraction of $P(\beta)$ of the high-z background at $\beta = 0$ is due to the small population of the foreground galaxies instead of the cluster members (see the $P(z)$ in Figure 5.3).

background from the reference field by selecting the galaxies with $|z - z_{\rm l}| \leq \Delta z$ and $z > z_{\rm l} + \Delta z$, respectively, where $z_{\rm l}$ is the redshift of the cluster and $\Delta z = 0.05$.

For each galaxy i with the magnitudes $\mathbf{m_i} = (g_i, r_i, i_i)$, we estimate the expected lensing efficiency $\beta(\mathbf{m_i})$ and the probabilities of being a cluster member and a fore/background galaxy from the galaxy sample drawn from the reference catalog within the hypersphere $|\mathbf{m} - \mathbf{m_i}| \leq 0.1$ mag. The $P(\beta)$ of the population is then derived from the β estimations of the selected galaxies. We weight each galaxy by the probability of being a cluster member in deriving the $P(\beta)$ of the cluster galaxy population, while no weight is applied in deriving the $P(\beta)$ of the background population. The different magnitude distributions seen in galaxies at the cluster redshift in the cluster and in the reference fields are taken into account by applying the weighting in deriving the $P(\beta)$ of the cluster galaxy population. Following the same procedure, we also estimate the observed $P(\beta)$ from the stacked background galaxies in each radial bin and in the outskirts ($1.5 \leq x \leq 2.5$), where $x = r/R_{500}$ and R_{500} is the cluster radius derived from the SZE-inferred mass. In this way we can decompose the observed $P(\beta)$ and extract the fraction of the cluster galaxies contaminating the backgrounds.

The comparison of the distributions for the colour selection at $0.35 \leq z_{\rm l} \leq 0.45$ is shown in Figure 5.4. There is excellent agreement between the distribution of lensing efficiency in the outskirts ($1.5 \leq x \leq 2.5$) and in the inner core ($0.1 \leq x \leq 0.2$) regions for both low- and high-z backgrounds. In addition, neither of them overlaps the distribution of the cluster galaxies. The same general picture emerges for the colour selections conducted in other redshift bins.

Following the same procedure in Gruen et al. (2014), we fit the function $P_{\rm m}(\beta, x)$ to the observed distribution of β for each radial bin to estimate the cluster contamination. Specifically, we fit the fractional cluster contamination $f_{\rm cl}(x)$ of equation (5.16) at each radial bin x.

$$P_{\rm m}(\beta, x) = f_{\rm cl}(x) P_{\rm cl}(\beta) + (1 - f_{\rm cl}(x)) P(\beta, 1.5 \leq x \leq 2.5)\,, \tag{5.16}$$

where $P_{\rm cl}(\beta)$ is the distribution of β of the cluster members estimated from the reference field and $P(\beta, 1.5 \leq x \leq 2.5)$ is the distribution of β of the cluster outskirt ($1.5 \leq x \leq 2.5$). We use the Cash (1979) statistic to derive the best-fit cluster contamination $f_{\rm cl}$ and uncertainty. Specifically, the best-fit parameters and the confidence intervals are estimated by using the likelihood estimator

$$\begin{aligned} C_\beta = 2 \sum_i \Bigg(& N(x) P_{\rm m}(\beta_i, x) - N(\beta_i, x) \\ & + N(\beta_i, x) \ln \frac{N(\beta_i, x)}{N(x) P_{\rm m}(\beta_i, x)} \Bigg)\,, \end{aligned} \tag{5.17}$$

where $N(\beta_i, x)$ is the observed counts at radius x for the given β_i bin, $N(x)$ is the total galaxy counts at radius x (i.e., $N(x) = \sum_i N(\beta_i, x)$) and i runs over the binning in β. The resulting fraction of the cluster galaxies is all zero for $x \geq 0.1$ for both backgrounds, indicating that the selected backgrounds are free from cluster galaxy contamination. We discuss the uncertainty of the measured $f_{\rm cl}$ and its impact on the mass estimates in Section 5.6.2.

5.5.5 Power Law Index of the Galaxy Counts

Estimating the power law index s (see equation (5.9)) is crucial in magnification studies, because the magnification signal is proportional to $\mu^{2.5s}$. In this analysis, we do not estimate s for each individual cluster due to the low number of background galaxies. Rather, we estimate s from the reference field with the same selection critera applied as in the cluster field. Specifically, we fit a polynomial model,

$$\log(N_{\rm m}(<m)) = \frac{1}{2}am^2 + bm + c\,, \tag{5.18}$$

to the observed cumulative number counts $\log(N(<m))$ brighter than magnitude m. In this way, the power law index at magnitude cut $m_{\rm cut}$ can be calculated as $s(m_{\rm cut}) = am_{\rm cut} + b$. To estimate $s(m_{\rm cut})$ the fit is done locally on the interval of $-0.25 \leq (m - m_{\rm cut}) \leq 0.25$ on binned counts with a bin width of 0.05 mag. In fitting the model we take into account the covariance among different magnitude bins in $N(<m)$; the covariance matrix is estimated by bootstrapping 2500 realizations from the catalog itself. Specifically, the covariance matrix between magnitude bin m_i and m_j is built as

$$C_{i,j} = \left\langle (C_i - \langle C_i \rangle)(C_j - \left\langle C_j \right\rangle) \right\rangle\,, \tag{5.19}$$

where $C_i = \log N(<m_i)$ and the brackets $\langle\rangle$ represent an ensemble average. The best-fit parameters of the model (a,b,c) are obtained by minimizing

$$\chi^2 = \sum_{i,j} D_i \times {C^{-1}}_{i,j} \times D_j\,, \tag{5.20}$$

where $D_i = \log N_{\rm m}(<m_i) - \log N(<m_i)$, C^{-1} is the matrix inverse of $\left[C_{i,j}\right]$ and i and j run over the ten magnitude bins in the range being fit.

We find that fitting this model with a range of 0.5 mag centred on the magnitude at which the slope is being measured provides an unbiased estimate of $s(m_{\rm cut})$ when the Poisson noise in the binned galaxy counts lies in the Gaussian regime. Typically, we obtain $\chi^2_{\rm red} \approx 1.0$ and $\chi^2_{\rm red} \approx 0.8$ at $m_{\rm cut} \approx 23.25$–$24.25$ and $m_{\rm cut} \approx 24.25$–$25.0$, respectively. Furthermore, the statistical uncertainty of s is at the level of $\leq 1\%$ for $23.0 \leq m_{\rm cut} \leq 25.0$. As we will discuss in Section 5.6, an uncertainty of this magnitude on s translates into a mass uncertainty of $\approx 3.5\%$, which is small enough to have no impact on this analysis. We show the estimation of s from the reference field for the bands g, r and i as a function of magnitude $m_{\rm cut}$ between 23 mag and 25 mag in Figure 5.5, for the colour selection done in the redshift bin between 0.35 and 0.45.

We also compare the values of s for the CFHTLS-DEEP reference field to the s measured from the cluster outskirts ($1.5 \leq x \leq 2.5$) by stacking all 19 clusters in Figure 5.5. The s estimates of the low-z background show good consistency between the reference and the stacked cluster fields for g, r and i down to the completeness limits of our data. However, the s estimates from the stacked cluster fields tend to be lower than the ones measured from the reference field for fainter magnitudes $m_{\rm cut} \geq 24.0$ and in r and i, as one would expect given the onset of incompleteness in our dataset.

The s measurements for the high-z background sources from the stacked clusters do not agree as well with those from the reference fields. For $m_{\rm cut} \gtrsim 23.6$ mag, the incompleteness of the high-z background in the cluster fields starts to dominate the curvature of the source count-magnitude

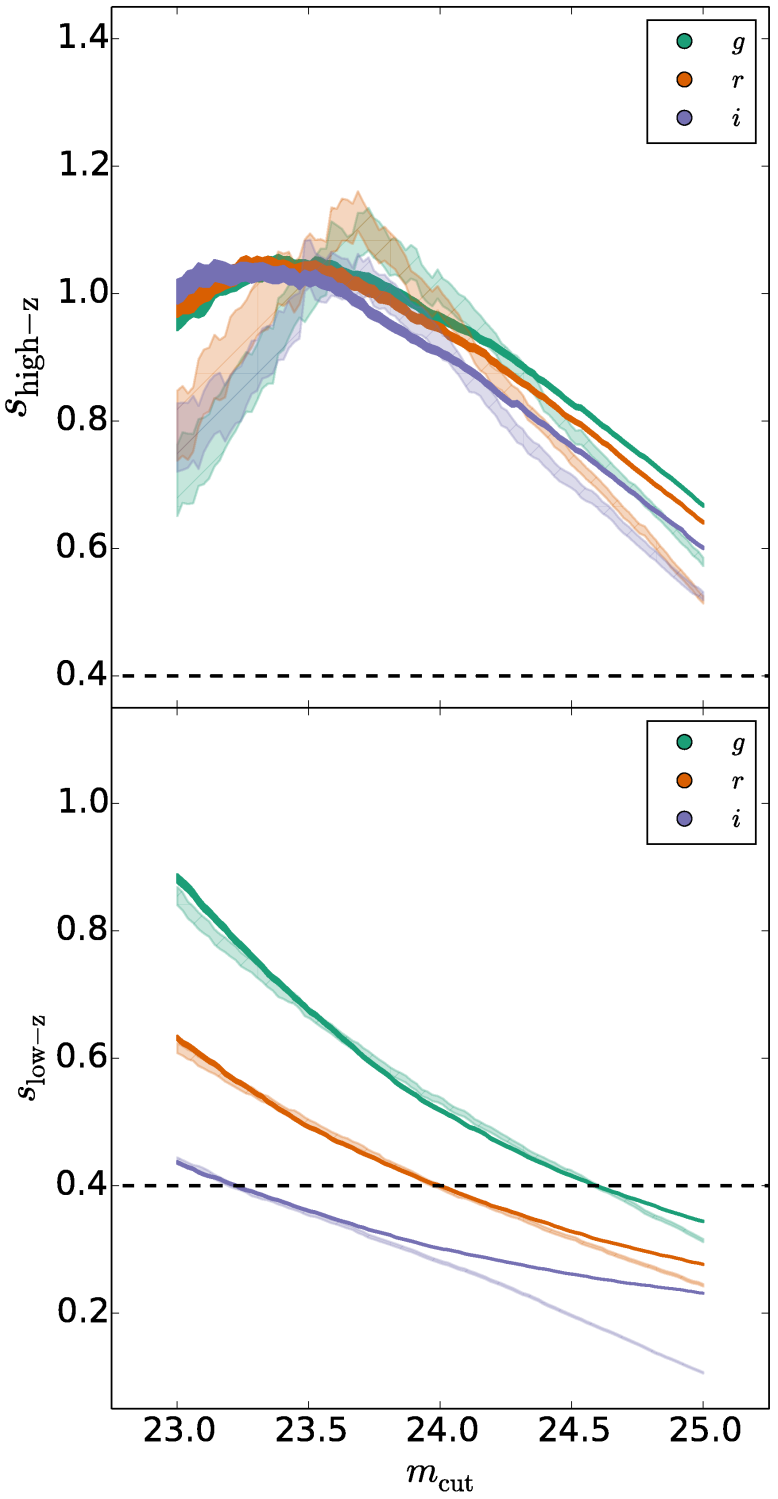

Figure 5.5: The power law index s of the galaxy flux-magnitude distribution as a function of magnitude m is shown for the high-z population (top) and the low-z population (bottom). The filled and transparent regions indicate the 1σ confidence levels of the power law index s extracted from the CFHTLS-DEEP reference and the stacked SPT cluster fields, respectively. The g, r and i bands are colour coded in green, orange and blue, respectively. The black dashed line indicates $s = 0.4$, where no magnification bias is expected.

relation, resulting in a power law index s that is systematically smaller than the reference field. Near $m_{\rm cut} \approx 23.5$ the two estimates are in agreement, but brighter than this the s is smaller in our cluster fields than in the reference fields. This can be explained by the impact of low galaxy counts on our s estimator. For $m_{\rm cut} \lesssim 23.6$ mag, the typical galaxy counts fall below 10 for the bin width of 0.05 mag. This leads to the bias in the fit, which is assuming Gaussian distributed errors. We examine this by randomly drawing 30 realizations from the reference field for the high-z background, where each realization has the same number of galaxies as the stacked cluster field. The bias toward low values in s from these random subsets of the reference field is consistent with that we see from the stacked cluster field, indicating that the underlying parent distributions in the cluster and reference fields are consistent.

In summary, the high-z background suffers more severely from low galaxy counts and incompleteness than the low-z background (see Section 5.5.2), and therefore the $s(m_{\rm cut})$ measurements in the stacked cluster and reference fields show better agreement. We will discuss errors in s as a source of systematic uncertainty in Section 5.6.

To choose a magnitude cut $m_{\rm cut}$ that maximizes the expected magnification signal, one must consider the slope s of the count-magnitude relation, the level of Poisson noise in the lensed sample and the onset of incompleteness. Given the depths of our photometry and the importance of the colour-colour cuts for identifying the background populations, we carry out the magnification bias analysis at $m_{\rm cut} = 23.5$ in g for the low- and high-z backgrounds. In particular, with this g cut the faintest required i magnitudes of the low- and high-z population galaxies are ≈ 22.3 mag and ≈ 23.5 mag. In our data set, i is the shallowest passband, but it reaches completeness levels of $> 80\%$ at these magnitudes except in the cluster SPT-CL J2138−6008. Note that incompleteness as a function of magnitude should in principle have no effect on the derived magnification profile ($\mu^{2.5s-1} = n(x)/n_0(1.5 \leq x \leq 2.5)$) as long as the incompleteness does not vary systematically with cluster radius. At this magnitude cut s is somewhat larger than 0.75, which corresponds to an $\approx 18\%$ density enhancement for $\kappa = 0.1$ assuming that $\mu \approx 1 + 2\kappa$ (see eq 5.11).

5.5.6 Masking Correction

When computing object surface densities we apply a masking correction to account for regions covered by bright cluster galaxies– mostly in the central region of the cluster– as well as bright and extended foreground objects, saturated stars, and other observational defects. Visually identifying masked areas is not feasible for a large cluster sample and could introduce non-uniformities. We adopt the method in Umetsu et al. (2011) to calculate the fractional area lost to galaxies, stars and defects as a function of distance from the cluster centre.

We tune the `SExtractor` configuration parameters by setting `DETECT_THRESH` = 5 and `DETECT_MINAREA` = 300 (corresponding to 7.68 arcsec^2) to detect bright and extended objects in the coadd image and mark them in the `CHECKIMAGE_TYPE` = `OBJECTS` mode. In addition, we visually inspect the images for effects like satellite trails that typically are not captured by the `SExtractor` run. We compute the fraction of unmasked area $f_{\rm umsk}$ where

$$f_{\rm umsk} = \frac{A_{\rm umsk}}{A_{\rm ann}}, \tag{5.21}$$

where $A_{\rm umsk}$ is the unmasked area of the annulus and $A_{\rm ann}$ is the geometric area of the annulus. We measure $f_{\rm umsk}$ as a function of cluster centric distance for each cluster and use it to apply a correction to the observed density profile. On average, the unmasked fraction (see Table 5.2) is $\approx$ 93–96% for all radii and greater than $\approx$ 94% towards the cluster centre ($0.1 \leq x \leq 0.2$). We take the masking effect into account by applying the $f_{\rm umsk}$ correction to the fitted model in each radial bin (see Section 5.5.8).

5.5.7 Background Profiles and Cluster Stack

We study the magnification bias of a flux-limited galaxy sample with $20.0 \leq g \leq 23.5$ for the low- and high-redshift background populations by stacking 19 SPT-selected clusters to enhance the signal. We stack the 19 clusters after rescaling the radii by the appropriate R_{500} derived from the SZE-inferred masses. This approach exploits the fact that the SZE-signature provides a low scatter mass proxy. Given the factor of two range in mass and redshift of our sample and the availability of the SZE-inferred masses, a stack in physical radius would not be advisable. For each of the two background populations we first derive the radial profile of the surface number density $n_i(x)$ as a function of $x = r/R_{500}$ at $0.1 \leq x \leq 2.5$ for each cluster i, adopting the BCG position as the cluster centre and using the SZE derived mass to define R_{500} (see Section 5.4.1).

$$n_i(x) = \frac{N_i(< m_{\rm cut}, x)}{A_{{\rm ann}i}(x) f_{{\rm umsk}i}(x) f_{\rm com}(x)}\,, \tag{5.22}$$

where $N_i(< m_{\rm cut}, x)$ is the observed cumulative number of galaxies brighter than the magnitude threshold $m_{\rm cut}$ that lie within a particular radial bin for the cluster and $A_{{\rm ann}i}$ is the area of the bin. The unmasked fraction $f_{\rm umsk}$ is used to correct the measured galaxy counts to the full expected galaxy counts in the absence of masking. The radial correction $f_{\rm com}$ is derived from our image simulations to account for the incompleteness due to blending (see Section 5.5.1), and it is the same for all clusters.

We choose bin widths of $\Delta x = 0.1$ for the range $0.1 \leq x \leq 0.5$ and $\Delta x = 0.25$ at $0.5 \leq x \leq 2.5$. The finer radial binning is used near the cluster centre because the gradient of the magnification signal is larger in the core. In the end, we stack the radial profiles to create the final stacked profile $n_{\rm tot}(x)$,

$$n_{\rm tot}(x) = \sum_{i=1}^{N_{\rm cl}} n_i(x), \tag{5.23}$$

where $n_i(x)$ is the radial surface density profile for cluster i as described above. Note that the observed profiles are directly stacked without applying weighting. The observed magnification profile is given by

$$\mu^{2.5s-1}(x) = \frac{n_{\rm tot}(x)}{n_{\rm tot}(1.5 \leq x \leq 2.5)}\,, \tag{5.24}$$

where the denominator is the mean of the counts profile in the radial range $1.5 \leq x \leq 2.5$. To compute uncertainties on the profiles, we include Poisson noise for the galaxy number counts in each radial bin. We ignore the variance in the profiles caused by local galaxy clustering in the

individual profiles because this variance is negligible compared to the Poisson noise (Zhang & Pen, 2005; Umetsu & Broadhurst, 2008; Umetsu, 2013). Through the stacking process both the variance due to local clustering and the Poisson noise are reduced because the cluster fields are independent.

The same stacking procedure is performed using the reference field as a null test. Specifically, we randomly draw 20 apertures each with R_{500} taken to be $3'$ while avoiding any region that has been heavily masked. We stack them as in equation (5.23) after applying the same background selection as for the cluster fields. Note that the remaining masked area of the selected apertures is negligible and the procedure of stacking apertures which are randomly drawn from the reference field can remove any systematic trend of the residual masking effect. We show the resulting profiles in Figure 5.6. The variation of the density profiles is consistent with the Poisson noise expectation and provides no evidence for an over- or under-density, providing an indication that our stacking procedure works.

After convincing ourselves that the stacking procedure on the reference field provides unbiased estimates, we then proceed to another null test on the cluster fields. This null test is defined by performing the same end-to-end analysis on the low-z background with magnitude cut at $r = 24$ mag instead of $g = 23.5$ mag used in our main analysis. The magnitude cut of $r = 24$ mag is chosen because the low-z background has $s \approx 0.4$ at $r = 24$ (see Figure 5.5), and therefore we expect no magnification signal. This is a powerful end to end test of our analysis; any signal detected in this null test indicates the spurious bias in our magnification analysis. The resulting low-z profile with the magnitude cut of $r = 24$ mag is shown in the black diamonds in Figure 5.6. The observed profile is consistent with $\mu = 1$, and no magnification signal is seen. We hence conclude that our analysis procedure provides unbiased magnification signals.

5.5.8 Model Fitting

To enable model fitting, we first create a stacked profile of the total observed number of galaxies $N_{\rm tot}$ above the magnitude threshold within each radial bin

$$N_{\rm tot}(x) = \sum_{i=1}^{N_{\rm cl}} N_i(x)\,, \tag{5.25}$$

where N_i is the observed number of galaxies in the bin $x = r/R_{500-{\rm SZE}i}$ for cluster i with radius $R_{500-{\rm SZE}i}$ derived using the SZE-inferred mass and the redshift.

We construct the model of the radial galaxy counts $N_{\rm mod}(x)$ by stacking the predicted galaxy counts for the 19 galaxy counts models $M_i(x)$ using– for each cluster i at radius of $x = r/R_{500-{\rm SZE}i}$– the average lensing efficiency $\langle\beta\rangle_i$, the power law index s, the observed background number density n_{0i}, the unmasked fraction $f_{{\rm umsk}i}$ and the completeness correction $f_{\rm com}$. Specifically, the model $N_{\rm mod}(x)$ is constructed as

$$N_{\rm mod}(x) = \sum_{i=1}^{N_{\rm cl}} n_{{\rm mod}i}(x) A_{{\rm ann}i}(x) f_{{\rm umsk}i}(x) f_{\rm com}(x)\,, \tag{5.26}$$

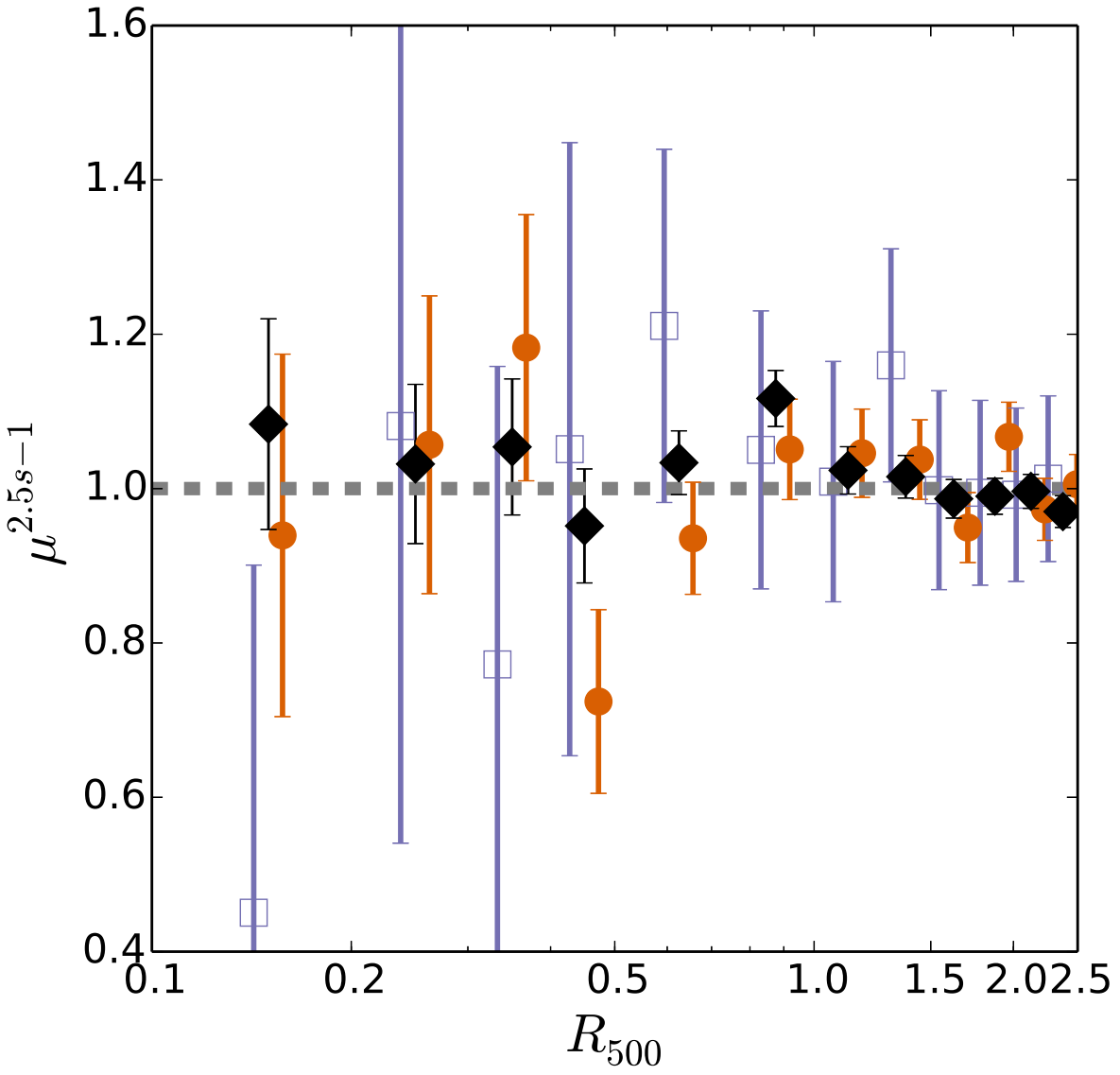

Figure 5.6: The null test on the reference field shows the normalized density profile of 20 randomly chosen apertures on the reference field after applying the same selection for the low-z (orange circles) and high-z (blue squares) backgrounds. The null test on the low-z background selected in the stacked cluster field with the magnitude cut at $r = 24$ mag (where $s = 0.4$ and no net effect is expected) is shown with the black diamonds. The red circles and blue squares are slightly offset along the horizontal axis for clarity.

Table 5.2: The observed background galaxies profiles, masking correction and completeness correction. Column 1–2: the lower and higher bound for each radial bin. Column 3: the observed galaxy counts for the low-z backgrounds. Column 4: the observed galaxy counts for the high-z backgrounds. Column 5: the fraction of the unmasked area $f_{\rm umsk}$. Column 6: the completeness correction $f_{\rm com}$ derived from the simulation.

$x_{\rm lo}$	$x_{\rm hi}$	$N_{\rm tot,low-z}$	$N_{\rm tot,high-z}$	$f_{\rm umsk}$	$f_{\rm com}$
0.10	0.20	35	4	0.953	0.979
0.20	0.30	34	2	0.948	0.977
0.30	0.40	50	4	0.946	0.987
0.40	0.50	66	3	0.942	0.997
0.50	0.75	224	16	0.932	0.996
0.75	1.00	326	18	0.948	0.998
1.00	1.25	352	24	0.931	1.000
1.25	1.50	445	18	0.932	0.998
1.50	1.75	514	37	0.939	0.999
1.75	2.00	576	26	0.943	0.998
2.00	2.25	668	43	0.946	1.000
2.25	2.50	726	49	0.959	1.000

and

$$n_{{\rm mod}i}(x) = n_{0i}\mu(M_{500i}, \langle\beta\rangle_i, x)^{2.5s-1}\,, \tag{5.27}$$

where n_{0i} is the number density measured in the range $1.5 \leq x \leq 2.5$ for cluster i with mass M_{500i}.

We parametrize the dark matter halo profile with the NFW model (Navarro et al., 1997b) assuming the mass-concentration relation of Duffy et al. (2008) for each cluster. During the fitting procedure we hold $\langle\beta\rangle_i$ and n_{0i} for each cluster fixed at their pre-determined values, and we use the appropriate s for each of the two background populations. We further simplify the model by fitting for a single multiplicative factor $\eta = M_{500i}/M_{500-{\rm SZE}i}$ for all the clusters. Where for $\eta = 1$ there is no net difference between the SZE-inferred and magnification masses within the full sample. As seen in equations (5.26) and (5.27), the model for the stacked observed galaxy counts $N_{\rm mod}(x)$ is then a function of only one variable.

To estimate the best-fit mass using the observed and theoretical total galaxy number profiles $N_{\rm tot}(x)$ and $N_{\rm mod}(x)$, we use the Cash (1979) statistic. The likelihood function for fitting the magnification bias models to the total galaxy number profiles is given by

$$\begin{aligned} C_{\rm stat} = 2\sum_t \sum_{j=1}^{N_{\rm bins}} \Bigg(& N_{\rm mod,t}(\tilde{x}_j) - N_{{\rm tot},t}(x_j) \\ & + N_{{\rm tot},t}(x_j) \ln \frac{N_{{\rm tot},t}(x_j)}{N_{{\rm mod},t}(\tilde{x}_j)} \Bigg)\,, \end{aligned} \tag{5.28}$$

where $t \in \{$low-z, high-z, combined$\}$ denotes the background populations. Note that to compare

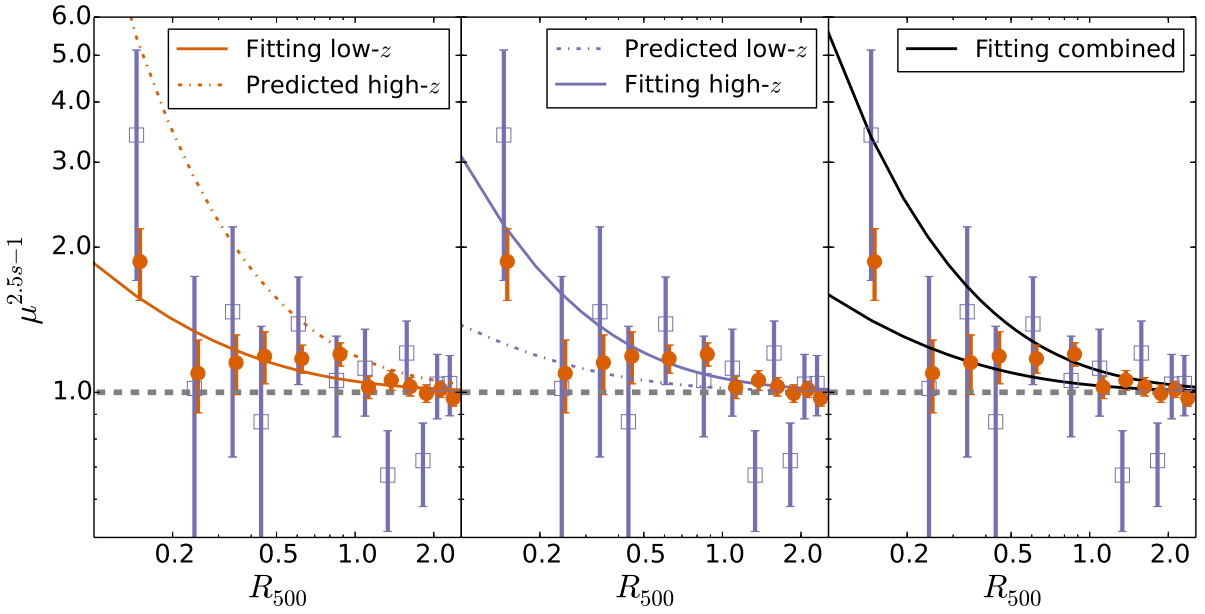

Figure 5.7: The stacked profiles for the low- and high-z background populations with the best-fit models from different scenarios. The panels contain the fit to the low-z background alone (left), the fit to the high-z population (middle), and the fit to the combined population (right). In all three panels the orange circles (blue squares) define the stacked profile of the low-z (high-z) population, the best-fit model is defined with solid lines and the predicted profile for the other population appears as a dot-dashed line. There is slight ($\approx 1.82\sigma$) tension between the low- and high-z populations, whereas the joint fit (right panel) is in good agreement with both populations.

the model and the observation at the same physical radius in the space of $x = r/R_{500}$ when $\eta \neq 1$ (i.e. $M_{500} \neq M_{500-\mathrm{SZE}}$), we compare the observed profile at x to the model profile at $\tilde{x}$, where $\tilde{x} = xR_{500-\mathrm{SZE}}/R_{500} = x\eta^{-\frac{1}{3}}$. When fitting to the combined sample, we simultaneously fit the models to the low-z and high-z background populations and then derive the best-fit η based on the sum of their C_{stat} values (see eq 5.28).

Note that the difference of the likelihood estimator from its best-fit value ΔC_{stat}, is distributed like a χ^2-distribution (Cash, 1979) and can be used to define parameter confidence intervals. Moreover, the best-fit value of C_{stat} can be used to test the consistency of the data and the model.

5.6 Results and Discussion

We present the results in Section 5.6.1 and then discuss several of the key systematic uncertainties in Section 5.6.2. Section 5.6.3 contains a comparison of the observed weak lensing shear profile with the predicted profile derived from the magnification analysis.

Table 5.3: Magnification analysis mass constraints, cross checks and detection significance. Column 1: background populations used in the fit. Column 2: best-fit η. Column 3–5: 1, 2, and 3 σ confidence level of the best-fit η. Column 6: reduced $C_{\rm stat}$ of the fit (degree of freedom: 10, 10 and 21 for the low-z, the high-z and the combined backgrounds, respectively). Columns 7–8: p-value that the best-fit model in Column 2 rejects the best-fit model in these columns. Column 9: detection significance over a model with $\eta = 0$.

Population	η	$1\sigma_\eta$	$2\sigma_\eta$	$3\sigma_\eta$	$C_{\rm stat}$/d.o.f	p-value to reject best-fit		Detection Significance
						Low-z	High-z	
Low-z	1.30	$^{+0.41}_{-0.39}$	$^{+0.85}_{-0.74}$	$^{+1.29}_{-1.04}$	1.23	0.268	0.075	3.34σ
High-z	0.46	$^{+0.33}_{-0.29}$	$^{+0.67}_{\cdots}$	$^{+1.00}_{\cdots}$	1.06	0.061	0.385	1.31σ
Combined	0.83	$^{+0.24}_{-0.24}$	$^{+0.49}_{-0.46}$	$^{+0.74}_{-0.65}$	1.22	0.186	0.289	3.57σ

5.6.1 Detection Significance and Mass Constraints

Using the procedure described in the previous section we construct the observed profiles for the ensemble of 19 massive galaxy clusters. Properties of these profiles, including the number of background galaxies in the low- and high-z populations and the masking and completeness corrections, are listed in Table 5.2; the profiles themselves appear in Figure 5.7.

We use these observed profiles to derive best-fit η of $1.30^{+0.41}_{-0.39}$, $0.46^{+0.33}_{-0.29}$ and 0.83 ± 0.24, for the low-z, high-z, and combined backgrounds respectively. We detect the magnification bias effect at 3.3σ, 1.3σ and 3.6σ for the low-z, high-z, and combined populations, respectively, where the confidence levels are defined via the $C_{\rm stat}$ goodness of fit statistic in comparing the observed profiles to a model with $\eta = 0$ (i.e. zero mass). Table 5.3 contains an overview of these fitting results and their statistical uncertainties.

In addition to the detection significances and confidence intervals of the best-fit masses, Table 5.3 provides information on the statistical consistency of the best-fit models of the low-z, high-z, and combined background best-fit models. The consistency between the observed profile and the best-fit model is derived using $C_{\rm stat}$. Given the best-fit model estimated from the low-z (high-z) background population, the probability of consistency with the high-z (low-z) background population is 0.075 (0.061). In other words, there is weak tension at the $\approx 1.82\sigma$ level.

Combing both backgrounds yields $\eta = 0.83 \pm 0.24$. The probabilities of consistency of the two populations with this model are 0.186 and 0.289 for the observed magnification profiles of the low- and high-z backgrounds, respectively.

Figure 5.7 contains not only the stacked profiles for the low- and high-redshift populations but also the best-fit models. In the left panel is the fit using only the low-z population (solid line), but the corresponding prediction for the high-z population is presented with the dot-dashed line. The middle panel shows the fit to only the high-z population (solid line) with the corresponding prediction for the low-z population (dot-dashed line). The right panel shows the joint fit to both populations (solid lines). All panels contain the same observed profiles for both populations. As is already clear from Table 5.3, there is weak tension between the independent fits to the low- and high-z populations ($\approx 1.82\sigma$) but the joint fit is fully consistent with both background

populations.

The posterior distributions of η derived by fitting the model to the low-z, high-z and combined background samples are shown in Figure 5.8. The $\eta = 1$ (dotted line) marks the value where the SZE-inferred and magnification masses would on average be equal. The mass factors η estimated from the magnification bias measurements of the low-z (dashed line) and high-z (dot-dashed line) backgrounds are marginally consistent with one another ($\approx 1.82\sigma$ difference). The magnification constraint from the low-z (high-z) sample yields mass estimates that are 30% higher (54% lower) than the SZE-inferred masses, corresponding to differences with $\approx 0.77\sigma$ ($\approx 1.6\sigma$) significance. The combined samples prefer magnification masses that are 17% lower than the SZE-inferred masses, corresponding to a difference of $\approx 0.71\sigma$. Overall, there is no significant tension between the magnification constraints and the masses extracted using the SZE observable-mass scaling relation.

5.6.2 Systematic Effects

In the following we study the influence of various sources of systematic errors on η including (1) differences in photometric noise in the cluster and reference fields, (2) colour biases between the two fields, (3) flux biases, (4) cluster contamination and (5) biases in the estimate of the power law slope s. We explain each of these tests and the resulting impact below. Table 5.4 contains the results of our systematics tests.

Noisy photometry $\sigma_{\rm mag}$*:* To explore whether the noisier photometry in the cluster fields is impacting our analysis, we degrade the photometry of the reference field and quantify how the change of the background properties impacts the final mass factor η. Specifically, we first apply a model of magnitude uncertainty versus magnitude distribution measured from the cluster field to the reference field to degrade the photometry. We then randomly perturb the magnitude for each object in the reference field assuming the magnitudes scatter randomly following a normal distribution with a standard deviation given by the degraded magnitude uncertainty. In the end we re-measure the background properties and repeat the whole analysis to study the impact on the final best-fit η. As can be seen in Table 5.4, the noisy photometry test results in negligible systematic uncertainties on the estimations of $\langle\beta\rangle$, s and η; this is due to the fact that the photometry noise for these bright – relative to the completeness limit – galaxies is small.

Biased colours Δ Colour*:* Galaxy colour biases between the reference and cluster fields could also impact our best-fit η. To illustrate this we measure the power law index s at $m_{\rm cut} = 23.5$ in g band in the reference field as a function of the colours of $g-r$ and $r-i$. The resulting s-map overplotted with the colour selection of the redshift bin $0.35 \leq z < 0.45$ is shown in Figure 5.9. The colour selection of the background populations can be adjusted to correspond to populations with common s and to ensure that colour boundaries do not lie where s is changing rapidly.

We test the impact of a bias in the galaxy colours, which are calibrated with respect to the stellar locus, by shifting the whole $g-r$ versus $r-i$ distribution systematically by the systematic colour uncertainty 0.03 mag (see Section 5.4.2). Specifically, we shift each object in the colour-colour space by decreasing the value of $g-r$ by 0.03 mag combined with the systematics shift ± 0.03 mag in the colour of $r-i$. The objects that shift across the colour cut into the background regions are then set to have redshift zero to estimate the largest possible impact from the fore-

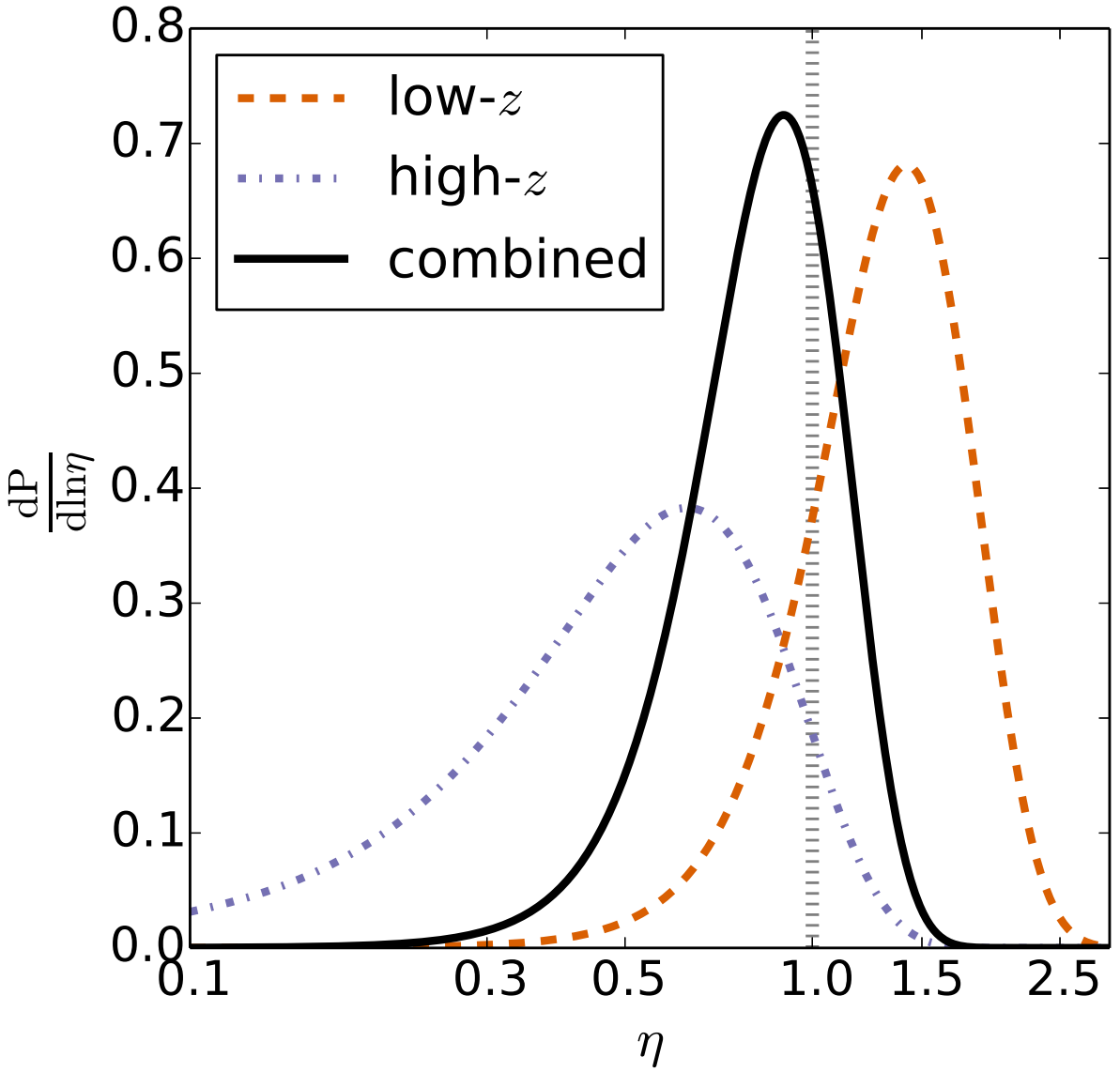

Figure 5.8: The posterior distribution $P(\eta)$ of the multiplicative factor η given the magnification constraints. The grey dotted line marks $\eta = 1$ (perfect consistency of SZE and magnification masses). The posterior distributions $P(\eta)$ estimated from fitting the magnification bias model to the low-z (orange dashed), high-z (blue dot-dashed), and combined (black solid) populations are plotted. None of the magnification constraints show significant tension with the SZE-inferred masses, indicating 0.77σ, 1.6σ and 0.71σ differences with $\eta = 1$ for the low-z, high-z and combined background populations, respectively. Note that we express the posterior distribution in $\frac{dP}{d\ln\eta} = P(\eta) \times \eta$.

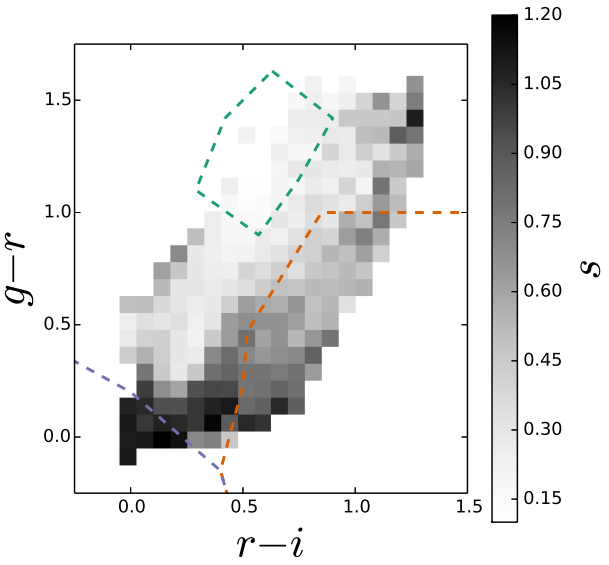

Figure 5.9: The power law index s at $m_{\rm cut} = 23.5$ in g band estimated from the reference field as a function of the colours ($g-r$ and $r-i$). The estimations of s are shown in greyscale. The green, orange and blue dashed lines indicate the colour selections of the cluster members, the low-z and the high-z backgrounds, respectively, for the cluster at the redshift bin $0.35 \leq z < 0.45$. The slope s changes rapidly with colour in the regions near the low-z and the high-z backgrounds.

ground or cluster members. We derive the systematic uncertainties of the mass factor η by taking the average of the systematic mass shifts associated with the shift of ± 0.03 mag in $r-i$ colour. We find that the slope s changes at the $\approx 2\%$ ($\approx 1\%$) level for the low-z (high-z) population, implying systematic uncertainties in η on the order of $\approx 8\%$ ($\approx 6.7\%$). The resulting systematic change in the combined analysis is at the level of $\approx 7\%$. We stress that this systematic uncertainty states the extreme case assuming all the galaxies with biased colours are cluster members. These uncertainties are smaller than the current statistical uncertainties.

Biased fluxes Δ Flux*:* A bias in the absolute magnitude calibration between the cluster field and reference field could lead to a biased estimation of s for a given $m_{\rm cut}$. To test a flux bias at the level of the systematic flux uncertainty of ≤ 0.05 mag (see Section 5.4.2), we extract the s estimation in g at the magnitude of $m_{\rm cut} + 0.05$ mag and repeat the whole analysis. This results in a change in the estimation of s by $\approx 1\%$ in the low-z population, leading to a shift in η at the $\approx 4\%$ level. The impact on the high-z population is smaller with a $\approx 0.6\%$ shift in s and a $\approx 2\%$ bias in η.

Contamination: In addition to studying the photometry effects, we also examine the impact of the cluster member contamination of the background populations. The cluster contamination in the innermost bin is $0 \pm 0.56\%$ inferred from the decomposition of the observed $P(\beta, 0.1 \leq x \leq 0.2)$ of the low-z background (see Section 5.5.3). The cluster contamination of the high-z background is 0% in the inner most bin with much larger uncertainty ($\approx 25\%$) because the

Table 5.4: Influence of systematic effects on the estimated η. Column 1: systematic. Column 2–3: change in $\langle\beta\rangle$ for the low- and high-z backgrounds. Column 4–5: change in s for the low- and high-z backgrounds. Column 6–8: change in η for fitting the low low-z, high-z and combined backgrounds.

Sources	$\frac{\Delta\langle\beta\rangle}{\langle\beta\rangle}$ [%]		$\frac{\Delta s}{s}$ [%]		$\frac{\Delta\eta}{\eta}$ [%]		
	Lo-z	Hi-z	Lo-z	Hi-z	Lo-z	Hi-z	Cmb
$\sigma_{\rm mag}$	-0.1	-1.5	0.3	1.5	1.2	-0.4	1.0
Δ Colour	-2.4	-4.0	-1.9	-0.9	8.0	6.7	7.4
Δ Flux	$\cdots$	$\cdots$	-1.0	0.6	3.8	-2.2	2.7
Contam	$\cdots$	$\cdots$	$\cdots$	$\cdots$	-2.9	-1.7	-2.5
Δs	$\cdots$	$\cdots$	-0.7	-1.6	3.5	3.0	3.2
$\sigma_{\rm sys}^{\rm tot}$	$\cdots$	$\cdots$	$\cdots$	$\cdots$	10.0	7.9	8.9

† $\Delta \equiv$ (Values considering the systematics) $-$ (Original values).

galaxy counts are ≈ 10 times lower than in the low-z case. However, because the $P(\beta)$ of the high-z background is further separated from the $P(\beta)$ of the cluster members than the low-z background (see Figure 5.4), the well constrained cluster contamination of the low-z background sets a reasonable upper bound for the cluster contamination also of the high-z population. We therefore use the uncertainty of the cluster contamination inferred from the low-z background as the baseline to quantify the systematic uncertainty for both populations.

We explore the impact of residual contamination by repeating the whole analysis after introducing cluster contamination into the $N_{\rm mod}(x)$ with 1% contamination in the innermost bin and decreasing towards the cluster outskirts following a projected NFW profile with concentration $C_{500} = 1.9$ (Lin et al., 2004). Contamination of this sort leads to a mass factor η biased high by $\approx 3\%$.

We further quantify the impact of cosmic variance of the derived $P_{\rm cl}(\beta)$ on the estimated cluster contamination $f_{\rm cl}$. Specifically, we derive the $P_{\rm cl}(\beta)$ from 20 realizations, where each realization has 200 cluster galaxy members randomly drawn from the reference field. We then estimate the contribution of cosmic variance to the derived $P_{\rm cl}(\beta)$ by calculating the uncertainty of the mean $P_{\rm cl}(\beta)$ of these 20 realizations. As a result, the cosmic variance contributing to the derived $P_{\rm cl}(\beta)$ is at the level of $\lesssim 3\%$ for a given β, indicating that the uncertainty of $f_{\rm cl}$ due to cosmic variance is at the same level of $\approx 3\%$. Accordingly, a 3% contamination would lead to a mass factor η biased high at the level of $\approx 9\%$. In this work we use the $f_{\rm cl}(0.1 \leq x \leq 0.2) = 1\%$, which is ≈ 2 times of the derived statistical uncertainty of $f_{\rm cl}$, to estimate the systematic uncertainty of η. The resulting change in mass estimates is shown in Table 5.4. We stress that the proper uncertainty of cluster contamination $f_{\rm cl}$ estimated from the method of Gruen et al. (2014) should include both the statistical variation of the observed $P(\beta)$ at each radial bin and the cosmic variance of the derived $P_{\rm cl}(\beta)$ of cluster members. In this work, we only use the statistical uncertainty of the radial fitting while fixing the derived $P_{\rm cl}(\beta)$ and $P(\beta, 1.5 \leq x \leq 2.5)$.

Biased slope Δs: We quantify the systematic uncertainty (see Section 5.5.5) caused by the differences between the values of s measured in the cluster and reference fields. The difference

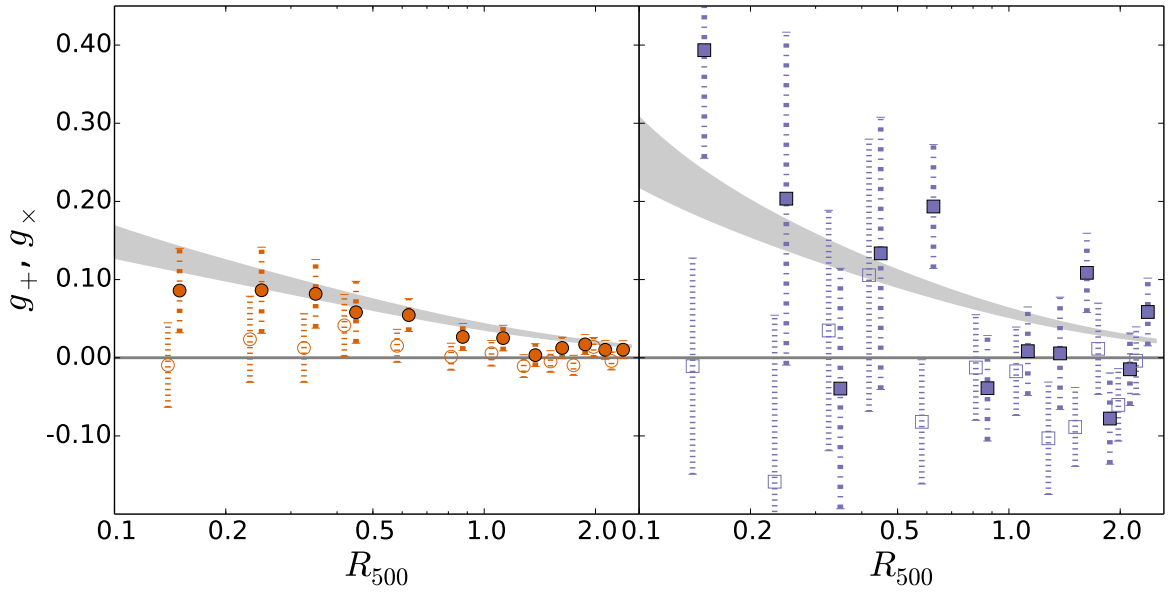

Figure 5.10: The shear profiles from the stacked catalogs with the model prediction based on the best-fit η of the magnification analysis. The η estimated from fitting to the combined background populations yields a mass estimate of $(5.37 \pm 1.56) \times 10^{14} \mathrm{M}_{\odot}$ given the mean of 19 SZE-inferred masses. The shear profile of the low-redshift background is shown in the left panel, and that of the high-redshift background is shown in the right panel. The open and solid points indicate the tangential shear (g_+) and cross shear ($g_\times$) components of the reduced shear, respectively. The gray shaded regions show the shear profile predictions with 1σ confidence region. Data points are horizontally offset for clarity.

of the measured s between the reference and cluster fields is negligible, causing the systematic uncertainties of η at the level $\lesssim 3.5\%$ for fitting the low-z, high-z and combined backgrounds.

Total systematic uncertainty $\sigma_{\rm sys}^{\rm tot}$*:* Reviewing these estimates, the most important source of systematic uncertainty in the best-fit η comes from colour biases. Thereafter, the other sources aside from noisy photometry are of roughly equal importance. It is important to note that if the cluster contamination cannot be controlled at the level of $\approx 1\%$ then it could easily become the dominant source of systematic uncertainty. The systematic uncertainties of the mass are normally distributed in the limit of small perturbations seen in the background properties ($\langle\beta\rangle$ and s). We therefore combine these estimates in quadrature. The total estimated systematic uncertainties for the mass of the low- and high-z populations and the combined analysis are $\sigma_{\rm sys}^{\rm tot} = 10.0\%$, $\sigma_{\rm sys}^{\rm tot} = 7.9\%$ and $\sigma_{\rm sys}^{\rm tot} = 8.9\%$, respectively. This results in the final mass factor η of $1.30^{+0.41}_{-0.39}(\mathrm{stat}) \pm 0.13(\mathrm{sys})$, $0.46^{+0.33}_{-0.29}(\mathrm{stat}) \pm 0.036(\mathrm{sys})$ and $0.83 \pm 0.24(\mathrm{stat}) \pm 0.074(\mathrm{sys})$ from the analysis of the low-z, high-z, and combined background populations, respectively. The statistical uncertainties are dominant in all cases.

5.6.3 Comparison to Shear Profile

As a cross-check we examine whether the weak lensing shear profiles agree with the expectation, given our weak lensing magnification constraints. To construct the shear profiles we use the shape catalogs derived as described elsewhere (Hoekstra et al., 2012, 2015, Dietrich et al. in prep.) of the low-z and high-z populations with exactly the same colour selections used in our magnification analysis. We stack the shape catalogs after the colour and magnitude selections. We find that 5.2% (3.3%) of the low-z (high-z) background galaxies do not have shape measurements, which is mainly due to blending issues associated with the different source finder (i.e. `hfindpeaks`) used in the shape measurement pipeline). We stress that the shear profile is less sensitive to the missing objects due to blending than the magnification analysis, we hence ignore this effect in deriving stacked shear profiles. We derive both tangential shear (g_+) and cross shear ($g_\times$) profiles including the lensing weight (Hoekstra et al., 2012, 2015, Dietrich et al. in prep.) of each single galaxy. We predict the g_+ profile using the best-fit η, the average lensing efficiency $\langle\beta\rangle$ for each background population, and a fiducial cluster located at the median redshift of the 19 clusters. Specifically, we use the mean of the 19 SZE-inferred masses ($6.47\times10^{14}\mathrm{M}_\odot$) multiplied by the η estimated from fitting the combined background populations, which is consistent with the SZE-inferred masses, as the input mass for predicting the shear profiles. As a result, the η estimated from fitting the combined background samples yields a mass estimate of $(5.37\pm1.56)\times10^{14}\mathrm{M}_\odot$.

Figure 5.10 shows the predicted and observed shear profiles for the low- and high-z populations. We emphasize that the gray shaded regions are model shear profiles derived from the magnification analysis and not fits to the observed shear profiles. Both low- and high-z population observed shear profiles are statistically consistent with the predicted shear profiles. The probabilities that the data are described by the model are 0.87 and 0.25, for the low- and high-z backgrounds, respectively. The observed cross shear ($g_\times$) profiles are both consistent with zero. The good consistency between the observed tangential shear (g_+) profiles and the models inferred from the magnification analysis provides a clear indication that the magnification bias signal we observe is not a spurious signal caused by cluster members. Such contaminating cluster member galaxies would not have a tangential alignment with respect to the cluster centre.

5.7 Conclusions

By stacking the signal from 19 massive clusters with a mean SZE-inferred mass of $M_{500}=(6.47\pm0.31)\times10^{14}\mathrm{M}_\odot$, we detect the enhancement in the number density of a flux-limited ($g\leq23.5$) and colour ($g-r$ and $r-i$) selected background population with $z\approx0.9$ at 3.3σ confidence. We find only very weak indications of the magnification bias signal using the same data but colour selecting for a higher redshift background population at $z\approx1.8$. This background sample at $z\approx1.8$ is significantly smaller than that at $z\approx0.9$, increasing the Poisson noise and thus reducing the significance of the measurement.

We estimate the mass factor η, which is the ratio of the magnification and SZE-inferred masses extracted from the whole cluster ensemble. We find a best-fit η of $0.83\pm0.24(\mathrm{stat})\pm$

0.074(sys) by fitting to the combined low- and high-redshift background populations. This indicates that there is no tension between the magnification masses and those estimated using the SZE observable-mass relation.

We analyze the potential impact of systematic errors caused by photometric scatter and bias, cluster galaxy contamination, and uncertainties in the estimation of the average lensing efficiency $\langle\beta\rangle$ and power law index s of the galaxy count-magnitude relation for each of the two background populations. We quantify how these effects impact the final mass factor η estimated from the fit. We find that the systematic source with the largest potential to affect η estimates (7.4% bias for the combined constraint) is the bias in the calibration of the photometric colour, which would lead to an inconsistency between the estimation of the background properties of the data and the reference field. The other biases each contribute systematic uncertainties at the $\leq 5\%$ level, which we combine in quadrature to estimate a final 7.4% systematic uncertainty on the combined η constraint. We conclude that the mass constraints can be reliably estimated using the magnification bias if the unbiased background properties can be estimated. The uncertainty of the η estimation in this work is currently dominated by the statistical uncertainty, which is due to the lack of background galaxies needed to suppress the Poisson noise.

This work underscores the promise of using magnification bias of normal background galaxy populations to calibrate the observable-mass scaling relation and measure cluster masses in multi-band imaging survey data with depths similar to those in the Dark Energy Survey. For the clusters detected in the 2500 deg^2 SPT-SZ survey, there are ≈ 200 with redshifts $0.3 \leq z \leq 0.6$. By carrying out the same analysis as discussed in this work, we expect the detection significance of the magnification effect would be increased to $\approx 10\sigma$ and $\approx 4\sigma$ for the low-z and high-z background populations, respectively. Therefore, by stacking samples of hundreds to thousands of clusters in such a dataset, it is possible to carry out important cross-checks of masses extracted through weak lensing shear, galaxy dynamics and other methods.

Acknowledgements

We acknowledge the support by the DFG Cluster of Excellence “Origin and Structure of the Universe” and the Transregio program TR33 “The Dark Universe”. D.A. and T.S. acknowledge support from the German Federal Ministry of Economics and Technology (BMWi) provided through DLR under projects 50 OR 1210, 50 OR 1308, and 50 OR 1407. CR acknowledges support from the Australian Research Council’s Discovery Projects scheme (DP150103208). The South Pole Telescope is supported by the National Science Foundation through grant ANT-0638937. Partial support is also provided by the NSF Physics Frontier Center grant PHY-0114422 to the Kavli Institute of Cosmological Physics at the University of Chicago, the Kavli Foundation and the Gordon and Betty Moore Foundation. Optical imaging data were obtained with Megacam on the 6.5 m Magellan Clay Telescope.

Facilities: South Pole Telescope, Magellan

Chapter 6

Summary and Outlook

In this chapter, I will first summarize this thesis and then present an outlook for the future work.

6.1 Summary

A short summary of each Chapter is listed as follows.

- In Chapter 2, we study the stellar mass function and baryon composition of 14 SPT-selected clusters at high redshift $0.57 < z < 1.33$ that have a median mass M_{500} of $6 \times 10^{14} \mathrm{M}_{\odot}$. We then combine our results with the ones previously published in literature after carefully removing the existing systematics. The stacked stellar mass function per unit total mass of the 14 clusters is significantly higher than the ones estimated from under-dense fields by a factor $\approx 1.6 \pm 0.2$. The resulting $M_{\star}^{\mathrm{BCG}}$–M_{500} relation implies that the BCG stellar mass constitutes $0.12 \pm 0.01\%$ of the halo mass and decreases as $M_{500}^{-0.58\pm0.07}$ with large scatter. The mass fractions of stellar $f_{\star}$, ICM f_{ICM}, collapsed baryon f_{c} and total baryon f_{b} derived from the combined sample are, respectively, $1.1 \pm 0.1\%$, $11.2 \pm 0.32\%$, $10.7 \pm 0.1\%$ and $10.7 \pm 0.6\%$ for the cluster with the characteristic mass $M_{500} = 6 \times 10^{14} \mathrm{M}_{\odot}$ at redshift $z = 0.9$; they scale as

$$
\begin{aligned}
f_{\star} &\propto M^{-0.37\pm0.09}(1+z)^{0.26\pm0.16\pm0.08}, \\
f_{\mathrm{ICM}} &\propto M^{0.22\pm0.06}(1+z)^{-0.20\pm0.11\pm0.22}, \\
f_{\mathrm{c}} &\propto M^{-0.65\pm0.10}(1+z)^{0.39\pm0.15\pm0.16}, \text{ and} \\
f_{\mathrm{b}} &\propto M^{0.22\pm0.06}(1+z)^{-0.17\pm0.11\pm0.22},
\end{aligned}
$$

  where the first (second) uncertainties stand for the statistical (systematic) uncertainties. These scaling relations with strong mass trends and mild redshift trends imply that significant amounts of under-dense fields fall into clusters during their formations, which is consistent with numerical simulations. However, this study is limited by the systematics raised from the heterogeneous samples used in this work and–therefore–large sample and uniform datasets must be used in the future.

- In Chapter 3, we derive the stellar mass-to-halo mass scaling relation of 46 X-ray selected low mass clusters and groups–that have masses in the range $2\times10^{13}\mathrm{M}_{\odot}\lesssim M_{500}\lesssim 2.5\times10^{14}\mathrm{M}_{\odot}$ (median mass $8\times10^{13}\mathrm{M}_{\odot}$) and redshifts in the range $0.1\leq z\leq 1.02$ (median redshift 0.47)–from the $6\,\mathrm{deg}^2$ XMM-BCS survey. We use IRAC [3.6] band photometry from the wide field SSDF survey together with blue fraction f_{blue} measurements relying on *griz* photometry from the BCS survey to estimate the stellar masses of these 46 systems. The best-fit stellar mass-halo mass scaling relation is

$$\frac{M_{\star}}{10^{12}\mathrm{M}_{\odot}}=1.87^{+0.13}_{-0.12}\left(\frac{M_{500}}{8\times10^{13}\mathrm{M}_{\odot}}\right)^{0.69\pm0.15}\left(\frac{1+z}{1.47}\right)^{-0.04\pm0.47},$$

  with log-normal intrinsic scatter $\sigma_{\ln M_{\star}|M_{500}}=0.36^{+0.07}_{-0.06}$. The derived scaling relation of low mass groups or clusters implies a picture consistent with high-mass systems that, as halos accrete and become more massive, the material from lower mass halos with higher stellar mass fractions is roughly balanced by accretion of material from the field that tends to have lower stellar mass fraction. As a result, the stellar mass fraction of clusters with $M_{500}\gtrsim 2\times10^{13}\mathrm{M}_{\odot}$ remains statistically constant since redshift $z\approx1$.

- In Chapter 4, we significantly extend the results of Chapter 2 by studying the scaling relations of M_{ICM}–M_{500} and $M_{\star}$–M_{500} based on the sample of 91 SPT-selected galaxy clusters. This sample spans a mass range from $\approx3.5\times10^{14}\mathrm{M}_{\odot}$ to $18.1\times10^{14}\mathrm{M}_{\odot}$ (with median of $6.48\times10^{14}\mathrm{M}_{\odot}$) at redshift from $z=0.278$ to $z=1.22$ (median of $z=0.58$). The total, ICM and stellar masses of these clusters are all determined by using the consistent methods and homogeneous datasets that include the mm map from the SPT-SZ survey, uniform X-ray data observed by the *Chandra* telescope, optical photometry of the *griz* bands taken by the DES and the dedicating IRAC imaging from the *Spitzer* follow-up observations. As a result, this study significantly reduces the systematic effects that are seen in the previous work and also leads to the largest and most uniform sample to date. With these measurements of total cluster, ICM and stellar masses, we confirm the strong mass trends $B_{\mathrm{ICM}}=1.24\pm0.06$ and $B_{\star}=0.76\pm0.14$ for the scaling relations of M_{ICM}–M_{500} and $M_{\star}$–M_{500}, respectively, which are also in good agreement with previous works. Most interestingly, no significant redshift trends are seen ($C_{\mathrm{ICM}}=-0.19\pm0.14$ and $C_{\star}=0.23\pm0.34$), although the uncertainties are too large to rule out any redshift trends for baryon content of massive galaxy clusters out to $z\approx1.2$. This chapter sets the milestone of studying baryon content of galaxy clusters and demonstrates the direction for the future work.

- In Chapter 5, we detect the lensing magnification effect that causes the enhancement in the number densities of flux-limited ($g\leq23.5$) and colour ($g-r$ and $r-i$) selected background populations at $\approx3.5\sigma$ confidence by stacking the signal from 19 SPT-selected clusters with a mean SZE-inferred mass of $M_{500}=(6.47\pm0.31)\times10^{14}\mathrm{M}_{\odot}$. With careful quantifying various systematic effects, we then estimate the mass factor η–which is the ratio of the magnification and SZE-inferred masses–and find a best-fit η of $0.83\pm0.24(\mathrm{stat})\pm0.074(\mathrm{sys})$, indicating that there is no tension between the magnification masses and those

estimated using the SZE observable-mass relation. This work underscores the promise of using magnification bias of normal background galaxy populations to calibrate the observable-mass scaling relation and measure cluster masses in multi-band imaging survey data with depths similar to those in the Dark Energy Survey or HSC survey.

6.2 Outlook

In the first three chapters of this thesis, I present the work of studying baryon content of large samples consisting of galaxy clusters consistently selected through either their X-ray or SZE signatures. Moreover, we apply uniform methods to estimate the total, ICM and stellar masses of each cluster based on the homogeneous, multi-wavelength datasets. Most importantly, we extend the analysis out to redshift $z \approx 1.3$ for the first time. In the last chapter, I develop a new method to calibrate mass proxies of galaxy clusters by utilizing the weak lensing magnification effect.

Based on the results and interpretations of this thesis, a clear path including the following ingredients is revealed for the future work regarding cluster cosmology and/or astrophysics:

First, as we enter the era of precise and accurate galaxy cluster science, significant efforts to eliminate various systematics and to consistently study samples with well-understood selection functions have to be made. This approach results in a reduction of systematic uncertainties, as we have demonstrated in this thesis.

Second, to reach the precision needed for meaningful interpretations, very large samples of galaxy clusters must be obtained and studied; this will suppress the statistical uncertainties that currently limit the studies presented in this thesis. These two items above can be achieved by wide and/or deep surveys in multiple wavelengths, such as the existing *GALEX* all-sky survey in ultraviolet, the ongoing DES or HSC surveys in optical, the *WISE* and SSDF surveys in NIR, the X-ray all-sky survey by the upcoming *eROSITA* mission, and the ongoing mm-wave surveys like those planned by SPT.

Third, while the high-mass galaxy clusters at $0.1 \lesssim z \lesssim 1.3$ are extensively studied in this thesis, the systems with lower masses– which also have greater abundance in the Universe– at higher redshift are the key to studies of cluster science, providing insights into the formation of galaxy clusters given that these systems link the under-dense field to the more massive cluster halos.

Fourth, as the community has recognized that any mass information is precious for studying galaxy clusters, the lensing magnification effect that only requires accurate photometry– which is frequently referred to as "the fruit that comes for free"– will be important for providing unbiased mass estimates of clusters at high redshift. This is especially true in the near future when the ultra-deep surveys begin (e.g., the *Euclid* mission) where it is nearly impossible to measure cluster masses by resolving the shapes of the background sources at the faint end of these datasets.

Bibliography

Abell G. O., 1958, ApJS, 3, 211

Adelberger K. L., Steidel C. C., Shapley A. E., Hunt M. P., Erb D. K., Reddy N. A., Pettini M., 2004, ApJ, 607, 226

Afonso C. et al., 2003, A&A, 400, 951

Alcock C. et al., 1997, ApJ, 479, 119

Alcock C. et al., 2000, ApJ, 542, 281

Andersson K. et al., 2011, ApJ, 738, 48

Andreon S., 2010, MNRAS, 407, 263

Annis J. et al., 2014, ApJ, 794, 120

Applegate D. E. et al., 2012, ArXiv e-prints

Applegate D. E. et al., 2014, MNRAS, 439, 48

Arnaud M., Evrard A. E., 1999, MNRAS, 305, 631

Arnaud M., Pointecouteau E., Pratt G. W., 2005, A&A, 441, 893

Arnaud M., Pratt G. W., Piffaretti R., Böhringer H., Croston J. H., Pointecouteau E., 2010, A&A, 517, A92+

Arnouts S., Cristiani S., Moscardini L., Matarrese S., Lucchin F., Fontana A., Giallongo E., 1999, MNRAS, 310, 540

Ashby M. L. N. et al., 2013, ApJS, 209, 22

Ashby M. L. N. et al., 2009, ApJ,, 701, 428

Austermann J. E. et al., 2012, in Proc. SPIE, Vol. 8452, Millimeter, Submillimeter, and Far-Infrared Detectors and Instrumentation for Astronomy VI, p. 84521E

Babcock H. W., 1939, Lick Observatory Bulletin, 19, 41

Balogh M. L., McCarthy I. G., Bower R. G., Eke V. R., 2008, MNRAS, 385, 1003

Balogh M. L. et al., 2014, MNRAS, 443, 2679

Banerji M. et al., 2013, MNRAS, 431, 2209

Banerji M. et al., 2015, MNRAS, 447, 325

Barmby P., Huang J.-S., Ashby M. L. N., Eisenhardt P. R. M., Fazio G. G., Willner S. P., Wright E. L., 2008, ApJS, 177, 431

Bauer A. H., Gaztañaga E., Martí P., Miquel R., 2014, MNRAS, 440, 3701

Bayliss M. B. et al., 2014, ApJ, 794, 12

Benson B. A. et al., 2014, in Proc. SPIE, Vol. 9153, Millimeter, Submillimeter, and Far-Infrared Detectors and Instrumentation for Astronomy VII, p. 91531P

Benson B. A. et al., 2013, ApJ, 763, 147

Bernstein G. M., Nichol R. C., Tyson J. A., Ulmer M. P., Wittman D., 1995, AJ, 110, 1507

Bertin E., Arnouts S., 1996, AAPS, 117, 393

Bertschinger E., 1985, ApJS, 58, 39

Bleem L. E. et al., 2015, ApJS, 216, 27

Bleem L. E. et al., 2014, ArXiv e-prints

Bocquet S., Saro A., Dolag K., Mohr J. J., 2015a, ArXiv e-prints

Bocquet S. et al., 2015b, ApJ, 799, 214

Bode P., Ostriker J. P., Turok N., 2001, ApJ, 556, 93

Böhmer C. G., Harko T., 2007, JCAP, 6, 025

Böhringer H., Chon G., Collins C. A., 2014, A&A, 570, A31

Böhringer H. et al., 2004, A&A, 425, 367

Bridle S. et al., 2010, MNRAS, 405, 2044

Broadhurst T. J., Taylor A. N., Peacock J. A., 1995, ApJ, 438, 49

Bruzual G., Charlot S., 2003, MNRAS, 344, 1000

Burstein D., Rubin V. C., Thonnard N., Ford, Jr. W. K., 1982, ApJ, 253, 70

Calzetti D., Armus L., Bohlin R. C., Kinney A. L., Koornneef J., Storchi-Bergmann T., 2000, ApJ, 533, 682

Capak P. et al., 2007, ApJS, 172, 99

Capak P. et al., 2012, SPLASH: Spitzer Large Area Survey with Hyper-Suprime-Cam. Spitzer Proposal

Cappellari M. et al., 2006, MNRAS, 366, 1126

Carlstrom J. E. et al., 2011, PASP, 123, 568

Carlstrom J. E., Holder G. P., Reese E. D., 2002, ARAA, 40, 643

Cash W., 1979, ApJ, 228, 939

Cavagnolo K. W., Donahue M., Voit G. M., Sun M., 2008, ApJ, 683, L107

Cavaliere A., Fusco-Femiano R., 1978, A&A, 70, 677

Cavaliere A., Menci N., Tozzi P., 1999, MNRAS, 308, 599

Chabrier G., 2003, PASP, 115, 763

Chavanis P.-H., 2011, Phys. Rev. D, 84, 043531

Chiu I. et al., 2016a, MNRAS, 457, 3050

Chiu I. et al., 2016b, MNRAS, 455, 258

Chiu I. et al., 2016c, MNRAS, 458, 379

Chiu I.-N. T., Molnar S. M., 2012, ApJ, 756, 1

Connelly J. L. et al., 2012, ApJ, 756, 139

Corless V. L., King L. J., 2009, MNRAS, 396, 315

Coupon J., Broadhurst T., Umetsu K., 2013, ApJ, 772, 65

Coupon J. et al., 2009, A&A, 500, 981

David L. P., Blumenthal G. R., 1992, ApJ, 389, 510

David L. P., Slyz A., Jones C., Forman W., Vrtilek S. D., Arnaud K. A., 1993, ApJ, 412, 479

DES Collaboration, 2005, ArXiv Astrophysics e-prints

Desai S. et al., 2012, ApJ, 757, 83

Desai V. et al., 2007, ApJ, 660, 1151

Djorgovski S., Davis M., 1987, ApJ, 313, 59

Dodelson S., 2003, Modern Cosmology, Academic Press. Academic Press, iSBN: 9780122191411

Donahue M. et al., 2014, ApJ, 794, 136

Dressler A., 1980, ApJ, 236, 351

Dressler A., Sandage A., 1983, ApJ, 265, 664

Dressler A., Shectman S. A., 1988, AJ, 95, 985

Duffy A. R., Schaye J., Kay S. T., Dalla Vecchia C., 2008, MNRAS, 390, L64

Duncan C. A. J., Joachimi B., Heavens A. F., Heymans C., Hildebrandt H., 2014, MNRAS, 437, 2471

Dunn R. J. H., Fabian A. C., 2006, MNRAS, 373, 959

Dye S. et al., 2002, A&A, 386, 12

Ebeling H., Voges W., Bohringer H., Edge A. C., Huchra J. P., Briel U. G., 1996, MNRAS, 281, 799

Eisenhardt P. R. M. et al., 2008, ApJ, 684, 905

Erben T. et al., 2005, Astronomische Nachrichten, 326, 432

Erben T., Van Waerbeke L., Bertin E., Mellier Y., Schneider P., 2001, A&A, 366, 717

Evrard A., Henry J., 1991, ApJ, 383, 95

Fabian A. C., 1994, ARAA, 32, 277

Fabian A. C., 2012, ARAA, 50, 455

Fazio G. G. et al., 2004, ApJS, 154, 10

Feldmeier J. J., Mihos J. C., Morrison H. L., Harding P., Kaib N., Dubinski J., 2004, ApJ, 609, 617

Feldmeier J. J., Mihos J. C., Morrison H. L., Rodney S. A., Harding P., 2002, ApJ, 575, 779

Felten J. E., Gould R. J., Stein W. A., Woolf N. J., 1966, ApJ, 146, 955

Fillmore J. A., Goldreich P., 1984, ApJ, 281, 1

Foley R. J. et al., 2011, ApJ, 731, 86

Ford J., Hildebrandt H., Van Waerbeke L., Erben T., Laigle C., Milkeraitis M., Morrison C. B., 2014, MNRAS, 439, 3755

Ford J. et al., 2012, ApJ, 754, 143

Foreman-Mackey D., Hogg D. W., Lang D., Goodman J., 2013, PASP, 125, 306

Forman W., Jones C., 1982, ARAA, 20, 547

Fowler J. W. et al., 2007, Applied Optics, 46, 3444

Frenk C. S., White S. D. M., Efstathiou G., Davis M., 1990, ApJ, 351, 10

Friedmann A., 1922, Zeitschrift fur Physik, 10, 377

Garg A., 2008, PhD thesis, Harvard University

Geller M. J., Beers T. C., 1982, PASP, 94, 421

Giodini S. et al., 2009, ApJ, 703, 982

Gladders M. D., Yee H. K. C., 2005, ApJS, 157, 1

Gonzalez A. H., Sivanandam S., Zabludoff A. I., Zaritsky D., 2013, ArXiv e-prints

Gonzalez A. H., Zabludoff A. I., Zaritsky D., Dalcanton J. J., 2000, ApJ, 536, 561

Gonzalez A. H., Zaritsky D., Zabludoff A. I., 2007, ApJ, 666, 147

Gregg M. D., West M. J., 1998, Nature, 396, 549

Gruen D. et al., 2014, MNRAS, 442, 1507

Gunn J. E., Gott, III J. R., 1972a, ApJ, 176, 1

Gunn J. E., Gott, III J. R., 1972b, ApJ, 176, 1

Haiman Z., Mohr J. J., Holder G. P., 2001, ApJ, 553, 545

Hasselfield M. et al., 2013, ArXiv e-prints

Heavens A. F., Joachimi B., 2011, MNRAS, 415, 1681

Hennig C. et al., 2016, ArXiv e-prints

Henry J. P., Arnaud K. A., 1991, ApJ, 372, 410

Heymans C. et al., 2006, MNRAS, 368, 1323

High F. W. et al., 2012, ApJ, 758, 68

High F. W., Stubbs C. W., Rest A., Stalder B., Challis P., 2009, AJ, 138, 110

Hildebrandt H. et al., 2011, ApJ, 733, L30

Hildebrandt H., Pielorz J., Erben T., van Waerbeke L., Simon P., Capak P., 2009, A&A, 498, 725

Hilton M. et al., 2013, MNRAS

Hlavacek-Larrondo J. et al., 2013a, ApJ, 777, 163

Hlavacek-Larrondo J., Fabian A. C., Edge A. C., Ebeling H., Allen S. W., Sanders J. S., Taylor G. B., 2013b, MNRAS, 431, 1638

Hlavacek-Larrondo J., Fabian A. C., Edge A. C., Ebeling H., Sanders J. S., Hogan M. T., Taylor G. B., 2012, MNRAS, 421, 1360

Hlavacek-Larrondo J. et al., 2015, ApJ, 805, 35

Hoekstra H., Bartelmann M., Dahle H., Israel H., Limousin M., Meneghetti M., 2013, Space Science Reviews, 177, 75

Hoekstra H., Herbonnet R., Muzzin A., Babul A., Mahdavi A., Viola M., Cacciato M., 2015, MNRAS, 449, 685

Hoekstra H., Mahdavi A., Babul A., Bildfell C., 2012, MNRAS, 427, 1298

Hoffman Y., Shaham J., 1985, ApJ, 297, 16

Hu W., Barkana R., Gruzinov A., 2000, Physical Review Letters, 85, 1158

Hubble E., 1929, Proceedings of the National Academy of Science, 15, 168

Hunter D. A., Rubin V. C., Gallagher, III J. S., 1986, AJ, 91, 1086

Ilbert O. et al., 2006, A&A, 457, 841

Ilbert O. et al., 2009, ApJ, 690, 1236

Ishibashi W., Fabian A. C., Canning R. E. A., 2013, MNRAS, 431, 2350

Jee M. J., Hughes J. P., Menanteau F., Sifón C., Mandelbaum R., Barrientos L. F., Infante L., Ng K. Y., 2014, ApJ, 785, 20

Jeltema T. E., Mulchaey J. S., Lubin L. M., Fassnacht C. D., 2007, ApJ, 658, 865

Jimeno P., Broadhurst T., Coupon J., Umetsu K., Lazkoz R., 2015, MNRAS, 448, 1999

Joachimi B., Bridle S. L., 2010, A&A, 523, A1

Johnston D. E. et al., 2007, ArXiv e-prints

Kaiser N., 1986, MNRAS, 222, 323

Kauffmann G. et al., 2003, MNRAS, 341, 33

Kent S. M., 1986, AJ, 91, 1301

Kettula K. et al., 2015, MNRAS, 451, 1460

Kitching T. D. et al., 2012, MNRAS, 423, 3163

Kochanek C. S. et al., 2001, ApJ, 560, 566

Koester B. P. et al., 2007, ApJ, 660, 239

Komatsu E. et al., 2011, ApJS, 192, 18

Kotulla R., Fritze U., Weilbacher P., Anders P., 2009, MNRAS, 396, 462

Kravtsov A. V., Vikhlinin A., Nagai D., 2006, ApJ, 650, 128

Kroupa P., 2001, MNRAS, 322, 231

Kuhn J. R., Kruglyak L., 1987, ApJ, 313, 1

Lacy M. et al., 2005, ApJS, 161, 41

Laigle C. et al., 2016, ArXiv e-prints

Leauthaud A. et al., 2012, ApJ, 746, 95

Leauthaud A. et al., 2007, ApJS, 172, 219

Lidman C. et al., 2012, MNRAS, 427, 550

Lilje P. B., 1992, ApJ, 386, L33

Limber D. N., 1959, ApJ, 130, 414

Lin Y., Mohr J. J., Gonzalez A. H., Stanford S. A., 2006, ApJ, 650, L99

Lin Y., Mohr J. J., Stanford S. A., 2003, ApJ, 591, 749

Lin Y., Mohr J. J., Stanford S. A., 2004, ApJ, 610, 745

Lin Y.-T., Mohr J. J., 2004, ApJ, 617, 879

Lin Y.-T., Stanford S. A., Eisenhardt P. R. M., Vikhlinin A., Maughan B. J., Kravtsov A., 2012, ApJ, 745, L3

Liu J. et al., 2014, ArXiv e-prints

Liu J. et al., 2015a, MNRAS, 449, 3370

Liu J. et al., 2015b, MNRAS, 448, 2085

Mancone C. L., Gonzalez A. H., 2012, PASP, 124, 606

Mandelbaum R. et al., 2014, ArXiv e-prints 1412.1825

Mantz A., Allen S. W., Ebeling H., Rapetti D., 2008, MNRAS, 387, 1179

Mantz A. B., Allen S. W., Morris R. G., Rapetti D. A., Applegate D. E., Kelly P. L., von der Linden A., Schmidt R. W., 2014, MNRAS, 440, 2077

Mantz A. B., Allen S. W., Morris R. G., Schmidt R. W., 2016, MNRAS, 456, 4020

Markevitch M., 1998, ApJ, 504, 27

Markevitch M., Gonzalez A. H., David L., Vikhlinin A., Murray S., Forman W., Jones C., Tucker W., 2002, ApJ, 567, L27

Marriage T. A. et al., 2011, ApJ, 737, 61

Martino R., Mazzotta P., Bourdin H., Smith G. P., Bartalucci I., Marrone D. P., Finoguenov A., Okabe N., 2014, ArXiv e-prints

Massey R. et al., 2007, MNRAS, 376, 13

Maughan B. J., 2007, ApJ, 668, 772

McDonald M. et al., 2012, Nature, 488, 349

McDonald M. et al., 2014a, ApJ, 794, 67

McDonald M. et al., 2013, ApJ, 774, 23

McDonald M. et al., 2015, ApJ, 811, 111

McDonald M. et al., 2014b, ApJ, 784, 18

McGee S. L., Balogh M. L., Bower R. G., Font A. S., McCarthy I. G., 2009, MNRAS, 400, 937

Medezinski E., Broadhurst T., Umetsu K., Oguri M., Rephaeli Y., Benítez N., 2010, MNRAS, 405, 257

Mei S. et al., 2009, ApJ, 690, 42

Menanteau F. et al., 2012, ApJ, 748, 7

Merlin E. et al., 2015, A&A, 582, A15

Messier C., 1781, Catalog of Nebulae and Star Clusters. Tech. rep.

Meszaros P., 1974, A&A, 37, 225

Mohr J., Evrard A., 1997, ApJ, 491, 38

Mohr J. J. et al., 2012, in Proc. SPIE, Vol. 8451, Software and Cyberinfrastructure for Astronomy II, p. 84510D

Mohr J. J., Evrard A. E., Fabricant D. G., Geller M. J., 1995, ApJ, 447, 8+

Mohr J. J., Mathiesen B., Evrard A. E., 1999, ApJ, 517, 627

Molnar S. M., Chiu I.-N., Umetsu K., Chen P., Hearn N., Broadhurst T., Bryan G., Shang C., 2010, ApJ, 724, L1

Mulroy S. L. et al., 2014, MNRAS, 443, 3309

Muzzin A. et al., 2013, ApJ, 777, 18

Muzzin A. et al., 2009, ApJ, 698, 1934

Muzzin A., Yee H. K. C., Hall P. B., Ellingson E., Lin H., 2007, ApJ, 659, 1106

Navarro J. F., Frenk C. S., White S. D. M., 1996, ApJ, 462, 563

Navarro J. F., Frenk C. S., White S. D. M., 1997a, ApJ, 490, 493

Navarro J. F., Frenk C. S., White S. D. M., 1997b, ApJ, 490, 493

Neumann D. M., Arnaud M., 1999, A&A, 348, 711

Neumann D. M., Arnaud M., 2001, A&A, 373, L33

Oemler A., 1973, ApJ, 180

Oemler, Jr. A., 1974, ApJ, 194, 1

Okabe N., Zhang Y.-Y., Finoguenov A., Takada M., Smith G. P., Umetsu K., Futamase T., 2010, ApJ, 721, 875

Papovich C. et al., 2010, ApJ, 716, 1503

Patel S. G., Kelson D. D., Williams R. J., Mulchaey J. S., Dressler A., McCarthy P. J., Shectman S. A., 2015, ApJ, 799, L17

Peccei R. D., Quinn H. R., 1977, Physical Review Letters, 38, 1440

Peebles P. J. E., 2000, ApJ, 534, L127

Peng Y.-j. et al., 2010, ApJ, 721, 193

Penzias A. A., Wilson R. W., 1965, ApJ, 142, 419

Perlmutter S. et al., 1999, ApJ, 517, 565

Persic M., Salucci P., Stel F., 1996, MNRAS, 281, 27

Pickles A. J., 1998, PASP, 110, 863

Pierre M. et al., 2004, JCAP, 9, 11

Pike S. R., Kay S. T., Newton R. D. A., Thomas P. A., Jenkins A., 2014, MNRAS, 445, 1774

Planck Collaboration et al., 2013, ArXiv e-prints, paper XVI

Planck Collaboration et al., 2011, A&A, 536, A8

Pozzetti L. et al., 2007, A&A, 474, 443

Pratt G. W., Croston J. H., Arnaud M., Böhringer H., 2009, A&A, 498, 361

Regnault N. et al., 2009, A&A, 506, 999

Reichardt C. L., de Putter R., Zahn O., Hou Z., 2012, ApJ, 749, L9

Reichardt C. L. et al., 2013, ApJ, 763, 127

Riess A. G. et al., 1998, AJ, 116, 1009

Rood H. J., 1969, ApJ, 158, 657

Rood H. J., Abell G. O., 1973, ApJ, 13, 69

Rood H. J., Turnrose B. E., 1968, ApJ, 152, 1057

Rosati P., della Ceca R., Norman C., Giacconi R., 1998, ApJ, 492, L21

Rowe B. T. P. et al., 2015, Astronomy and Computing, 10, 121

Rozo E. et al., 2009, ApJ, 699, 768

Ruan J. J., McQuinn M., Anderson S. F., 2015, ApJ, 802, 135

Rubin V. C., Ford, Jr. W. K., Thonnard N., Burstein D., 1982a, ApJ, 261, 439

Rubin V. C., Ford W. K. J., . Thonnard N., 1980, ApJ, 238, 471

Rubin V. C., Thonnard N., Ford, Jr. W. K., 1978, ApJ, 225, L107

Rubin V. C., Thonnard N. T., Ford, Jr. W. K., 1982b, AJ, 87, 477

Ruel J. et al., 2014, ApJ, 792, 45

Saliwanchik B. R. et al., 2013, ArXiv e-prints

Salpeter E. E., 1955, ApJ, 121, 161

Sanders D. B. et al., 2007, ApJS, 172, 86

Saro A., Bazin G., Mohr J., Dolag K., 2012, ArXiv e-prints

Saro A. et al., 2015, ArXiv e-prints

Saro A., Mohr J. J., Bazin G., Dolag K., 2013, ApJ, 772, 47

Schechter P., 1976, ApJ, 203, 297

Schellenberger G., Reiprich T. H., Lovisari L., Nevalainen J., David L., 2014, ArXiv e-prints

Schirmer M., 2013, ApJS, 209, 21

Schive H.-Y., Chiueh T., Broadhurst T., 2014, Nature Physics, 10, 496

Schmidt F., Leauthaud A., Massey R., Rhodes J., George M. R., Koekemoer A. M., Finoguenov A., Tanaka M., 2012, ApJ, 744, L22

Schneider P., King L., Erben T., 2000, A&A, 353, 41

Seielstad G. A., Whiteoak J. B., 1965, ApJ, 142, 616

Seitz C., Schneider P., 1997, A&A, 318, 687

Shan Y., McDonald M., Courteau S., 2015, ApJ, 800, 122

Sifón C. et al., 2013, ApJ, 772, 25

Smoot G. F., et al., 1992, ApJ, 396, L1

Song J., Mohr J. J., Barkhouse W. A., Warren M. S., Rude C., 2012a, ApJ, 747, 58

Song J. et al., 2012b, ApJ, 761, 22

Song J. et al., 2012c, ApJ, 761, 22

Spitzer, Jr. L., Baade W., 1951, ApJ, 113, 413

Stalder B. et al., 2013, ApJ, 763, 93

Stanek R., Evrard A. E., Böhringer H., Schuecker P., Nord B., 2006, ApJ, 648, 956

Stanford S. A., Gonzalez A. H., Brodwin M., Gettings D. P., Eisenhardt P. R. M., Stern D., Wylezalek D., 2014, ApJS, 213, 25

Staniszewski Z. et al., 2009, ApJ, 701, 32

Sunyaev R. A., Zel'dovich Y. B., 1970a, Ap&SS, 7, 3

Sunyaev R. A., Zel'dovich Y. B., 1970b, Comments on Astrophysics and Space Physics, 2, 66

Sunyaev R. A., Zel'dovich Y. B., 1972, Comments on Astrophysics and Space Physics, 4, 173

Swindle R., Gal R. R., La Barbera F., de Carvalho R. R., 2011, AJ, 142, 118

Tauber J. A., 2000, in IAU Symposium 201: New Cosmological Data and the Values of the Fundamental Parameters, Lasenby A., Wilkinson A., eds., ASP

Taylor A. N., Dye S., Broadhurst T. J., Benitez N., van Kampen E., 1998, ApJ, 501, 539

Taylor E. N. et al., 2011, MNRAS, 418, 1587

Tegmark M., Zaldarriaga M., 2002, Phys. Rev. D, 66, 103508

The Planck Collaboration, 2006, ArXiv:astro-ph/0604069

Thuan T. X., Kormendy J., 1977, PASP, 89, 466

Tinker J., Kravtsov A. V., Klypin A., Abazajian K., Warren M., Yepes G., Gottlöber S., Holz D. E., 2008, ApJ, 688, 709

Tisserand P. et al., 2007, A&A, 469, 387

Truemper J., 1993, Science, 260, 1769

Udalski A., Kubiak M., Szymanski M., 1997, Acta Astronomica, 47, 319

Umetsu K., 2011, in International School of Physics 'Enrico Fermi': Astrophysics of Galaxy Clusters, Cavaliere A., Rephaeli Y., eds., Vol. 172, IOS Press, pp. 269–300

Umetsu K., 2013, ApJ, 769, 13

Umetsu K., Broadhurst T., 2008, ApJ, 684, 177

Umetsu K., Broadhurst T., Zitrin A., Medezinski E., Hsu L.-Y., 2011, ApJ, 729, 127

Umetsu K. et al., 2014, ApJ, 795, 163

Urquhart S. A., Willis J. P., Hoekstra H., Pierre M., 2010, ArXiv e-prints

Šuhada R. et al., 2012, A&A, 537, A39

van der Burg R. F. J. et al., 2013a, A&A, 557, A15

van der Burg R. F. J. et al., 2013b, A&A, 557, A15

van der Burg R. F. J., Muzzin A., Hoekstra H., Wilson G., Lidman C., Yee H. K. C., 2014, A&A, 561, A79

van Haarlem M. P., Frenk C. S., White S. D. M., 1997, MNRAS, 287, 817

Van Waerbeke L., Hildebrandt H., Ford J., Milkeraitis M., 2010, ApJ, 723, L13

Vanderlinde K. et al., 2010, ApJ, 722, 1180

Vikhlinin A. et al., 2009a, ApJ, 692, 1033

Vikhlinin A., Kravtsov A., Forman W., Jones C., Markevitch M., Murray S. S., Van Speybroeck L., 2006, ApJ, 640, 691

Vikhlinin A. et al., 2009b, ApJ, 692, 1060

Vikhlinin A. et al., 2009c, ApJ, 692, 1060

Viola M., Melchior P., Bartelmann M., 2011, MNRAS, 410, 2156

von der Linden A. et al., 2014a, MNRAS, 439, 2

von der Linden A. et al., 2014b, MNRAS, 443, 1973

Vulcani B. et al., 2013, A&A, 550, A58

Weller J., Battye R. A., 2003, New Astronomy Review, 47, 775

White M., Cohn J. D., Smit R., 2010, MNRAS, 408, 1818

White S., Navarro J., Evrard A., Frenk C., 1993, Nature, 366, 429

White S. D. M., Efstathiou G., Frenk C. S., 1993, MNRAS, 262, 1023

Williamson R. et al., 2011a, ApJ, 738, 139

Williamson R. et al., 2011b, ApJ, 738, 139

Wylezalek D. et al., 2014, ApJ, 786, 17

Zenteno A. et al., 2011, ApJ, 734, 3

Zhang P., Pen U.-L., 2005, Physical Review Letters, 95, 241302

Zhang Y.-Y., Laganá T. F., Pierini D., Puchwein E., Schneider P., Reiprich T. H., 2011, A&A, 535, A78

Zhang Y.-Y., Laganá T. F., Pierini D., Puchwein E., Schneider P., Reiprich T. H., 2012, A&A, 544, C3

Zibetti S., White S. D. M., Schneider D. P., Brinkmann J., 2005, MNRAS, 358, 949

Ziparo F. et al., 2013, MNRAS, 434, 3089

Ziparo F. et al., 2015, ArXiv e-prints

Zwicky F., 1933, Helvetica Physica Acta, 6, 110

Zwicky F., 1951, PASP, 63, 61

Zwicky F., Kowal C. T., 1968, "Catalogue of Galaxies and of Clusters of Galaxies", Volume VI